

Solidification of cast iron - A study on the effect of microalloy elements on cast iron

Moumeni, Elham; Hattel, Jesper Henri; Tiedje, Niels Skat; Horsewell, Andy

Publication date:
2013

Document Version
Publisher's PDF, also known as Version of record

[Link back to DTU Orbit](#)

Citation (APA):

Moumeni, E., Hattel, J. H., Tiedje, N. S., & Horsewell, A. (2013). Solidification of cast iron - A study on the effect of microalloy elements on cast iron. Kgs. Lyngby: Technical University of Denmark (DTU).

DTU Library

Technical Information Center of Denmark

General rights

Copyright and moral rights for the publications made accessible in the public portal are retained by the authors and/or other copyright owners and it is a condition of accessing publications that users recognise and abide by the legal requirements associated with these rights.

- Users may download and print one copy of any publication from the public portal for the purpose of private study or research.
- You may not further distribute the material or use it for any profit-making activity or commercial gain
- You may freely distribute the URL identifying the publication in the public portal

If you believe that this document breaches copyright please contact us providing details, and we will remove access to the work immediately and investigate your claim.



Solidification of cast iron - A study on the effect of microalloy elements on cast iron

By
Elham Moumeni

Department of Mechanical Engineering

Process Modelling Group

Technical University of Denmark

Preface

This PhD project has been carried out in the Department of Mechanical Engineering, Technical University of Denmark over the period of May 2010 - April 2013.

The present work has been performed under the supervision of Professor Jesper J. Hattel and co-supervision of Associate Professor Niels S. Tiedje, Professor Andy Horsewell and Dr. Cem C. Tutum. I would like to express my gratitude for their leading role as well as their encouragements and supports.

This work has been partially accomplished in the laboratories of Department of Materials Science and Engineering at Ohio State University during fall 2011 in collaboration with Professor Doru Stefanescu and Dr. Sarum Bonmee.

I am grateful to the staff of the Centre for Electron Nanoscopy (CEN) at DTU for their technical and scientific support as well as the colleagues at the Section of Materials and Surface Engineering.

My gratitude also goes to my colleagues in the Process Modelling Group for their unlimited support, friends for their sincere help and family for their unconditional love.

Elham Moumeni
April 2013

Abstract

The present thesis deals with the heat transfer and solidification of ductile and microalloyed grey cast iron. Heterogeneous nucleation of nodular graphite at inclusions in ductile iron during eutectic solidification has been investigated. A series of ductile iron samples with two different inoculants in four different thicknesses has been produced and studied; chemical analysis, metallographic investigation and thermal analysis of the specimens have been carried out.

A numerical model for solidification of ductile iron has been implemented and the results (i.e. cooling curve, cooling rate, nodule count and fraction of solid phases) have shown a good agreement with experimental studies; following this, inoculation parameters in the model have been studied and discussed.

The effect of Ti and S on the microstructure of grey iron is studied. Optical and electron microscopy are used to examine the unetched, colour-etched and deep-etched samples. It was confirmed that in irons with high sulphur content (0.12 wt%) nucleation of type-A and type-D graphite occurs on Mn sulphides that have a core of complex Al, Ca, Mg oxide. An increased titanium level of 0.35% produced superfine interdendritic graphite ($\sim 10\mu\text{m}$) at low (0.012 wt%) as well as at high S contents. Ti also caused increased segregation in the microstructure of the analysed irons and larger eutectic grains (cells). The inclusions have been identified in an effort to explain the nucleation of the phases of interest. The reasons for increase in the fraction of primary austenite and formation of superfine interdendritic graphite have been investigated using Thermocalc simulations and metallographic studies. TiC did not appear to be a nucleation site for the primary austenite as it was found mostly at the periphery of the secondary arms of the austenite, in the last region to solidify.

The superfine graphite which forms in this type of irons is short (10-20 μm) and stubby. The microstructure of this kind of graphite flakes in titanium alloyed cast iron is studied using electron microscopy techniques. The methods to prepare samples of cast iron for comprehensive transmission electron microscopy of graphite and the surrounding iron matrix have been developed and explained. Dual beam microscopes are used for sample preparation. A TEM study has been carried out on graphite flakes in grey cast iron using selected area electron diffraction (SAED). Based on the SAED pattern analysis, crystallographic orientations are identified and compared. Subsequently, the orientation relationship between iron and graphite crystals at the interface is studied and discussed.

Based on this information, growth models for the platelets in the fine graphite flakes in cast iron are suggested and discussed.

Table of Contents

Introduction.....	3
1.1. Motivation of the work.....	3
1.2. Graphite in cast iron	4
1.3. Structure of the thesis.....	5
Theory	7
2.1. Heat transfer modelling.....	7
2.2. Cast iron solidification	8
2.2.1. Nucleation of graphite in the melt.....	10
2.2.2. Ductile iron.....	11
2.2.3. Flaky graphite iron	13
2.3. Effect of alloy elements on the solidification and microstructure.....	15
2.3.1. Titanium in cast iron	16
2.4. Effect of cooling rate on the microstructure of cast iron.....	17
Heat transfer and solidification of ductile iron.....	19
3.1. The microstructure evolution model	20
3.1.1 Nucleation and growth of primary graphite	21
3.1.2 Eutectic solidification.....	24
3.1.3 The 1D explicit model of heat transfer.....	27
3.2. Experimental results.....	28
3.2.1. Microstructure, nodule count, size distribution and cooling curves.....	29
3.3. Effect of the nucleation parameters on the numerical results.....	32
3.4. Summary	36
A study on the microalloyed cast iron	37
4.1. Experimental set-up.....	37
4.1.1. Casting procedure.....	38
4.2. Metallography/optical microscopy investigation	39
4.3. Methodology and the instruments for electron microscopy investigations.....	44

4.3.1. Instruments and techniques	45
i) In-situ Lift-out technique	45
ii) TEM techniques	47
4.4. SEM study	48
4.5. TEM results	55
4.5.1. Bright field imaging	56
4.5.2. Diffraction patterns and dark field imaging	58
4.5.3. Orientation relationship between graphite and iron	61
4.6. Discussion	62
4.6.1. Inclusions and the primary austenite	62
4.6.2. Superfine interdendritic graphite	64
Summary of the articles	66
5.1. Paper I	66
5.2. Paper II	66
5.3. Paper III	67
5.4. Paper IV	67
Conclusions and future work	68
Bibliography	71
Appendixes	74
A Paper-I	75
B Paper-II	84
C Paper-III	93
D Paper-IV	115

Chapter 1

Introduction

The solidification and graphitization of cast iron have been attracting many scientists over the last decades, but still the mechanism of formation of some types of graphite is not well understood. The graphite microstructure remains the most important factor influencing the required properties of cast iron [1] [2] [3]. Therefore, its exact characterization is one of the main indicators for mechanical properties [4].

Graphite morphology, size and distribution can be more or less efficiently controlled in the modern foundry industry using certain alloying elements and inoculation, as well as varying processing technology such as cooling rates and overheating of the melt [5]. Among all, addition of alloying elements is the main interest in this work, whereas small amounts of alloy elements in the cast iron can improve the depth of chill, hardness and strength. Moreover, alloy elements are responsible for the amount and shape of graphite precipitated in the casting, as well as for the constitution of the iron matrix and inclusions precipitated during solidification and subsequent cooling to room temperature [6].

1.1. Motivation of the work

The main solidification parameters affecting the mechanical properties of hypoeutectic grey (lamellar graphite) irons include the fraction of primary austenite and the shape, size and distribution of graphite. In foundry practice they are controlled through the chemical composition (carbon equivalent and alloying elements) and inoculation. Recently, using appropriate titanium (Ti) addition in a low sulphur (S) 4% carbon equivalent grey iron, Larrañaga *et al.* [7] [8] increased significantly the austenite fraction. This was accompanied by the solidification of, what they termed, superfine lamellar interdendritic graphite, which was associated with high tensile strength of 300-350 MPa, without a significant increase in hardness, which remained in the range of 185-200HB. The superfine graphite is short (10-20 μ m) and stubby. Thermal analysis on standard cooling curve cups and keel blocks indicated an increase of the liquidus temperature with Ti, suggesting an austenite nucleation effect. The eutectic temperature decreased and overall the liquidus/eutectic temperature interval significantly increased. This was interpreted as increased time for austenite solidification, which explains the increase in the austenite fraction. Since increasing the amount of primary austenite increases the strength of cast iron, this is a matter of importance and is analysed in the present project [Moumeni; Tiedje; and Hattel, Paper II] [9] and [Moumeni; Stefanescu; Tiedje; Larrañaga and Hattel, Paper III] [10].

Titanium is well-known to be a deoxidizer and structure refiner in steel. For the case of cast iron, it has been argued that Ti addition refines the secondary arm spacing in both grey and ductile iron [11] [12] and increases the number of austenite dendrites by reducing the carbon equivalent [13]. It has also been observed that Ti addition favours formation of type-D graphite [14] [9] and increases the graphite type A-to-D transition temperature [15].

Part of the present work was undertaken in an attempt to clarify the role of Ti with and without S in promoting increased fraction of austenite and superfine graphite [9] [10]. The microstructure investigations also involved the use of the commercial software ThermoCalc for thermodynamical analyses. A detailed analysis of the graphite through optical and electronic microscopy is also provided, with particular attention given to the various inclusions that may serve as nuclei for the phases of interest.

1.2. Graphite in cast iron

The crystallographic structure of graphite has been studied by many scientists such as in Refs. [16] [17] [18] [19] [20]. It has been suggested that the growth of graphite is mainly determined by the composition of the liquid iron in which the graphite grows during solidification [21]. For nodular graphite the radial growth of the conical crystals is suggested by Double and Hellawell [22]. They also believe that spheroidal graphite is the preferred morphology in a clean melt, while flaky graphite is an impurity modified form. For the flaky graphite, the growth direction of the graphite lattice is observed to be mainly perpendicular to the graphite-basal planes [16]. The usual structure of graphite which is hexagonal was proposed by Hull [23] and confirmed by Bernal [24] and Hassel and Mark [25]. It is basically consisting of basal layers of carbon atoms bonded in a continuous hexagonal network and is composed of four atoms per unit cell. The layers are stacked ideally in an ABAB sequence but since the layers are relatively wide spaced and bonds are weak they may easily slide or tilt relative to one another.

Later, an X-ray diffraction study of graphite showed inexplicable peaks not belonging to hexagonal graphite [26]. It was concluded that graphite may also have a rhombohedral structure when stacking faults occur in the crystal. On the basis of a rhombohedral unit cell including six atoms the stacking sequence becomes ABCABC [27]. A schematic picture of these two models are shown in Fig. 1. In the 1960es, dislocation structure and twins in graphite were observed. In a graphite crystal, with the layers of planes arranged in the hexagonal stacking sequence, the associated stacking fault will be a region of the crystal arranged in the rhombohedral stacking sequence.

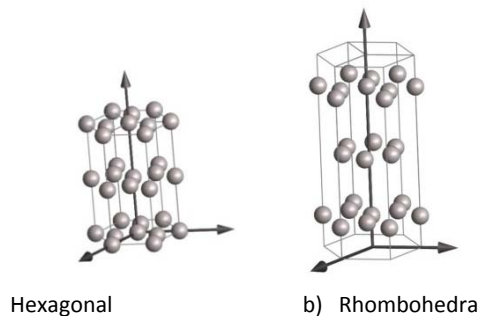


Fig. 1. Two models for graphite crystal structure (made by the software "JEMS" student edition, CIME-EPFL Lausanne)

Several different reactions normally contribute to graphite formation in cast irons. The bulk of the graphite formed by eutectic solidification forms the inner part of the larger particles, while precipitation from austenite and the stable eutectoid reaction deposit the outer layers. Therefore, the remaining iron/Graphite interface is believed to be formed in the solid state [28]. Thus in order to understand the evolution of the interface, all three phases must be considered.

Ferrite/graphite interfaces in commercial cast irons have been shown to prefer two particular orientation relationships [28]. Both relationships are found in both grey and ductile irons. Adsorption of impurities at the graphite/liquid interface plays an important role in the formation of lamellar graphite. S and oxygen (O) are found by Scanning Auger Microscope (SAM) adsorbed at the graphite/melt interface during solidification of grey iron [29]. The adsorbed elements influence the growth sites on the basal planes and thereby stabilize the interface, resulting in the formation of flakes. In the present work it is shown that this phenomenon in the case of interdendritic superfine graphite is different.

The experimental part of the present work is directed towards analysis of how microstructures in the microalloyed cast iron develop during solidification [Moumeni; Tiedje; Grumsen; Danielsen; Horsewell and Hattel, Paper IV] [30]. Highly advanced 3D methods using a range of new techniques provided by the new electron microscopes at the CEN DTU are used to prepare samples for electron microscopy study. These new techniques allowed us to characterize the materials from nano-scale to mm-scale. The primary new electron microscopy tool of relevance to this project was a dual beam instrument in which one column provides a focused ion beam (FIB). The FIB is used to sputter down through the microstructure layer-by-layer, while the second column comprises a scanning electron microscope (SEM) which can collect sequential images of the successive layers. This technique enabled us to prepare samples of graphite and the surrounding iron matrix in the form of thin foils for TEM investigation. Consequently, the mechanism of formation of new forms of graphite (superfine interdendritic) was carried out and confronted with the regular flaky graphite in grey iron. Moreover, the selected area electron diffraction (SAED) pattern technique has been applied to investigate the orientation relationship between the graphite and the iron matrix in detail at the interfaces of graphite and iron. The microstructure investigations also involved the use of JEMS commercial software package for a detailed crystallographic analysis.

The final goal of this project is to build more reliable wind turbine cast parts (hub, etc.) with better physical and mechanical characteristics and perhaps lower cost.

1.3. Structure of the thesis

The thesis includes 5 chapters which are followed by 4 appended articles.

In *Chapter 1*, the motivation of the work and a brief background has been given with an overview of the microalloyed cast iron.

Chapter 2, consists of the theory and the literature survey about solidification of cast iron including the nucleation and the growth of primary and eutectic phases. Different types of graphite are explained in this chapter too.

Chapter 3, is focused on applying numerical process modelling and experimental analysis tools for the prediction and characterization of microstructure of cast iron. In particular, the solidification of hypereutectic ductile iron has been studied.

The model developed by Pedersen has been used to simulate the microstructure evolution during solidification in the technical computer language MATLAB. The model has mainly been used for test and validation of the experiments. Moreover, a parameter study for the nucleation model has been carried out and the experimental results have been compared with the numerical outputs.

Chapter 4, presents a comprehensive study on the effect of S and Ti on the microstructure of grey iron. In this chapter the experimental results including metallographic investigations of this group of irons by both optical and electron microscopy methods are presented and discussed. A comprehensive TEM study on the superfine interdendritic graphite which is the result of the addition of Ti in the grey cast iron has been conducted and explained.

In *Chapter 5*, a summary of the appended articles is given.

Finally in *Chapter 6*, the conclusions of this PhD thesis and suggestions for the future work are presented.

The articles are enclosed in the *Appendixes*.

Chapter 2

Theory

2.1. Heat transfer

The casting process is in essence characterized by three main steps: Pouring the melt into the mould cavity, solidification of the melt and subsequent solid state cooling. The distinction between these steps is however not totally sharp for the casting as a whole since one step can actually start before the preceding one has been totally finalized (solid state cooling might start in some areas of the casting while others are still solidifying).

So, if we want to describe and model casting mathematically we in general need proper models for the physical phenomena taking place such as fluid flow, heat transfer, microstructural evolution, formation of transient and residual stresses and so forth.

However, since the purpose of the present thesis is the solidification of cast iron we will naturally limit ourselves to focus on the heat transfer and microstructural evolution which takes place during solidification. In essence heat flows from the casting to the mould and to the surrounding environment. At some point during solidification, the casting at the macro-scale constitutes of at least two phases which are solid and liquid and depending on the alloy composition, cooling conditions, mould material, etc. the solidification morphology can take various forms, e.g. columnar, equi-axed, and planar.

Any solidification model is in essence based on the energy equation with release of latent heat which in turn comes from energy conservation or the first law of thermodynamics within a volume element, i.e.:

Net heat flux into the element + heat generated inside element per unite time (e.g. latent heat) = change in heat content per time

The heat flux is given by Fourier's law of heat conduction which states that there is an energy transfer due to conduction from the high temperature region to the low temperature region

$$\frac{q}{A} = k \frac{\partial T}{\partial x} \quad \text{Eq. 1}$$

where q/A [W] is the heat flux normal to the surface of the area A ; A [m^2] is area of the surface, through which the heat flows; k [W/mK]; is the thermal conductivity; T [K] is the temperature and x [m] is the descriptive space parameter perpendicular to the surface. The minus sign is due to the opposite direction of the heat flow and the temperature gradient. Fourier's law is the defining equation for the thermal conductivity (k) which may be measured for each material.

Now, combining with energy conservation we obtain the heat conduction equation in 1-D on the following form:

$$\rho c_p \frac{\partial T}{\partial t} = \frac{\partial}{\partial x} \left(k \frac{\partial T}{\partial x} \right) + \dot{Q} \quad \text{Eq. 2}$$

Where ρ is density [W/m^3], c_p is specific heat capacity [$J/(kgK)$] and \dot{Q} is the volumetric heat generation per time [W/m^3]. In the 3-D case eq.(2) takes the form:

$$\rho c_p \frac{\partial T}{\partial t} = \frac{\partial}{\partial x} \left(k \frac{\partial T}{\partial x} \right) + \frac{\partial}{\partial y} \left(k \frac{\partial T}{\partial y} \right) + \frac{\partial}{\partial z} \left(k \frac{\partial T}{\partial z} \right) + \dot{Q} \quad \text{Eq. 3}$$

The derivation of these equations is explained in details in many text books on heat conduction, see for example the references [31] [32].

The heat conduction equation which is a partial differential equation (PDE) needs proper information on geometry, boundary conditions and material data. So when doing actual solidification simulation the related empirical information such as the material data and the geometry should be defined first. More specifically, the required thermophysical material data such as densities, specific heat capacities, and thermal conductivities for all of the materials in the casting system and the latent heat of fusion for the cast alloy should be defined with the highest possible accuracy. In addition, the process parameters such as the initial conditions for the unknown quantities need to be specified. For instance, initial temperatures and the interface heat transfer coefficient between the various materials in the casting system are required.

After defining all this, the mesh generation can be performed and the governing differential equation - in essence eq.(3) in the case of solidification simulation can be solved together with the relevant expressions for microstructural evolution. This will all be addressed in more detail in chapter three where the developed model for the solidification of cast iron is presented.

2.2. Cast iron solidification

Cast iron is one of the most complex alloys used in industry. The complexity is mainly because it can solidify with formation of either a stable (austenite-graphite) or a metastable (austenite- Fe_3C) eutectic. Moreover, various graphite shapes exist depending on chemical composition and cooling rate.

The microstructure formation in cast iron during the liquid-solid transformation includes two stages. The first stage is solidification of proeutectic or off-eutectic phases which are austenite (γ) dendrites in hypoeutectic irons, and graphite crystallization from the liquid in hypereutectic

cast irons (before the onset of eutectic solidification). The second stage is solidification of stable/metastable eutectics and includes the eutectic austenite and the various shapes of the carbon-rich phases (graphite or carbide). In cast irons, the eutectic solidification involves coupled growth of eutectic phases which is highly dependent on chemical composition and cooling rate. This phenomenon will be explained later in the following sections.

The phase diagram for Fe-C is shown in Fig. 2. In order to ensure that carbon precipitates as graphite during solidification, silicon is commonly added to the Fe-C system.

Addition of Si to cast iron is essential because it increases the carbon equivalent and stabilizes the Fe-C phase diagram (Fig. 3). In other words, it increases the stable and decreases the metastable eutectic temperature [33].

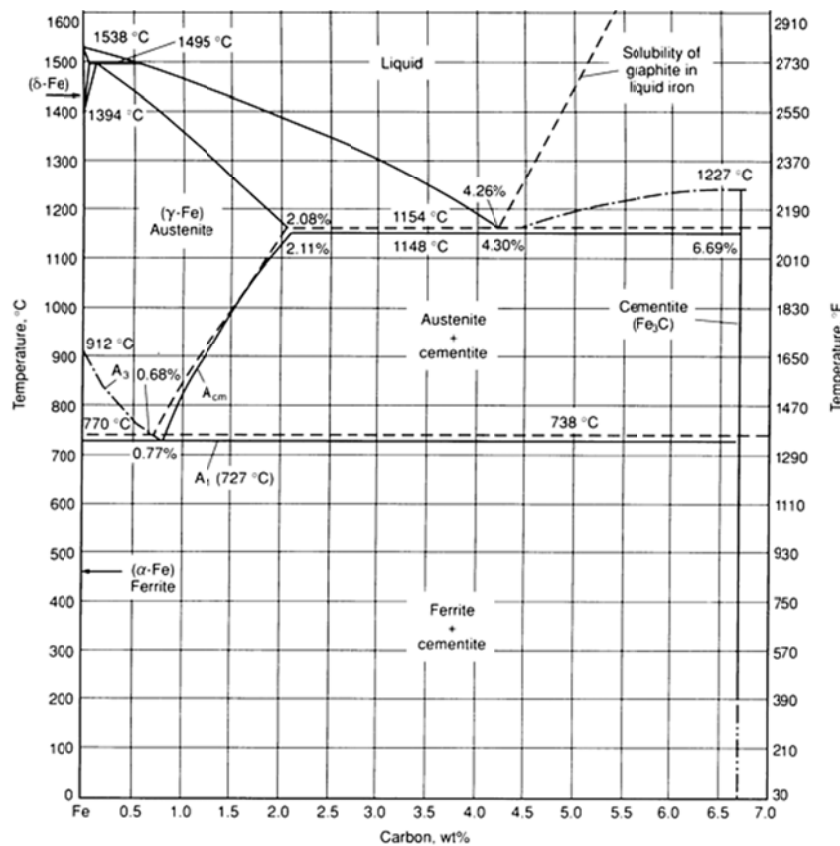


Fig. 2. Phase diagram for Fe-C. Solid line shows the metastable and dash line shows the stable diagram [34]

The carbon Equivalent (CE) is an empirical value, relating the combined effects of different alloying elements (in weight percent) used in the making of cast iron and steels to an equivalent amount of carbon. This value can be calculated using various mathematical expressions. One of the suggested expressions for calculating the carbon equivalent value for cast iron at the presence of Si and P is presented in the equation below [35]:

$$C_{EV} = \%C + 0.317.\%Si + 0.33.\%P \quad \text{Eq. 4}$$

Depending on chemical composition and cooling rate, graphite can be precipitated in various shapes. The graphite classification represented in the DIN standard [36] is shown in Fig. 4.

Solidification of flaky graphite (FG) iron (mainly containing graphite class I) and ductile iron (containing graphite class VI) will be explained in more details in the following. In order to decrease the risk of a metastable eutectic reaction, cast iron is usually inoculated. The addition of inoculant can be early (in the ladle) or late (during pouring to the mould or in the mould) during the casting process.

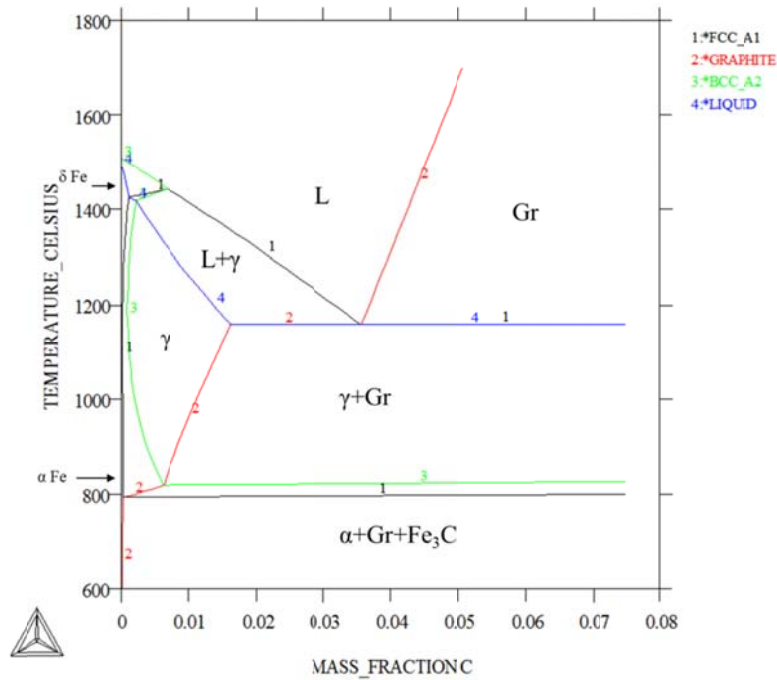


Fig. 3. Stable isopleth Fe-C-Si phase diagram at 2.5% Si (mass per cent), calculated by ThermoCalc.

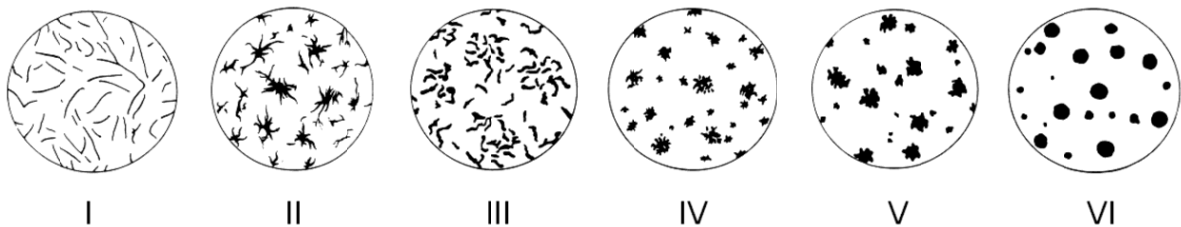


Fig. 4. Schematics of the six types of graphite - DIN EN ISO 945 [36]

2.2.1. Nucleation of graphite in the melt

Crystallization of graphite in the melt starts with nucleation, which is strongly affected by undercooling. In 1961 Oldfield [33] quantified the nucleation and growth of eutectic cells and that was the beginning of the effort of building the extensive database required for solidification modelling of cast iron. Lux [37] suggested in 1968 that, when Ca, Ba and Sr in the inoculation of FG iron are present in molten iron, these metals form salt-like carbides that provide epitaxial planes with the graphite, and hence forms nuclei for graphite. Later, Weis [38] assumed that nucleation of FG occurs on SiO₂ oxides formed by heterogeneous catalysis of CaO, Al₂O₃, and oxides of other alkaline metals. A similar theory of double-layered nucleation was proposed at the same time for nodular graphite. Using the results of SEM analysis, it was shown that [9] SG nucleates on duplex sulfide-oxide inclusions of about 1 μm diameter; the core is made of Ca-Mg or Ca-Mg-Sr sulfides, while the outer shell is made of complex Mg-Al-Si-Ti oxides. The idea

was to a greater extent developed by Skaland et al. [39]. They contended that nuclei for nodular graphite are sulfides (MgS, CaS) covered by Mg silicates (e.g., MgO·SiO₂) or oxides (Fig. 5). After inoculation with FeSi that contains another metal (X) such as Al, Ca, Sr or Ba, hexagonal silicates (XO·SiO₂ or XO·Al₂O₃·2SiO₂) form at the surface of the oxides, with coherent/semicoherent low energy interfaces between substrate and graphite [40].

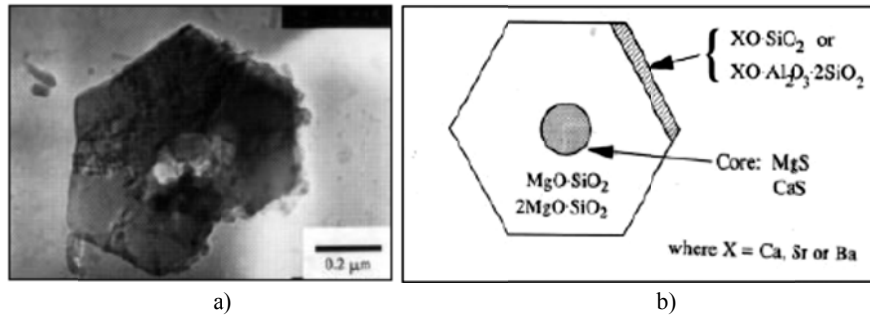


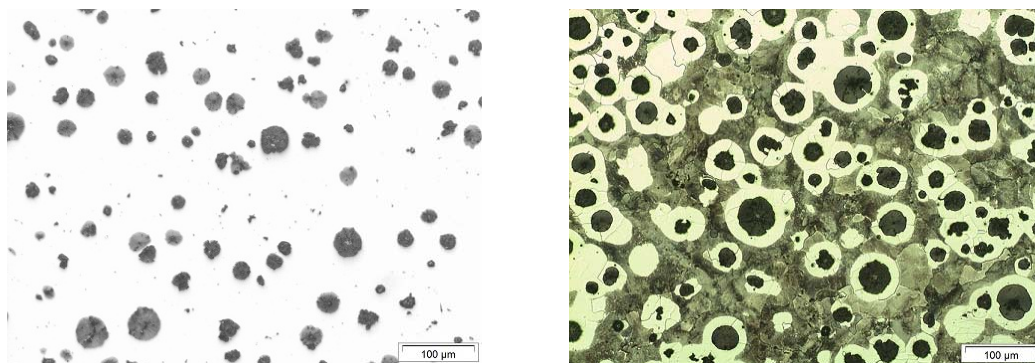
Fig. 5. (a) Example of duplex sulphide/oxide nuclei particle in ductile iron at large magnification in a transmission electron microscope (70,000X). (b) Schematic representation of a nucleus particle containing complex sulphide and oxide phases after nodularizing and inoculation of the iron [41].

As mentioned before, C and Si are mainly added to obtain free graphite in the amount and distribution to give the material the desired properties. The manganese content is selected to give the required matrix properties. Usually, it can be chosen as about 0.1% for ferritic matrix and about 1.2% for pearlitic matrix, as Mn is a strong pearlite promoter [34].

2.2.2. Ductile iron

Ductile iron is an Fe-C-Si alloy in which spheroidal or nodular graphite (typically denoted SG) precipitates and has excellent mechanical properties. The nodular shape of graphite increases the ductility and decreases the risk of crack initiation as in the flaky graphite iron. Moreover, ductile iron shows good ductility and toughness because the graphite morphology is spherical. In the conditions of good nodularity and distribution of nodules, further strengthening and toughening of ductile iron can be obtained by changing the matrix.

In Fig. 6, one of the typical microstructures for ductile iron is depicted. A higher volume fraction of ferrite in the structure of iron will lead to lower strength and hardness, but higher ductility and machinability compared to the iron with a higher volume fraction of pearlite.



a) Ductile iron polished and un-etched
b) Pearlitic-ferritic ductile iron, etched by Nital 2%
Fig. 6. Ductile iron, optical microscopy images, taken by the author.

The production of ductile iron is performed under accurate metallurgical and metallographic control. The typical composition of ductile iron is presented in Table 1 [42]. Melt treatment with Mg is commonly used to obtain spheroidal graphite (SG). In order to avoid the risk of explosion, Mg is often alloyed with other elements such as Fe, Si or Ni. After Mg treatment, due to oxidation and evaporation, the magnesium fades away. Thus, casting needs to be done within a certain time after Mg-treatment; otherwise the spheroidized graphite will partly disappear. Cerium and lanthanum are also two alternatives to Mg for spheroidizing the graphite. Ce can be added to the melt as NiCe or SiCe [42].

Table 1. the average composition of ductile iron

Element	Content (wt-%)
C	3.3-3.8
Si	1.8-2.5
Mn	0.1-0.7
P	≤ 0.1
S	≤ 0.1

In the absence of impurities such as S and O, the normal growth of the graphite phase leads to a nodular morphology [17]. In fact, the role of modifiers such as Mg and Ce is scavenging the impurities.

The graphite nodules form in the melt and will be surrounded by an austenite shell. Graphite grows mainly by diffusion of carbon through this austenite shell. The γ -SG eutectic is a divorced eutectic. However, a number of studies have shown that primary austenite dendrites play a significant role in the eutectic solidification of SG. Two types of dendrites exhibiting non-similar morphologies can be identified: primary austenite dendrites and eutectic SG grains [32]. The morphology of the primary austenite dendrites is typical for dendrites in metallic alloys. They exhibit clear primary and secondary arms (Fig. 7a). The eutectic SG grains (Fig. 7b) are thick and rounded, suggesting a cauliflower shape. There is no clear distinction to be found between primary and secondary arms. It is observed that the SG grains are made of several graphite nodules surrounded by quasi-spherical austenite envelopes. This multi-nodular morphology of the SG eutectic grain can be revealed with other techniques, such as colour etching metallography, first introduced by Rivera et al. (1997).

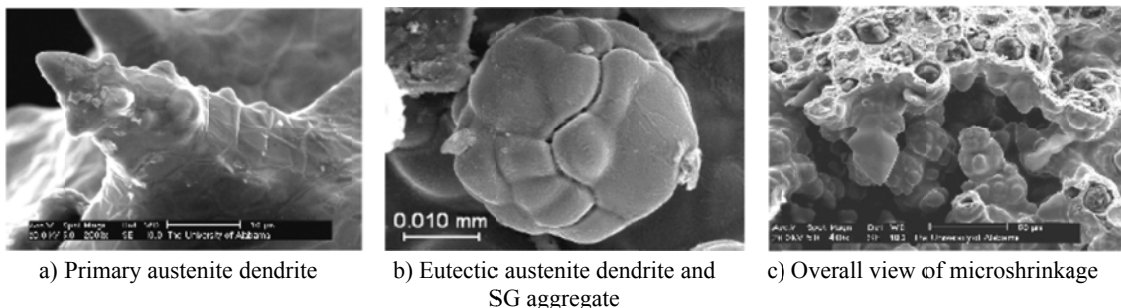


Fig. 7. Microstructures of ductile iron found in the same microshrinkage cavity from a SG iron plate (Ruxanda et al., 2001). Copyright 2001 AFS.

2.2.3. Flaky graphite iron

In FG iron, graphite lamellae start growing from a common centre and stay in contact with the melt as austenite fills the spaces between the lamellae (Fig. 8). It is considered as a cooperative irregular eutectic which grows with a non-isothermal interface.

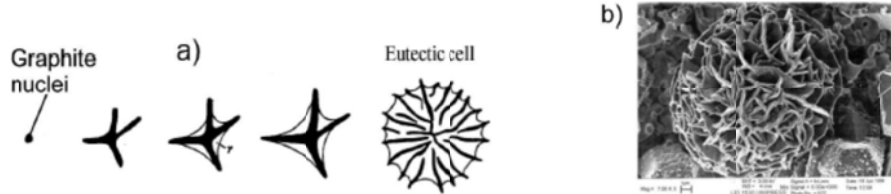


Fig. 8. (a) Sequence of solidification of graphite eutectic cell, (b) scanning electron photograph of eutectic cell [43]

Lamellar graphite in flaky graphite iron in general shows a variety of different morphologies. Commonly they have been classified as types A to E (Fig. 9). The chemical composition and cooling rate controls the formation of different classes of graphite. In fact, both major and minor elements directly influence the morphology of flaky graphite. Type A graphite is the result of good inoculation and moderate cooling rates and usually it is associated with the best mechanical properties. Type B graphite can be commonly found in irons of near-eutectic composition, and is associated with a large eutectic cell size and low undercooling, solidifying on a limited number of nuclei. Hypereutectic irons solidified with minimum undercooling will result in type C. Types D and E occur when undercooling is high [34].

Diószegi et al. [44] have discussed the mechanical properties of FG iron in a study of the fracture mechanism of the material at failure. They showed that the most important microstructure components determining the strength of grey iron are primary solidification phases (primary austenite and primary carbides) and the graphite flakes.

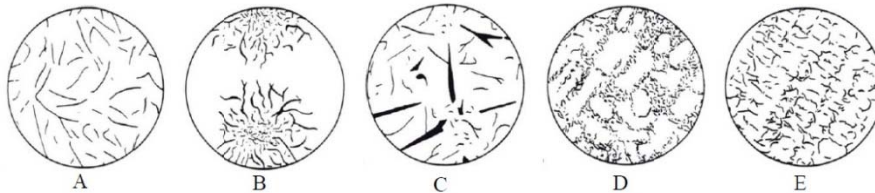


Fig. 9. Schematics of the five classes of flaky graphite - DIN EN ISO 945 [36]

Several studies have shown that flaky graphite is produced as a result of modification with S and O. These elements are believed to adsorb on the graphite-liquid interface and thereby changing the interface energy so that graphite growth is affected. According to the present literature survey, the debate on the preferred growth direction of graphite was initiated by Herfurth [45] who in 1965 argued that the change from lamellar to spheroidal graphite occurs because of the change in the ratio between growth on the $[1\ 0\ \bar{1}\ 0]$ face (the $-a$ - direction) and growth on the $[0\ 0\ 0\ 1]$ face of the graphite prism ($-c$ - direction). Experimental evidence for growth on both of these directions was provided by Lux et al. [46] in 1974.

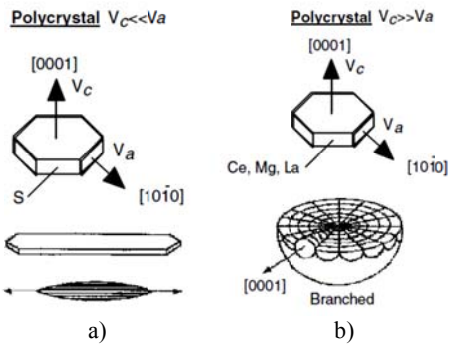


Fig. 10. Change in the growth velocity of graphite according to Herfurth (1965):
 a) Due to adsorption of S and O on the prism faces; b) Due to spheroidizers added as scavengers of impurities [32].

The preferred sites for adsorption will not be on the basal planes (which grow in the $-c$ -direction), but rather at the $[1\ 0\ \bar{1}\ 0]$ plane (in the $-a$ -directions). As evidence, Auger analyses confirm concentrations of O and S in iron adjacent to the metal-graphite interfaces in two or three atomic layers [29]. The adsorbed impurities poison the growth sides on the basal planes and result in formation of flakes. Sulfur and oxygen (solute) atoms will be rejected into the liquid, sideways at the growing edges, so that the flakes are enveloped by metal as Auger analysis shows.

For FG iron, the growth rate of austenite and that of graphite along the $[1\ 0\ \bar{1}\ 0]$ direction is approximately the same; thus austenite and graphite grow as a regular eutectic (Fig. 11).

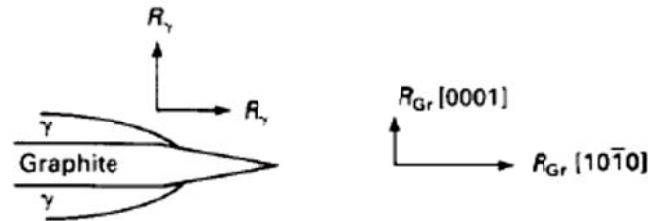


Fig. 11. Different graphite growth rates in lamellar growth. $R_{Gr}[1\ 0\ \bar{1}\ 0]$, determines the lamellar habits of graphite flakes, while $R_{Gr}[0001]$ gives the rate of thickening for the flake. [47]

Graphite type-D or undercooled graphite has a very fine graphite structure compared to the A-type and it occurs in the shape of rods (Fig. 12). The solidification front of type-D graphite is relatively even. The formation process in general can be characterized as a normal cooperative eutectic reaction. The formation of this type of graphite is favoured by high undercooling but is also promoted by some elements. Low-concentration of sulphur and oxygen is shown to be promoting the formation of undercooled graphite [48].

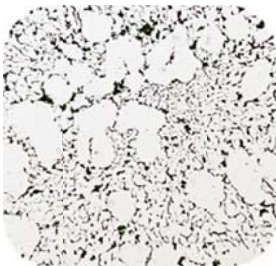


Fig. 12. Graphite type-D, (also called undercooled), optical microscopy image

For the inoculated cast iron, there is a greater tendency towards the formation of type A (lower growth rate) than in the uninoculated cast iron, while the higher growth rate gives a higher chance for the formation of type D.

The interfacial distance λ is the distance between the branches of a continuous skeleton of graphite in the eutectic cell. The distance is much lower in the type D than in the type A (Fig. 13).

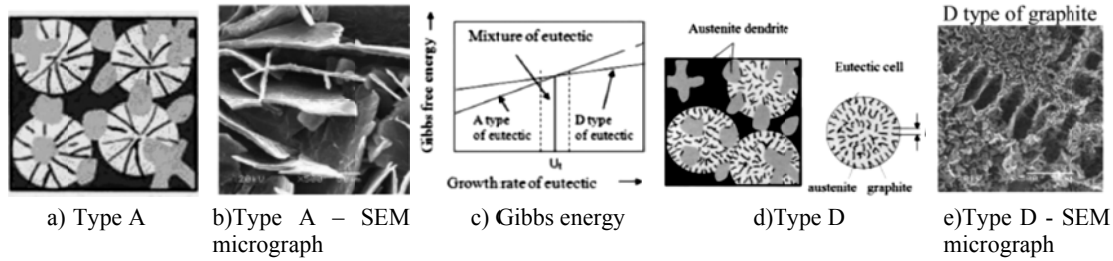


Fig. 13. Schemes of solidification of hypereutectic cast iron and interfacial distances between graphite precipitations (a,d); appearance of graphite type A and D in scanning electron microscopy (b,e); Influence of growth rate on free energy of eutectics (c) [49]

The theory of eutectic growth [50] indicates that the eutectic lamellar spacing depends on the solute rejecting and it has an inverse relationship with the growth rate. Below a critical growth rate [51] [52], the type A is formed since it has the lowest free energy, while above this range, the type D is produced because its free energy is lower than that of the A type.

2.3. Effect of alloy elements on the solidification and microstructure

Alloy elements can be added to cast iron to meliorate some of the mechanical properties. They influence both the graphitizing potential and the structure of matrix.

The graphitizing effect of some common alloy elements for cast iron is illustrated in the so-called principal diagram of Bunyin in Fig. 14. As seen in this figure, carbon and silicon play the most important role in graphitizing of cast iron. Sulfur is a strong carbide promoter, although in the presence of manganese, these two elements can combine and neutralize each other [34]. As mentioned in section 2.2.1. , the resultant MnS can also serve as nucleation site for graphite.

It is well-known that in the two component Fe-C alloy system, the carbon content of the eutectic composition is about 4.26%. The alloys composition relative to the eutectic point is of great importance, since the hypoeutectic composition is more favourable with regards to the mechanical properties. Addition of alloy elements other than Fe and C can considerably change the location of the eutectic point, even in small quantities. The influence of some of the important alloy elements for cast iron on the location of eutectic point can be calculated as below [53]:

$$C_{eut} = 4.26 - 0.317Si - 0.33P + 0.027Mn \quad \text{Eq. 5}$$

Addition of alloy elements can also change the austenite-liquidus and graphite-liquidus temperature. As a quantitative example, the influence of Si on the austenite-liquidus temperature ($T_{Aus-Liq}$) is calculated in Thermocalc as below [54]:

$$T_{Aus-Liq} [^{\circ}C] = 1569 - 97.3(\%C + 0.23.\%Si)$$

Eq. 6

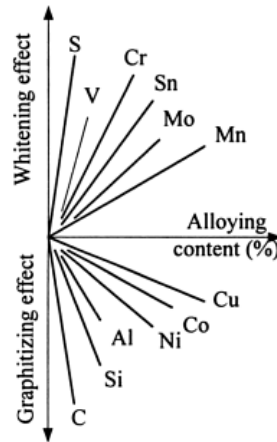


Fig. 14. Effect of alloy elements on the microstructure of cast iron [53]

Moreover, it is generally accepted that in the FG iron, the chemical composition must be chosen in a way to meet the following requirements:

- a) The desired graphite shape and distribution
- b) The required matrix
- c) A carbide free structure

An important part of the present work has been carried out to study the effects of titanium on grey cast iron. Hence, the following section provides some theories about the results of addition of this element in particular.

2.3.1. Titanium in cast iron

Ti is present in minor amounts in almost all cast irons, entering through the melt stock most typically in the pig iron or recycled material containing certain commonly used structural steels. When Ti is added to ductile iron, the shape of graphite is changed to become less spherical. As the Ti content increases, the nodules gradually break up and become “worm like”, vermicular and compacted. In fact, the balanced usage of Mg and Ti is a preferred method of producing CG cast iron [55].

In FG iron, Ti is routinely added to stabilize nitrogen due to its ability to suppress or eliminate porosity caused by an excess of nitrogen dissolved in the liquid in the melting and holding furnaces [56]. Basutkar *et al.* [57] argued that titanium additions nucleate dendrites favouring the formation of small equiaxed dendrites. Wallace and co-workers [11] [12] found that titanium additions refined the secondary arm spacing in both grey and ductile iron. Ruff and Wallace [13] concluded that the number of austenite dendrites can be increased by reducing the carbon equivalent, adding elements, such as Ti and B, which increase the undercooling by reducing the nucleation potential for graphite or restricting the growth of the eutectic cell, or by adding materials that serve as substrates for austenite nucleation (nitrides, carbonitrides and carbides of various elements such as Ti and V). Okada [14] suggested that Ti additions resulting in the formation of TiC, produce low carbon regions at the solid/liquid interface, favouring formation of type-D graphite. Using SEM/EDS analysis, Zeng *et al.* [58] identified the presence of

different Ti compounds in hypoeutectic grey irons containing about 0.08%S and up to 0.02%Ti. The compounds included TiN (35at%N), (MnTi)S and TiC. Nakae and Fujimoto [15] identified a graphite type A-to-D transition temperature, $T_{A/D}$, using thermal analysis. Titanium additions increase the $T_{A/D}$ temperature and thus favour type-D graphite formation at smaller undercooling. Yet, no explanation for this behaviour has been provided.

The three reaction products of titanium observed most frequently in cast iron are titanium nitride (TiN), titanium carbide (TiC) and titanium sulfide (TiS₂) [56]. Titanium sulfide apparently is not very effective as a nucleation site for graphite. This results in a reduction in graphite nuclei and increased undercooling which may produce more primary austenitic dendrites by increasing the time between the initial formation of the dendrites and the nucleation of the eutectic. Sommerfeld and Ton [59] who used thermodynamic modelling suggested the following sequence of phase formation for a hypoeutectic iron (3.4%C, 1.5%Si, 0.7%Mn, 0.05%S, 0.04%Ti): austenite at 1195C, followed by Ti₄C₂S₂ at 1185C, followed by graphite at 1148C, followed by MnS at 1146C. Note that their calculation is based on the assumption of thermodynamical equilibrium which ignores kinetic effects. In addition to the sulfides, square-shaped TiN inclusions were also observed.

Wilford and Wilson [60] studied the influence of up to 0.4% Ti in grey iron. They stated that first, Ti will react with N producing TiN or Ti(CN) that affects the solidification of primary austenite. The excess Ti will then react with S. Formation of TiS decreases the available S for MnS formation and increases undercooling which is responsible for type-D graphite formation.

Under the rapid solidification conditions produced when Ti increased the amount of undercooling, large quantities of graphite type D and/or type E will form. This fine, highly branched structure of the graphite provides shorter diffusion distances for C and results in the austenite being able to decompose to ferrite in the areas immediately adjacent to the graphite. Thus, the iron matrix is more ferritic due to the shorter diffusion distance for C with the type D graphite, compared to type A. In this case the strength and hardness will be lowered. Okada [14] suggested that Ti additions result in the formation of TiC, produce low carbon regions at the solid/liquid interface, favouring the formation of type-D graphite. Nakae and Fujimoto [15] defined a graphite type A-to-D transition temperature, $T_{A/D}$, using thermal analysis. Titanium additions increase the $T_{A/D}$ temperature and thus favour type-D graphite formation at smaller undercooling. Yet, no explanation for this behaviour has been provided.

Ruff and Wallace showed that [13] titanium refines the secondary dendrite arm spacing in irons of higher CE (by enhancing austenite nucleation) but increases secondary dendrite arm spacing with lower CE where the dendrites grow to a considerable extent before the eutectic forms.

In summary, Titanium refines graphite, promotes formation of undercooled, type D graphite, reduces state of nucleation [61], refines secondary dendrite arm spacing in grey iron [11], segregates out of solidifying eutectic cells [62] and nucleates austenitic dendrites [57].

2.4. Effect of cooling rate on the microstructure of cast iron

The cooling rate can also remarkably affect the as-cast structure and mechanical properties of cast iron. The cooling rate of a casting is primarily a result of the casting module. As a section size increases, the cooling rate becomes smaller and vice versa. Increasing the cooling rate will first refine both graphite size and matrix structure. Consequently, this will cause a higher strength and hardness. Another effect of increased cooling rate will be increasing the chill

tendency. In this case, the hardness might increase, but the ductility decreases. Therefore, the composition must be chosen in such a way that the required graphitization potency for a given cooling rate can be obtained.

One suggestion for quantification of the effect of cooling rate and resulting undercooling on the nucleation during solidification was Oldfield's model [33]. The modified Oldfield's continuous model which is more specific for nucleation of nodular graphite is discussed in more detail in Chapter 3.

Chapter 3

Heat transfer and solidification of ductile iron

As earlier discussed in chapter two a model has been developed as part of the present work in solidification of cast iron. The aim of such model is generally to predict the thermal behaviour during solidification, the evolution of microstructures and the subsequent metallurgical characteristics and associated mechanical properties of the final product.

In essence there are two theoretical prediction methods namely analytical methods and numerical methods. The first result in closed-form solutions and hence give the possibility of performing many parameter variations in a very short time however they are often based on rather limiting assumptions regarding the complexity of the geometry and the physics which can be taken into account. For the second group of methods it is more or less the other way around. Numerical methods open up for taking more complex phenomena into account however they also inherently result in calculation times which make parameter variations much more time consuming as compared to analytical models. So, very often a compromise must be established between modelling complexity and the need for a fast answer.

During the last couple of decades numerical models have really shown their strength over analytical methods when it comes to obtaining accurate results in simulation of heat transfer during solidification. They have also made it possible to simulate microstructure evolution during the process. Since the gradual process of evolution of microstructures during solidification is closely coupled with its thermal history, numerical models are very useful to investigate relations between process conditions and microstructure.

For this purpose, in the present work a 1-dimensional numerical model has been implemented and the results (i.e. cooling curve, cooling rate, nodule count and size distribution and fraction of solid phases) have shown good agreement with corresponding experimental studies [Moumeni, Tutum, Tiedje and Hattel, Paper I] [63].

More specifically, heterogeneous nucleation of nodular graphite in ductile iron during eutectic solidification has been investigated. The experimental part of this work deals with casting of ductile iron samples with two different inoculants in four different thicknesses. Chemical analysis, metallographic investigation and thermal analysis of the specimens have been carried out.

Finally, inoculation parameters have been studied and discussed and the numerical model has been used as a simple tool for inverse analysis to obtain these parameters based on the experiments [Moumeni, Tutum, Tiedje and Hattel, Paper I].

3.1. The microstructure evolution model

It is widely accepted that eutectic solidification of hypereutectic ductile iron begins with the nucleation and growth of graphite in the liquid, and is followed by early encapsulation of the graphite spheroids in austenite shells (envelopes). Once the austenite shell is formed, further growth of graphite can occur only by diffusion of carbon from liquid through the austenite. It has been observed that during solidification of eutectic and slightly hypereutectic cast iron austenite dendrites are present which should appear only in hypoeutectic alloys according to the phase diagram. As a matter of fact the interaction between nucleation of graphite and austenite dendrites plays a significant role in eutectic solidification. Even for hypereutectic irons, the graphite spheroids do not grow in independent austenite envelopes, but rather are associated with austenite dendrites.

Rappaz et al. [64] presented a general approach to solidification modelling of nodular cast iron, based on global mass and solute balances performed at the scale of the whole grain which is a representative SG iron grain at a given time during solidification (Fig. 15). Although, they did not take into account the presence of austenite dendrites.

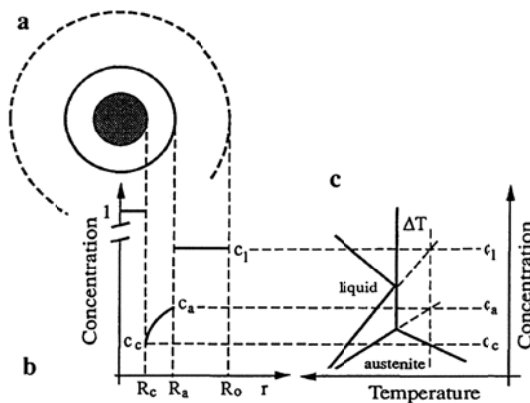


Fig. 15. The schematic representative grain for SG iron during solidification, a) Graphite nodule encapsulated in an austenite shell; b) The related carbon concentration profile of the phases and interfaces; c) The related phase diagram [64].

Lesoult et al. [65] developed a model which includes the description of the nucleation and growth of the pro-eutectic graphite in hypereutectic iron. They considered the formation of pro-eutectic austenite dendrites during solidification of both hypo- and hyper-eutectic (SG) iron too. The schematic representation of SG iron grain during eutectic solidification and the associated carbon concentration profile are depicted in Fig. 18.a. However, they assumed uniform temperature in the metal and heat extraction controlled by heat conduction in the sand.

Pedersen et al. [66] enhanced that model by applying a numerical calculation of heat flow in casting and mould, taking into account the heat transfer coefficient between the casting and the mould which can be very important for thin-walled castings. The segregation of alloying elements other than carbon, such as silicon, manganese or chromium was ignored. The model implemented in the present work [Moumeni, Tutum, Tiedje and Hattel, Paper I] is based on the same model.

This solidification model is based on the 1-dimensional version of the conduction equation which was presented in section 2.1. The generated heat per unit time per unit volume can be calculated by:

$$\dot{Q}_{gen} = \Delta H_f \rho \frac{\partial f_s}{\partial t} \quad \text{Eq. 7}$$

where $\frac{\partial f_s}{\partial t}$ is the derivative of the volume fraction of solid phase generated with respect to time and ΔH_f is the latent heat for change from the liquid to the solid phase.

A schematic illustration of the solidification path is shown in Fig. 16.a. It begins by the nucleation and growth of primary graphite particles from the melt. These two processes take place with some deviation from equilibrium. Therefore, the solidification path related to the formation of primary graphite is located somewhere below the graphite liquidus line. A typical cooling curve associated with the solidification is depicted in Fig. 16.b. Every change in the slope is representing the onset of a new phase transformation. T_{min} and T_{max} are defined as the minimum and maximum temperature during eutectic reactions.

The stages of the model are discussed in more detail in the following sections.

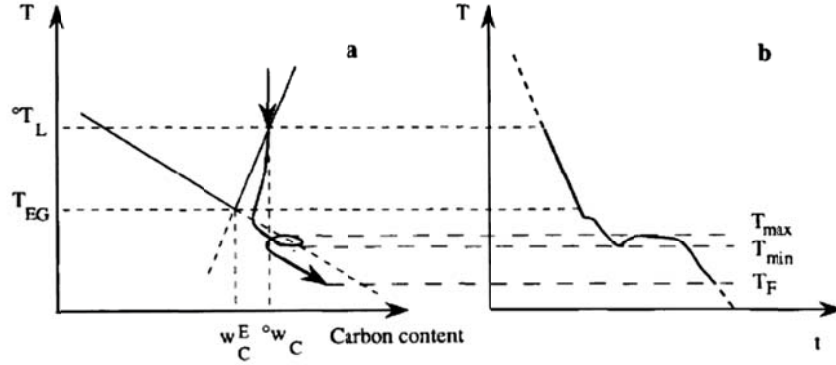


Fig. 16. a) The solidification sequence of hypereutectic iron (segregation of other elements ignored); b) The schematic associated cooling curve [65]

3.1.1 Nucleation and growth of primary graphite

As already stated in Chapter 2, the basic idea of the nucleation model of graphite nodules is taken from Oldfield [33]. The Oldfield's continuous model was modified by Lacaze et.al. [67] to include the residual volume fraction of liquid. The nucleation model in the present work is based on the model proposed by Lesoult et. al. [65]. In this model the number of nucleated graphite nodules in time step i , ΔN_i , is governed by the undercooling with respect to the graphite liquidus (ΔT_L^g). Thus, the nucleation rate can be calculated as follows:

$$\Delta N_i = A_n \cdot (\Delta T_L^g)^{n-1} \cdot f_l \cdot V^{off} \cdot \frac{d(\Delta T_L^g)}{dt} \quad \text{when } \frac{d(\Delta T_L^g)}{dt} > 0 \quad \text{Eq. 8}$$

$$\Delta N_i = 0 \quad \text{when } \frac{d(\Delta T_L^g)}{dt} < 0$$

where:

f_l is the volume fraction of the liquid;

n is a constant characterizing the inoculation efficiency;

A_n is a constant related to the amount of inoculant;

V^{off} is the volume of off-eutectic phases (at this stage only liquid);

And therefore, $f^l V^{off}$ is the volume of remaining liquid (available for nucleation).

According to the conditions, the nucleation of nodules proceeds as long as the rate of undercooling is a positive value. As explained before, graphite nodules will always be directly in contact with the liquid during the proeutectic stage (Fig. 17).

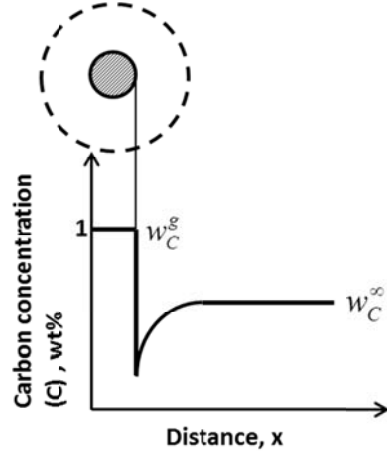


Fig. 17. Concentration profile during growth of spheroidal graphite in contact with melt, schematic illustration [68]

In the growth model, emphasis has been put on the analysis of the carbon redistribution between the graphite, the eutectic austenite, the liquid, and the non-eutectic phases. This step is based on a quasi-stationary diffusion of Carbon. The rate of growth of the nucleated graphite nodules is controlled partly by the diffusion of carbon in the liquid phase and partly by the interfacial reaction. The redistribution of carbon during the growth of primary graphite will ensure a flux of carbon, ϕ [65] :

$$\phi = -\rho^g (w_C^g - w_C^i) \frac{dr^g}{dt} \quad \text{Eq. 9}$$

where

r^g is the radius of the graphite nodules;

w_C^g is the carbon content of graphite;

w_C^i is the C content in liquid next to the interface;

ρ^g is the density of Graphite.

The flux of carbon is based on a mass balance, first the overall mass balance and then the carbon mass balance to be combined with the local mass balance at the interface g/L to lead to appropriate equations that give the growth rate of the graphite during the pro-eutectic stage. The parameters governing the flux of carbon are the interfacial chemical reaction and the diffusion of carbon from liquid to build up the graphite. The interfacial chemical reaction is given by [65]:

$$\phi = -K \rho^l (w_C^i - w_C^{l/g})^2 \quad \text{Eq. 10}$$

Where:

K is the constant which characterizes the interfacial process;

$w_C^{x/y}$ is the C content of the phase x at the x/y interface in local equilibrium with graphite;
 ρ^l is the density of liquid.

And the diffusion reaction is given by [65]:

$$\phi = -D_C^l \cdot \rho^l \cdot \left. \frac{\partial w_C^l}{\partial r} \right|_{r_g} \quad \text{Eq. 11}$$

Where:

D_C^l is the diffusion coefficient of Carbon in liquid iron;

$\left. \frac{\partial w_C^l}{\partial r} \right|_{r_g}$ is the carbon gradient in liquid at the interface.

It is assumed that diffusion of the carbon is a quasi-stationary process, so:

$$w_C^l = w_C^\infty + \left(\frac{r^g}{r} \right) (w_C^i - w_C^\infty) \quad \text{Eq. 12}$$

where w_C^∞ is the carbon content of the bulk liquid far from interface. Since the flux in both cases is the same, by equalling the equations Eq. 10 and Eq. 11, the composition of the liquid at the melt/graphite interface can be calculated as [65]:

$$w_C^i = w_C^{l/g} + \sqrt{\left(\frac{D_C^l}{2K \cdot r^g} \right)^2 + \frac{D_C^l}{K \cdot r^g} (w_C^\infty - w_C^{l/g})} - \frac{D_C^l}{2K \cdot r^g} \quad \text{Eq. 13}$$

The simple mass balance and carbon balance in the melt, according to the lever rule, can be estimated as below to relate w_c^∞ and f^g :

$$V^0 \cdot \rho^l = V^t \cdot [\rho^l \cdot (1 - f^g) + \rho^g \cdot f^g] \quad \text{Total mass balance}$$

$$V^0 \cdot \rho^l \cdot w_c^0 = V^t \cdot [\rho^l \cdot (1 - f^g) \cdot w_c^\infty + \rho^g \cdot f^g] \quad \text{Carbon mass balance}$$

where:

V^0 is the initial volume of the grain

V^t is the volume of the grain at the time t

It is assumed that the nodules are sufficiently far away from each other so that their concentration fields do not overlap. Finally, combining Eq. 9 and Eq. 10 the following expression Eq. 14) is obtained to calculate the growth of the graphite nodules [65]:

$$\frac{dr^g}{dt} = \frac{K \cdot \rho^l \cdot (w_C^i - w_C^{l/g})^2}{\rho^g \cdot (w_C^g - w_C^i)} \quad \text{Eq. 14}$$

Then the temperature will be calculated, considering the generated heat due to the formation of the solid phase (graphite). At the end of the proeutectic stage of the solidification, the volume fraction of graphite will always be small even for highly hypereutectic cast irons.

3.1.2 Eutectic solidification

A real image of ductile iron, which has been squeezed during directional solidification, is shown in Fig. 18.a. The dark areas are amorphous. We can see the nodules of graphite and the austenite shell around them, and the austenite dendrites. A small part of this structure has been enlarged and is illustrated schematically in the Fig. 18.b. The volume element for the interaction between phases is assumed to be a spherical grain with the initial radius of r^0 and initial volume of V^0 . The grain is composed of one graphite nodule with the radius of r^g in the centre encapsulated by an austenite shell with the outer radius of r^γ , the liquid and possibly some off-eutectic phase(s). The volume of the sphere can change with time as heat is extracted and solidification proceeds, so that the radius, r , will be calculated at time “t” at each time step. The profile of the concentration of carbon in each phase is also depicted schematically in Fig. 18.c.

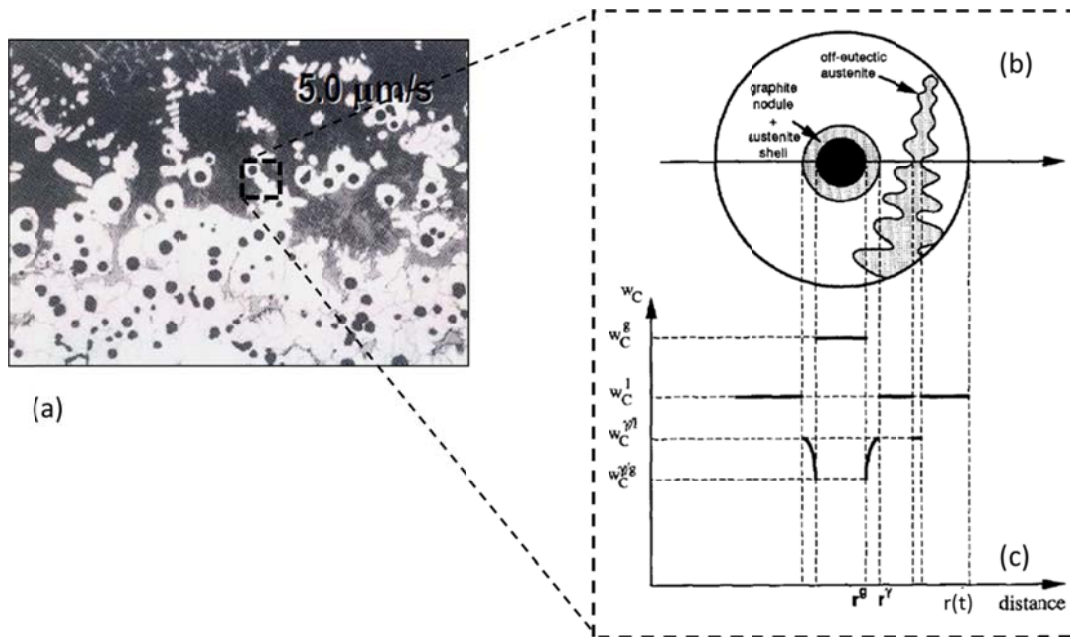


Fig. 18. a) Solid-liquid interface during unidirectional solidification of ductile iron [69]; b) the schematic illustration of SG grain during solidification; c) the profile of the concentration of carbon in each phase [65]

In the model at the eutectic solidification stage, nucleation and growth of new-born graphite nuclei will proceed according to the conditions similar to those of primary graphite. Remaining liquid and off-eutectic phases are assumed to be chemically homogeneous. Additionally, the redistribution of carbon at each time step takes place within the previous volume element. Each graphite nucleus in this stage is given an austenite shell immediately. Nucleated graphite nodules are assigned the initial radius equal to the primary graphite nuclei, r_0^g , and the immediately encapsulating austenite shell is given the initial thickness of δr_0^γ . The growth of

graphite nodules and their associated austenite shells for each group which are nucleated in the same time step will be calculated too.

The liquid is assumed to be homogeneous from the view point of the overall mass balance. However, when the metal cools down, the concentration must increase in the liquid for local chemical equilibrium between γ and L in order to follow the austenite liquidus. This will result in the precipitation of some extra austenite (eutectic or off eutectic) in one of the following ways:

- a) To build up carbon in the liquid in front of fast growing eutectic γ shells;
- b) To build up carbon around growing off-eutectic dendrites which diffuse in the bulk liquid.

One should notice that during the eutectic stage of the solidification, no extra off-eutectic graphite will precipitate on cooling or on reheating (in the case of recalescence). The reason is that

- a) During cooling, the C concentration follows the γ -L line, i.e. the concentration has to increase. Therefore, only precipitation of austenite is possible.
- b) During recalescence, the principal condition for the nucleation of graphite, which is $\frac{d(\Delta T_L^g)}{dt} > 0$, is not met.

Since reheating of the metal during the eutectic stage of the solidification must result in a decrease in carbon content of the liquid, there is either precipitation of off-eutectic graphite (which is impossible), or dissolution of some pre-existing off-eutectic austenite dendrites, or the growth of the eutectic austenite shell must slow down.

The rate of growth is based on a mass balance, first the overall mass balance and then C mass balance to be combined with the local mass balances at the interfaces g/γ and γ/L . These will result in appropriate equations that give the growth rate of the various phases during eutectic reaction.

The overall mass balance during eutectic reaction is expressed as below [65]:

$$\rho^l \cdot \frac{(r^0)^3}{3} = \rho^g \int_0^{r^g} r^2 \cdot dr + \rho^\gamma \int_{r^g}^{r^\gamma} r^2 \cdot dr + [\rho^l \cdot (1 - f^\gamma - f^g) + \rho^\gamma \cdot f^\gamma + \rho^g \cdot f^g] \int_{r^\gamma}^{r^l} r^2 \cdot dr \quad \text{Eq. 15}$$

This equation includes both the eutectic sphere (the first two terms in the right hand side of the equation) and the off-eutectic phases (the third term in the right hand side).

The carbon mass balance can be expressed as below [65]:

$$w_C^0 \cdot \rho^l \cdot \frac{(r^0)^3}{3} = \rho^g \int_0^{r^g} r^2 \cdot dr + \rho^\gamma \int_{r^g}^{r^\gamma} w_C^\gamma \cdot r^2 \cdot dr + [w_C^l \cdot \rho^l \cdot (1 - f^\gamma - f^g) + k_C \cdot w_C^l \cdot \rho^\gamma \cdot f^\gamma + \rho^g \cdot f^g] \int_{r^\gamma}^{r^l} r^2 \cdot dr \quad \text{Eq. 16}$$

Where:

w_C^l is the carbon content in the liquid phase;

w_C^γ is the carbon content in the eutectic austenite;

After differentiating Eq. 16 with respect to time and combining it with chemical mass balances at the interfaces graphite/austenite and austenite/liquid, we are able to find the proper equations to calculate the growth rate of the solid phases.

In the model [65] the parameter “ Φ ” has been introduced to make the calculations easier. This quantity equals the ratio of the actual mass of C in the off-eutectic volume over the mass of carbon in the same off-eutectic volume if it would be completely liquid and in equilibrium with the eutectic austenite. Therefore, if $\Phi = 1$, the off-eutectic volume would be completely liquid. And if $k_C \leq \Phi \leq 1$, the off-eutectic volume is composed of both austenite dendrites and liquid. The quantity of Φ is expressed as bellow [65]:

$$\Phi = \frac{\rho^l \cdot (1 - f^\gamma) + \rho^\gamma \cdot f^\gamma \cdot k_C}{\rho^l \cdot (1 - f^\gamma) + \rho^\gamma \cdot f^\gamma}$$

If there is no off-eutectic austenite precipitated, a straight differentiation of the carbon mass balance will result in the equation below:

$$\frac{d\Phi}{dt} w_C^l = X_C$$

While

$$X_C = - \frac{\rho^\gamma w_C^l [1 - \Phi] \frac{dV_{eut}}{dt} - (\rho^\gamma - \rho^g) [(1 - \Phi) \cdot w_C^l + w_C^{\gamma/g} - w_C^{\gamma/l}] \frac{dV_g}{dt}}{[\rho^l V^0 - \rho^l V_g - \rho^\gamma (V_{eut} - V_g)]}$$

Where:

V_g is the volume of graphite;

V_{eut} is the volume of eutectic spheres.

The growth of graphite nodule radius will be calculated by the following equation [65]:

$$\frac{dr_i^g}{dt} = \frac{\rho^\gamma}{\rho^g} D_C^\gamma \frac{r_i^\gamma}{(r_i^\gamma - r_i^g) r_i^g} \cdot \frac{w_C^{\gamma/l} - w_C^{\gamma/g}}{w_C^g - w_C^{\gamma/l}}$$

D_C^γ is the diffusion coefficient of Carbon in austenite

ρ^γ is the density of austenite

k_C is the partition coefficient of carbon between austenite and liquid

m_C^γ is the slope of austenite liquidus

The growth of the austenite shell will be found by the following [65]:

$$\frac{dr_i^\gamma}{dt} = D_C^\gamma \frac{r_i^g}{(r_i^\gamma - r_i^g) r_i^\gamma} \cdot \frac{w_C^{l/\gamma} - w_C^{\gamma/g}}{w_C^g - w_C^{\gamma/g}} \left[1 + \frac{\rho^\gamma - \rho^g}{\rho^g} \cdot \frac{w_C^{l/\gamma} - w_C^{\gamma/l}}{w_C^g - w_C^{\gamma/g}} \right] + \Delta(r^\gamma) \quad \text{Eq. 17}$$

Where:

$$\Delta(r^\gamma) = \frac{\partial T}{m_C^\gamma} \cdot \frac{\rho^l (1 - f^\gamma) + \rho^\gamma \cdot f^\gamma \cdot k_C}{\rho^l (1 - f^\gamma) + \rho^\gamma \cdot f^\gamma} \cdot \frac{\rho^l (r^0)^3 - \rho^g \cdot (r_i^g)^3 - \rho^\gamma \cdot [(r_i^\gamma)^3 - (r_i^g)^3]}{3 \cdot \rho^\gamma \cdot (w_C^{l/\gamma} - w_C^{\gamma/l}) \cdot (r_i^\gamma)^2}$$

If off-eutectic austenite is present in a particular casting cell, $\Delta(\rho^s)$ is assumed to be zero; otherwise it should be taken into account.

A comprehensive description of derivation of the equations is provided in the references [64] [65] [70].

3.1.3 The 1D explicit model of heat transfer

The heat transfer model (section 2.1) together with the solidification model (sections 3.1.1&3.1.2) have been used in a 1D grid using the Control Volume-based Finite Difference Method (Fig. 19). The heat transfer model is written according to the Ref [31]. The heat balance for a control volume can be written as:

“The change of heat content per time equals sum of heat fluxes into the volume over 2 surfaces plus volumetric heat generation”, which can be expressed as Eq. 18.

$$\dot{Q}_i = \sum q_{\rightarrow i} + \dot{Q}_{gen,i} \quad \text{Eq. 18}$$

where Q_i is the total heat content of the control volume i , $\sum q_i$ is the total heat flow into the control volume i and \dot{Q}_{gen} is the heat generated in the control volume i . The generated heat per control volume i per time is given by the expression:

$$\dot{Q}_{gen,i} = \Delta H_i \rho_i \frac{dV_i^s}{dt} \quad \text{Eq. 19}$$

Where ΔH_i is the latent heat for the control volume i and $\frac{dV_i^s}{dt}$ is the change of the fraction of solid for the control volume i per time step dt (or Δt).

Before calculating the temperature, it is useful to define the parameters H_i^{Cap} and H_i^{Con} .

H_i^{Cap} is defined as the capacity function and it is expressed as [31]: $H_i^{Cap} = \frac{\Delta x_i (\rho c_p)_i}{\Delta t}$

where Δx_i is the size of the cell i and Δt is size of the time step.

H_i^{Con} is defined as the conductivity function [31]: $H_i^{Con} = \frac{1}{\frac{\Delta x_{i-1}}{2\lambda_{i-1}} + \frac{\Delta x_i}{2\lambda_i} + \frac{1}{HTC_{i-1 \rightarrow i}}}$

where λ is the thermal conductivity and HTC is the heat transfer coefficient between the two materials.

For the case of a 1D Cartesian control volume mentioned above, using the explicit method, the change of temperature in control volume i can be expressed as [31]:

$$T_i^{t+\Delta t} = T_i^t + \frac{H_i^{Con}(T_{i-1}^t - T_i^t) + H_{i+1}^{Con}(T_{i+1}^t - T_i^t) + \frac{\dot{Q}_{gen,i}^t}{A}}{H_i^{Cap}} \quad \text{Eq. 20}$$

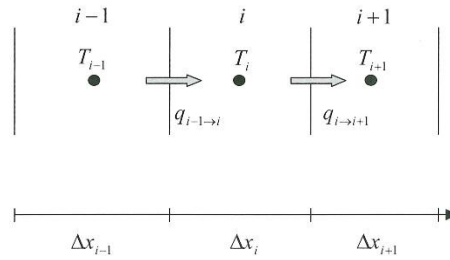


Fig. 19. Heat balance in 1D Cartesian control volume [31]

A schematic figure of the casting plate and the sand mould geometry which with a good estimation is assumed to be a simple 1D problem, is shown in Fig. 20.a. In the case of complex geometries or thick plates, a full 3-D heat conduction analysis should be applied. A schematic example of the 1D enmeshment is illustrated in Fig. 20.

A detailed flowchart of the model was provided by Pedersen et. al. [66].

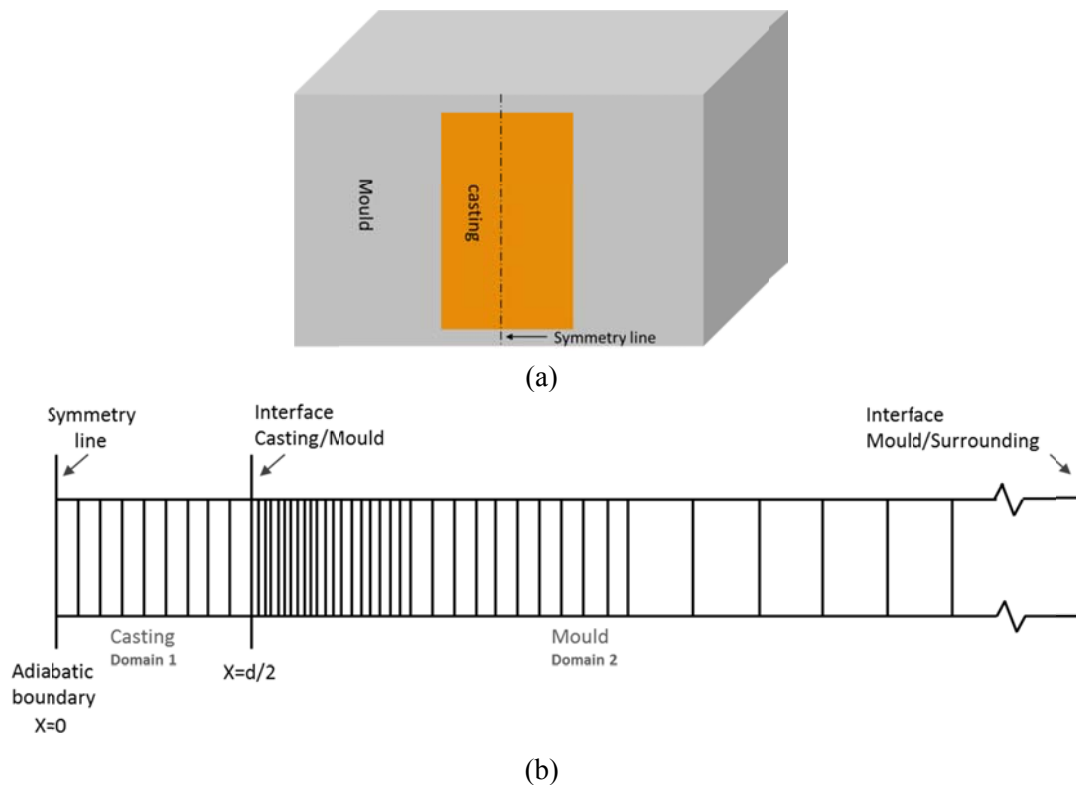


Fig. 20. The schematic illustration of casting geometry and enmeshment; a) Schematic lay-out of casting and mould for plate geometry; b) 1D enmeshment of casting plate and sand mould

3.2. Experimental results

A hypereutectic cast iron melt was prepared in a batch of 150 kg. The specimens were cast in sand moulds as tensile test specimens (Fig. 21), their thicknesses are shown in Table 2. Magnesium treatment and inoculation with two inoculants were made; the compositions of inoculants are indicated in Table 3. The temperature was measured in the middle of each plate using 0.5 mm diameter stainless steel sheathed K-type thermocouples. Some key points on the cooling curve, showing different stages of solidification, are shown in Fig. 22. The

recalescence, ΔT_{rec} , is defined as the difference between T_{max} and T_{min} . Generally, the lower the ΔT_{rec} is, the more efficient is the inoculation.



Fig. 21. The lay-out of casting specimens [Moumeni, Tutum, Tiedje and Hattel, Paper I]

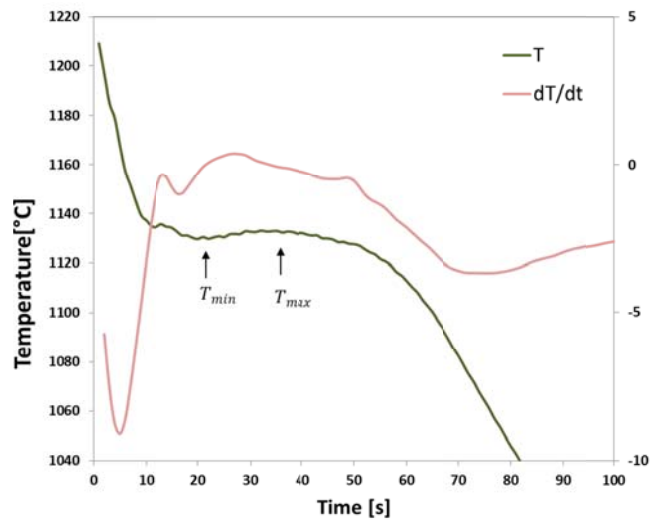


Fig. 22. Definition of temperatures on cooling curves (from 4.3mm plate)

Table 2. Thickness of casting sections [Moumeni, Tutum, Tiedje and Hattel, Paper I]

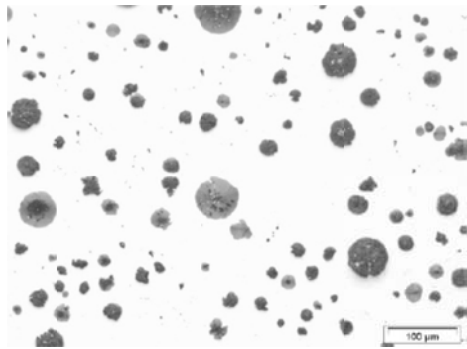
	Section 1	Section 2	Section 3	Section 4
Thickness(mm)	10	6	4	2

Table 3. Composition of inoculants (%wt) [Moumeni, Tutum, Tiedje and Hattel, Paper I]

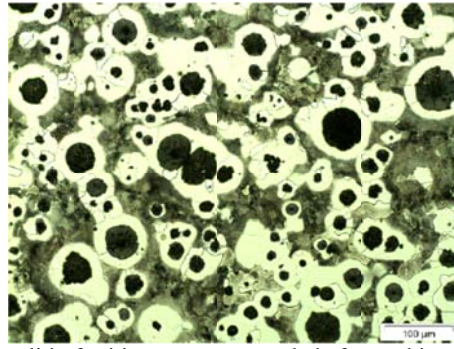
	Si	Al	Ca	La	Fe
Inoculant 1	52.8	0.6	-	-	Bal.
Inoculant 2	50	-	2	2	Bal.

3.2.1. Microstructure, nodule count, size distribution and cooling curves

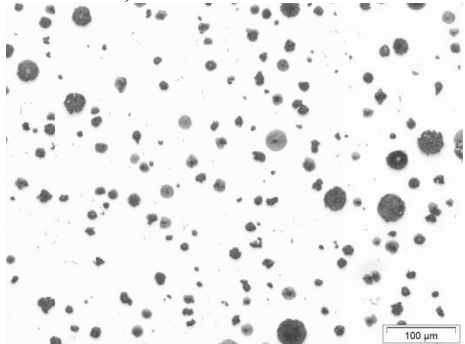
Metallographic investigation of all of the samples was done using an optical microscope. Nodularity, nodule count and size distribution as well as iron matrix microstructure were examined. No noticeable difference was observed between two castings with the same thicknesses. Representative images of the castings' microstructures are selected and shown in Fig. 23. As expected, a trend of reduction in average nodule size and increase in nodule count can be seen from thicker to thinner parts. In the 2 mm section, carbide is formed in the matrix due to inverse segregation and increased cooling rates at the end of solidification [66].



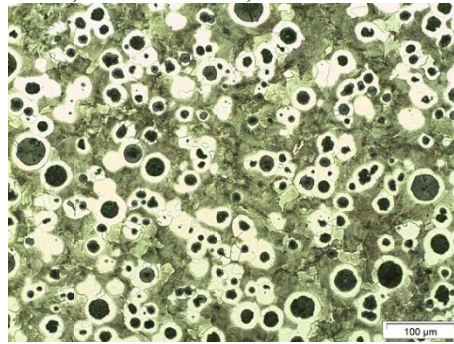
i) Graphite nodules in as-cast specimen 10 mm thickness;



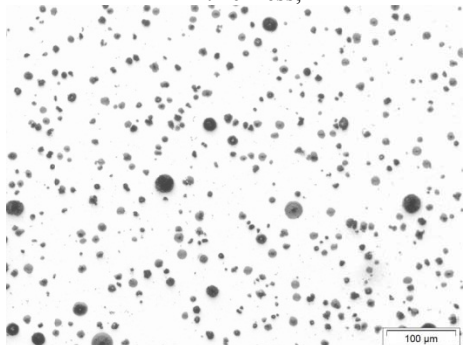
ii) Pearlitic-ferritic structure, revealed after etching with Nital 2%; 10 mm thickness;



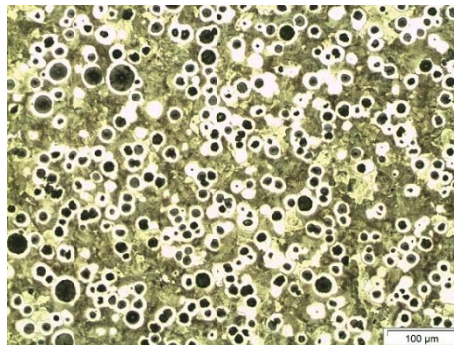
iii) Graphite nodules in as-cast specimen 6 mm thickness;



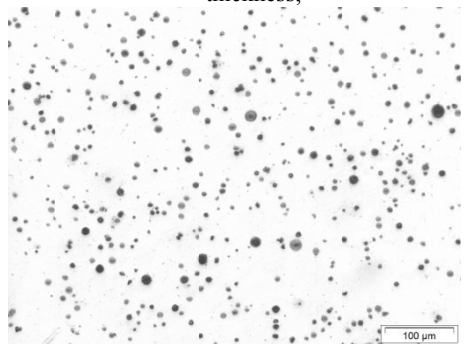
iv) Pearlitic-ferritic structure, revealed after etching with Nital 2%; 6 mm thickness;



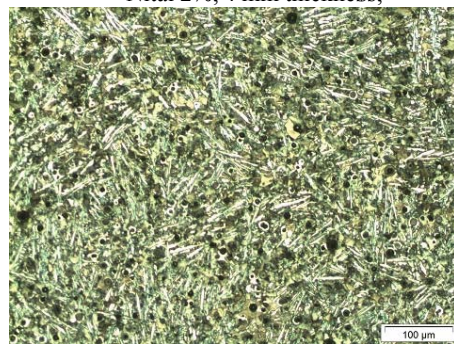
v) Graphite nodules in as-cast specimen 4 mm thickness;



vi) Pearlitic-ferritic structure, revealed after etching with Nital 2%; 4 mm thickness;



vii) Graphite nodules in as-cast specimen 2 mm thickness;



viii) Pearlitic-ferritic-carbide structure, revealed after etching with Nital 2%; 2 mm thickness;

Fig. 23. Micrographs obtained by optical microscope; the centre of the section.

The size distribution of graphite nodules per unit volume is measured and is shown in Fig. 24 for all of the samples. Small particles which had a size between 0-5µm are considered as inclusions, and are not counted. The mean diameter of graphite nodules and nodule counts are

calculated using the average of data from 5 images and has been converted from 2D to 3D applying the Schwartz-Saltykov method [71]. It can be seen that the nodule size distribution differs from a single normal distribution, but it can be composed by addition of more than one normal distribution. The width of the distribution, i.e. the difference in size between the smallest nodule and the largest is here called the “range” of the distribution. As expected, the nodule count, i.e. the total number of nodules per mm^3 in the thicker samples is lower, but the range of nodule size is wider and also the average size of the nodules is bigger.

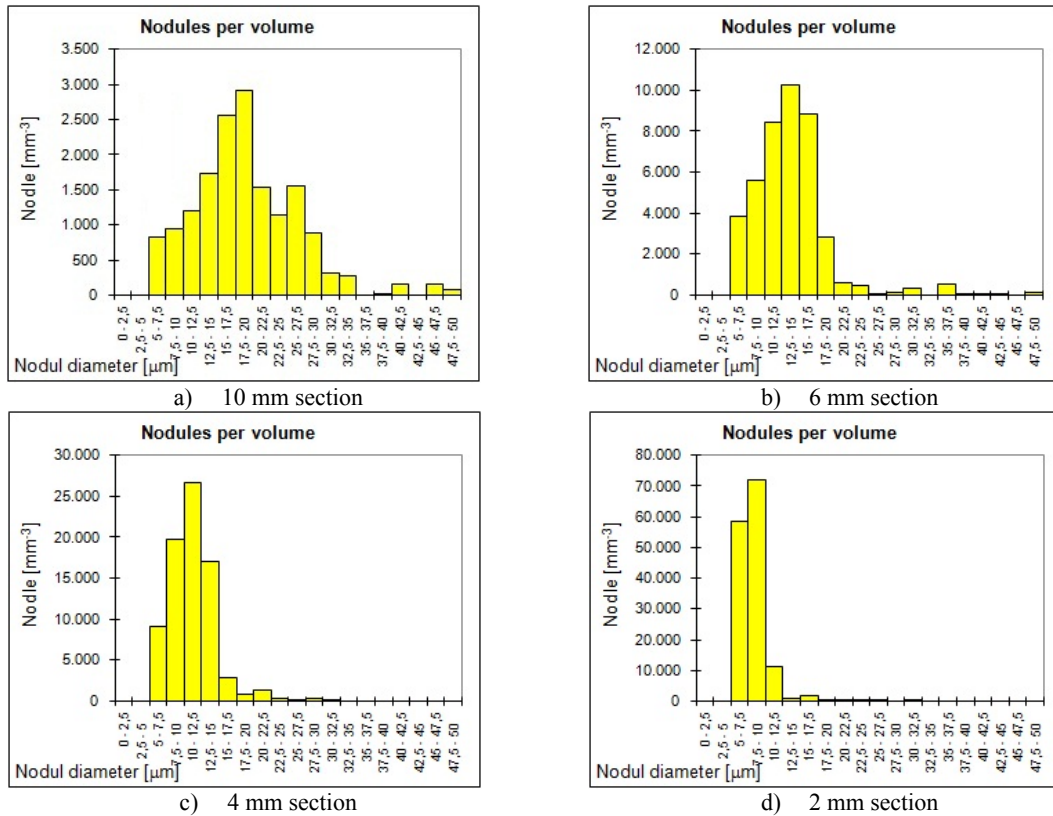
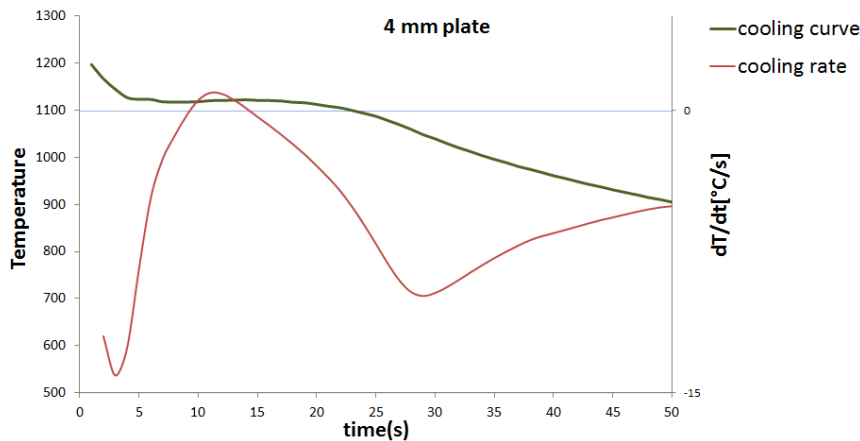
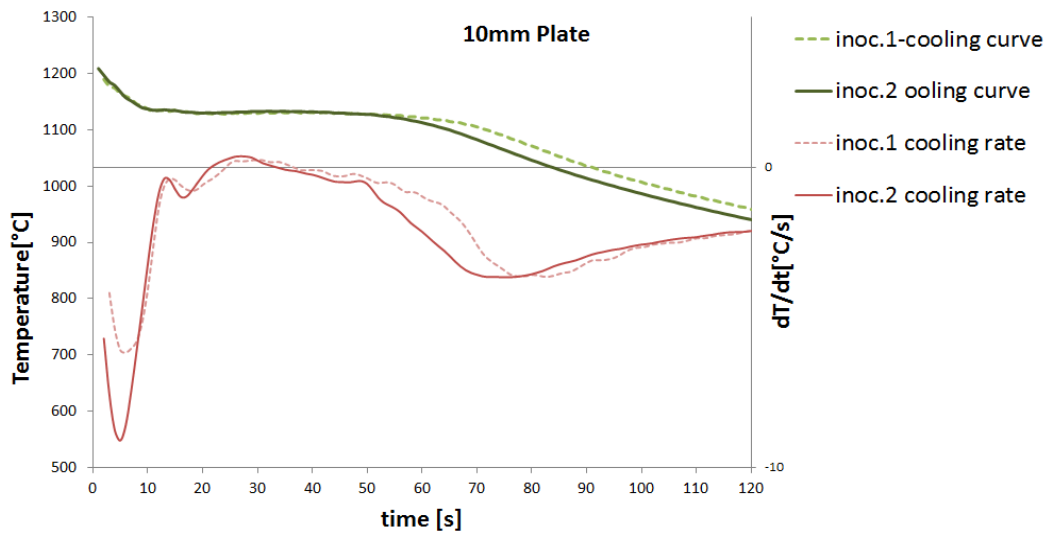


Fig. 24. Size distribution of nodules [Moumeni, Tutum, Tiedje and Hattel, Paper I]

The measured cooling curves for the two different sections (4 and 10mm thick) are illustrated in Fig. 25.



a) Casting 1 for plate 4 mm.



b) Casting 1(dashed line) and casting 2 (solid line), for plate 10 mm.
 Fig. 25. Measured cooling curves (green) and cooling rates (red) [Moumeni, Tutum, Tiedje and Hattel, Paper I].

3.3. Effect of the nucleation parameters on the numerical results

The model is now used to investigate how the nucleation parameters can be assessed. According to the nucleation law shown in Eq. 8, “ A_n ” is the constant related to the amount of inoculant and “ n ” is a constant characterizing the inoculation efficiency. The effect of these two parameters on the range of nodule size and the shape of the cooling curve is studied.

It can be seen in Fig. 26 that for a given combination of A_n and r_0^s , and for a casting with a thickness of 4mm, decreasing the value of n results in a wider range of nodule size distribution.

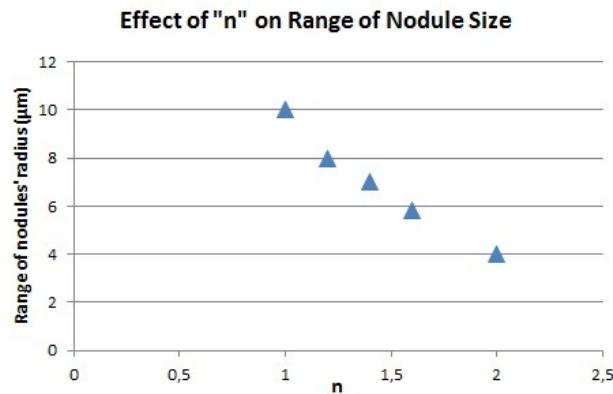


Fig. 26. Effect of n on Size distribution of nodules (numerical result) [Moumeni, Tutum, Tiedje and Hattel, Paper I]

In Fig. 27, the numerical results are compared with the experimental results. As shown, the closest result to the experimental results for the range of nodule size for the thickness of 4 mm, can be obtained by $n=2$.

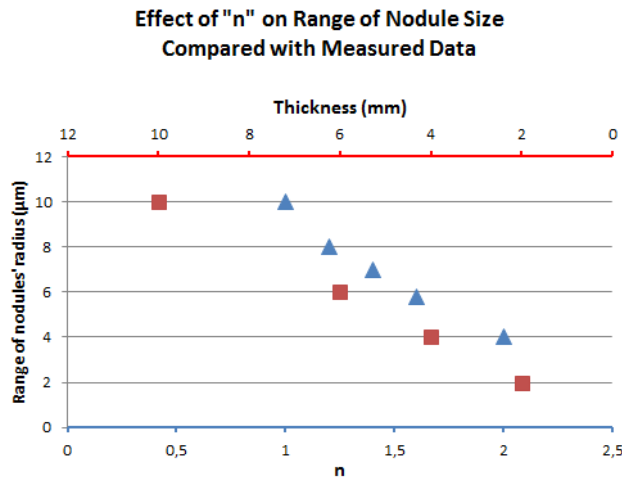


Fig. 27. Comparison of experimental results (squares) with numerical results (triangles) from the model.

In Fig. 28, the effect of n on the cooling curve is depicted. It can be seen that increasing n , which means increasing the efficiency of the inoculation, results in a higher eutectic temperature and a flatter shape of the cooling curve during eutectic transformation.

Increasing the quantity of A_n also results in raising the eutectic temperature and the solidification time. However, it does not change the shape of the cooling curve.

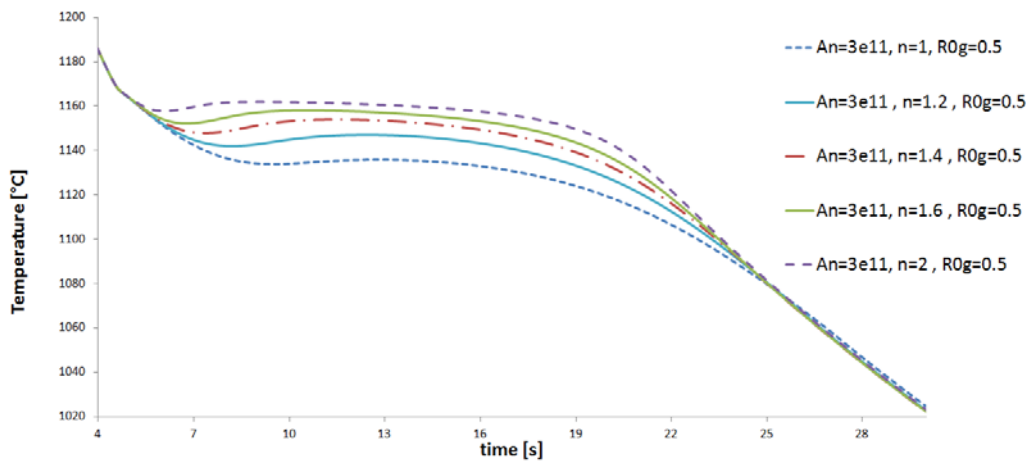


Fig. 28. Effect of n on the shape of cooling curve; numerical results [Moumeni, Tutum, Tiedje and Hattel, Paper I].

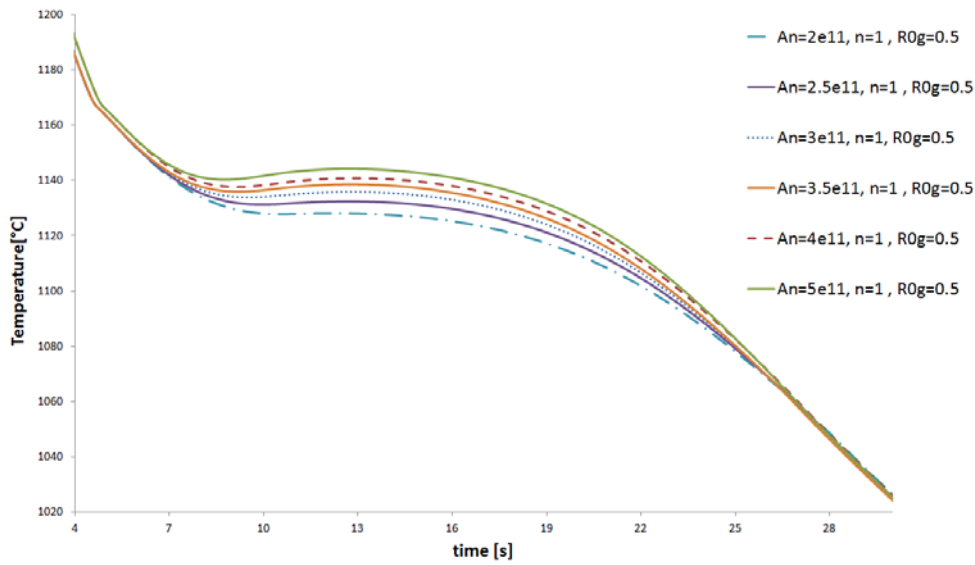


Fig. 29. Effect of A_n on the shape of cooling curve; numerical results [Moumeni, Tutum, Tiedje and Hattel, Paper I]

The effect of initial radius on graphite was investigated too. It was observed that by changing r_0^g , only T_{min} changes slightly. The related diagram is depicted in the Fig. 30.

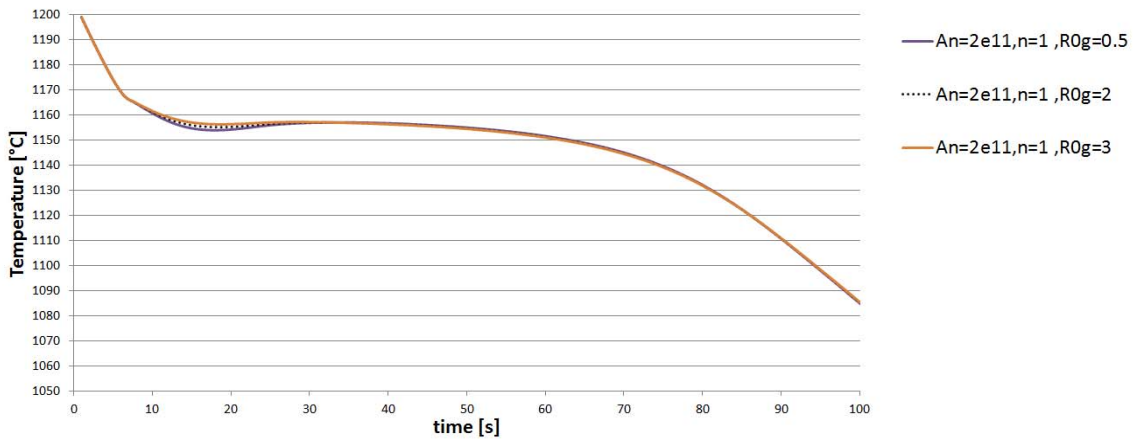


Fig. 30. Effect of r_0^g on the shape of cooling curve; numerical results.

In Fig. 31, the measured cooling curve for the specimen with the thickness of 10mm is compared with the numerical results in order to find the quantity of n to fit the cooling curve with the experimental results. It can be seen that the measured solidification time for the experiments is shorter than the results obtained from the model. The reason can be that the one dimensional assumption is not so well-describing for the thickness of 10mm. Since the thickness to the width is larger than acceptable for a one dimensional model. Therefore, the results for the specimen with the thickness of 10mm in the one dimensional model will not be discussed.

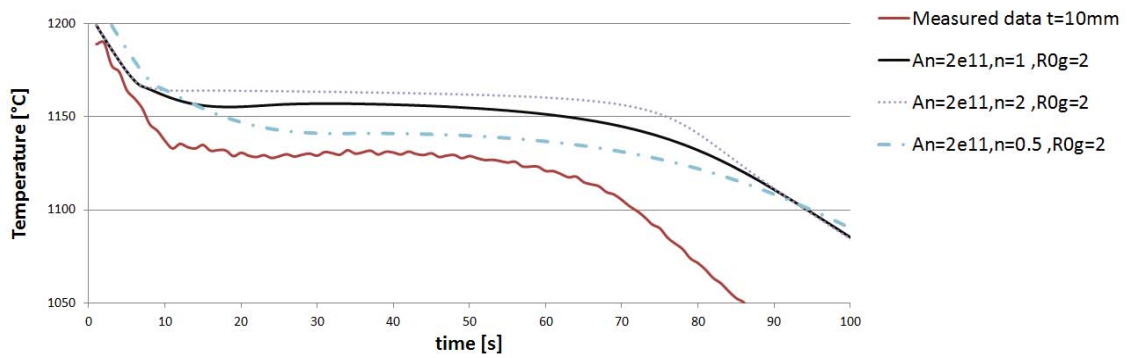


Fig. 31. Effect of n on the shape of cooling curve; experimental vs. numerical results

In the following figures, the empirical and numerical cooling curves for the thickness of 4mm are illustrated. The effect of the parameter n for a given A_n is shown in Fig. 32. The closest eutectic temperature to the empirical values is obtained for n equal to 1. But the shape of the cooling curve is matched better for the numerical results of $n=2$.

In the next diagram (Fig. 33), the effect of A_n for a given value for n ($n=1$) is studied. The best value for the eutectic temperature is related to the numerical curve for $A_n = 2.5e11$.

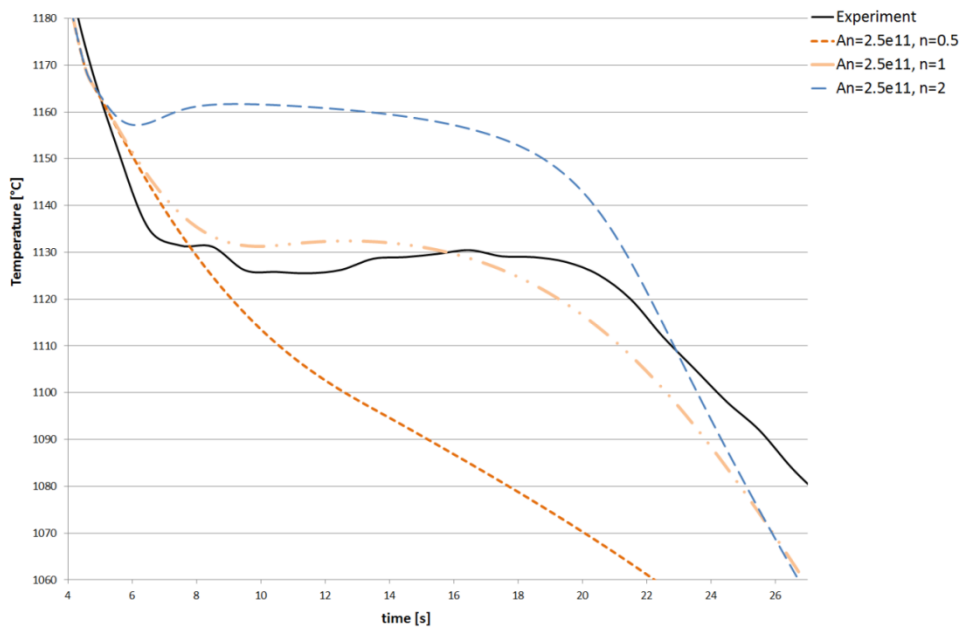


Fig. 32. Effect of n on the shape of cooling curve; experimental vs. numerical results

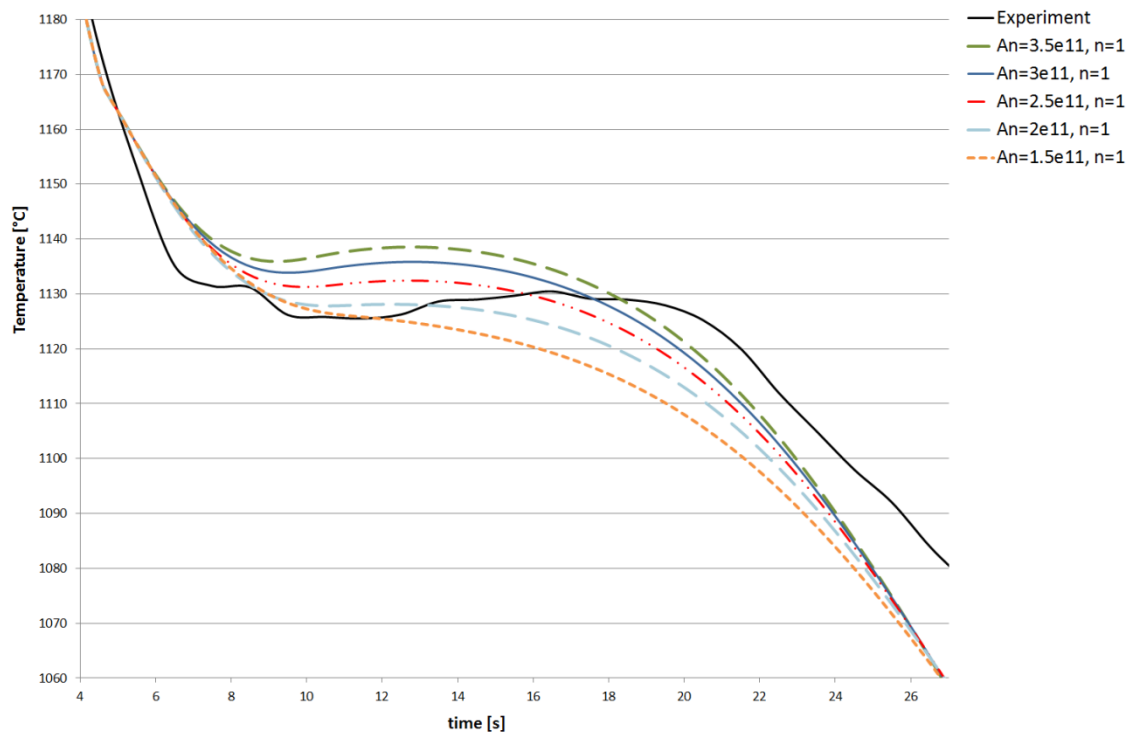


Fig. 33. Effect of A_n on the shape of cooling curve; experimental vs. numerical results

3.4. Summary

The numerical model is used to analyse the effect of inoculation on graphite size and distribution and in general on coupled zone growth and growth of austenite and graphite. It is demonstrated how a 1-D numerical model for solidification of ductile cast iron in the form of a plate, taking into account the formation of off-eutectic austenite can be used to analyse nucleation and solidification. The experimental results have shown good agreement with the numerical results regarding the cooling curve and nodule count and size distribution.

The sensitivity of the numerical results to the empirical nucleation parameters has been analysed and it is shown how these parameters such as A_n and n can affect the numerical results, e.g. cooling curve. Moreover, T_{max} , T_{min} and ΔT_{rec} strongly depend on the above mentioned parameters. The parameter A_n is the constant related to the amount of inoculant, therefore, by increasing this parameter the eutectic reaction happens at higher temperature. The parameter n is the constant characterizing the inoculation efficiency; increasing this parameter results in a significant shift of the cooling curve.

In Chapter 4 it is shown by experimental tools how the nucleation potential can affect the shape of the cooling curve. For grey iron, by decreasing the available amount of Mn and S in the melt for nucleation of the regular flaky graphite it will be explained how the fraction of this type of graphite decreases drastically and will be accompanied by a noticeable increase in the fraction of primary austenite.

Chapter 4

A study on micro-alloyed cast iron

In this investigation the effect of Ti and S on the microstructure of grey iron is studied [Moumeni; Tiedje and Hattel, Paper II] [Moumeni; Stefanescu; Tiedje; Larrañaga and Hattel, Paper III]. Optical and electron microscopy are used to examine the unetched, colour-etched and deep-etched samples. The inclusions are identified in an effort to explain the nucleation of the phases of interest. The superfine graphite which forms in this type of irons is short (10-20 μm) and stubby. The microstructure of this kind of graphite flakes in titanium alloyed cast iron is studied using electron microscopy techniques [30]. An important part of this work has been to develop methods to prepare samples of cast iron for comprehensive transmission electron microscopy of graphite and the surrounding iron matrix. Dual beam microscopes are used for sample preparation. A TEM study has been carried out on graphite flakes in grey cast iron using selected area electron diffraction (SAED). Based on the SAED pattern analysis, crystallographic orientations are identified and compared. Subsequently, the orientation relationship between iron and graphite crystals at the interface is studied and discussed.

Based on this information, growth models for the platelets in the fine graphite flakes in cast iron are suggested and discussed.

4.1. Experimental set-up

The first series of experiments were carried out to identify the inclusions in lamellar graphite cast iron in an effort to explain the nucleation of the phases of interest. Four samples of approximately the same carbon equivalent but different levels of sulphur and titanium were studied. Their chemical composition is shown in Table 4 (row 1-4). The samples were produced by Azterlan, Spain and part of the metallographic study was carried out at Ohio State University.

The second series of experiments and a comprehensive electron microscopy study were performed at the Technical University of Denmark (DTU). Tensile test bars of grey cast iron of near eutectic alloys with different levels of Ti were made in green sand moulds. The effect of Titanium on the structure of graphite was investigated. A TEM study was performed in order to observe the effect of Ti on the structure of the graphite in details. The chemical composition of the specimens is shown in the Table 4 (row 5-8).

Table 4. Chemical composition (wt%) of the test samples [Moumeni; Tiedje and Hattel, Paper II] [Moumeni; Stefanescu; Tiedje; Larrañaga and Hattel, Paper III]

Sample no.	CE	C	Si	Mn	P	S	Ti
401.1	4.07	3.44	2.07	0.54	0.036	0.120	0.018
401.5	4.03	3.42	2.02	0.50	0.037	0.120	0.360
621.1	4.12	3.51	2.01	0.55	0.015	0.018	0.060
621.5	4.06	3.45	2.03	0.58	0.015	0.012	0.350
GI-1	4.16	3.34	2.57	0.16	0.030	0.015	0.01
GI-2	4.26	3.45	2.54	0.23	0.024	0.012	0.10
GI-3	4.39	3.50	2.80	0.22	0.019	0.007	0.26
GI-4	4.21	3.30	2.83	0.21	0.025	0.012	0.35

4.1.1. Casting procedure

Regarding the first series of experiments, two grey iron melts, B401 (high in sulphur) and B621 (low in sulphur), were produced in a medium frequency induction furnace. The complete melting procedure is described in [7]. After melt down and superheating at 1500°C, a 50kg ladle was used to pour iron into two EN-1563 Type II keel blocks. An amount of 0.2% of the commercial inoculant was deposited on the bottom of each keel block mould before pouring. The remaining of the iron in the ladle was returned to the furnace. After adjustment of carbon, ferro-titanium (65%Ti) was added to the melt. The melt was superheated again and a second set of keel blocks was poured.

A detailed metallographic investigation was performed on samples obtained from the keel blocks through both optical and electron microscopy. The images have been taken before and after etching. Some of the samples were colour-etched using the etchant: %25 (80g) NaOH, 6% (20g) KOH, 6% (20g), picric acid, and (200mL) 63% water. A 2%Nital was used for deep etching for the SEM analysis.

For the second series of samples (GI-1 to 4), the iron was melted in an induction furnace in a batch of 150 kg. The composition was near eutectic and was adjusted by addition of pig iron, cast iron returns, industrial grade silicon and steel plates. After pouring the first ladle of 30kg, ferro-titanium was added to the melt in the furnace and to reach a Ti content of 0.11%. Afterwards, the second ladle was poured with the same procedure and again ferro-titanium was added to the rest of the melt increasing the weight percent of Ti to 0.26%. The same procedure was repeated for the remaining melt so that a Ti content of 0.35% was reached. The inoculant was each time added to the melt in the pouring ladle. The composition of inoculant is presented in Table 5. The pattern for these experiments is the same as in Fig. 21 (explained in section 3.2), consisting of a gating system and four tensile test samples which are different in dimensions. The thicknesses of tensile test specimens are 2, 4, 6 and 10mm.

Table 5-chemical composition of inoculant (weight percent) [Moumeni; Tiedje and Hattel, Paper II]

Si	Al	Fe
52.89	0.609	Bal.

4.2. Metallography/optical microscopy investigation

The effect of S and Ti on the morphology and size of the graphite on the first series of experiments [10] is shown in Fig. 34. It is seen that the low-Ti irons in all cases exhibit mostly coarse type-A graphite (Fig. 34a, c). Increasing the Ti/S ratio produces finer graphite at the same S level (compare Fig. 34a and b, or Fig. 34c and d). However, a clear difference is seen between the samples having low- or high-S. At the same Ti/S ratio, the sample with high S and Ti (401.5) exhibits finer graphite. Indeed, some type-A graphite persists in the microstructure of sample 621.5.

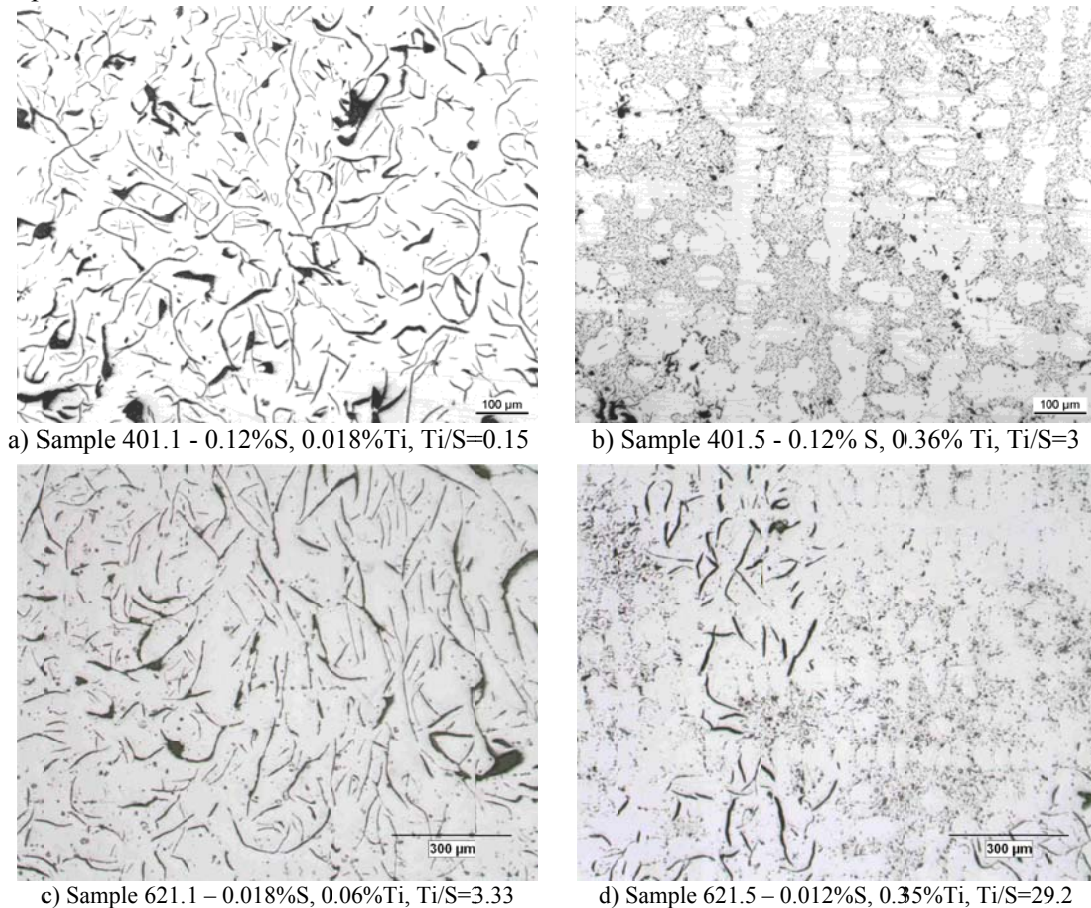
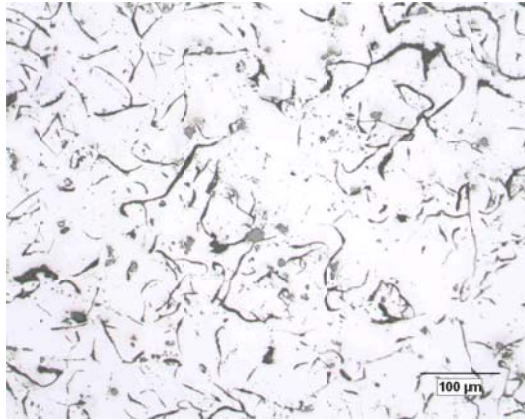
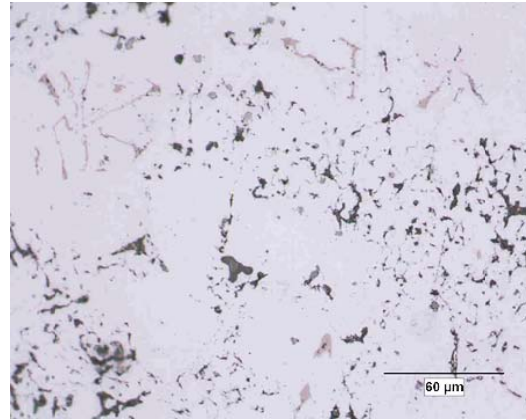


Fig. 34. Unetched microstructures; originally 100x [Moumeni; Stefanescu; Tiedje; Larrañaga and Hattel, Paper III]

A higher magnification of the high-S iron 401 reveals a large number of inclusions (Fig. 35). These inclusions will be identified later through SEM analysis. Titanium addition refines the graphite and also changes the morphology of the inclusions (Fig. 35b). Indeed, as seen in Fig. 35b, some very large star-like inclusions are noticed in the middle of the secondary arms of the austenite dendrites. These star-like inclusions are not present in the microstructure of the low-S high-Ti irons, as evident from Fig. 36. In the low-S high-Ti iron (Ti/S=29.2) the inclusions are mostly located at the borders of secondary dendrite arms.



a) 401.1, 0.12%S, 0.018%Ti, originally at 200x



b) 401.5, 0.12%S, 0.36%Ti, originally at 500x

Fig. 35. Microstructure of high-S irons; originally at 500x unetched [Moumeni; Stefanescu; Tiedje; Larrañaga and Hattel, Paper III]

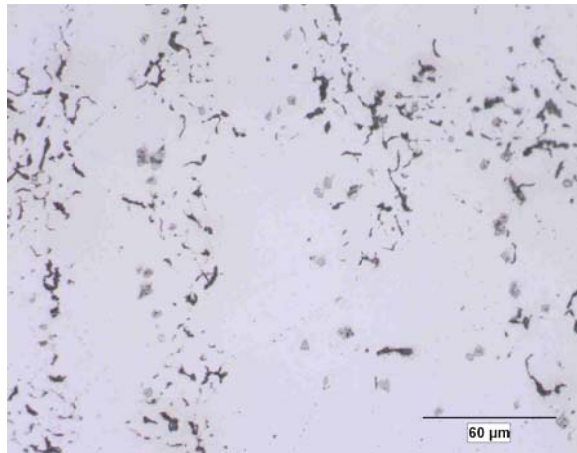
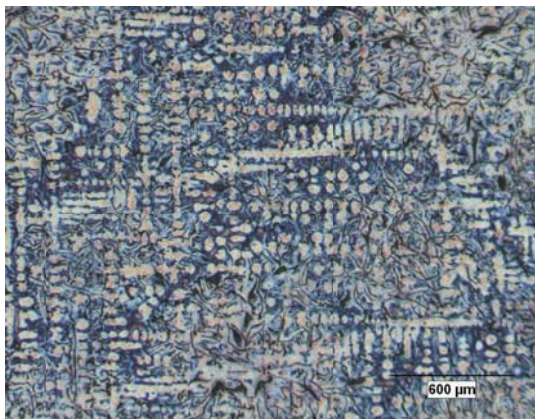
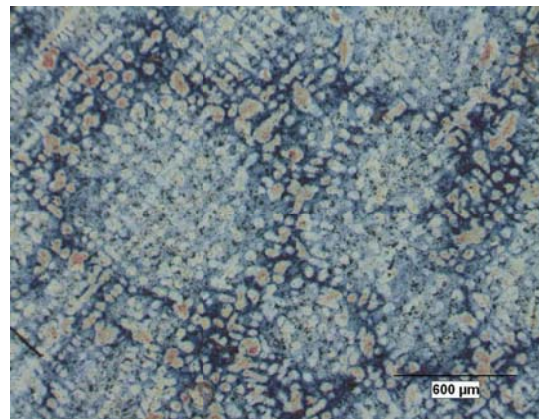


Fig. 36. Microstructure of high Ti/S sample 621.5 – 0.012%S, 0.35%Ti - originally at 500x; unetched [Moumeni; Stefanescu; Tiedje; Larrañaga and Hattel, Paper III]

The effect of high Ti/S ratio on the microstructure is clearly illustrated in Fig. 37 for the case of the high-S irons. Larger eutectic cells and less oriented dendrites are noticed in Fig. 37.b. The segregation pattern is more pronounced for the high-Ti irons.



a) Sample. 401.1 - 0.12%S, 0.018%Ti



b) Sample. 401.5 - 0.12%S, 0.36%Ti

Fig. 37. Colour etched micrographs of the high-S irons at low magnification, originally at 50x [Moumeni; Stefanescu; Tiedje; Larrañaga and Hattel, Paper III]

The high magnification colour micrograph of low Ti/S ratio low-S iron in Fig. 38 shows few inclusions, one TiC and one MnS. The Ti carbide is in the middle of the matrix, while the Mn sulphide is attached to a graphite flake.

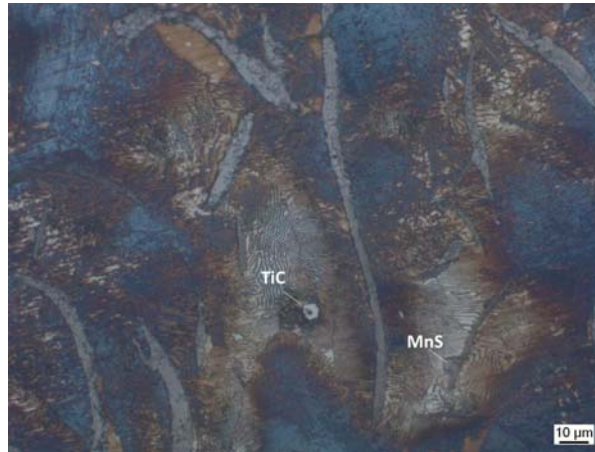


Fig. 38. Colour etched micrographs of the sample. 621.1 – 0.018% S, 0.06% Ti at 500X [Moumeni; Stefanescu; Tiedje; Larrañaga and Hattel, Paper III]

Increasing the Ti/S ratio in the low S iron, raises manifold the number of inclusions. In Fig. 39.a&b it is seen that the inclusions are pushed by the growing dendrites into the last regions to solidify. In Fig. 39.c the short and stubby superfine graphite with a typical length of 10 to 20µm can be seen. It was shown [8] that the fraction of primary austenite in the high-S iron 401.5 increased from 0.17 to 0.27 as the Ti/S ratio increased (Ti increased from 0.018 to 0.36%). However, titanium carbides do not seem to act as nuclei for the austenite since they are positioned in the interdendritic regions.

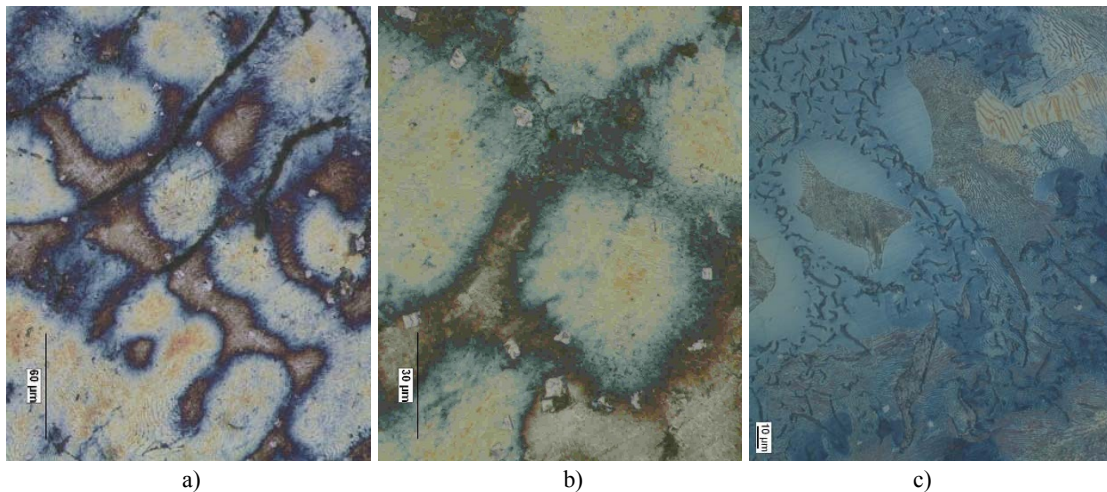


Fig. 39. Colour etched micrographs of the sample. 621.5 – 0.012% S, 0.35% Ti [Moumeni; Stefanescu; Tiedje; Larrañaga and Hattel, Paper III]

According to the ternary phase diagram of Fe-C-Ti presented in Fig. 40, for a 3.5%C iron, TiC can precipitate at temperatures considerably higher than the liquidus of cast iron. Thus, it is reasonable to assume that Ti carbides form in the liquid, before the beginning of the austenite solidification, and are pushed into the last regions to solidify by the austenite dendrites.

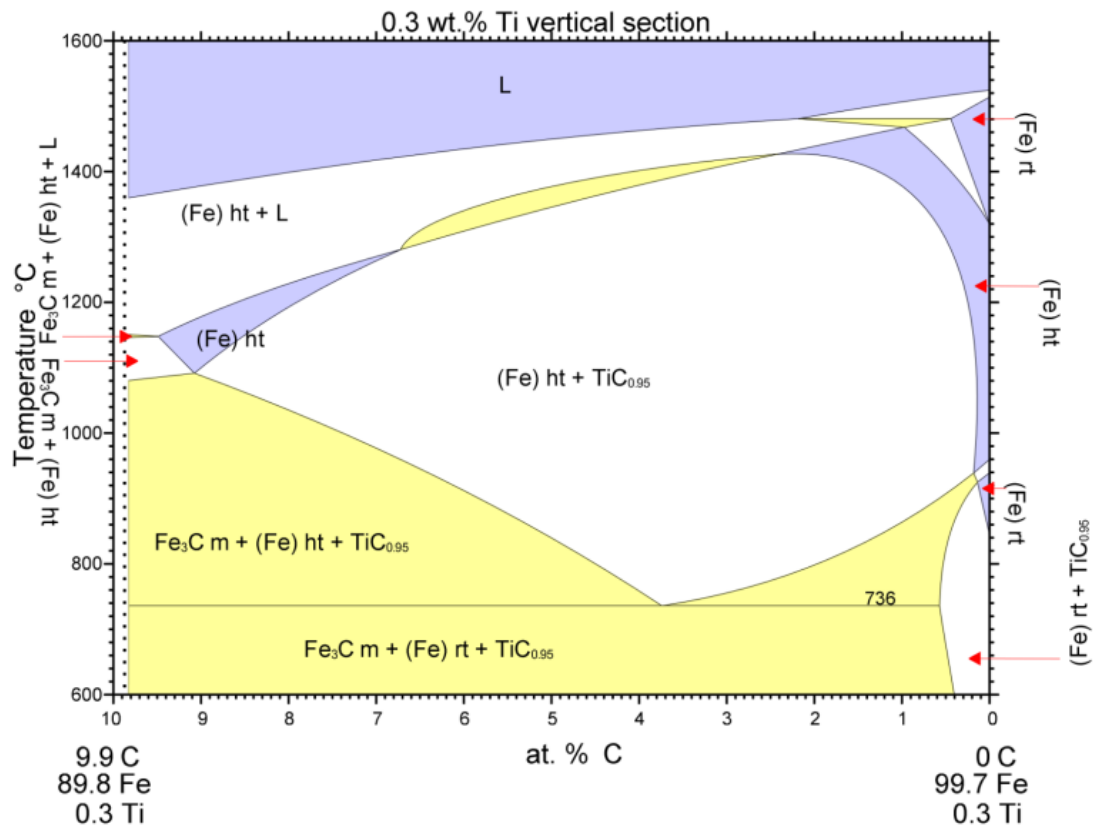
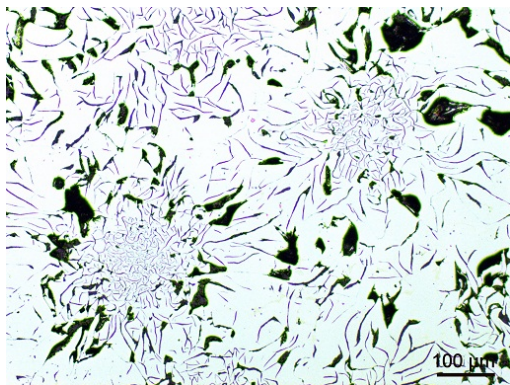
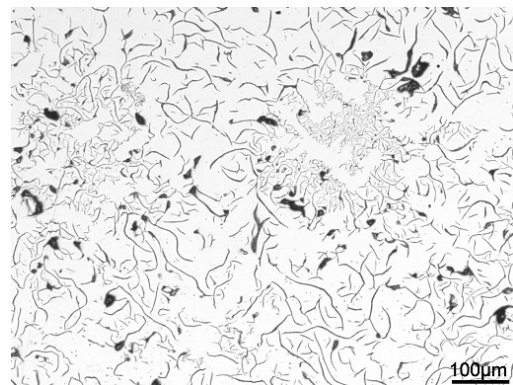


Fig. 40. Section through the Fe-Ti-C ternary phase diagram [72]

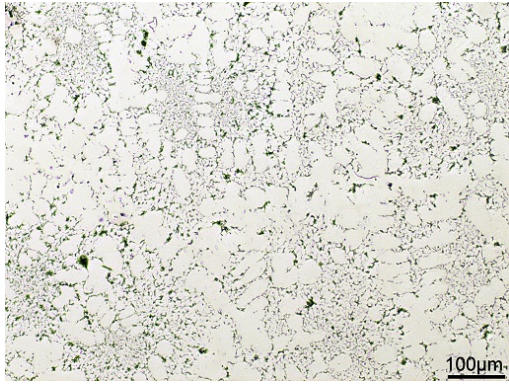
On the second series of the experiments [9] metallographic investigation was performed as below. As explained earlier, the only difference in the chemical composition of the samples from the second series is in the Ti content (see Table 4, row 5-8). The images were taken with and without chemical etching. As shown in Fig. 41.a, in the sample GI.1 the graphite is mostly type B, C and A. Sample GI.2 shows finer graphite flakes in the form of type A and B (Fig. 41.b). In some areas, fine graphite is formed as type D. However, in the high-Ti samples graphite is mostly formed as fine type D (Fig. 41.c&d). Fig. 41.b & c show that the graphite becomes finer with increasing addition of Ti.



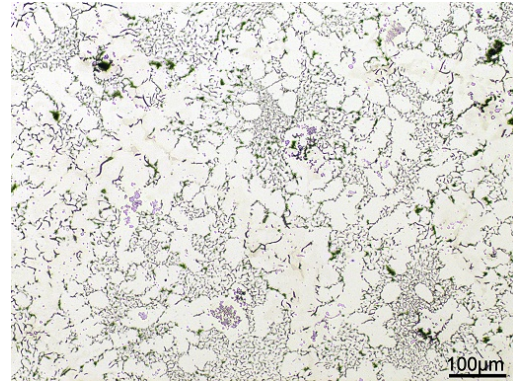
a) Sample GI.1, 0.01%Ti



b) Sample GI.2, 0.1%Ti



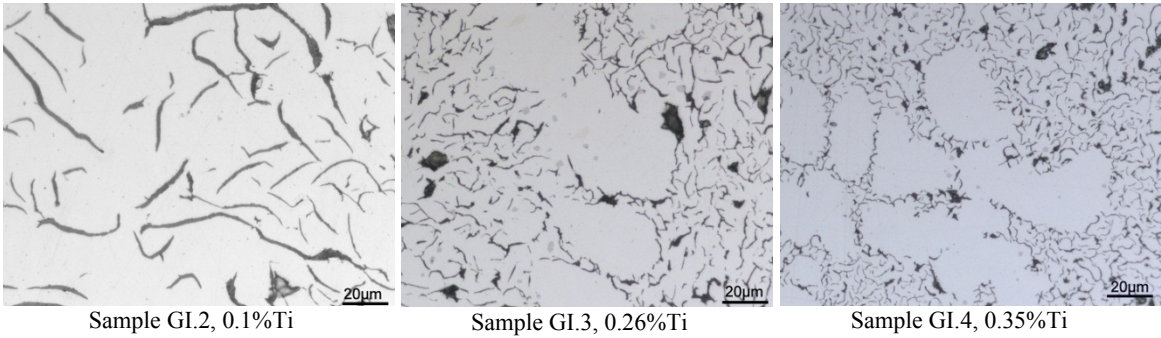
c) Sample GI.3, 0.26%Ti



d) Sample GI.4, 0.35%Ti

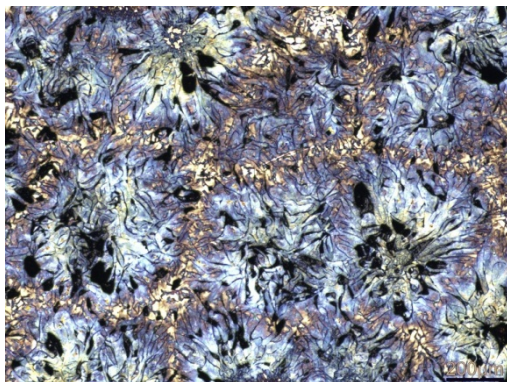
Fig. 41- As-cast microstructure of samples GI.1-4, 100X [Moumeni; Tiedje and Hattel, Paper II]

As expected, TiC inclusions were identified in the medium and high-Ti samples (Fig. 42). Sample GI.3 and 4 have very similar microstructure. The only difference which could be addressed is the scale of the graphite and higher number of TiC(N) inclusions in the sample GI.4.

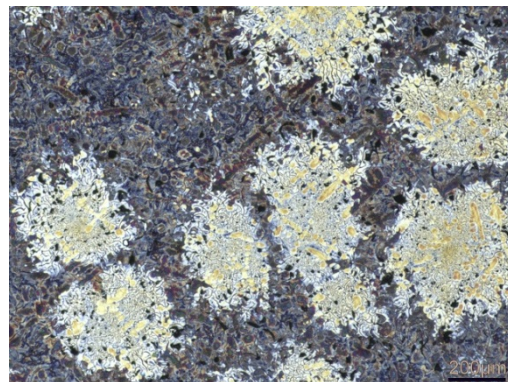


Sample GI.2, 0.1%Ti Sample GI.3, 0.26%Ti Sample GI.4, 0.35%Ti
 Fig. 42- As-cast microstructure of samples GI. 2, GI.3 and GI.4; 500X [Moumeni; Tiedje and Hattel, Paper II]

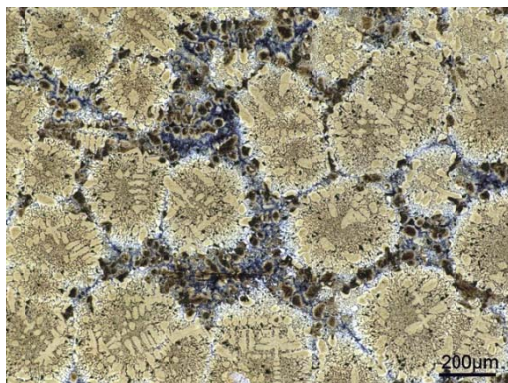
Additionally, the metallography samples were colour etched by the same procedure as the first series of the experiments. As shown in Fig. 43, addition of titanium promotes significant segregation in the microstructure. Besides, dendrites are more pronounced in the Ti containing samples.



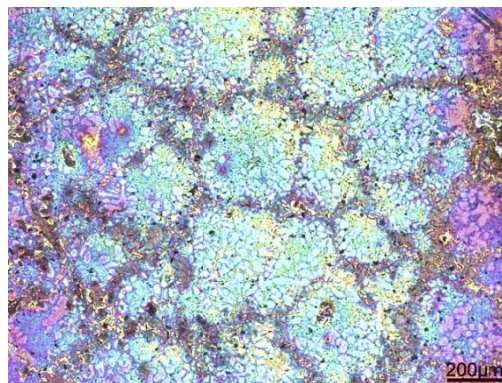
Sample GI.1, 0.01%Ti



Sample GI.2, 0.1%Ti



Sample GI.3, 0.26%Ti



Sample GI.4, 0.35%Ti

Fig. 43- Colour etched, 50x [Moumeni; Tiedje and Hattel, Paper II]

TiC inclusions are mostly observed at the intercellular areas (Fig. 44.a), at the borders of the secondary arms of dendrites (Fig. 44.b).

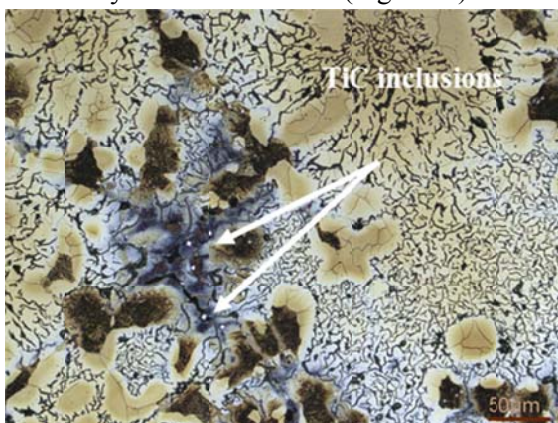


Fig. 44- Colour etched sample GI.3; TiC inclusions indicated [Moumeni; Tiedje and Hattel, Paper II]

4.3. Methodology and the instruments for electron microscopy investigations

In this work a dual beam microscope in which both electron beam and focused ion beam columns are applied is used for TEM sample preparation. For this purpose an FEI Helios EBS3 dual beam FIB/SEM microscope was used at DTU-CEN. Three specimens were prepared as explained in section 4.3.1.

The TEM samples were studied using an FEI Tecnai T20 G2 located at DTU-CEN and a JEOL JEM 3000F TEM (300 kV) located at DTU-Risø.

The SEM investigation on the first series of samples was performed at the Ohio State University by an XL-30 ESEM equipped with an EDAX.

The software “Jems” has been used to index SAED patterns. Jems is developed at CIME-EPFL for simulation of TEM diffraction patterns and images. This software offers tools for the automatic indexing of SAED or Kikuchi patterns.

4.3.1. Instruments and techniques

A dual beam microscope combines a focused ion beam (FIB) column and a scanning electron microscopy column in one unit. This combined system enables us to carry out TEM sample preparation, precision cross-sectioning and automated 3D process control. The ion beam is applied for material removal, while the SEM is used for imaging and chemical analysis. In other words, it is possible to view the cross-section face using the electron beam while the ion beam mills a thin sample out of the bulk material to be analysed. Therefore, this monitoring allows the milling to be stopped when the feature of interest is exposed. In addition, the electron beam can be used to monitor sample thickness and to check that the protective layer on the sample is intact. In-situ lift-out is the technique which is applied for this kind of sample preparation. While preparing the TEM sample, it is important that the ion-beam does not pollute it with Ga ions, which can be avoided by using low voltage and current cleaning at the end.

i) In-situ Lift-out technique

One of the main advantages of the lift-out technique over other sample preparation methods is that most of the time the original bulk sample does not need to be initially prepared itself or only a minor preparation is needed. A series of secondary electron images is presented in Fig. 45 to illustrate the in-situ lift-out technique sequences.

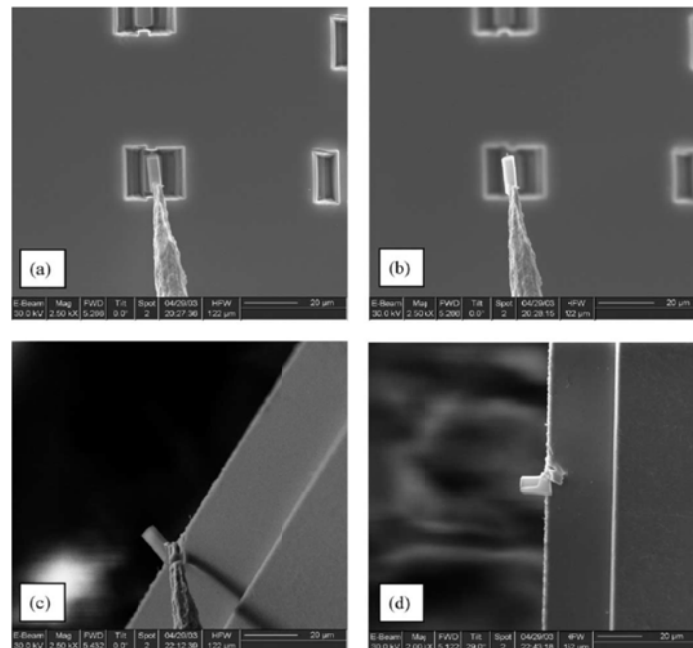


Fig. 45. Secondary electron images of (a) a cantilever shape specimen milled into the substrate with a needle Pt welded to it, (b) a wedge shaped piece of material attached to a needle raised above the sample, (c) the wedge being attached to TEM grid and (d) a wedge shape specimen attached to a grid bar into which a TEM specimen has been milled [73].

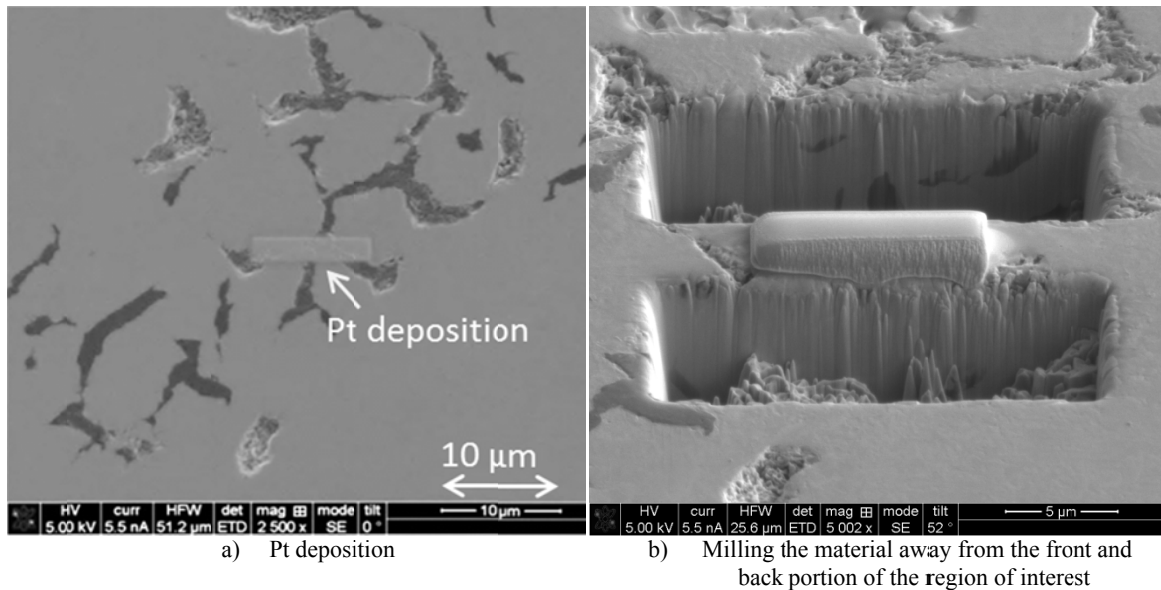
Before starting the sample preparation, one has to decide on the final dimensions of the sample. The final dimensions of the FIB lift-out will depend on several parameters such as the dimensions of the final sample; the analysing method that will be applied to study the lift-out specimen (the TEM samples for this work were thinned down to about 80-130 nm); the free

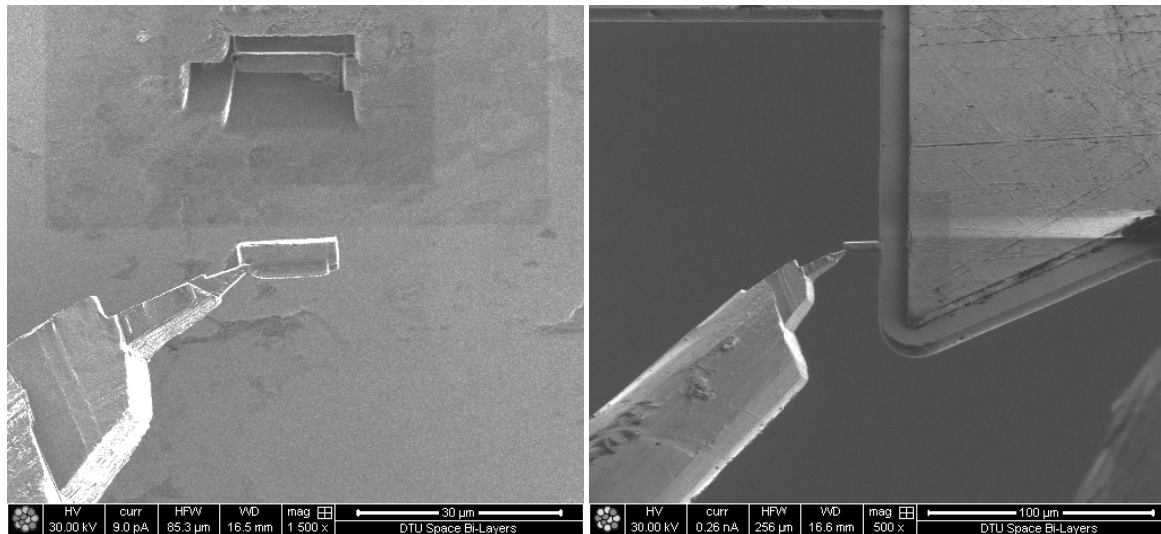
space between the mesh hole openings in the grids to support the lift-out specimen, the size of the features of interest and the FIB milling time available [74].

Most FIB lift-outs begin by using the ion beam assisted chemical vapour deposition (CVD) process to deposit a 0.5-2 μm thick platinum metal line onto the specimen surface (Fig. 46.a). The platinum line may be used to mark the region of interest, and to protect the underlying region from being sputtered away during subsequent milling steps (Fig. 46.b). Next, high beam currents with correspondingly large beam sizes are used to mill large amounts of material away from the front and back portion of the region of interest. The front and back trenches are usually positioned about 0.5 μm from the Pt layer. The larger trench opening allows SEM viewing of the specimen from both sides.

Once the specimen reaches a thickness of about 1 μm due to the FIB milling at the both sides, it is tilted 45° or more with respect to the ion beam. Then, the remaining edges of the specimen are cut free. The Omniprobe, which is used to handle the sample, is positioned to touch the FIB milled sample foil. The FIB is then used to attach the Omniprobe to the sample by deposition of Pt using the FIB's CVD and the sample will be lifted out by manipulating the Omniprobe (Fig. 46.c).

Then, the Omniprobe/sample assembly is positioned onto a grid and the CVD operation is again used to attach the sample to the grid (Fig. 46.d). The sample will then be FIB milled to electron transparency using conventional FIB milling practices. An example of the final prepared specimen is shown in the Fig. 47.





c) Sample, attached to the Omniprobe, lifted out of the bulk material

d) The Omniprobe/sample assembly positioned onto a grid

Fig. 46. In-situ lift-out sequences [Moumeni; Tiedje; Grumsen; Danielsen; Horsewell and Hattel, Paper IV]

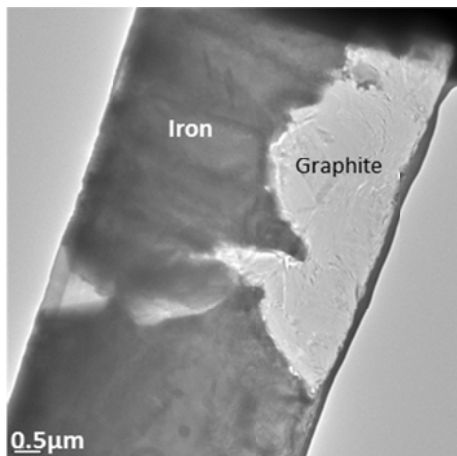


Fig. 47. TEM image of the sample prepared for TEM study at low magnification [Moumeni; Tiedje; Grumsen; Danielsen; Horsewell and Hattel, Paper IV].

ii) TEM techniques

Transmission electron microscopy (TEM) is one of the important methods for studying microstructures at very small scales (down to nano-) in great details. Using TEM, we look through a piece of material with electron beams, usually at high magnification (in our experiments up to 30000x). The techniques that we have applied in this work are bright field (BF) and dark field (DF) imaging and selected area electron diffraction patterns (SAED).

Bright field images contain information from all electrons that have passed through the sample. These images show a combination of absorption and diffraction contrast. With dark field images, specific crystallographic planes that are oriented such that they are diffracting, can be viewed in order to see specific features such as dislocations, regions of ordering or strain fields etc. Dark field images typically have considerably higher contrast than bright field images although the overall intensity is greatly reduced. The aperture can be moved so that either electrons that have gone directly through the sample are viewed or so that electrons scattered by the selected crystallographic planes go through it. An image created by electrons from the direct

beam is called a bright-field image. If a diffracted beam is used it will create a dark-field image (Fig. 48).

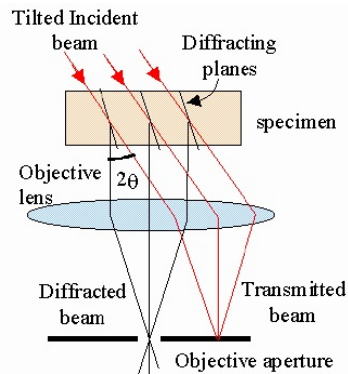


Fig. 48. Dark field imaging on TEM [74]

Diffraction contrast arises because the intensity of the diffracted beams is different in different regions of the specimen. These variations arise because of changing Bragg conditions. From diffraction patterns we can 1) measure the spacing between crystal layers; 2) determine the orientation of a single crystal or grain; 3) find the crystal structure of an unknown material and 4) measure the size, shape and internal stress of small crystalline regions.

4.4. SEM study

The first series of samples studied were un-etched and deep-etched by Nital 2%. In the high-S low-Ti iron (B401.1), a large number of polygonal MnS inclusions were found (Fig. 49). More than 50% of these inclusions seem to be attached to the sides of the graphite flakes (Fig. 50a & b). Complex Al-Mg-Si-Ca oxide compounds were identified at the centre of some of the MnS particles (Fig. 50c, d, e and f).

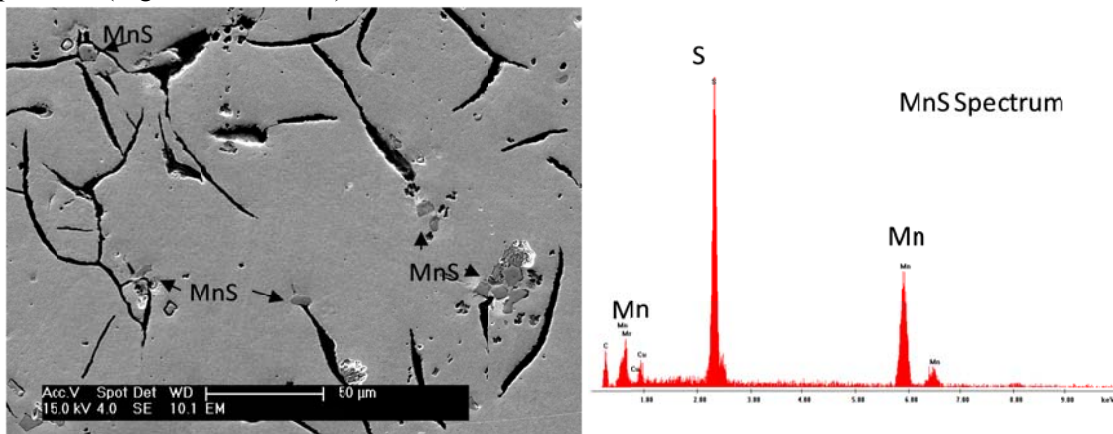


Fig. 49. Unetched sample 401.1- 0.12% S, 0.018% Ti

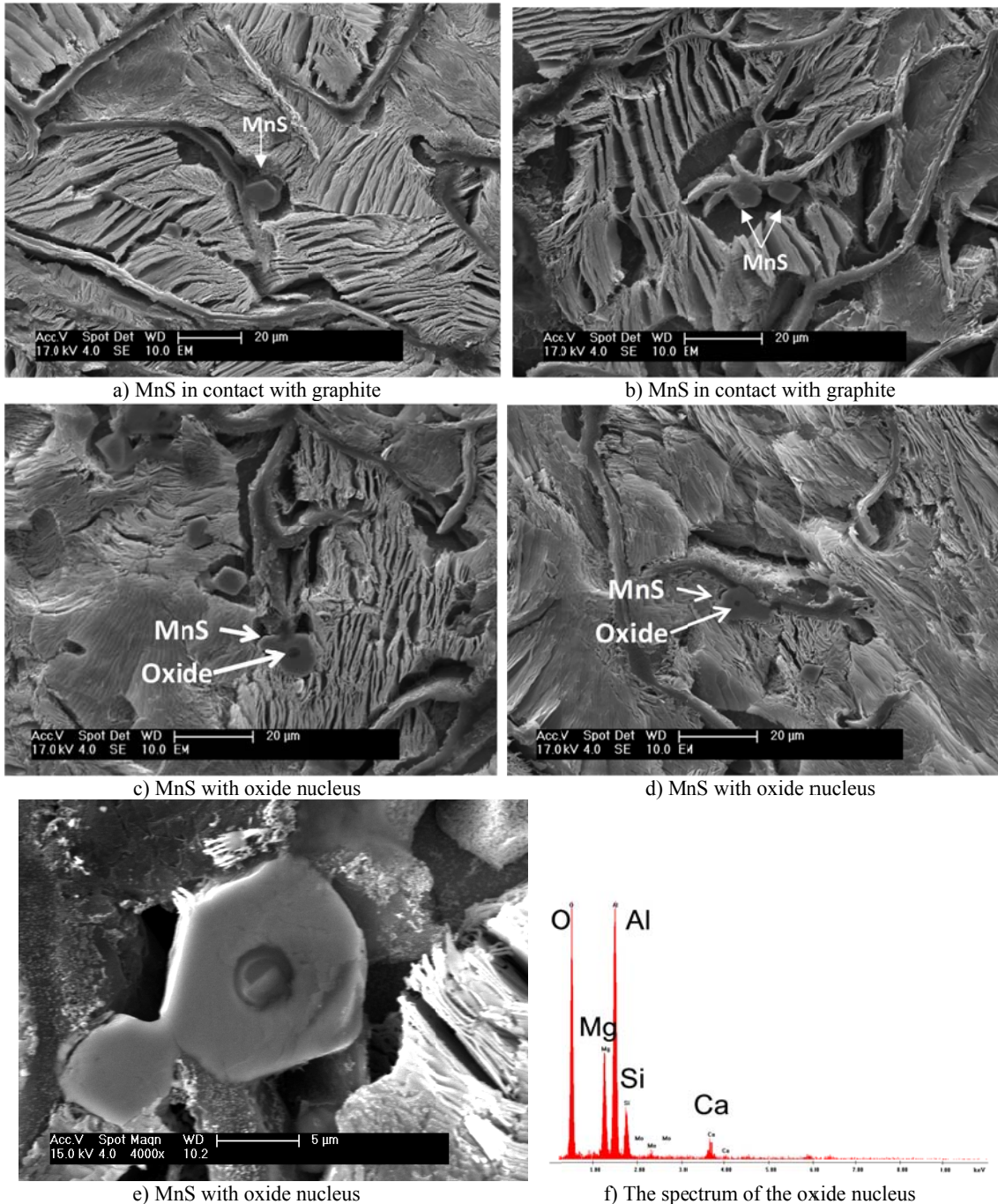


Fig. 50. Sample 401.1 – Deep-etched with Nital 2% [Moumeni; Stefanescu; Tiedje; Larrañaga and Hattel, Paper III]

In the presence of both Ti and S (sample B401.5) a variety of inclusions with different morphologies was found. The smaller inclusions and their spectrum are shown in Fig. 51. The majority of the inclusions in this sample are (MnTi)S, with a variety of morphologies (Fig. 52). As also shown in Fig. 35b, the (MnTi)S inclusions are mostly formed in the middle of the secondary arms of dendrites. It is reasonable to assume that they have acted as nuclei for the austenite dendrites. This would explain the significant increase in the fraction of austenite as the Ti/S ratio increased from 0.15 (sample B401.1) to 3 (sample B401.5). MnS inclusions were also found in this iron (Fig. 52d), and again, they seemed to act as nuclei for the graphite.

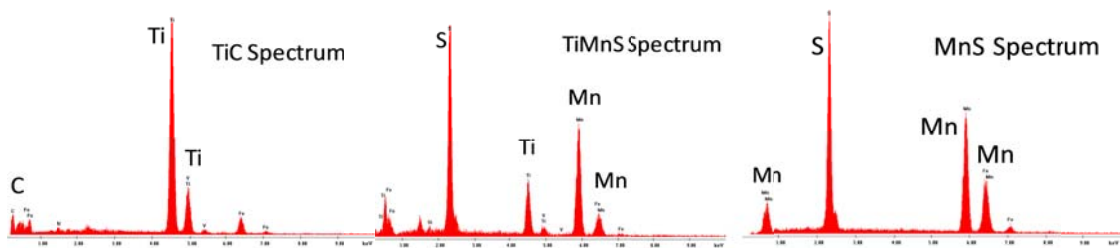
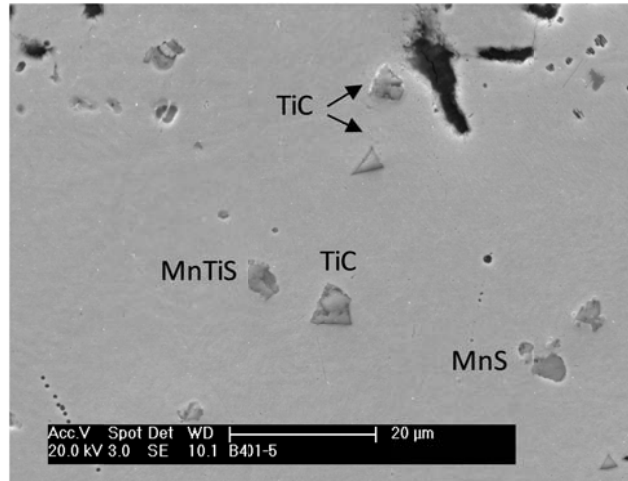
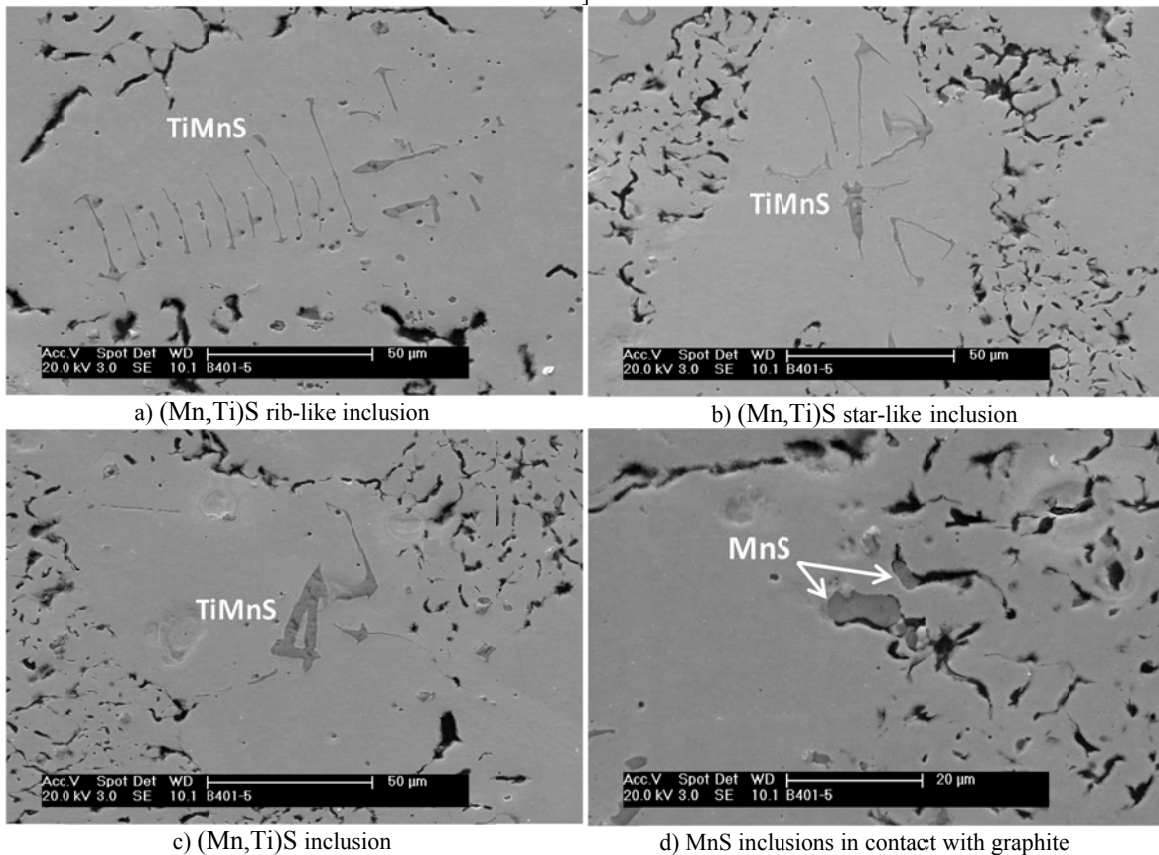


Fig. 51. Unetched sample. 401.5 - 0.120% S, 0.36% Ti [Moumeni; Stefanescu; Tiedje; Larrañaga and Hattel, Paper III]



a) (Mn,Ti)S rib-like inclusion

b) (Mn,Ti)S star-like inclusion

c) (Mn,Ti)S inclusion

d) MnS inclusions in contact with graphite

Fig. 52. Unetched SEM micrographs of sample 401.5 showing (Mn,Ti)S and MnS inclusions [Moumeni; Stefanescu; Tiedje; Larrañaga and Hattel, Paper III]

Deep etched microstructures of sample B401.5 (Ti/S=3) are shown in Fig. 53. The presence of (MnTi)S inclusions in the austenite is confirmed (Fig. 53 a, b and c). These inclusions are the most dominant kind of inclusions found in this alloy. A few TiC inclusions were found in the austenite (Fig. 53.b), and many TiC inclusions were found in the proximity of the superfine graphite flakes (Fig. 53.c, d). Yet, as they do not show clear contact with graphite (they seem not to be on the side of the graphite), in our opinion, the appearance is not that of graphite nuclei.

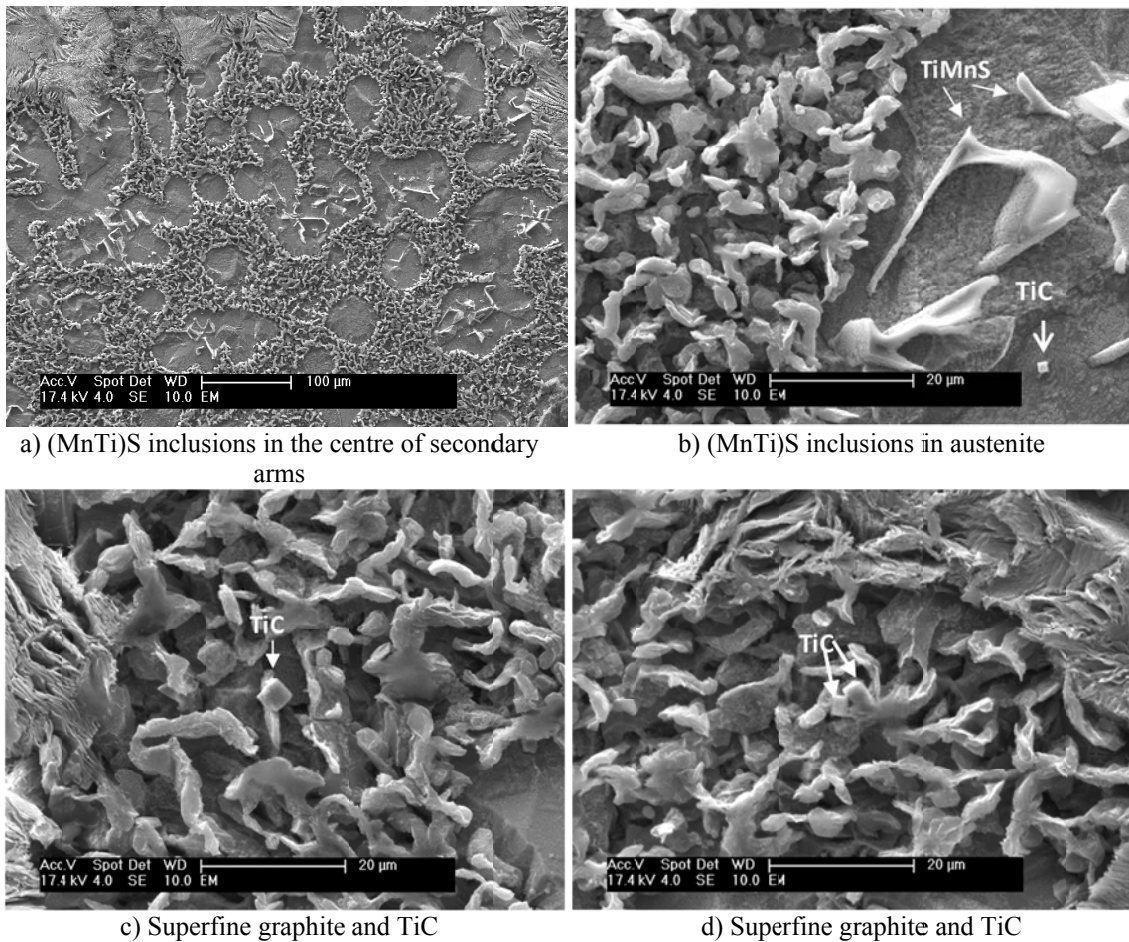


Fig. 53. Deep etched micrographs of sample 401.5 - 0.120%S, 0.36%Ti [Moumeni; Stefanescu; Tiedje; Larrañaga and Hattel, Paper III]

The images of the deep-etched sample B621.1 (low-S low-Ti, medium Ti/S ratio) are presented in Fig. 54. The microstructure exhibits coarse type-A graphite (length 100 to 200 μ m) and almost no inclusions. The spectrum of these few cubic inclusions found indicates the composition of a titanium carbonitride Ti(NC). While the peak of Ti and N are at the same keV, this peak was very small in other TiC spectra.

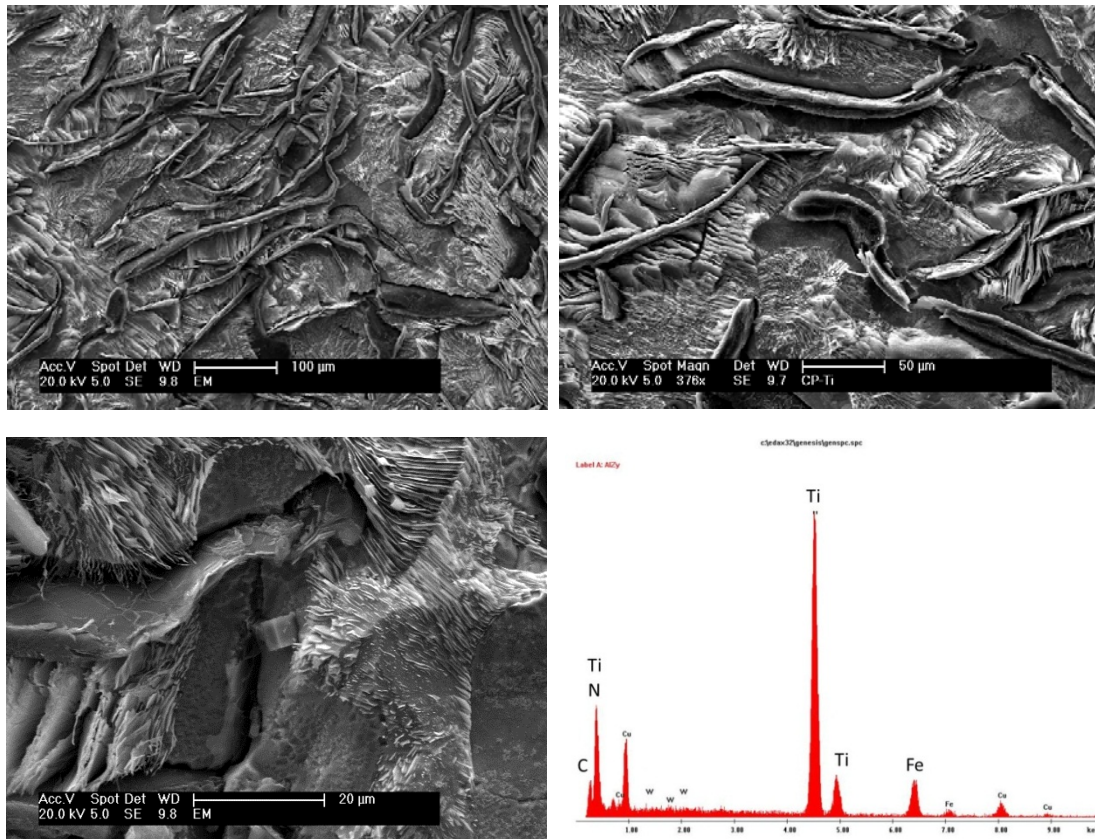


Fig. 54. Deep etched micrographs of sample 621.1 – 0.018%S, 0.06%Ti [Moumeni; Stefanescu; Tiedje; Larrañaga and Hattel, Paper III]

A dramatic change in the microstructure occurs when the Ti/S ratio is raised to 29.2 for sample 621.5 with low-S high-Ti (0.012% S, 0.35%Ti). A large number of cubic TiC particles are observed (Fig. 55). This is consistent with previous research [7] where it was found that the number of Ti compounds increases significantly as the Ti content in the iron increases. They are the dominant inclusions at this composition. As also documented earlier, the TiC particles are pushed by the austenite dendrites to the last regions to solidify (Fig. 55 a). There is no evidence showing that TiC could act as nuclei for the primary austenite. However, isolated instances where the TiC is in contact with the graphite have been found (Fig. 55c). We do not feel that this is enough proof to demonstrate a graphite nucleation effect by the TiC. A few MnS inclusions were also observed. The graphite flakes are thick and short with a high branching tendency (Fig. 55c, d).

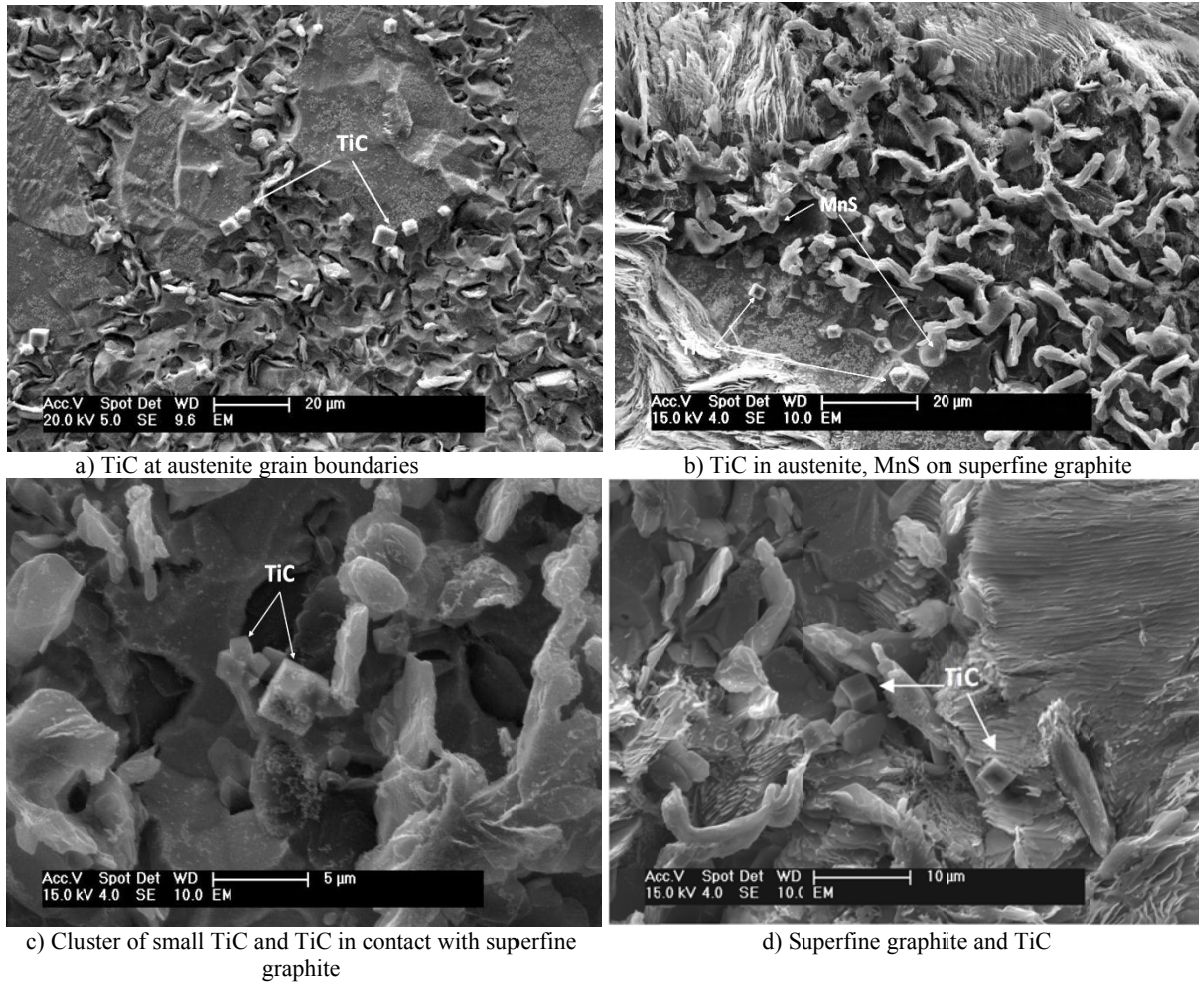


Fig. 55. Deep etched micrographs of sample 621.5 - 0.012%S, 0.35%Ti [Moumeni; Stefanescu; Tiedje; Larrañaga and Hattel, Paper III]

A summary of the type and location of inclusions as a function of composition and the Ti/S ratio is given in Table 6. Note again that the amount of inclusions in the low-S low-Ti sample (621.1) was minimal.

Table 6. Summary of types and location of inclusions from SEM analysis [Moumeni; Stefanescu; Tiedje; Larrañaga and Hattel, Paper III]

Sample	%S	%Ti	Ti/S	Mn/S	Graphite	Dominant inclusion	Inclusion location	Other inclusions
401.1	0.12	0.018	0.15	4.5	type-A	MnS	in contact with Gr	none
401.5	0.12	0.36	3	4.2	interdendritic/ superfine	(Mn,Ti)S	in austenite	MnS, TiC
621.1	0.018	0.06	3.33	30.6	type-A	TiC, Ti(CN)	in austenite	MnS
621.5	0.012	0.35	29.2	48.3	superfine + some type A	TiC	at austenite grain boundaries; in contact with Gr	MnS

Some high magnification pictures of the superfine graphite are presented in Fig. 56. It is seen that the graphite flakes are very short, thick and that they bend and twist significantly.

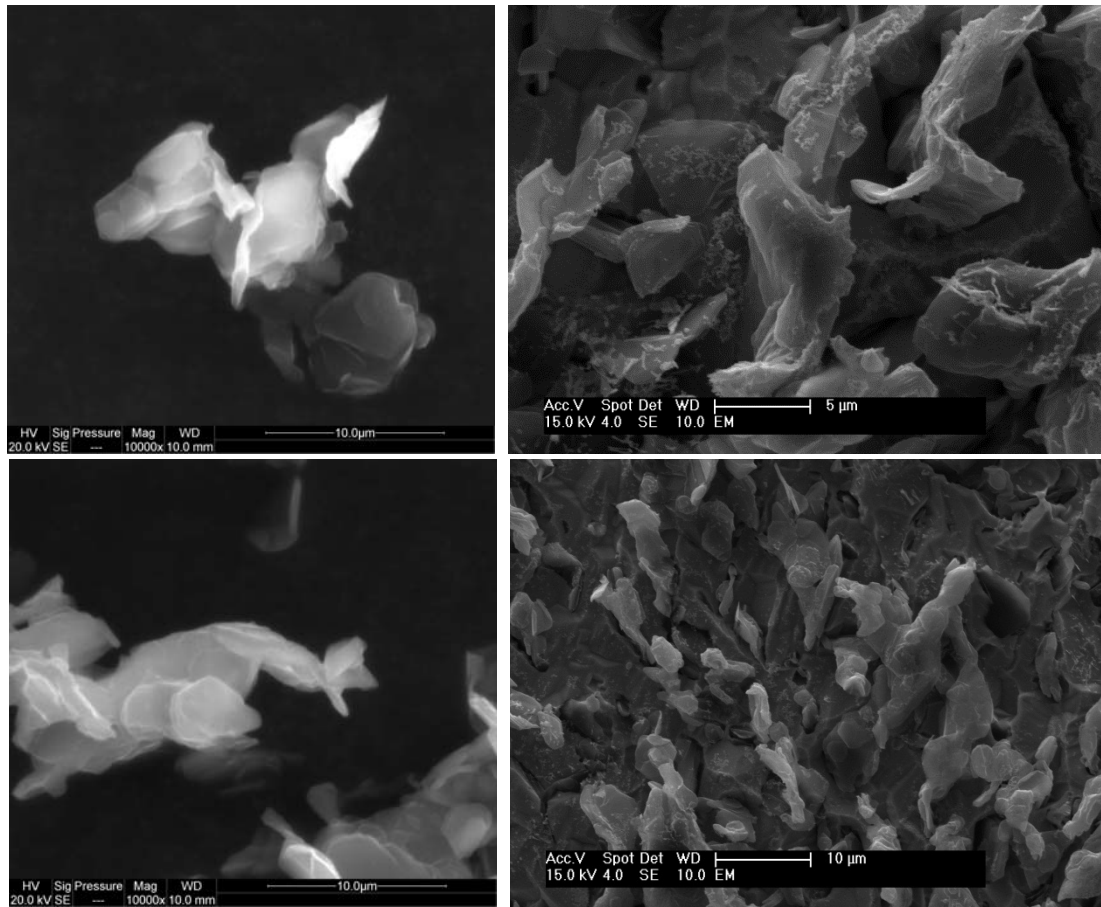
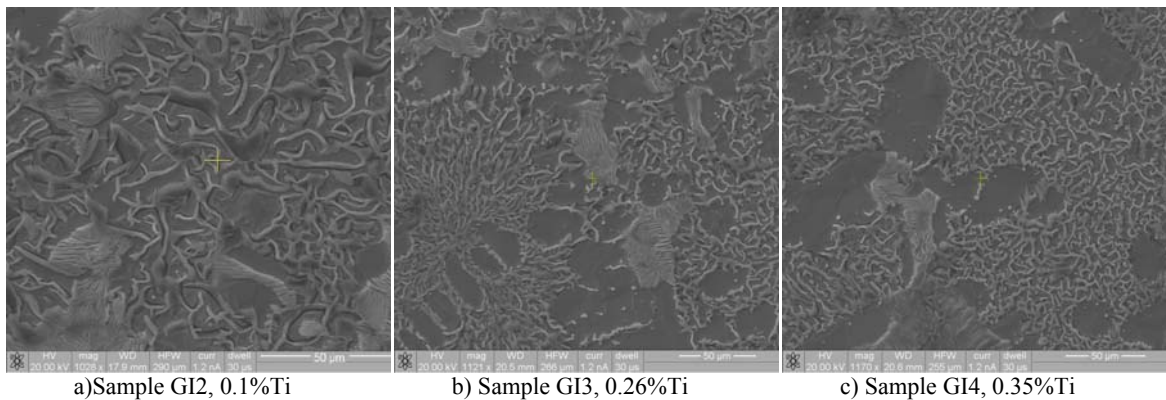


Fig. 56. SEM micrographs of superfine graphite from deep etched sample 621.5 [Moumeni; Stefanescu; Tiedje; Larrañaga and Hattel, Paper III]

The specimens from the second series of experiments were also deep etched using a 2% Nital etchant, so that the graphite and inclusions were brought forward for closer analysis. The SEM images are presented in Fig. 57 & Fig. 58. The trend of changes in the shape and size of graphite, which was shown and explained in Fig. 41 and Fig. 42, could be seen in these images.



a) Sample GI2, 0.1%Ti

b) Sample GI3, 0.26%Ti
Fig. 57- As-cast, SEM images

c) Sample GI4, 0.35%Ti

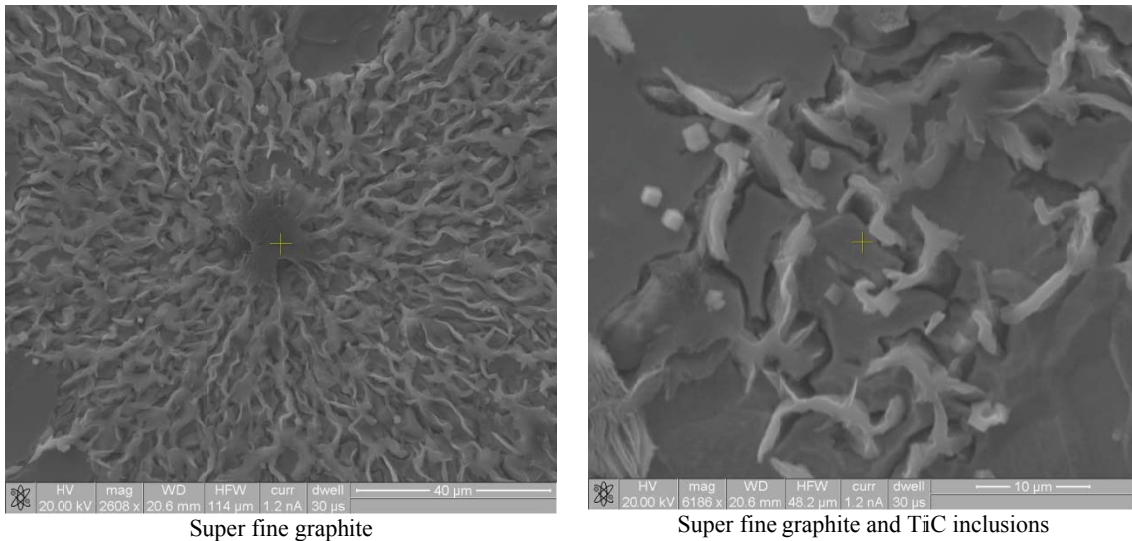


Fig. 58- sample G13, 0.26% Ti, SEM images [Moumeni; Tiedje; and Hattel, Paper II]

4.5. TEM results

The low-Ti (621.1) and high-Ti (621.5) samples were investigated to find their overall differences and similarities [30]. A detailed crystallographic analysis was done on the samples. Diffraction patterns were taken in several different areas to analyse grain boundaries and coherency between the two phases.

The sampling areas of interest are depicted in Fig. 59. The low-Ti TEM sample is taken longitudinally from a relatively coarse flake. Thus, it does not include any graphite/iron interface (Fig. 60.a). The high-Ti samples include the graphite/iron interface. This has enabled us to study the orientation relationships between two phases (Fig. 60.b).

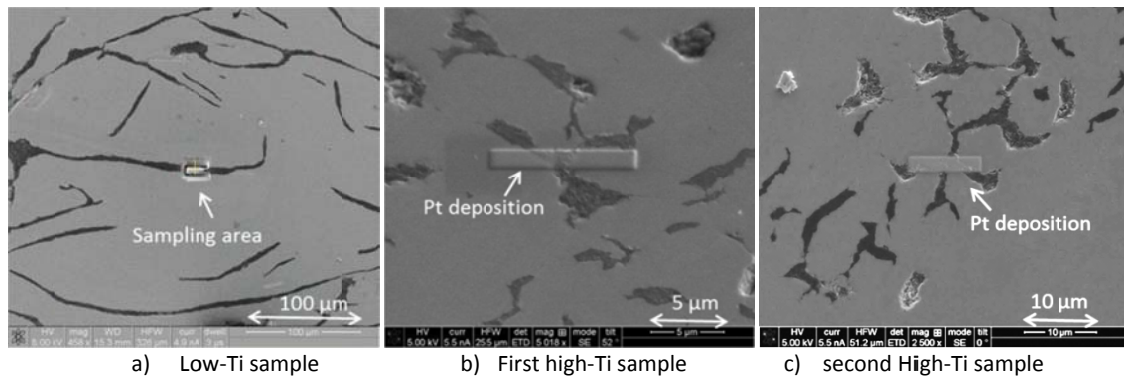
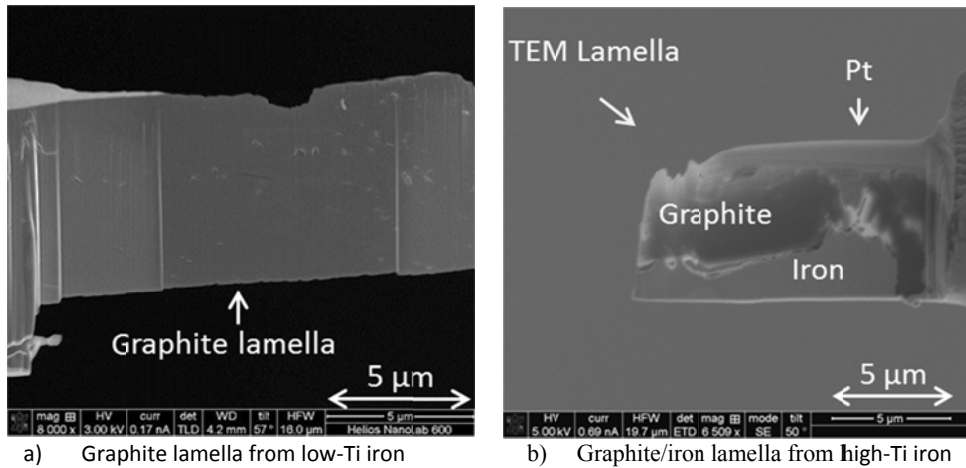


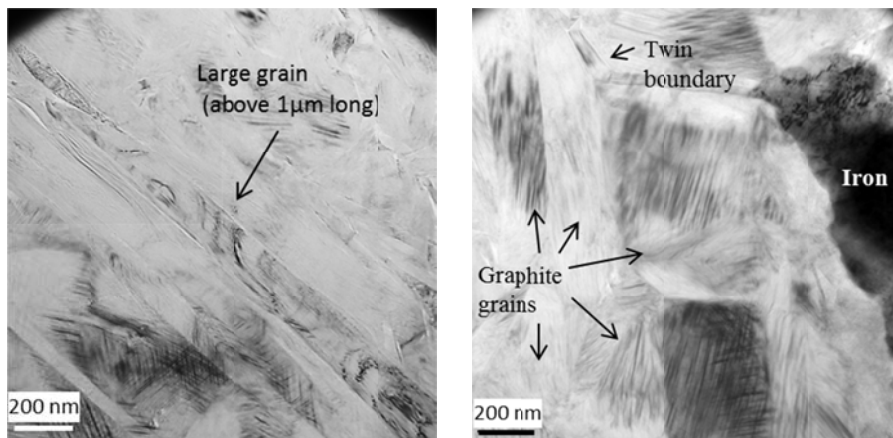
Fig. 59. Smapping area of the TEM specimens [Moumeni; Tiedje; Grumsen; Danielsen; Horsewell and Hattel, Paper IV].



a) Graphite lamella from low-Ti iron b) Graphite/iron lamella from high-Ti iron
 Fig. 60. The prepared lamellae for TEM investigation

4.5.1. Bright field imaging

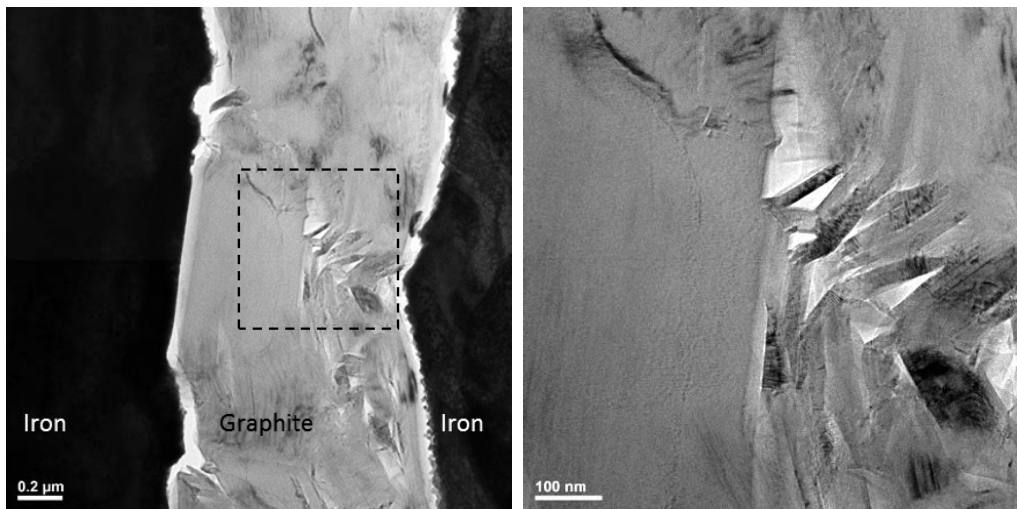
TEM bright field (BF) imaging was carried out to get an overview of the graphite microstructure. In Fig. 61, Fig. 62 and Fig. 63 some of the BF images of the above mentioned samples are shown. In Fig. 61.a from the low-Ti sample, a long grain (above 1 micrometre) of graphite can be seen. The High-Ti samples have finer microstructure. The twin boundaries can be seen in Fig. 61.b. They outline the very fine grains indicating that twinning plays an important role in the growth of the graphite lamellae.



a) Low-Ti sample, large graphite grains b) High-Ti Sample, graphite/iron grains

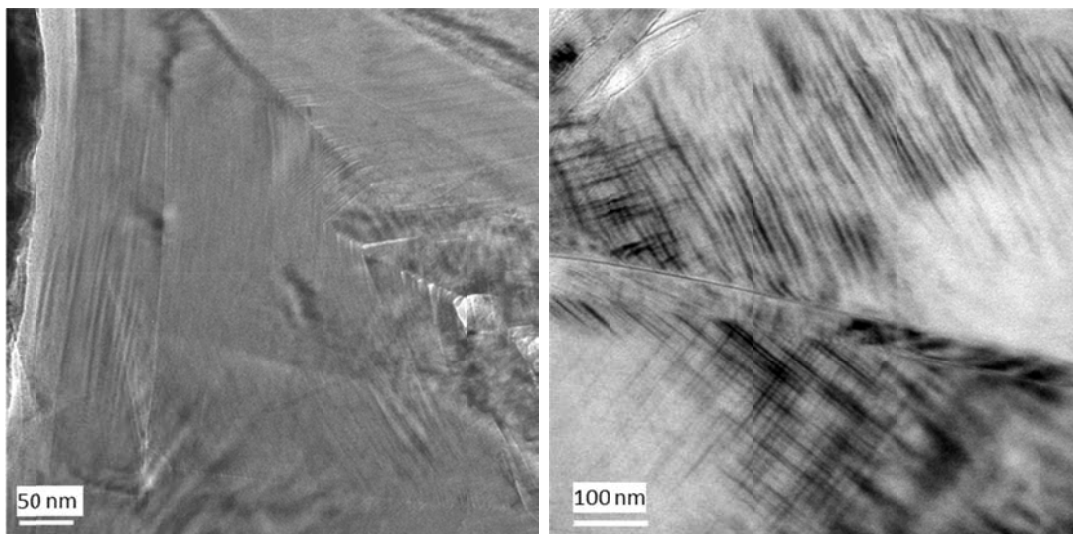
Fig. 61. TEM bright field images [Moumeni; Tiedje; Grumsen; Danielsen; Horsewell and Hattel, Paper IV]

The lamella, part of which is shown in Fig. 62, includes a longitudinal cross section of graphite and its interface with the iron matrix on both sides. As shown earlier, the TEM specimens of the high-Ti iron include the branching areas and a higher disorder is promoted in the structure of the graphite precipitates. The microstructure consists of many small grains and a higher number of voids and defects are found too (Fig. 62). The platelets of graphite are predicted to have weak and brittle attachment to each other. The cracks or voids which are seen in Fig. 62 may occur during the growth of the graphite or during TEM sample preparation. Considering the fact that graphite is a very brittle material, one could say that the fractures or voids in the crystals would happen during solidification as stresses caused by cooling and growth of the solid phase impose forces to the graphite so that it deforms and breaks.



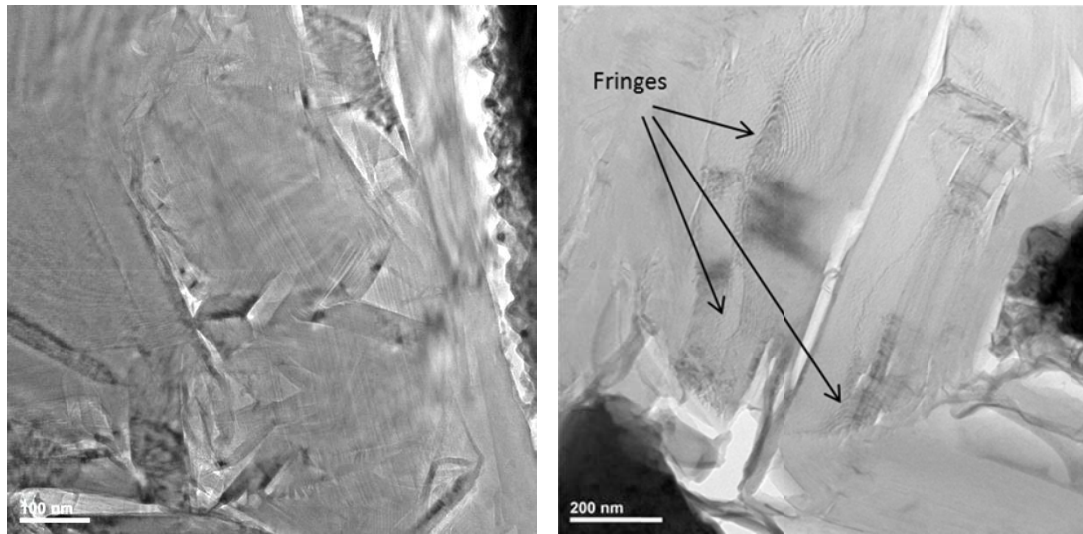
Voids and defects
 Fig. 62. High-Ti sample, bright field imaging [Moumeni; Tiedje; Grumsen; Danielsen; Horsewell and Hattel, Paper IV] b) High-Ti Sample, the marked area in Fig. 62a

Twinning seems to be one of the main mechanisms of the anisotropic growth of this type of graphite which has grown at a relatively high undercooling (Fig. 63). Twins are seen as planar interfaces, often with several parallel twin boundaries. One possibility is that rotation of the precipitated graphite could also be determined or facilitated by some form of repeated crystal twinning. The adsorption of atoms at the solid liquid interface is controlled by kinetics.



a) Growth of graphite with multiple twin boundaries b) Characteristic platelet-like morphology of graphite
 Fig. 63. High-Ti samples, bright field imaging [Moumeni; Tiedje; Grumsen; Danielsen; Horsewell and Hattel, Paper IV]

As it is shown in Fig. 64, an aggregate of multiple twins are seen in different areas. Also, some regions show rounded fringes (Fig. 64.b), indicative of another mechanism of growth. These images indicate two modes of growth of this type of graphite, with twinning being the predominant mechanism.



a) Dispersed batches with planar boundaries, assumed to be twin boundaries. b) Rounded fringes showing the possibility of conical lay-out of graphite plates.

Fig. 64. High-Ti samples, bright field imaging [75]

4.5.2. Diffraction patterns and dark field imaging

The Kikuchi lines in the iron structure close to the interface of iron/graphite were followed when tilting the sample in order to find the major zone axes of iron. Since the SAD pattern is only a 2D projection of the reciprocal lattice, a tilting test technique should be applied to determine the 3D parameters in a unit cell. The Kikuchi patterns in the graphite areas were not clear enough for this method. Using SAED patterns were acquired in both iron and graphite at either side of the interface at the iron zone axes. When doing SAED on the graphite, diffraction patterns belonging to both the rhombohedral and hexagonal crystal structure of graphite were found.

In order to identify the grains belonging to hexagonal and rhombohedral crystal structures, dark field imaging technique was applied. The graphite structure in the high-Ti samples was found to be expanded considerably in the “c” direction, that is the (001) interplanar spacings where higher than expected. The value of expansion varies in different areas; the expansion measured in the diffraction pattern images was up to 8%. The expansion in the “a” direction, along (001) planes, was significantly lower i.e. below 3%. The expansion was not found in the low-Ti specimens. Interstitial Ti atoms in the graphite structure were thought to be the reason for it, but no titanium was detected in the graphite areas by EDS. It can be speculated that the many defects in the graphite crystal structure such as stacking faults might cause the expansion in the high-Ti samples. Besides, the graphite in the low-Ti iron (flaky graphite) in the investigated areas belongs to the hexagonal unit cell and no match with rhombohedral unit cell was found in the investigated specimen.

Fig. 65 shows an area with three different diffraction patterns. The SAED pattern shown in Fig. 65.a belongs to the area shown in the bright field image (Fig. 65.b). The indicated spots 1,2 and 3 were chosen for dark field imaging and the results proved that the pattern 1 belongs to the rhombohedral unit cell while pattern 2 and 3 belong to the hexagonal unit cell. The dark field images show that the rhombohedral grain is very elongated (Fig. 65.c) and has a very straight interface with both hexagonal grains on either side of it (Fig. 65.e&f). The spots which belong to the same unit cell are depicted in Fig. 65.d.

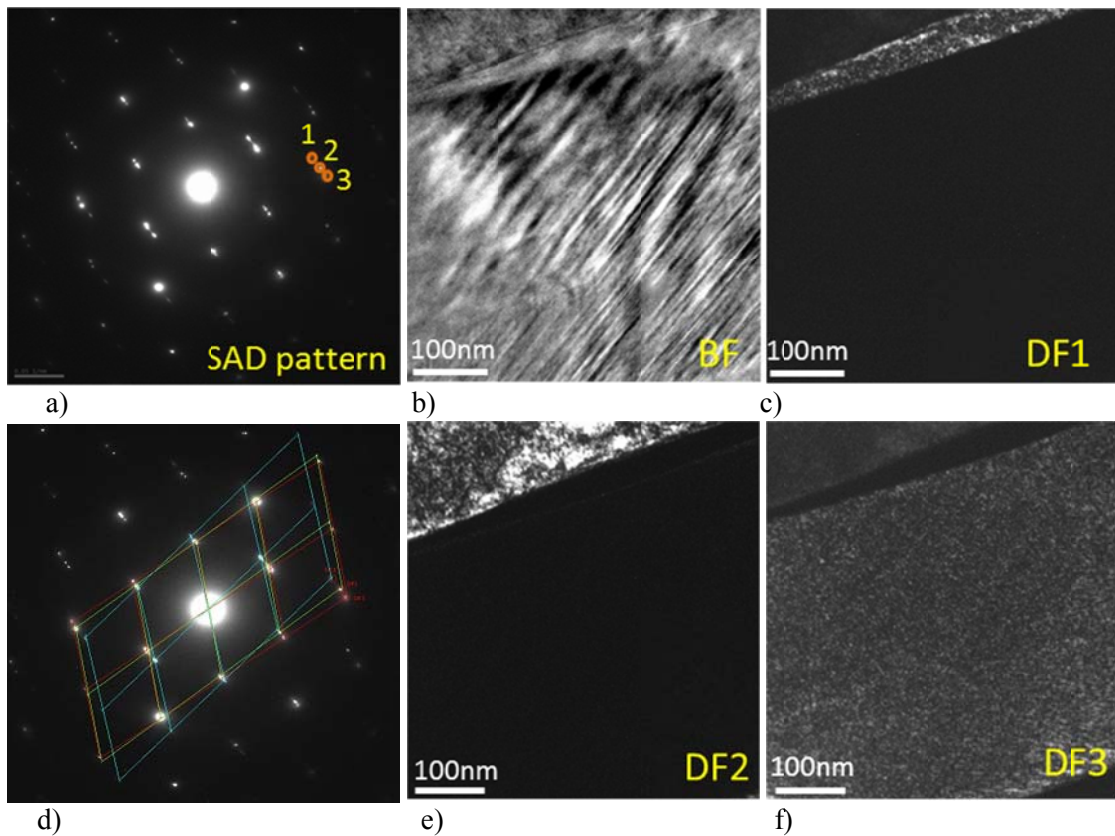
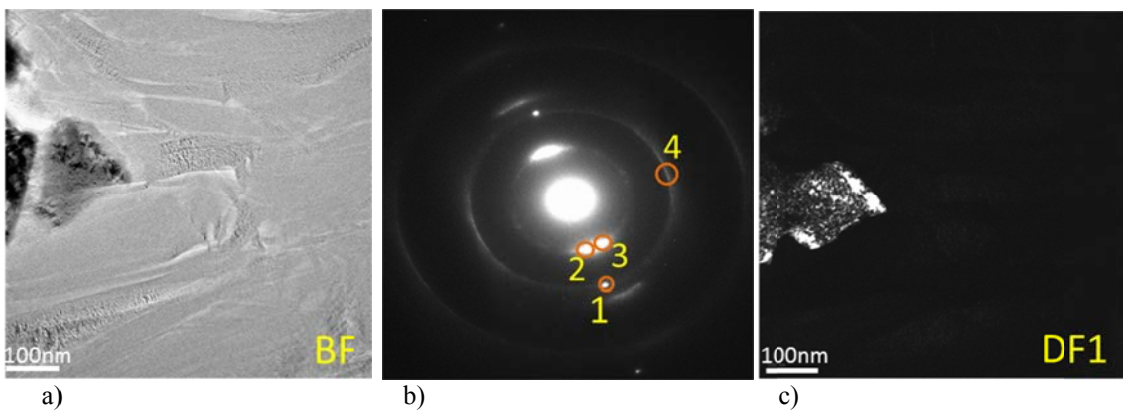


Fig. 65. a) SAED pattern of the shown area in the brightfield image (b) contains three different diffraction patterns (indexed in image d). Darkfield imaging was carried out on each of the patterns (c,e & f) [Moumeni; Tiedje; Grumsen; Danielsen; Horsewell and Hattel, Paper IV].

Fig. 66 shows an area with many smaller grains where the diffraction pattern (not in zone axis) shows a ring pattern with clear preferred orientations. This indicates that the graphite grains have some preferred orientations to each other, but do not have completely the same orientation. Every ring in the SAED pattern corresponds to a group of lattice planes of the same miller index family in this polycrystalline structure.

Some diffraction from iron is also visible in the pattern as single spots, not ring patterns.



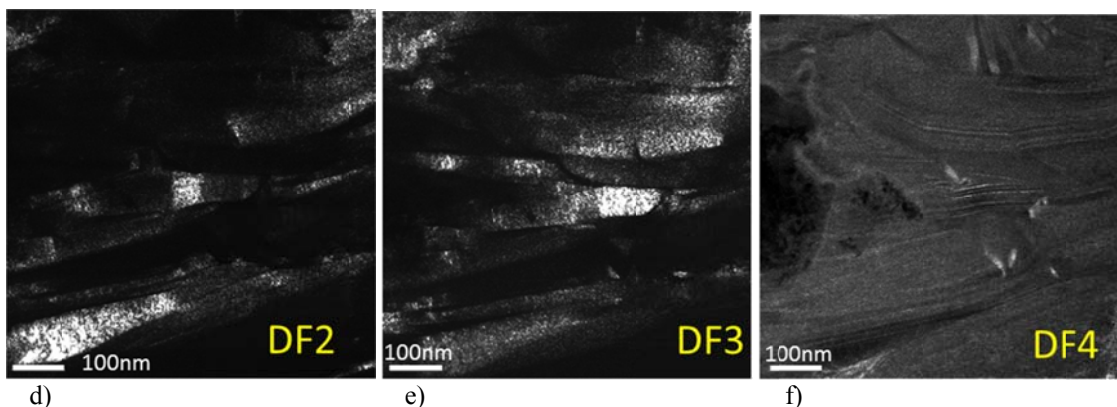


Fig. 66. TEM images of ferrite/graphite interface: a) the bright field image (BF) shows the region that the diffraction pattern (SAED) is taken from (b). Darkfield imaging (DF1-4); c) area 1 originates from the iron matrix while d,e,f) areas 2-4 are from the graphite [Moumeni; Tiedje; Grumsen; Danielsen; Horsewell and Hattel, Paper IV].

In Fig. 66 a branching area of graphite composed of a high number of microcrystalline grains is studied. The selected area for the SAED pattern (Fig. 67.b) is indicated in Fig. 67.a. Two spots D1 and D2 on the second ring (Fig. 67.b) are chosen for dark field imaging. The dark field images are shown in Fig. 67.c&d. Although the diffraction pattern is consisting of rings, some preferred orientation is also observed in this SAED.

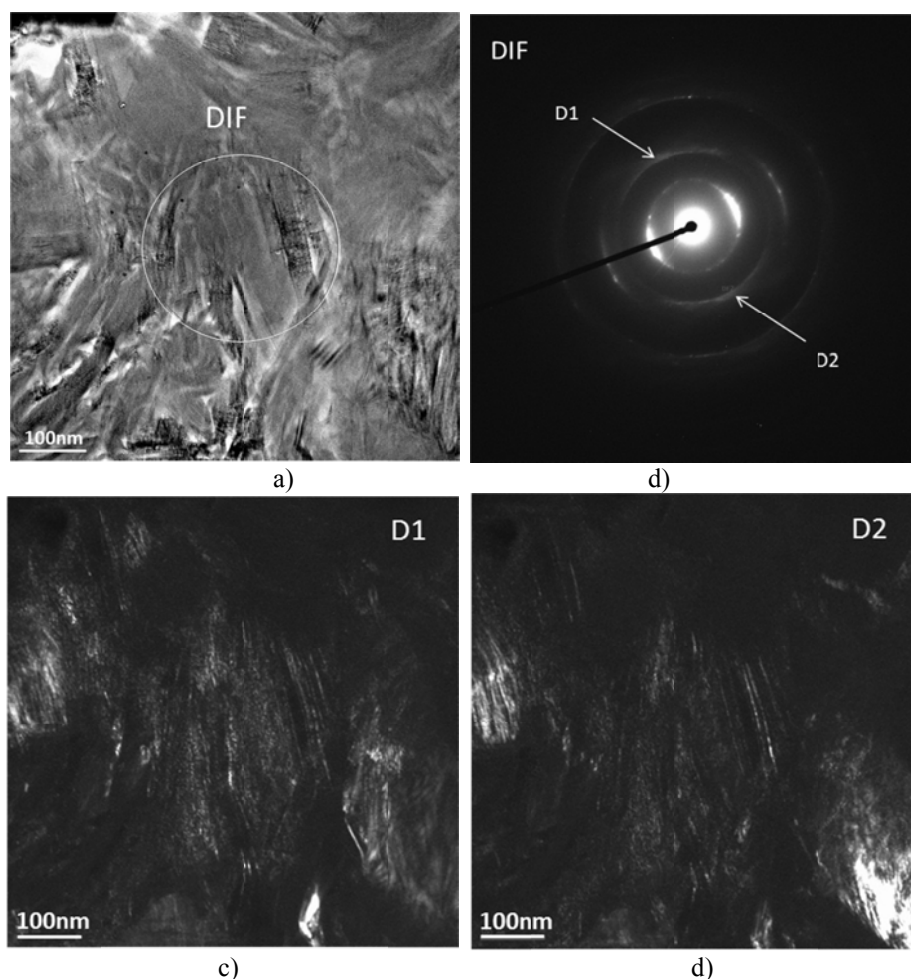


Fig. 67. a) The bright field, b) diffraction pattern, c&d) dark field images of graphite; high-Ti specimen; diffraction pattern consisting of rings with some preferred orientation.

As mentioned before, twinning is a feature which is observed frequently in the structure of graphite. In Fig. 68 a twinning area is shown. The BF image (Fig. 68.a) and the related diffraction pattern (Fig. 68.b) and three spots chosen for dark field imaging are depicted below. The dark field images related to the three spots are shown in Fig. 68.c,d&f.

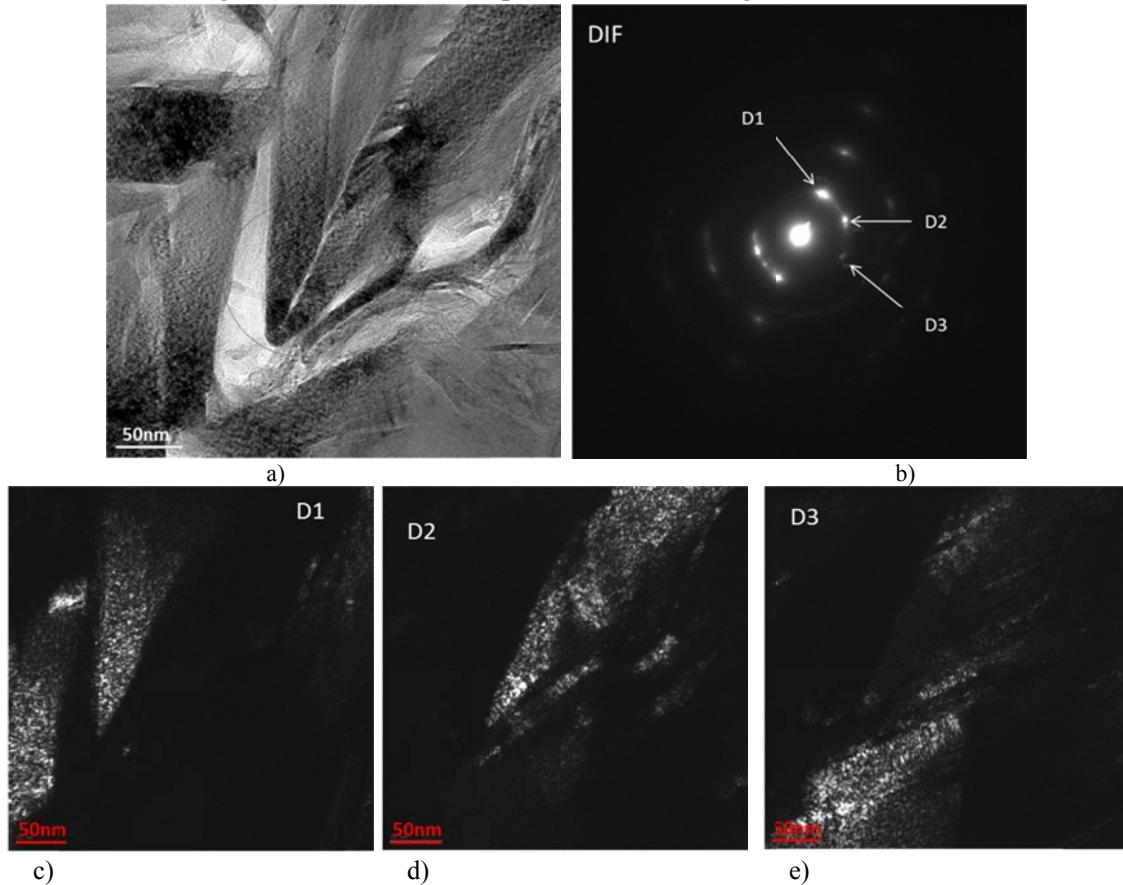


Fig. 68. Twinning; a) bright field, b) diffraction pattern, c,d&f) dark field images from high-Ti specimen.

4.5.3. Orientation relationship between graphite and iron

Several interface areas were investigated in an effort to find the orientation relationship between the graphite and the iron. The zone axis in the iron at the interface were found by tilting the specimen and SAED patterns were taken from both iron and graphite at the interface.

As an example, in Fig. 69 one interface area in the bright field and dark field images is shown. The diffraction pattern from both phases was studied. There was no specific orientation relationship between the iron and the investigated graphite grains. But since the orientation relationship between the graphite grains themselves varied slightly, it could be argued that some of them do correlate with the iron crystal structure. Meanwhile, it has been reported [28] that iron and graphite in both grey and ductile iron show a very strong orientation relationship. This difference is probably due to the mechanism of formation of superfine interdendritic graphite which varies in normal lamellar and nodular graphite.

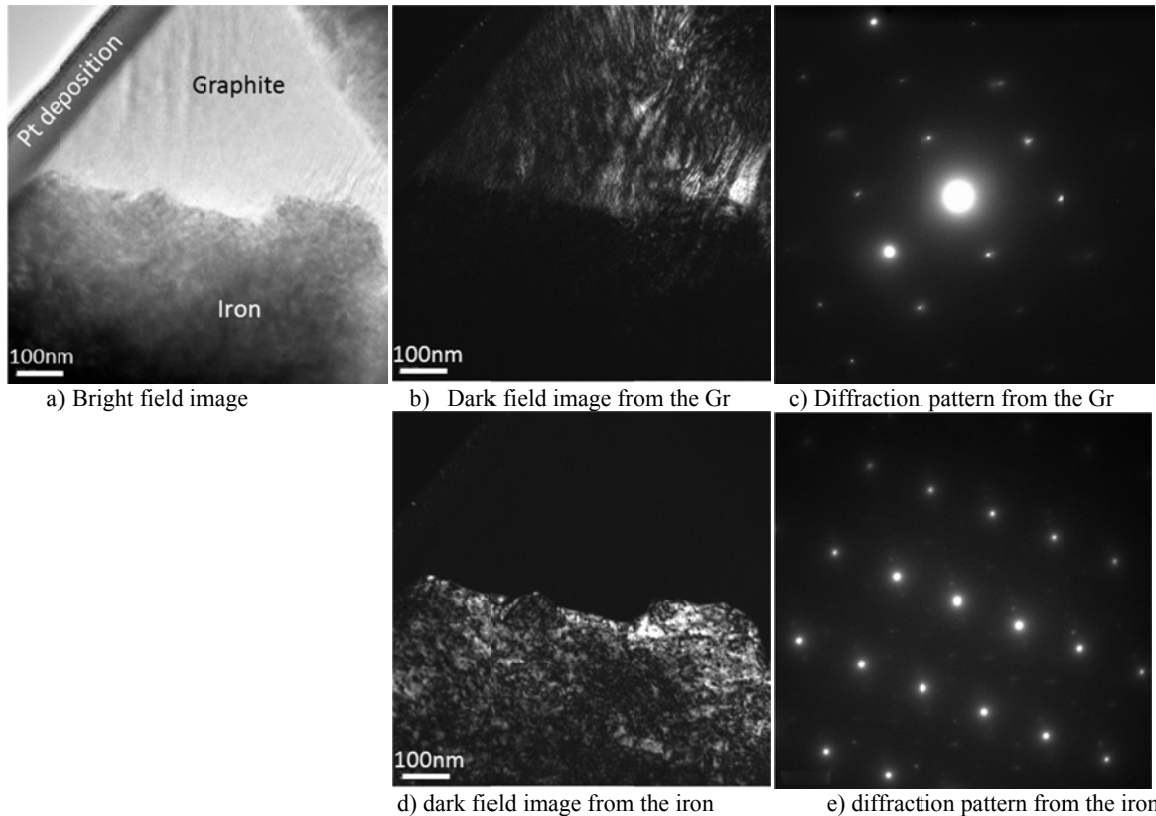


Fig. 69. An interface area in the high-Ti specimen; from the diffraction patterns no specific relationship between Gr and Iron matrix was found.

4.6. Discussion

There are two major effects of the Ti additions that need to be understood: the increased amount of austenite and the formation of the superfine interdendritic graphite. In relation to these, arguments involving nucleation and growth kinetics of the phases must be considered.

4.6.1. Inclusions and the primary austenite

As shown in Table 7, Ti addition to both low and high S irons results in an increase of the liquidus temperature, T_L , and a decrease of the minimum eutectic temperature, T_{min} . The classic explanation for the first effect is an increase in the nucleation potential. In the following, this is going to be discussed for both low-S and high-S titanium alloyed irons.

i) High-Ti high-S iron

In the previous chapter it was described that (MnTi)S precipitates form early in solidification, and that they are located at the core of the austenite dendrites. Their fish bone or Chinese script morphology indicate that they form just before, or together with the first pre eutectic austenite that forms at T_L . Indeed, Ti addition to a melt with sufficient S (401.5 – 0.12%S), produces complex (MnTi)S that are nucleation sites for austenite but not for graphite. As formation of (MnTi)S depletes the melt from sulphur, less S is available for the precipitation of MnS inclusions that are the main nucleant for type-A graphite. This is also confirmed by the Thermo-

Calc simulations done by the author and also confirmed beforehand by Sommerfeld and Tonn [59] and Stets and Macher [76].

This depletion results in the depression of the eutectic temperature. Thus, for high S iron, Ti additions will increase the amount of austenite through enhanced austenite nucleation and an increased liquidus-eutectic interval, which allows more time for austenite growth before the eutectic reaction. A higher amount of dendritic austenite will favour a type-A to type-D transition for graphite, as the graphite is constrained to grow between the dendrite arms. This is in agreement with the previous statements by Larrañaga et. al [8].

ii) High-Ti low-S iron

For the low S irons, no clear nucleation site for austenite can be observed. The higher amount of austenite produced by Ti additions can still be attributed to the higher liquidus-eutectic interval (see Table 7). The increased undercooling prior to eutectic solidification and poor graphite inoculation can also be the reasons for the increase in primary austenite. Another probable explanation for the higher liquidus temperature is increased nucleation. Yet, we were not able to identify nucleation sites for the austenite in iron 621.5. The higher T_{min} in the absence of Ti, and the highest T_{min} for the highest purity iron from the series (621.1) can be understood through equilibrium thermodynamics. Indeed, low S and Ti content decrease the stable eutectic temperature by similar amounts and thus, purer irons should have higher eutectic equilibrium temperature.

Table 7. Thermal analysis data and fraction of austenite [Moumeni; Stefanescu; Tiedje; Larrañaga and Hattel, Paper III]

Sample no.	T_L	T_{min}	$T_L - T_{min}$	Austenite fraction
401.1	1182	1147	35	0.17
401.5	1192	1145	47	0.27
621.1	1187	1148	39	0.27
621.5	1198	1144	54	0.38

The fact that Ti addition produced larger eutectic cells supports the theory that Ti introduces lower nucleation rate of the graphite in between the dendrite arms of a larger fraction of austenite; although, the main driver for formation of finer graphite in high-Ti graphite remains the change in the nucleation potential. The ThermoCalc simulation carried out by author as well as in [76] confirms the formation of inclusions containing C, S and Ti ($Ti_4C_2S_2$) at the temperatures above solidification till 1152°C (see Fig. 70). As mentioned earlier, this has been confirmed by other authors too [59] [76]. Below this temperature, according to the ThermoCalc simulation, $Ti_4C_2S_2$ breaks down into TiC and MnS.

Respecting the fact that calculations of Thermo-Calc are only in thermodynamical equilibrium, the phases and their formation temperatures under non equilibrium solidification conditions can be different. For that reason using other software such as MICRESS are suggested for future work.

Please note that nitrogen and oxygen have not been measured in the melt; therefore, they are not taken into consideration in the solidification.

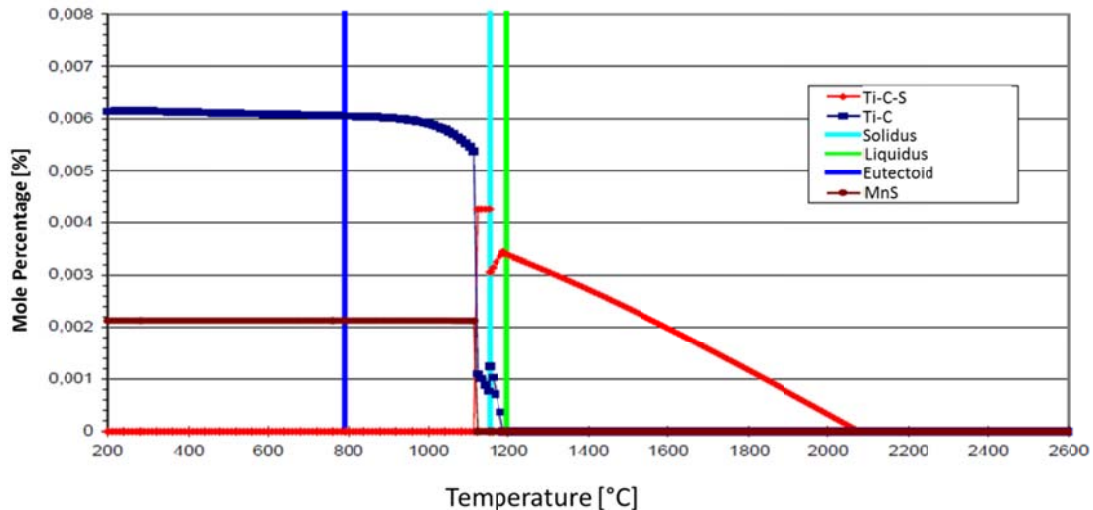


Fig. 70. Thermocalc simulation; Grey iron, 0.3%Ti [76]

iii) Some notes on the solidification sequences

When austenite is forming, the local temperature of the dendrite tip is high, just below the local liquidus temperature. Also carbon and titanium are pushed out into the liquid; thus, TiC inclusions form in these areas. This can also be confirmed by Thermocalc simulations [76] [59]. On this hypothesis, one of the consequences would be depletion of carbon in the liquid.

If the TiC inclusions are formed at the beginning of solidification before the onset of austenite formation, in the liquid surrounding the TiC inclusions carbon locally decreases. And austenite would form easier. Therefore, TiC in this case indirectly works as promoter for austenite to form.

In the high-Ti high-S iron, as the Thermocalc calculation shows, before formation of austenite $Ti_4C_2S_2$ inclusions form and the level of S depletes in the melt. Even though there is no metallographic proof for existence of this phase. Consequently, fewer nucleation sites for precipitation of graphite would be available and naturally less graphite would form.

It was observed that TiC particles and graphite are in contact. It could not be stated that TiC is the nucleation site for graphite. This needs further electron microscopy studies to find the relationship between the two phases.

As it has been measured Ti increases the undercooling. In fact, the eutectic reaction in Ti-alloyed iron needs a higher driving force to start. Titanium also promotes metastable solidification and it is known as a carbide promoter.

4.6.2. Superfine interdendritic graphite

The graphite precipitates in Ti-containing cast iron were found to consist of many small grains which have slightly different orientation relationships. In the deep etched samples investigated by SEM and in the lamellae studied by TEM, no impurities, inclusions or heterogeneous nucleation sites have been seen in the area of fine graphite by the authors so far.

It was shown that a severe segregation occurs due to the presence of titanium. While trying to understand this issue and its relation with the crystallization of graphite, it could be considered that the growth mode would be determined either due to the segregation and therefore, concentration of some elements such as Ti or S at the growth front, or due to the changes in the

kinetics of growth at the solid liquid interface. This matter needs to be investigated more in detail in the future work.

The results of the TEM study also indicated that some areas of the graphite structure in the high-Ti iron consist of several elongated grains which had similar but slightly different orientation relationships. Some of the grains had a rhombohedral crystal structure and the orientation of these grains was similar to the hexagonal grains, the (001) planes being almost parallel. There was no specific orientation relationship between the iron and the investigated graphite grains, but since the orientation relationship between the graphite grains themselves varied slightly, perhaps some of them do correlate with the iron crystal structure.

The graphite structure in the high-Ti samples was found to be expanded considerably in the “c” direction, that is the (001) interplanar spacings were higher than expected. The value of expansion varies in different areas; the expansion measured in the diffraction pattern images was up to 8%. The expansion was not found in the low-Ti specimens. The high number of defects in the graphite crystal structure such as stacking faults might cause the expansion in the high-Ti samples. The graphite in the low-Ti iron (flaky graphite) in the investigated areas matches with the hexagonal unit cell and shows no expansion.

A high tendency of branching of graphite in the presence of titanium was observed in the specimens. This has also been reported in [77], although, there is no explanation for this phenomenon yet.

Chapter 5

Summary of the articles

5.1. Paper I

E.Moumeni, C.C.Tutum, N.S.Tiedje and J.H.Hattel, “*Analysis of nucleation modelling in ductile cast iron*”, ICASP 3 -The 3rd International Conference on Advances in Solidification Processes June 2011, published in IOP Conf. Ser.: Mater. Sci. Eng. 27, 2012

In this paper heterogeneous nucleation of nodular graphite at inclusions in ductile iron during eutectic solidification has been investigated. The experimental part of this work deals with casting of ductile iron samples with two different inoculants in four different thicknesses. Chemical analysis, metallographic investigation and thermal analysis of the specimens have been carried out.

A numerical model has been implemented and the results (i.e. cooling curve, cooling rate, nodule count and solid fraction) have shown a good agreement with experimental studies; following this, inoculation parameters such as n and A_n in the model have been studied and discussed.

5.2. Paper II

E. Moumeni, N.S.Tiedje and J.H.Hattel, “*Effect of titanium on the near eutectic grey iron*”, 12th International Foundrymen Conference, Sustainable Development in Foundry Materials and Technologies, May 2012, Opatija, Croatia, published in the journal International Foundry Research, Issue 2/2013.

The effect of Titanium on the microstructure of grey iron is investigated experimentally in this paper. Plates of grey cast iron of near eutectic alloys containing 0.01, 0.1, 0.26 and 0.35% Ti, have been made in green sand moulds. The results of chemical analysis, metallographic investigation and thermal analysis of the specimens are shown and discussed.

An SEM and TEM study have been performed in order to observe the effect of Ti on the microstructure of the alloys in smaller scale. Furthermore, the microstructure and thermal analysis are related and discussed.

5.3. Paper III

E. Moumeni, D.M. Stefanescu, N.S. Tiedje, P. Larrañaga, J.H. Hattel, “*Investigation on the Effect of Sulfur and Titanium on the Microstructure of Lamellar Graphite Iron*”, Accepted for the Metallurgical and Materials Transactions A (In press), 2012 Dec.

In this paper the inclusions in lamellar graphite cast iron are identified in an effort to explain the nucleation of the phases of interest. Four samples of approximately the same carbon equivalent but different levels of sulphur and titanium have been studied. The Ti/S ratios are of 0.15 to 29.2 and the Mn/S ratios of 4.2 to 48.3. Optical and electron microscopy have been used to examine the unetched, colour-etched and deep-etched samples.

The effect of titanium in refining the graphite and increasing the austenite fraction is explained through the widening of the liquidus-eutectic temperature interval (more time for austenite growth) and the decrease in the growth rate of the graphite because of Ti absorption on the graphite.

5.4. Paper IV

E. Moumeni, N.S. Tiedje, F.B. Grumsen, H.K. Danielsen, A. Horsewell, J.H. Hattel, “*A TEM Study on the Ti-alloyed grey iron*”, Submitted to the journal of Materials Science and Technology, April 2013

In this investigation the microstructure of the graphite flakes in titanium alloyed cast iron is studied using electron microscopy techniques. The method of TEM sample preparation using dual beam microscopes is explained. A TEM study has been carried out on graphite flakes in grey cast iron using selected area electron diffraction based on which crystallographic orientations are identified and compared. The orientation relationship between iron and graphite crystals at the interface is studied and discussed.

Based on this information, growth models for the platelets in the fine graphite flakes in cast iron are discussed.

Chapter 5

Conclusions and future work

It is demonstrated how a numerical model for solidification of ductile cast iron can be used to analyse nucleation and solidification. The numerical results have shown a good agreement with the experiments. The effects of nucleation parameters on the numerical results are investigated and discussed. As a future work, it would be interesting to optimize the nucleation parameters to get the best fit to the experimental results.

The effects of addition of titanium and sulphur on the grey iron have been studied. It was confirmed that when sufficient sulphur is present in the iron, nucleation occurs on Mn sulphides that have a core of complex Al, Ca, Mg oxide. Both type-A and type-D graphite were observed to grow on the Mn sulphide. An increased titanium level of 0.35% produced superfine interdendritic graphite (~10µm) at low as well as at high S contents. The shape of the graphite was also dramatically altered.

While TiC additions increased the liquidus temperature, TiC did not appear to be a nucleation site for the primary austenite as it was found mostly at the periphery of the secondary arms of the austenite, in the last region to solidify. The effect of titanium in refining the graphite and increasing the austenite fraction can be explained through the widening of the liquidus-eutectic temperature interval (more time for austenite growth) and the decrease in the growth rate of the graphite.

In the presence of high Ti and S, (MnTi)S star-like and rib-like inclusions were found in the middle of the secondary arms of the austenite dendrites. It is reasonable to assume that they are acting as nuclei for the austenite.

The fact that Ti addition produced larger eutectic cells supports the theory that Ti is not producing finer graphite because of a change in the nucleation potential, but because of lower growth rate of the graphite in between the dendrite arms of a larger fraction of austenite.

Ti also caused increased segregation in the microstructure of the analysed irons and larger eutectic cells.

The microstructure of the graphite flakes in titanium alloyed cast iron was studied using electron microscopy techniques. FIB lift-out of TEM lamellae has been used successfully to make electron transparent thin foils. The FIB lift-out technique has allowed for selection of specimen areas containing regions of flaky graphite and the surrounding cast iron matrix. The thin foils are uniform in thickness and show no apparent damage resulting from the FIB.

A TEM study has been carried out on graphite flakes in grey cast iron using selected area electron diffraction. The graphite particles in Ti-containing cast iron were investigated and found to consist of many small grains which have slightly different orientation relationships. Most of these grains have a hexagonal crystal structure, but a few of them have a rhombohedral crystal structure. There seems to be a good correlation between the orientation of two crystal structures, the (001) planes being almost parallel. There did not seem to be any specific orientation relationship between the investigated graphite grains and the iron matrix.

While trying to understand the severe segregation due to the presence of titanium and its relation with the crystallization of graphite, it could be considered that the growth mode would be determined either due to the segregation and therefore, concentration of some elements such as Ti or S at the growth front, or due to the changes in the kinetics of growth at the solid liquid interface. In future work, this matter could be investigated more in detail.

In the deep etched samples investigated by SEM and in the lamellae studied by TEM, no impurities, inclusions or heterogeneous nucleation sites have been seen in the area of fine graphite so far. In future work, a higher number of TEM specimens could be studied to investigate the nucleation of this type of graphite.

The platelets of graphite are predicted to have a weak and brittle attachment to each other. The cracks or voids may occur during the growth of the graphite or during TEM sample preparation. Considering the fact that graphite is a very brittle material, one could say that the fractures or voids in the crystals would happen during solidification as stresses caused by cooling and growth of the solid phase imposes forces on the graphite to deform and break. Twinning seems to be one of the main mechanisms of the anisotropic growth of this type of graphite which has taken place at high undercooling.

Bibliography

- [1] Yakovlev, *Metal Science and Heat Treatment*, vol. 28, no. 5, p. 378–380, 1986.
- [2] M. Hatate, *Wear*, vol. 251, pp. 885-889, 2001.
- [3] J. Chou, M. Hon and J. Lee, *J. of Mat. Science*, vol. 25, p. 1965–1972, 1990.
- [4] . A. Velichko, “Quantitative 3D Characterization of Graphite Morphologies in Cast Iron using FIB Microstructure Tomography,” in *PHD Thesis*, 2008.
- [5] N. Tiedje, “Solidification, processing and properties of ductile cast iron,” *Mat Sci Tech*, vol. 26, pp. 505-514, 2010.
- [6] A. Handbook, *Properties and Selection: Irons, Steels, and High-Performance Alloys*, Volume 1..
- [7] P. Larrañaga, J. Sertucha, A. Loizaga, R. Suárez and D. Stefanescu, *Trans. AFS*, vol. 120, no. paper 12-034, 2012.
- [8] P. Larrañaga, J. Sertucha, A. Loizaga, R. Suárez and D. Stefanescu, *Trans. AFS*, vol. 120, no. paper 12-034, 2012.
- [9] E. Moumeni, N. Tiedje and J. Hattel, “Effect of titanium on the near eutectic grey iron,” in *International Foundry Research*, 2012.
- [10] E. Moumeni, D. Stefanescu, N. Tiedje, P. Larrañaga and J. Hattel, “Investigation on the Effect of Sulfur and Titanium on the Microstructure of Lamellar Graphite Iron,” *Metallurgical and Materials Transactions A*, 2013.
- [11] J. Wallace, “Effects of Minor Elements on the structure of Cast Irons,” *AFS Transactions*, vol. 83, 1975.
- [12] “Naro. R.; Wallace, J.F.,” *AFS Transactions*, vol. 77, pp. 311-320, 1969.
- [13] G. Ruff and . J. F. Wallace, “Control of graphite structure and its effect on mechanical properties of gray iron,” *AFS Transactions*, vol. 84, p. 705, 1976.
- [14] A. Okada and H. Miyake, *KANSAI Univ. Press*, p. 141, 1996.
- [15] H. Nakaee and K. Fujimoto, “Influence of Ti on Graphite Morphological Transition in Flake Graphite Cast Iron,” *Key Engineering Materials*, vol. 457, pp. 25-30, 2011.
- [16] A. Velichko, A. Wiegmann and F. Mücklich, “Estimation of the effective conductivities of complex cast iron microstructures using FIB-tomographic analysis,” *Acta Materialia*, vol. 57, no. 5023–5035, 2009.
- [17] D. Double and A. Hellawell, “The nucleation and growth of graphite - The modification of cast iron,” *Acta metallurgica materialia*, vol. 43, no. 6, pp. 2435-2442, 1994.
- [18] N. Llorca-Isern, J. Tartera, M. Espanol, M. Marsal, G. Bertran and S. Castel, “Internal features of graphite in cast irons. Confocal microscopy: useful tool for graphite growth imaging,” *Micron*, vol. 33, no. 4, pp. 357-64, 2002.
- [19] A. Velichko, C. Holzapfel and F. Mücklich, “3D Characterization of Graphite Morphologies in Cast Iron,” *Advanced Engineering Materials*, vol. 9, no. 1-2, 2007.

- [20] M. Baihe, F. Keming and B. Weimin, "On The Microstructure of Graphite Spherulites in Cast Irons by TEM and HREM," *Acta metall. mater.*, vol. 38, p. 2167, 1990.
- [21] J. Tartera, N. Llorca-Isern, M. Marsal and J. Rojas, "Similarities of nucleation and growth of spheroidal and compacted graphite," *Int. Journal of Cast Metals Research*, vol. 16, p. 131, 2003.
- [22] D. Double and A. Hellawell, "Cone- helix growth forms of graphite," *Acta Metallurgica*, vol. 22, pp. 481-466, 1974.
- [23] A. W. Hull, "A New Method of X-Ray Crystal Analysis," *Phys. Rev.*, vol. 10, no. 2, p. 661-696, 1917.
- [24] J. D. Bernal, "The Structure of Graphite," *Proceedings of the Royal Society of London, Series A*, vol. 106, pp. 749-773, 1924.
- [25] O. Hassel and H. MARK, *Z. Phys.*, vol. 25, p. 317, 1924.
- [26] E. Freise and A. Kelly, "The deformation of graphite crystals and the production of the rhombohedral form," *Philosophical Magazine*, vol. 8, no. 93, pp. 1519-1533, 1963.
- [27] F. Laves and Y. Baskin, "On the Formation of the Rhombohedral Graphite Modification," *Zeitschrift für Kristallographie - Crystalline Materials*, vol. 107, no. 5-6, pp. 337-356, 1956.
- [28] Sooho Kim and D. Phillips, "Orientation relationships in graphitic cast irons," *Metallurgical Transactions A*, vol. 18A, pp. 1907-1913, 1987.
- [29] W. Johnson and H. Smartt, "The Role of Interphase Boundary Adsorption in the Formation of Spheroidal Graphite in Cast Iron," *Metallurgical Transactions A*, vol. 8A, pp. 553-565, 1977.
- [30] E. Moumeni, N. Tiedje, F. Grumsen, H. Danielsen, A. Horsewell and J. Hattel, "A TEM Study on the Ti-alloyed grey iron".
- [31] J. Hattel, D. Lipinski, N. Pryds, M. Schneider and J. Thorborg, *Fundamentals of numerical modelling of casting processes*, Polyteknisk Forlag, 2005.
- [32] D. Stefanescu, *Science and engineering of casting solidification*, N.Y.: Kluwer academic / Plenum publiser, 2002.
- [33] W. Oldfield, *The Solidification of Hypoeutectic Cast Iron*, M.Sc. Thesis, Manchester University, 1961.
- [34] *Cast Irons*, ASM International, 1996.
- [35] R. Heine, C. Loper Jr and M. Chaudhari, "Characterization and interpretation of ductile iron cooling curves," *AFS Transactions*, vol. 79, pp. 399-410, 1971.
- [36] *Microstructure of cast irons - Part 1: Graphite classification by visual analysis*, DIN EN ISO 945-1, 2010-09.
- [37] B. Lux, "Recent research on cast iron," in *H.D. Merchant (ed), New York, Gordon and Breach*, proceedings of a seminar held in Detroit, Michigan, June 16-18, 1964, 1968.
- [38] W. Weis, "The Metallurgy of Cast Iron," in *B. Lux, I. Minkoff, F. Mollard (Eds.), Georgi Publishing Co., pp. 69-79*, St. Saphorin, Switzerland, 1974.
- [39] T. Skaland, O. Gron and T. Gron, "A model for graphite formation in ductile cast iron," *Metall. Trans.*, vol. 24A, p. 2321, 1993.

- [40] D. Stefanescu, "Solidification and modeling of cast iron—A short history of the defining moments," *Materials Science and Engineering: A*, vol. 413–414, p. 322–333, 2005.
- [41] T. Skaland, PhD Thesis, 1992.
- [42] H. Fredriksson and U. Åkerlind, "Precipitation of pores and slag inclusions during casting processes," in *Materials processing during castin*, Wiley, 2006, pp. 299-301.
- [43] E. Frás, M. Gorny and H. Lopez, "Eutectic cell and nodule count in grey and nodular cast irons," *Materials Science and Technology*, vol. 23, no. 9, p. 1109 , 2007.
- [44] A. Diószegi, V. Furlakidis and I. Svensson, "Microstructure and tensile properties of grey cast iron," *Research report, Jönköping University*, 2004.
- [45] K. Herfurth, *Freiberg Forschungs*, vol. 105, p. 267, 1965.
- [46] B. Lux, I. Minkoff, F. Mollard and E. Thury, "Second International Symposium on the Metallurgy of Cast Iron," in *pp. 495–508*, Georgi Publishing Co., St. Saphorin, Switzerland, 1974.
- [47] I. Minkoff, *Physical Metallurgy of Cast Iron*, Wiley, Chichester, 1983.
- [48] H. Fredriksson and U. Åkerlind, "Structure and structure formation in cast materials," in *Materials processing during castin*, Wiley, 2006, pp. 150-2.
- [49] E. FRAS and M. GÓRNY, "Innucleation phenomenon in cast iron," *Archives of metallurgy and materials*, vol. 57, no. 3, pp. 767-777, 2012.
- [50] E. Frás, in *Krystalizacja metali WNT*, Warszawa , 2003.
- [51] A. Meehan. USA Patent 1499068, 1924.
- [52] W. Kurz and P. Magnin, "Competitive growth of stable and metastable Fe-C-X eutectics: Part II. Mechanism," *Metallurgical Transactions A .*, vol. 19A, pp. 1965-71, 1988.
- [53] M. Tisza, *Physical Metallurgy for Engineers*, ASM International, 2001.
- [54] J. Lacaze and B. Sundman, "An assesment of the Fe-C-Si system," *Metallurgical Transactions A*, vol. 22A, pp. 2211-23, 1991.
- [55] *Ductile Iron Handbook*, AFS Inc., 1992.
- [56] J. Hitchings and J. Klein, "Titanium in Cast Iron: Its Reactions and Effects," *AFS Transactions*, vol. 97, p. 579, 1989.
- [57] P. Basutkar , S. Yew and C. J. Loper, "Effect of certain additions to the melt on the as-cast dendritic microstructure of gray cast iron," 1969.
- [58] D. Zeng, Y. Zhang, J. Liu, H. He and X. Hong, *Science and Processing of Cast Iron VIII*, pp. 86-91, 2006.
- [59] A. Sommerfeld and B. Tonn, "Theory of graphite nucleation in lamellar graphite cast iron," in *The Carl Loper cast iron symposium*, Madison, WI USA, 2009.
- [60] K. Wilford and F. Wilson, *British Foundryman* , vol. 78, p. 301 and 364, 1985.
- [61] J. Wallace and P. Wieser, "Trace Elements and Pinholes in Gray Iron.," *American Foundrymen's Society*, 1965.
- [62] L. KOZHINSKY, "Titanium alloying of grey iron," *RUSS CAST PROD*, pp. 419-420 , 1969.
- [63] E. Moumeni, C. Tutum, N. Tiedje and J. Hattel, "Analysis of nucleation modelling in ductile cast iron," *IOP Conf. Series: Materials Science and Engineering*, vol. 27, 2011.

- [64] M. Rappaz, D. Richoz and P. Thevoz, “Modelling of Solidification of Nodular Cast Iron,” in *Euromat 89, E-MRS, Aachen - RFA*, 1989.
- [65] G. Lesoult, M. Castro and J. Lacaze, “Solidification of spheroidal graphite cast irons -I. Physical modelling,” *Acta mater.*, vol. 46, no. 3, pp. 983-995, 1998.
- [66] K. Pedersen, J. Hattel and N. Tiedje, “Numerical modelling of thin-walled hypereutectic ductile cast iron parts,” *Acta Materialia*, vol. 54, pp. 5103-5114, 2006.
- [67] J. Lacaze, M. Castro and G. Lesoult, “Nucleation of Graphite Particles in Grey and Nodular Irons,” *Advanced Materials and Processes*, vol. 1, no. Proceedings of the First European Conference. EUROMAT'89, pp. 147-152, 1989.
- [68] “Volume 15: Casting,” in *Handbook, ASM*, ASM International, 2008, pp. 317-329.
- [69] Y. Li, B. Liu and C. Loper, “Study of the solidliquid interface during unidirectional solidification of cast iron,” *AFS Transactions*, vol. 98, pp. 483-8, 1990.
- [70] K. Pedersen, PhD Thesis, Technical University of Denmark, 2006.
- [71] U. EE, *Addison-Wesley Publishing Company*, pp. 109-45, 1970.
- [72] “Ohtani H., Tanaka T., Hasebe M., Nishizawa; T. CCULATION OF THE Fe-C-Ti TERNARY PHASE DIAGRAM,” *Calphad*, vol. 12, p. 225–246, 1988.
- [73] R. Langford and C. Clinton, “In situ lift-out using a FIB-SEM system,” *Micron*, vol. 35, p. 607–611, 2004.
- [74] D. B. Williams and C. B. Carter, *Transmission electron microscopy*, Springer, 2009.
- [75] E. Moumeni, N.S.Tiedje, A. Horsewell and J.H.Hattel, “A TEM Study on the Microstructure of Fine Flaky Graphite,” in *52nd International Foundry Conference, Slovenia, Portoroz*, 2012.
- [76] W. Stets and T. Macher, “Legieren mit Titan,” *Fachausschuss Eisenguss - IfG Institut für Gießereitechnik*, 2012.
- [77] M. CHIŞAMERA, I. RIPOŞAN, S. STAN, G. Grasmö and D. Wilkinson, “Preconditioning of electrically melted grey cast irons,” *U.P.B. Sci. Bull., Series B*, vol. 71, no. 3, 2009.
- [78] J. Mouchoux, C. Verdu, G. Thollet, A. Reynaud and R. Fougères, “Morphological changes of graphite spheroids during heat treatment of ductile cast irons,” *Acta mater.*, vol. 49, p. 4355–4362, 2001 .
- [79] K. Pedersen and N. Tiedje, “Graphite nodule count and size distribution in thin-walled ductile cast iron,” *Materials Characterization*, vol. 59, no. 8, p. 1111–1121, 2008.
- [80] K. Theuwissen, M. Lafont, L. Laffont, B. Viguier and J. Lacaze, “Microstructural Characterization of Graphite Spheroids,” *Transactions Indian Institute of Metals*, vol. online, 2012.
- [81] B. Miao, K. Fang, W. Bian and G. Liu, “On the microstructure of graphite spherulites in cast irons by TEM and HREM,” *Acta metall mater.*, vol. 38, no. 11, pp. 2167-2174, 1990.
- [82] S. Zhang, “Mechanism of the forming of nodular graphite,” *Mater. Sci. Technol.*, vol. 16, no. 6, p. 615, 2000.
- [83] A. Velichko, “Quantitative 3D Characterization of Graphite Morphologies in Cast Iron using FIB Microstructure Tomography,” in *Doctoral thesis*, 2008, p. 109.

Appendixes

A paper-I

E.Moumeni, C.C.Tutum, N.S.Tiedje and J.H.Hattel, "*Analysis of nucleation modelling in ductile cast iron*", ICASP 3 -The 3rd International Conference on Advances in Solidification Processes June 2011, published in IOP Conf. Ser.: Mater. Sci. Eng. 27,2012

Analysis of nucleation modelling in ductile cast iron

This article has been downloaded from IOPscience. Please scroll down to see the full text article.

2012 IOP Conf. Ser.: Mater. Sci. Eng. 27 012062

(<http://iopscience.iop.org/1757-899X/27/1/012062>)

View [the table of contents for this issue](#), or go to the [journal homepage](#) for more

Download details:

IP Address: 130.226.18.136

The article was downloaded on 03/05/2013 at 10:55

Please note that [terms and conditions apply](#).

Analysis of nucleation modelling in ductile cast iron

E Moumeni, C C Tutum, N S Tiedje and J H Hattel

Technical University of Denmark, Department of Mechanical Engineering, Building 425 - DK 2800 Kgs. Lyngby, Denmark

E-mail: elmo@mek.dtu.dk

Abstract. Heterogeneous nucleation of nodular graphite at inclusions in ductile iron during eutectic solidification has been investigated. The experimental part of this work deals with casting of ductile iron samples with two different inoculants in four different thicknesses. Chemical analysis, metallographic investigation and thermal analysis of the specimens have been carried out. A numerical model has been implemented and the results (i.e. cooling curve, cooling rate, nodule count and solid fraction) have shown a good agreement with experimental studies; following this, inoculation parameters in the model have been studied and discussed.

1. Introduction

During the last 50 years ductile iron has been one of the most important casting alloys in industry. This is due to its high strength and ductility, good castability and competitive price. Prediction of thermal behaviour during solidification and metallurgical characteristics of the final product, and therefore, mechanical properties have always been of interest; therefore, several analytical and numerical models have been developed and applied to achieve these purposes.

Numerical models have shown more realistic results as compared to analytical models in simulation of heat transfer during solidification. They have also made it possible to simulate microstructure evolution during the process. Since formation of microstructures during solidification is closely coupled with its thermal history, numerical models are very useful to investigate relations between process conditions and microstructure [1].

It is widely accepted that eutectic solidification of hypereutectic ductile iron begins with the nucleation and growth of graphite in the liquid, and is followed by early encapsulation of the graphite spheroids in austenite shells (envelopes). Once the austenite shell is formed, further growth of graphite can occur only by diffusion of carbon from liquid through the austenite. However, the interaction between nucleation of graphite and austenite dendrites plays a significant role in eutectic solidification [2],[3]. Even for hypereutectic irons, the graphite spheroids do not grow in independent austenite envelopes, but rather are associated with austenite dendrites [4]. Lesoult et al. [2] developed a model which includes the description of the nucleation and growth of the pro-eutectic graphite in hypereutectic iron and for the first time they also considered the formation of pro-eutectic austenite during solidification of both hypo- and hyper-eutectic spheroidised graphite (SG) iron [5].

Later, K.M Pedersen et al. [3] enhanced that model by applying a numerical calculation of heat flow in casting and mould, taking into account the heat transfer coefficient between the casting and the mould which can be very important for thin-walled castings. The model implemented in the present work is based on the same model.

In this work solidification of eutectic transformation of hypereutectic ductile iron produced by using two different inoculants (table 2), is investigated. The samples were cast in four different thicknesses (table 1), and their metallurgical properties are investigated and discussed. The model is used to investigate how nucleation parameters can be assessed.

2. Numerical model

Applying the first law of thermodynamics and Fourier's law, the 1-D heat conduction equation governing all domains (casting and mould) is given in equation(1):

$$\rho c_p \frac{\partial T}{\partial t} = \frac{\partial}{\partial x} \left(k \frac{\partial T}{\partial x} \right) + q_{gen} \quad (1)$$

Where ρ is density, c_p is specific heat capacity, T is the temperature, t is time and k is thermal conductivity, and q_{gen} [w/mm³] is the generated heat which can be expressed by f_s (solid fraction), ΔH_f (latent heat) and density as shown below:

$$q_{gen} = \Delta H_f \rho \frac{\partial f_s}{\partial t} \quad (2)$$

The above mentioned model is used to calculate heat flow throughout the casting and the mould. The predicted cooling conditions result from the coupling of macro heat transfer from casting to environment with the microstructure evolution during solidification, which is dictated by transformation kinetics [6].

As mentioned before, the model for solidification of ductile iron proposed by Lesoult et al. [2] is applied in this work, though the basic idea of the nucleation model of graphite nodules is taken from Oldfield [7]. Nucleation of graphite nodules is the first part of every time step. The number of nucleated graphite nodules in time step i , dN , is governed by the undercooling with respect to the graphite liquidus (ΔT_L^g). Therefore, when $\frac{d(\Delta T_L^g)}{dt} > 0$ the nucleation rate can be calculated as shown below:

$$dN = A_n (\Delta T_L^g)^{n-1} f_l \frac{d(\Delta T_L^g)}{dt} V^{off} dt \quad (3)$$

when f_l is liquid fraction and V^{off} is the volume of off-eutectic phases. Lesoult et al. presented a physical model of eutectic solidification of SG cast iron which quantitatively accounts for the formation of non-eutectic austenite during solidification (see figure 1).

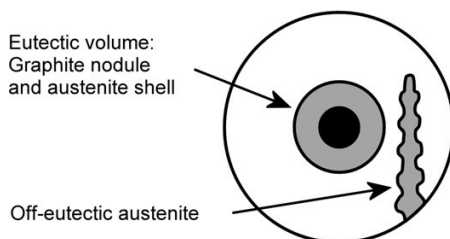


Figure 1. Eutectic stage of solidification of ductile iron. Austenite dendrite is present as part of the off-eutectic volume [2].

As far as the model is concerned emphasis has been put on the analysis of the carbon redistribution between the graphite, the eutectic austenite, the liquid, and the non-eutectic phases; thus a careful expression of the carbon mass balance within the volume has been obtained.

A comprehensive description of the model including nucleation and growth of primary graphite and eutectic transformation taking into account the formation of off-eutectic austenite can be found in the references: [3],[2].

3. Experiments

A hypereutectic cast iron melt was prepared in a batch of 150 kg. The specimens were cast in sand moulds as tensile test specimens (2), their thicknesses are shown in table 1. Magnesium treatment and inoculation with two inoculants was made; the compositions of inoculants are indicated in table 2. The temperature was measured in the middle of each plate using 0.5 mm diameter stainless steel sheathed K-type thermocouples. Some key points on the cooling curve, showing different stages of solidification, are shown in 3 [3]. The recalescence ΔT_{rec} is defined as the difference between T_{max} and T_{min} . Generally, the lower the ΔT_{rec} is, the more efficient the inoculation is.



Figure 2. As cast specimen.

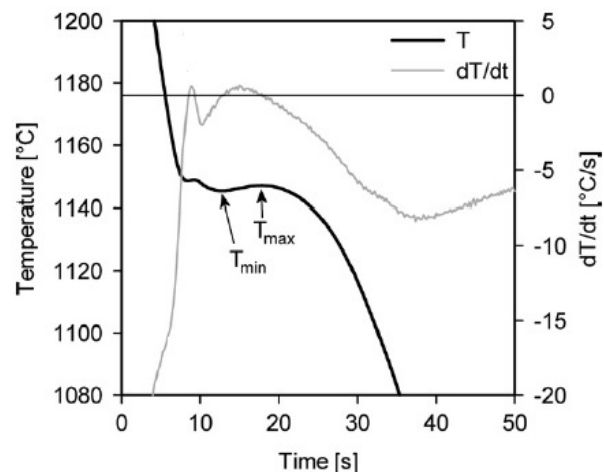


Figure 3. Definition of temperatures on cooling curves (from 4.3 mm plate) [3].

Table 1. Thickness of casting.

	section 1	section 2	section 3	section 4
Thickness(mm)	10	2	4	6

Table 2. Composition of inoculants (%wt)

	Si	Al	Ca	La	Fe
inoculant 1	52.8	0.6	-	-	Bal.
inoculant 2	50	-	2	2	Bal.

Chemical composition of casting parts and their casting temperature are shown in table 3. casting 1 was inoculated by inoculant 1 and casting 2 was inoculated by inoculant 2.

4. Results and Discussion

4.1. Microstructure and cooling curves

Metallographic investigations of all of the samples were done with optical microscope. Nodularity, nodule count and size distribution as well as iron matrix microstructure were examined. No noticeable difference was observed between two castings with the same thicknesses. Examples of microstructure images and cooling curves for the two different plate thicknesses are shown in figures 4 to 7.

Table 3. Chemical Composition of castings

	%C	%Si	%Mn	%Mg	casting temperature
Casting 1	3.86	2.64	0.22	0.043	1400
Casting 2	3.76	2.60	0.23	0.048	1400

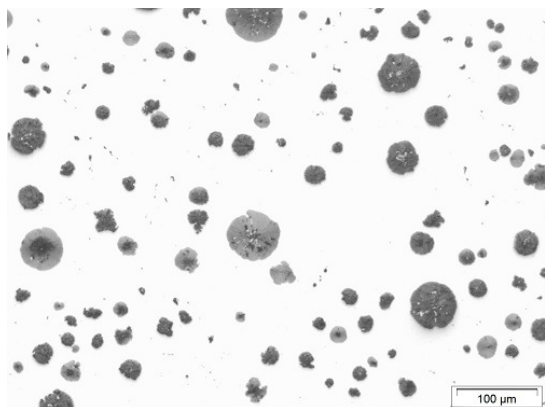


Figure 4. Graphite nodules in as-cast specimen of casting 1, 10 mm thickness, image taken from center of section.

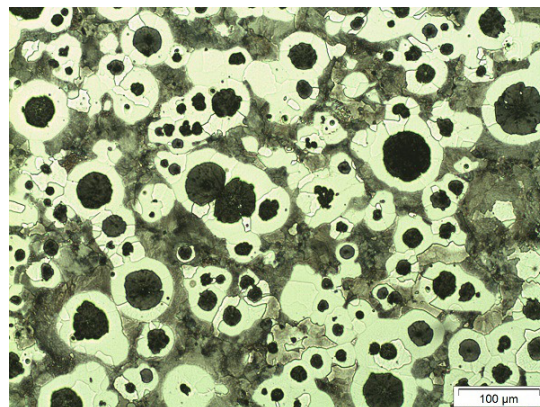


Figure 5. Pearlitic-ferritic structure of the same sample as figure 4, revealed after etching with Nital 2%.

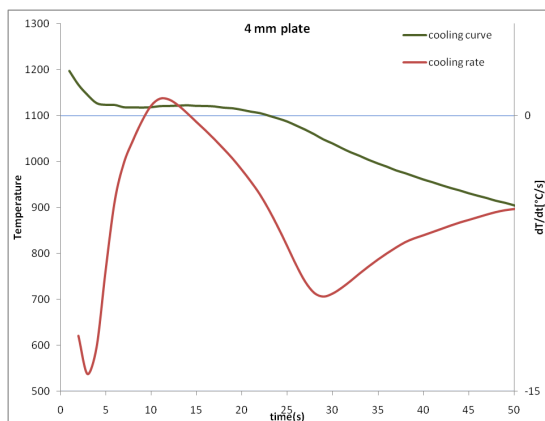


Figure 6. Measured cooling curve (green) and cooling rate (red), casting 1 for plate 4 mm.

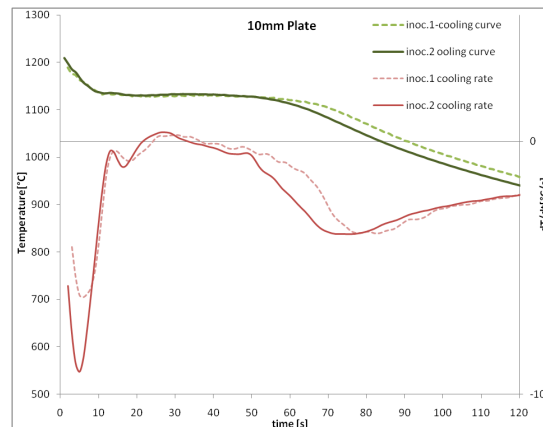


Figure 7. Measured cooling curves (green) and cooling rates (red), casting 1 (dashed line) and casting 2 (solid line), for plate 10 mm.

4.2. Nodule Count and Size Distribution

The size distribution of graphite nodules per unit volume is measured and is shown in figure 8 and figure 9 for the samples from the 4 and 6 mm plates. Small particles which had a size between 0 to 5 μm are considered as inclusions, and are not counted. The mean diameter of graphite nodules and nodule count has been converted from 2D to 3D by the applying Schwartz-Saltykov method [8]. We can see the nodule distribution differ from a single normal distribution, but it can be composed by addition of more than one normal distribution. The width of the

distribution, i.e.: the difference in size between the smallest nodule and the largest is in this paper called the "range" of distribution. As expected, the nodule count, i.e. the total number for nodules per mm^3 in thicker samples is lower, but the range of nodule size is wider and also the average size of nodules are bigger.

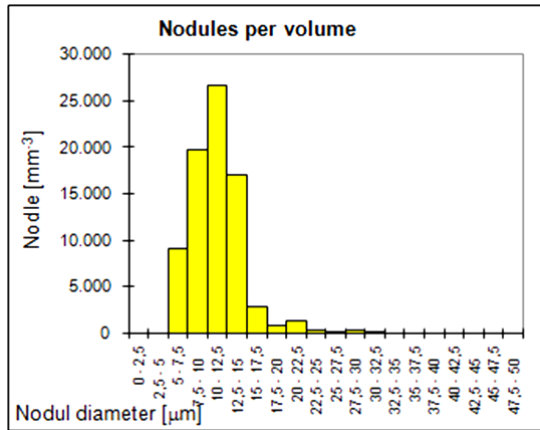


Figure 8. Size distribution of nodules, 4 mm plate, casting 1.

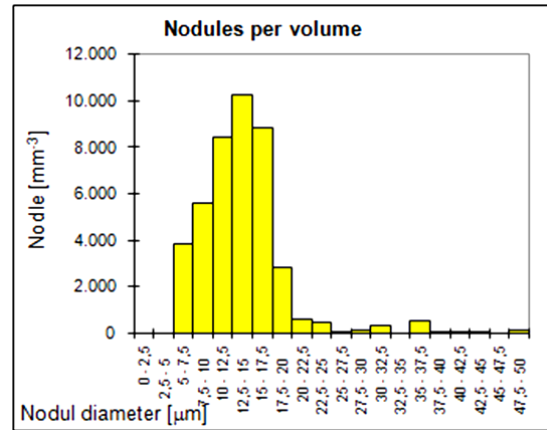


Figure 9. Size distribution of nodules, 6 mm plate, casting 1.

4.3. Nucleation Parameters in the Model

According to the nucleation law shown in Equation (3), A_n is the constant related to the amount of inoculant and n is a constant characteristic of the inoculation efficiency [2]. The effect of these two parameters on the range of nodule size and the shape of the cooling curve has been studied. As seen in figure 10, for a given A_n and initial radius of graphite (rg_0), decreasing n leads to a wider range of nodule size distribution (figure 10). In figure 11, the effect of n on cooling curve is depicted. It can be seen that increasing n which means increasing the efficiency of inoculation, leads to a higher eutectic temperature and a flatter shape of the cooling curve during eutectic transformation.

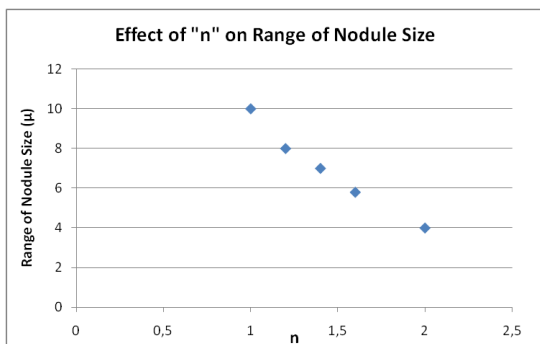


Figure 10. Effect of n on Size distribution of nodules.

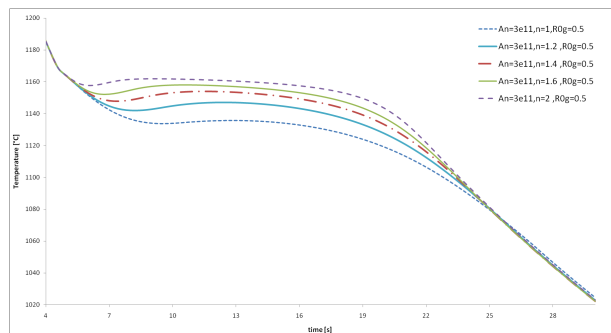


Figure 11. Effect of n on cooling curve.

In addition, the effect of A_n and initial radius of graphite (rg_0) on ΔT_{rec} has been investigated too. Increasing A_n means that there are more nuclei available in the melt. This has two effects on solidification: recalescence begins at a higher temperature, and the reheating during recalescence, ΔT_{rec} is increased (figure 12 and figure 14). Increasing rg_0 allows more latent heat to be released immediately after nucleation so that the recalescence, ΔT_{rec} , is reduced, as shown in figure 13.

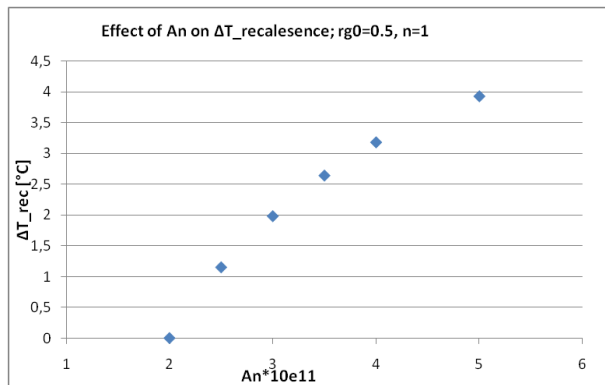


Figure 12. Effect of A_n on ΔT_{rec} .

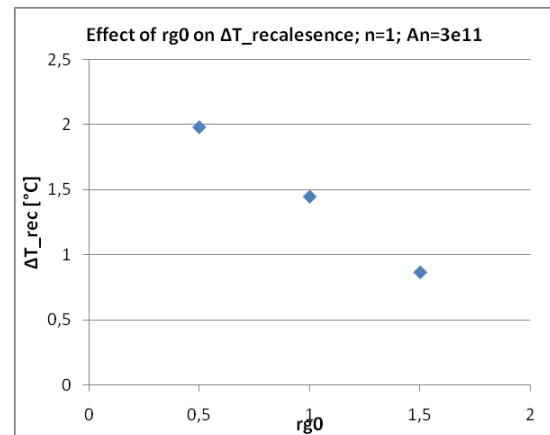


Figure 13. Effect of rg_0 on ΔT_{rec} .

Due to the space limitation, only the results related to the 4mm plate are discussed in this paper. But in the rest of results it is observed that some of the parameters in the model such as A_n and rg_0 should be different for different thicknesses to give the more realistic results, i.e. cooling curve, nodule size, nodule count.

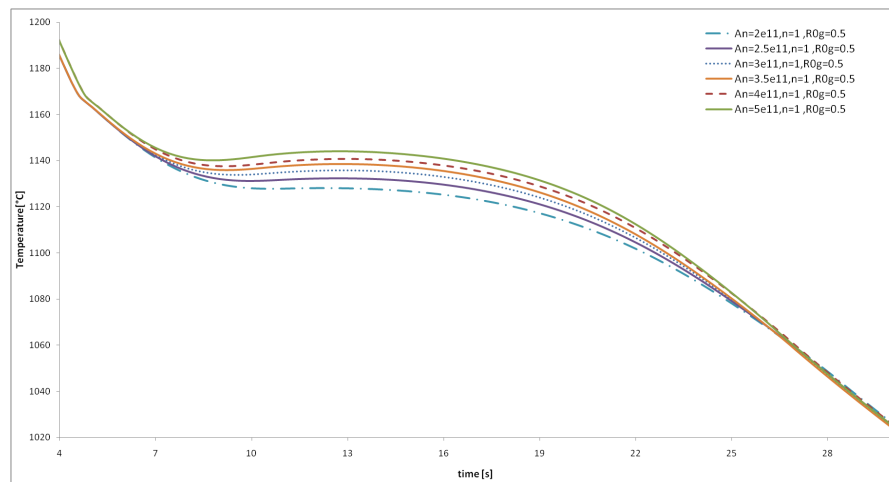


Figure 14. Effect of A_n on cooling curve.

5. Conclusion

It is demonstrated how a numerical model for solidification of ductile cast iron can be used to analyse nucleation and solidification. Based on results from the experiments used in this investigation it is realistic to assume that rg_0 is equal to $0.5 \mu\text{m}$ for thin plates. And it is observed that some of the parameters in the model such as A_n and rg_0 should be different for different thicknesses to give the more realistic results, i.e. cooling curve, nodule size, nodule count. The population of nuclei in the experimental alloys is high and the nucleation efficiency factor, n , is larger than one.

Acknowledgement

The authors would like to thank Dr. Karl Martin Pedersen at Siemens Wind Power A/S, for providing valuable assistance and help during the work.

References

- [1] Hattel J, Lipinski D M, Pryds N H, Schneider M, Thorborg J 2005 *Fundamentals of Numerical Modelling of Casting Processes*, ed. Hattel J H, (Kgs. Lyngby (Denmark): Polyteknisk Forlag)
- [2] Lesoult G, Castro M and Lacaze J 1998 *Acta Materialia*, **46** 983.
- [3] Pedersen K M, Hattel J H , Tiedje N 2006 *Acta Materialia* **54** 5103-5114.
- [4] Michael F. Burditt ed. 1992 *Ductile Iron Handbook* (Des Plaines, IL: American Foundrymen Society) 9-10.
- [5] Stefanescu D M 2007, *Advanced Materials Research* **23** 9-16.
- [6] Stefanescu D M 1997, *Advanced Materials Research* **4-5** 89-104.
- [7] Oldfield W 1996 *Trans. of the ASM*, **59** 945.
- [8] Underwood E E 1970 *Quantitative Stereology* (Reading, MA: Addison-Wesley) 109-145

B paper-II

E. Moumeni, N.S.Tiedje and J.H.Hattel, "*Effect of titanium on the near eutectic grey iron*", 12th International Foundrymen Conference, Sustainable Development in Foundry Materials and Technologies, May 2012, Opatija, Croatia, published in the journal International Foundry Research, Issue 2/2013.

Effect of titanium on the near eutectic grey iron

The effect of Titanium on the microstructure of grey iron was investigated experimentally in this work. Tensile test bars of grey cast iron of near eutectic alloys containing 0.01, 0.1, 0.26 and 0.35 % Ti, respectively were made in green sand moulds.

Chemical analysis, metallographic investigation and thermal analysis of the specimens were carried out thoroughly.

An SEM and TEM study were performed in order to observe the effect of Ti on the microstructure of the alloys in smaller scale. Furthermore, the microstructure and thermal analysis are related and discussed.

Elham Moumeni, Niels Skat Tiedje and Jesper Henri Hattel, Lyngby, Denmark

Manuscript received 17 July 2012; accepted 20 July 2012

1 Introduction

The solidification and graphitization of cast iron has been attracting many scientists over the last decades, but still the mechanism is not well understood. The graphite microstructure stays the most important factor influencing the required properties of cast iron [1, 2, 3]. Therefore, its exact characterization is the only reliable indicator for mechanical properties proposed by foundries and required by customers [4].

Graphite morphology, size and distribution can be more or less efficiently controlled in the modern foundry industry using certain alloying elements and inoculation, as well as varying processing technology such as cooling rates and overheating of the melt [5]. Among all, addition of alloying elements is of the main interest in this work, whereas small amounts of alloy elements in the cast iron can improve the depth of chill, hardness and strength. Moreover, alloy elements are responsible for the amount and shape of graphite precipitated in the casting, as well as for the constitution of the iron matrix and inclusions precipitated during solidification and subsequent cooling to room temperature [6].

For instance, titanium is usually found in the grey iron as a trace element or added as an alloying element to increase strength or improve wear resistance [7]. A microstructure study showed that titanium is a relatively strong element in controlling solidification structure by increasing undercooling and thus promoting type D graphite. The effectiveness of titanium addition depends on the base iron carbon equivalent (CE). Lerner [8] showed that changes made by Ti addition results in tensile strength improvement, but the effect depends on base iron CE. In 4.44% CE iron, tensile strength was maximized at about 0.075% Ti, while the maximum tensile strength in 4.5% CE iron took place at about 0.085% Ti. Larrañaga et. al. [9] showed that addition of appropriate sulfur and titanium contents will increase the primary austenite-to-eutectic ratio, while super-

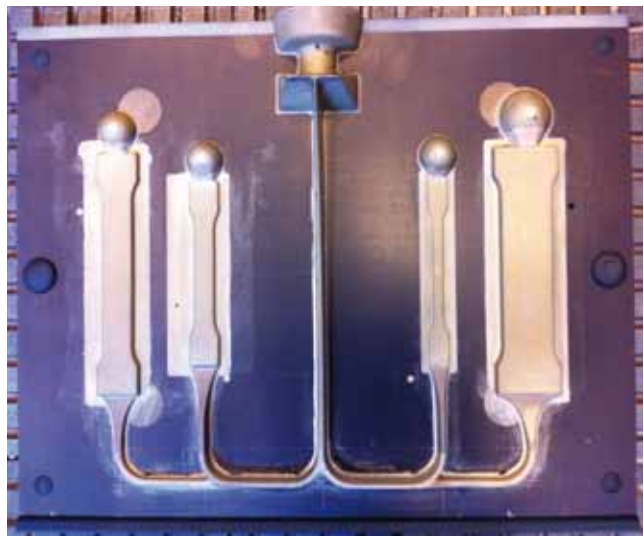


Figure 1: The pattern

Table 1: Chemical composition of inoculant

Chemical elements, wt %		
Si	Al	Fe
52.89	0.609	bal.

fine interdendritic graphite will be produced. They demonstrated that tensile strength of grey iron of average 4% CE can be increased to 300-350 MPa, without a significant increase in hardness, which remains in the range of 185-200 HB. It is worth mentioning that the influence of primary austenite dendrites on the mechanical properties

of gray iron is similar to the reinforced steel bars effect in concrete or fibers in composites acting as a support frame. This means that eutectic cells will be reinforced by dendrites [10].

The work presented in this paper represents part of a comprehensive effort to develop a fundamental understanding of the function of Ti in grey iron.

Table 2: Chemical composition analysis of the melt

Sample	Chemical elements, wt %								
	C	Si	Mn	S	P	Cu	Ti	Al	CE
DI-1	3.34	2.57	0.16	0.015	0.030	0.04	0.01	0.006	4.16
DI-2	3.45	2.54	0.23	0.012	0.024	0.06	0.10	0.011	4.26
DI-3	3.50	2.80	0.22	0.007	0.019	0.06	0.26	0.017	4.39
DI-4	3.30	2.83	0.21	0.012	0.025	0.06	0.35	0.015	4.21

2 Experimental

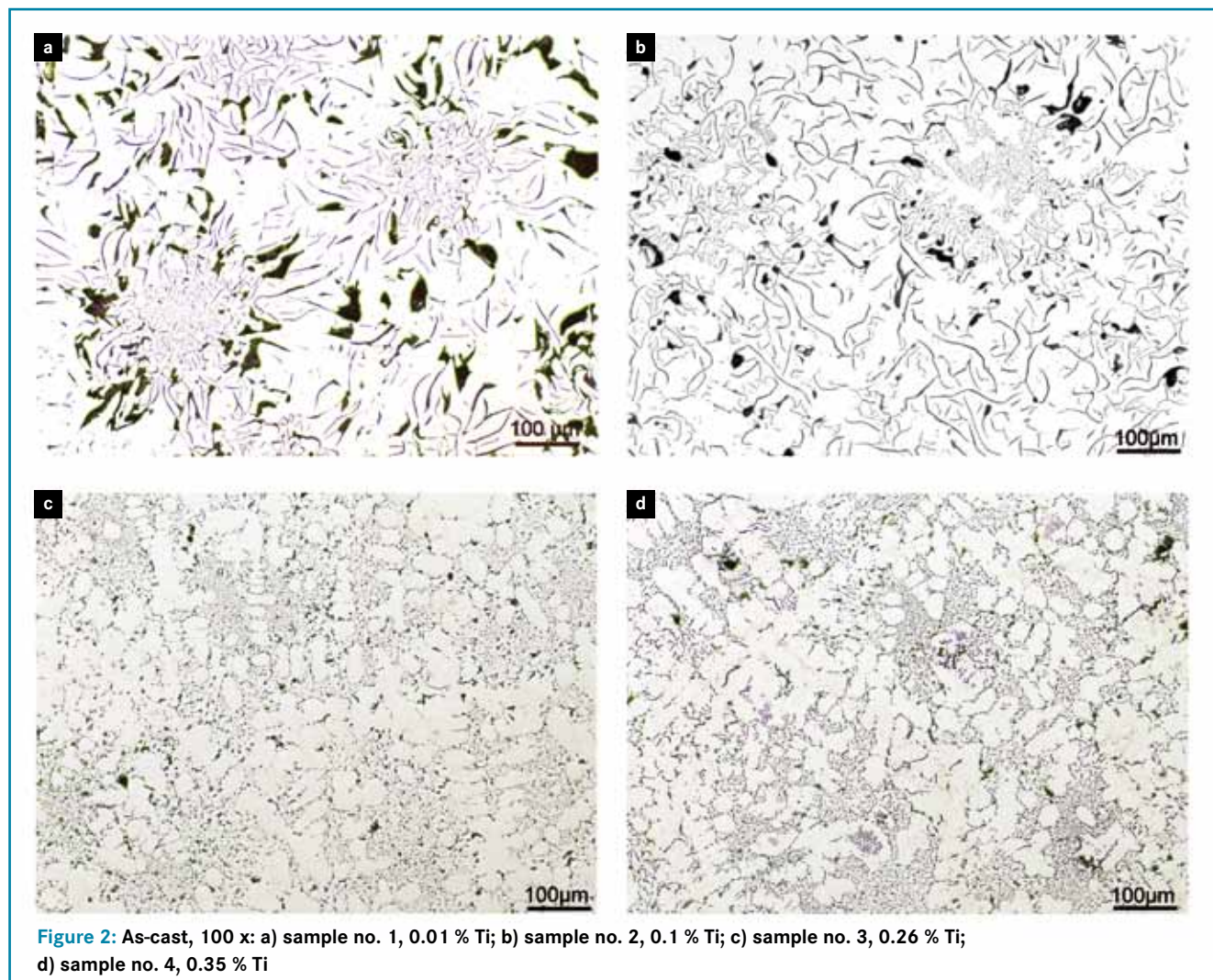
This experimental work was carried out in the foundry of department of Mechanical Engineering at Technical University of Denmark. The green sand moulds were made on a Disamatic 2110 moulding machine. As it is shown in **Figure 1**, the pattern is consisting of gating system and four tensile test samples which are different in dimensions. The thicknesses of tensile test specimens are 2, 4, 6 and 10 mm.

The iron was melted in an induction furnace in a batch of 150 kg. The composition was near eutectic and was adjusted by addition of pig iron, cast iron returns, industrial grade silicon and steel plates. After pouring the first ladle of 30 kg, ferro-titanium was added to the melt in the furnace and to reach a Ti content of 0.11 %. Afterwards, the second ladle was poured with the same procedure and again ferro-titanium was added to the rest of the melt increasing the

weight percent of titanium to 0.26 %. The same procedure was repeated for the remaining melt so that a Ti content of 0.35 % was reached. The inoculant was each time added to the melt in the pouring ladle. The composition of inoculant is presented in **Table 1**. The chemical composition of the melt of each ladle is presented in **Table 2**. The carbon equivalent is calculated according to:

$$CE = \% C + 0.317 \cdot \% Si + 0.33 \cdot \% P \quad (1)$$

The temperature was measured in the induction furnace and the melt was superheated to 1450 °C before pouring. Two “Quick Cup” samples were cast from each melt for thermal analysis. The samples for metallographic analysis were taken from the 10 mm thickness specimen. The SEM im-



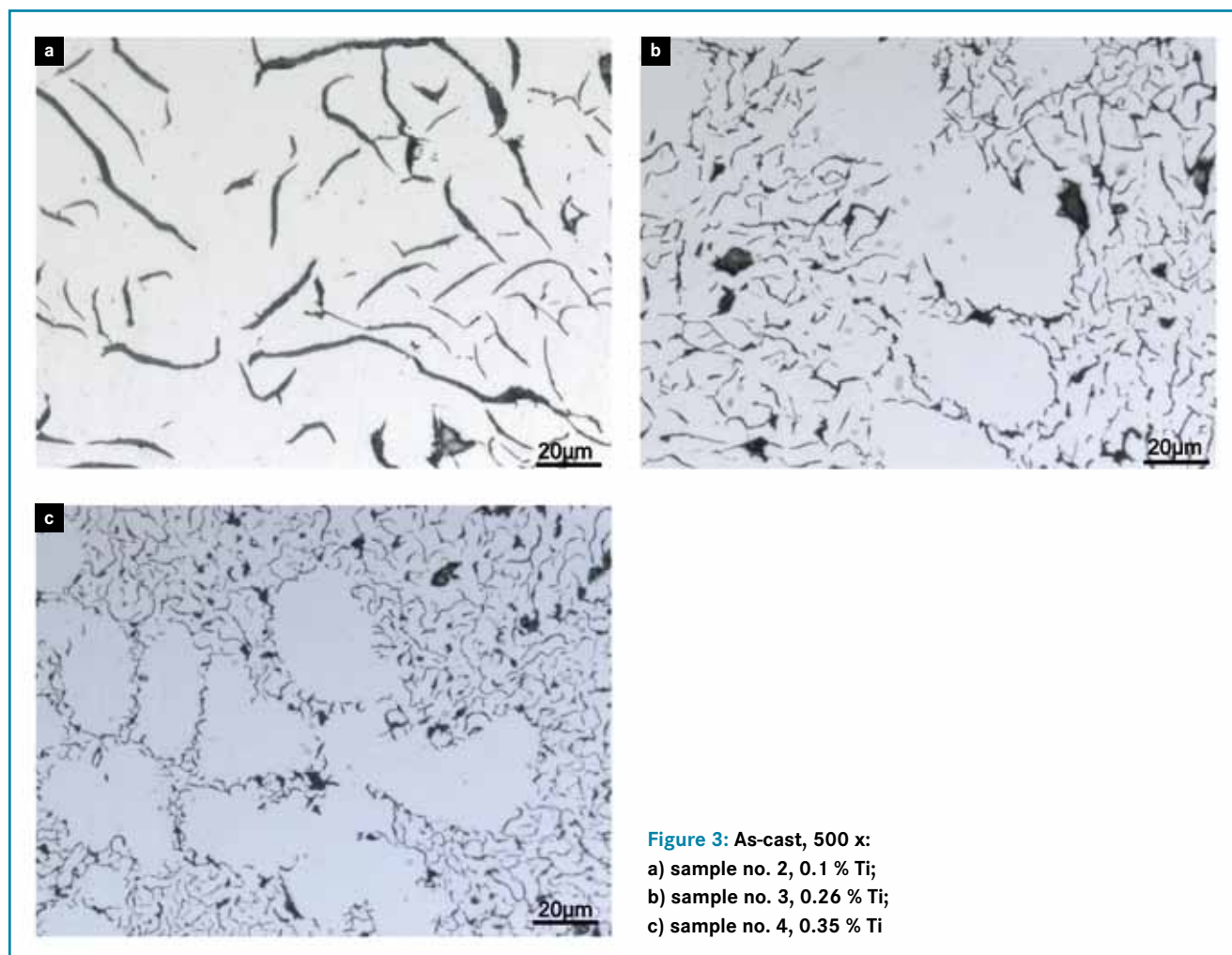


Figure 3: As-cast, 500 x:
 a) sample no. 2, 0.1 % Ti;
 b) sample no. 3, 0.26 % Ti;
 c) sample no. 4, 0.35 % Ti

ages were also acquired from metallography samples. The 8 mm thickness specimens were used for tensile test. Although after surface machining their thickness were lowered to 5.5 mm.

3 Results and discussion

3.1 Metallography

The metallographic investigation initiated by using an optical microscope. First, the images were taken after preparation without any chemical etching. As shown in Figure 2a, in the sample no. 1 the graphite is mostly type B, C and A. Sample no. 2 shows finer graphite flakes in the form of type A and B (Figure 2b). In some areas, fine graphite is formed as type D. However, in the high-Ti samples graphite is mostly formed as fine type D (Figure 2c and d). Figure 2b and c shows that the graphite becomes finer with increasing addition of Ti.

As expected, TiC inclusions were identified in the medium and high-Ti samples (Figure 3). Sample no. 3 and 4 have very similar microstructure. The only difference which could be addressed is the scale of the graphite and higher number of TiC inclusions in the sample no. 4.

Later, the metallography samples were color etched at 70 °C using the etchant 80 g NaOH, 20 g Picric acid in 200 ml water. As it can be seen in Figure 4, addition of titanium promotes significant segregation in the microstructure. Besides, dendrites are more pronounced in the Ti containing samples.

TiC inclusions are mostly observed at the intercellular areas (Figure 5a), at the borders of the secondary arms of dendrites (Figure 5b).

3.2 Electron microscopy investigation

The SEM analysis was carried out using Quanta 200 3D, dual-beam scanning electron microscope. This microscope has resolution of 50 nm at 30 kV (SE) and the accelerating voltage of 500 V to 30 kV with the capability of using a focused ion beam for removing material by milling. The in situ lift-out technique was applied to obtain TEM lamellae. A short description of this technique is explained in the subsection 3.2.1.

TEM studies (conventional and high resolution) were done using a Tecnai T20 G2 transmission electron microscope equipped to carry out chemical analysis. It has point resolution of 0.24 nm at 200 kV and its electron source is thermionic – LaB6.

3.2.1 In situ lift-out technique

To apply in situ lift-out technique a secondary electron imaging within the chamber of a focused ion beam-SEM system is needed. Navigation to a region of interest can be performed using secondary electron (SE) imaging. After choosing the region of interest, ion beam induced platinum will be deposited on its surface and around this area will be milled by FIB milling.

The lift-out sequence starts with maneuvering the lift-out needle into position, to the side of a pre-milled section, which is only attached to the bulk sample at one point. Then the needle will be welded to the section and a cut will be

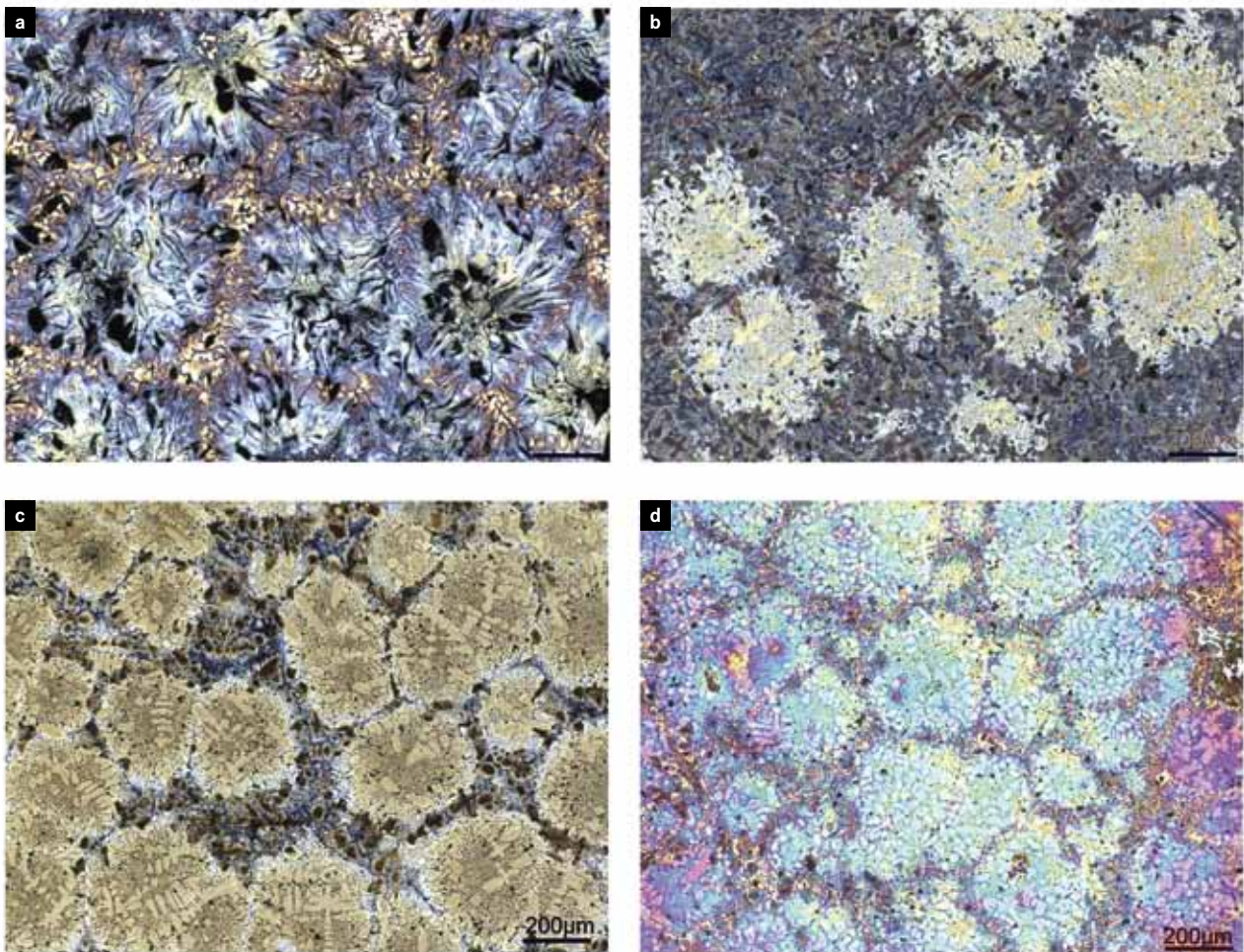


Figure 4: Color etched, 50 x: a) sample no. 1, 0.01 % Ti; b) sample no. 2, 0.1 % Ti; c) sample no. 3, 0.26 % Ti; d) sample no. 4, 0.35 % Ti

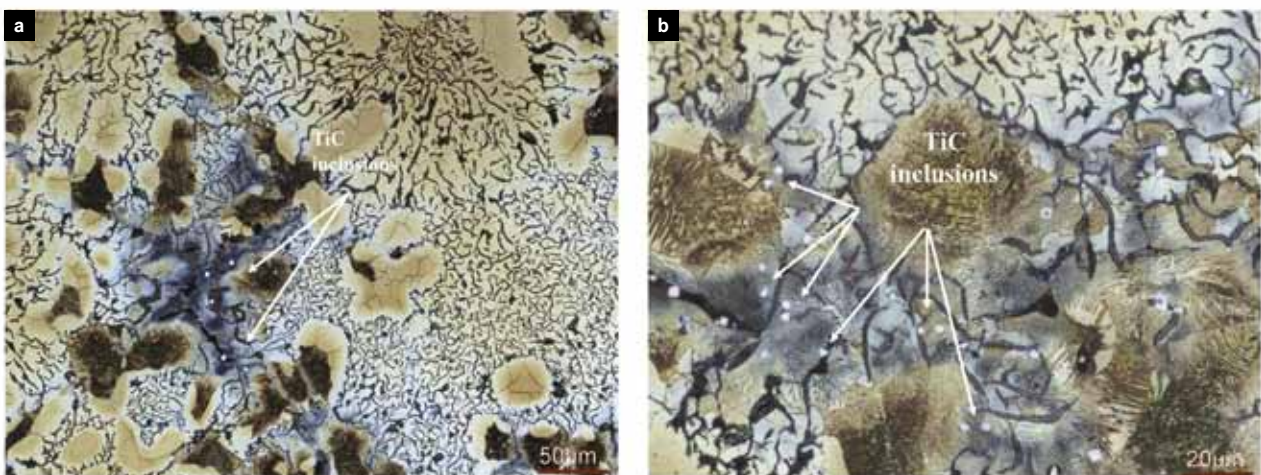


Figure 5: Color etched: a) sample no. 3, 200 x; b) sample no. 3, 500 x

made to detach the section from the bulk sample. At this point, the lamella is ready to be picked up in order to transfer to a TEM grid [11, 12]. The lift-out sequences has been shown in [Figure 6](#).

3.2.2 SEM results

The specimens were deep etched using a 2% HNO₃ solution in alcohol for 10-15 minutes, so that the graphite and inclu-

sions were brought forward for closer analysis. The SEM images are presented in [Figure 7](#) and [Figure 8](#). The trend of changes in the shape and size of graphite could be seen in these images.

3.2.3 TEM results

A thin film sample was prepared from the fine graphite of the 0.35% Ti sample for TEM study applying the in situ lift-

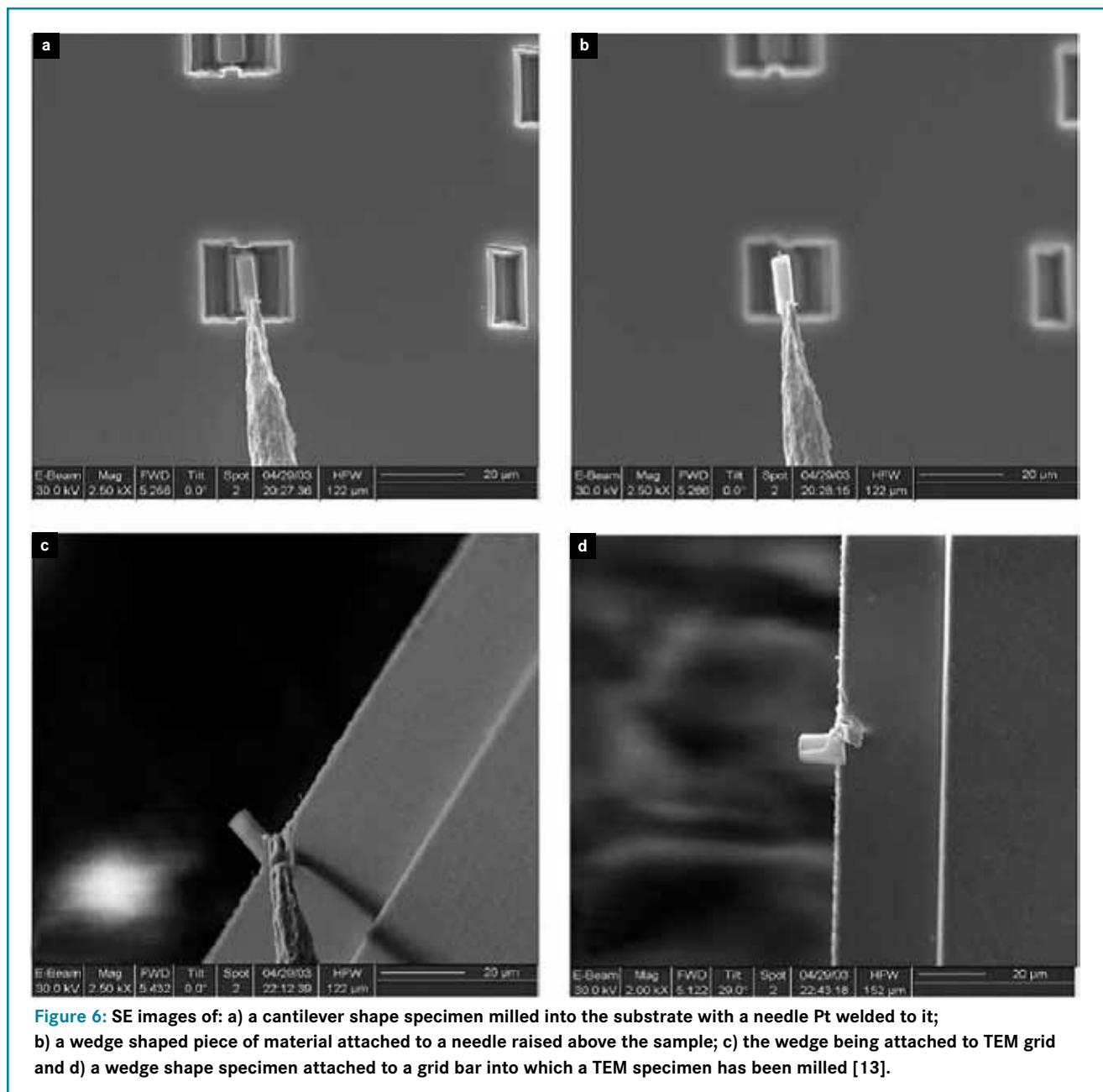


Figure 6: SE images of: a) a cantilever shape specimen milled into the substrate with a needle Pt welded to it; b) a wedge shaped piece of material attached to a needle raised above the sample; c) the wedge being attached to TEM grid and d) a wedge shape specimen attached to a grid bar into which a TEM specimen has been milled [13].

out technique. This sample was initially milled out of the polished sample by ion beam milling in a Helios EBS3 FIB-SEM. It was subsequently thinned for use in the TEM.

Figure 9 shows the layered structure and fine grains of graphite. Twin boundaries outline the very fine grains indicating that twinning plays an important role in the growth of the graphite lamellae.

3.3 Thermal analysis

Cooling curves were obtained from melt 1, 2 and 3. As it is depicted in Figure 10, it can be seen that addition of titanium changes the shape of the cooling curve. Even though the carbon equivalent for melt 2 and 3 (as calculated using Equation (1)) is marginally higher than that of melt 1, the fraction of primary austenite increases with addition of Ti to the cast iron. This shows that Equation (1) needs to be modified to correctly calculate the carbon equivalent when cast irons are alloyed with Ti. The cooling curves in Figure 10 shows that eutectic temperatures for grey irons are not changed due to the addition of Ti.

4 Conclusions

Addition of 0.1% Ti or more (up to 0.36% was tested in this work), promotes fine type D graphite and a significant segregation in the microstructure.

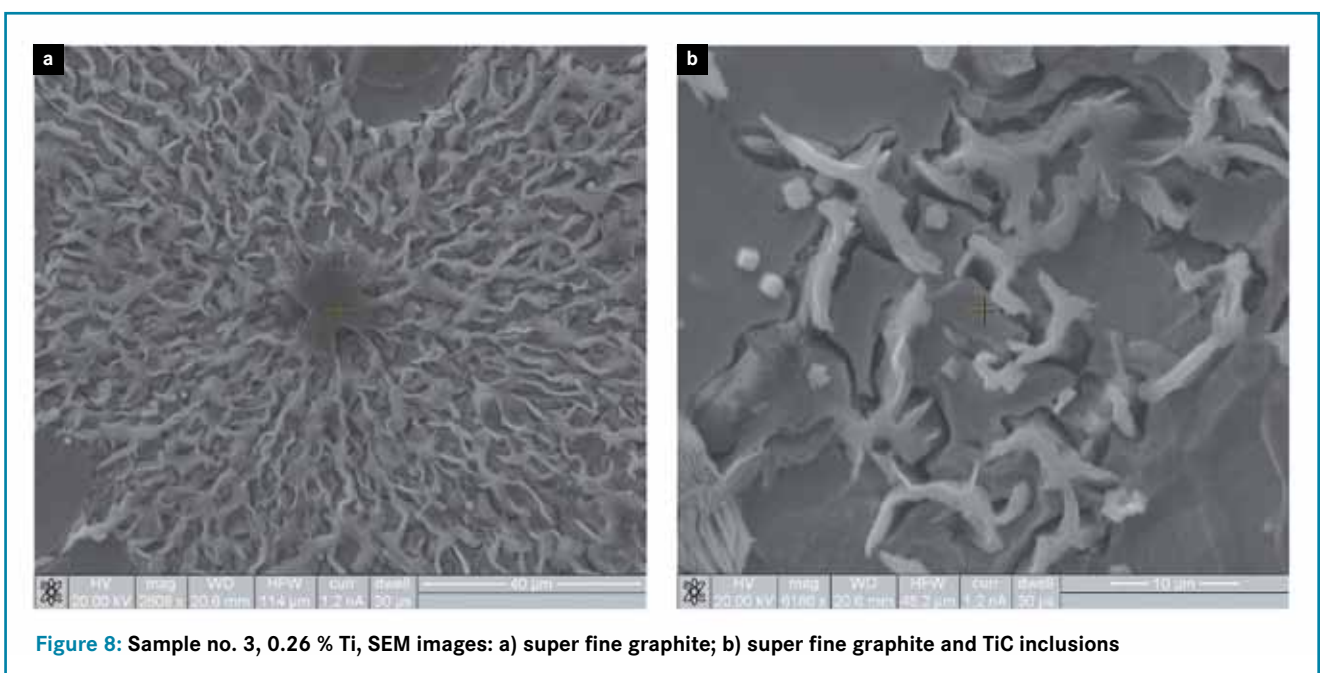
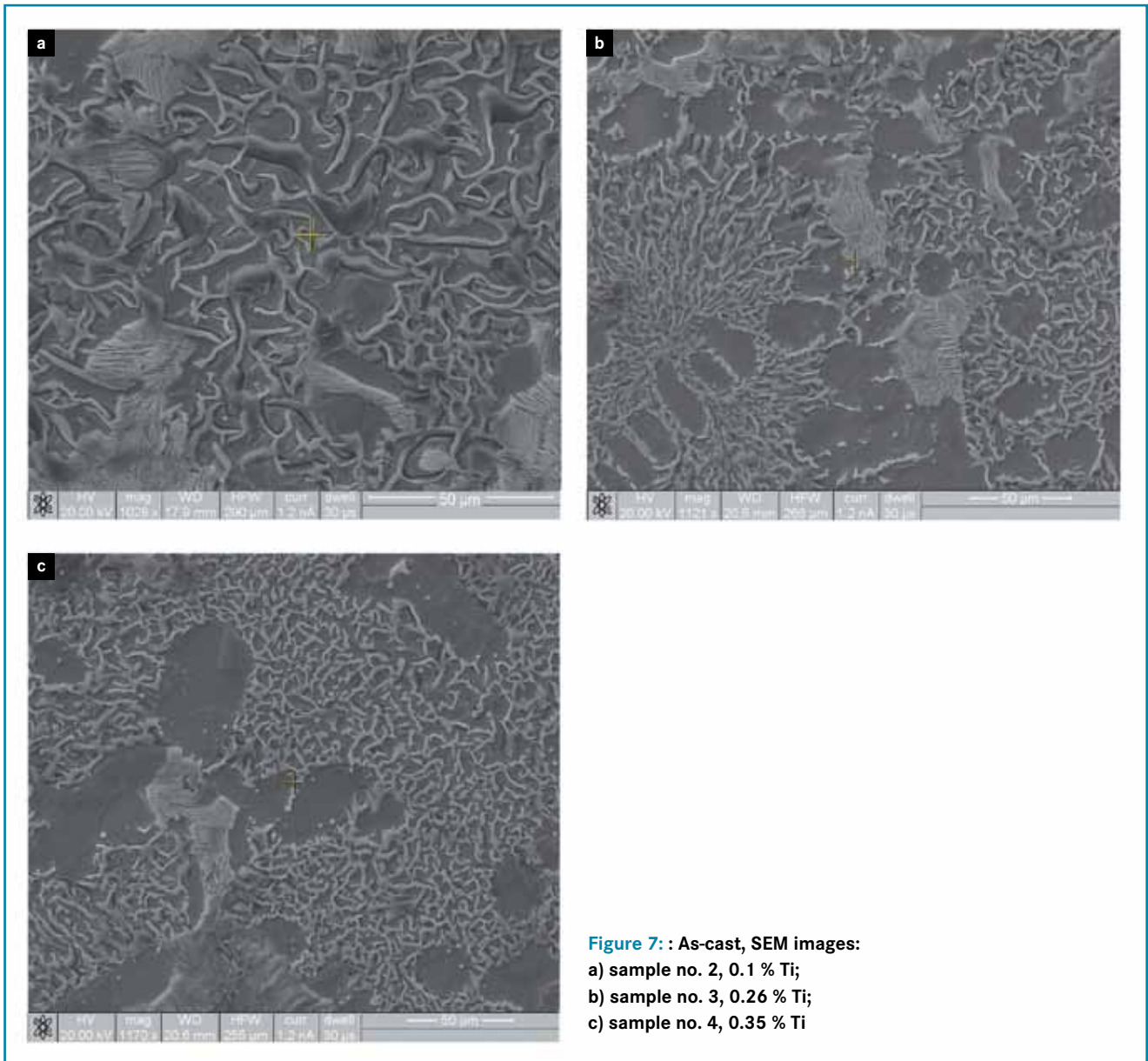
Titanium carbide inclusions are mostly located at the intercellular areas.

Fraction of primary austenite increases at the presence of Ti.

TEM studies shows that addition of Ti to grey cast iron makes the graphite very fine grained with twin boundaries between grains. Twin boundaries could be seen between the graphite crystals.

Cooling curves confirm the raise of formation of primary austenite dendrites with increasing the weight percent of titanium in the composition of iron.

This article is based on a paper presented at the 12th International Foundrymen Conference – Sustainable Development in Foundry Materials and Technologies – on Mai 24 to 25, 2012, in Opatija, Croatia



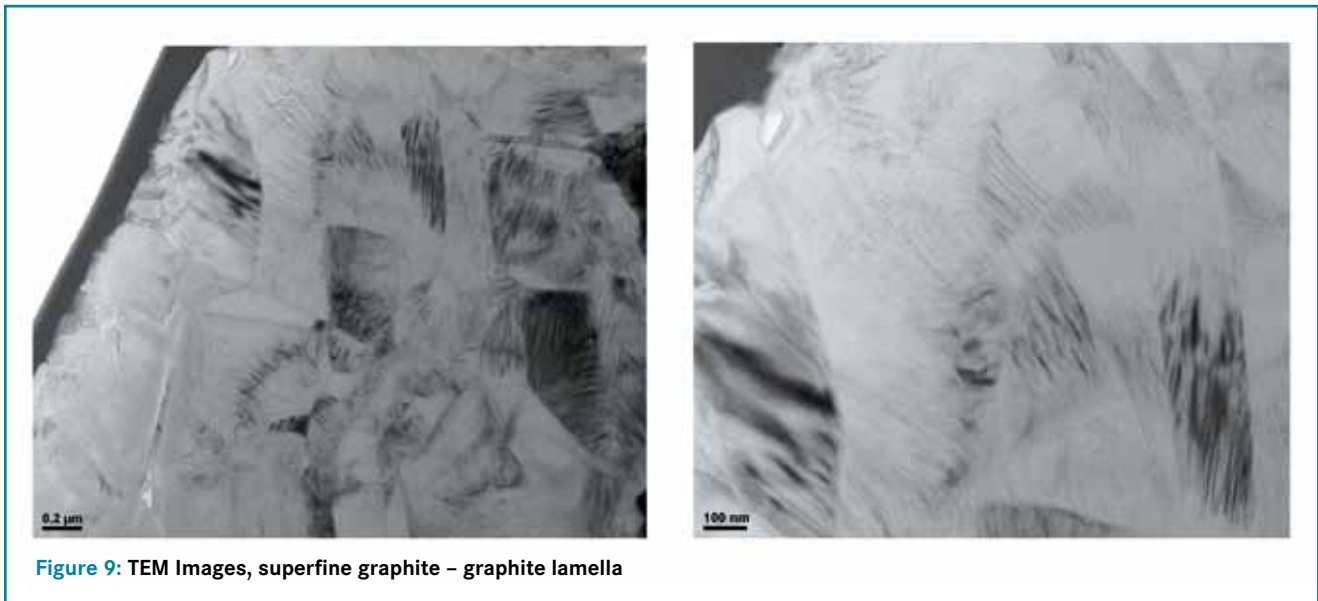


Figure 9: TEM Images, superfine graphite – graphite lamella

The authors would like to thank the Center of Electron Nanoscopy at Technical University of Denmark for providing us with their equipment and knowledge. They would also like to thank Jakob S. Nielsen and Robert V. Mackay for their technical support at the foundry.

E. Moumeni, N. S. Tiedje and J. H. Hattel, Department of Mechanical Engineering, Technical University of Denmark, Anker Engelundsvej 1, 2800 Kgs. Lyngby, Denmark

Literature

- [1] Yakovlev, F. I.: Metal Science and Heat Treatment 28 (1986) no. 5, p. 378-380.
- [2] Hatate, M.: Wear 251 (2001), pp. 885-889.
- [3] Chou, J.; Hon, M.; Lee, J.: Mat. Science 25 (1990), pp. 1965-1972.
- [4] Velichko, A.: Quantitative 3D characterization of graphite morphologies in cast iron using FIB microstructure tomography. PHD Thesis, Univ. of Saarland, Germany, 2008.
- [5] Tiedje, N.: Solidification, processing and properties of ductile cast iron. Mat Sci Tech, 26 (2010), pp. 505-514.
- [6] ASM Handbook, Volume 1: Properties and Selection: Irons, Steels, and High-Performance Alloys. 1990.
- [7] Wang, Z.; Zhang, K.; Jun Ye; Fan, C.: Titanium in cast iron (in Chinese). Modern Cast Iron 2 (2003), p. 31-33.
- [8] Lerner, Y.: Titanium in the rapidly cooled hypereutectic gray iron. Journal of Materials Engineering and Performance 12 (April 2003) no. 2, pp. 141-146.
- [9] Larrañaga, P.; Sertucha, J.; Loizaga, A.; Suárez, R.; Stefanescu, D.: Gray cast iron with high austenite-to-eutectic ratio. Part III. AFS Transactions, 2012.

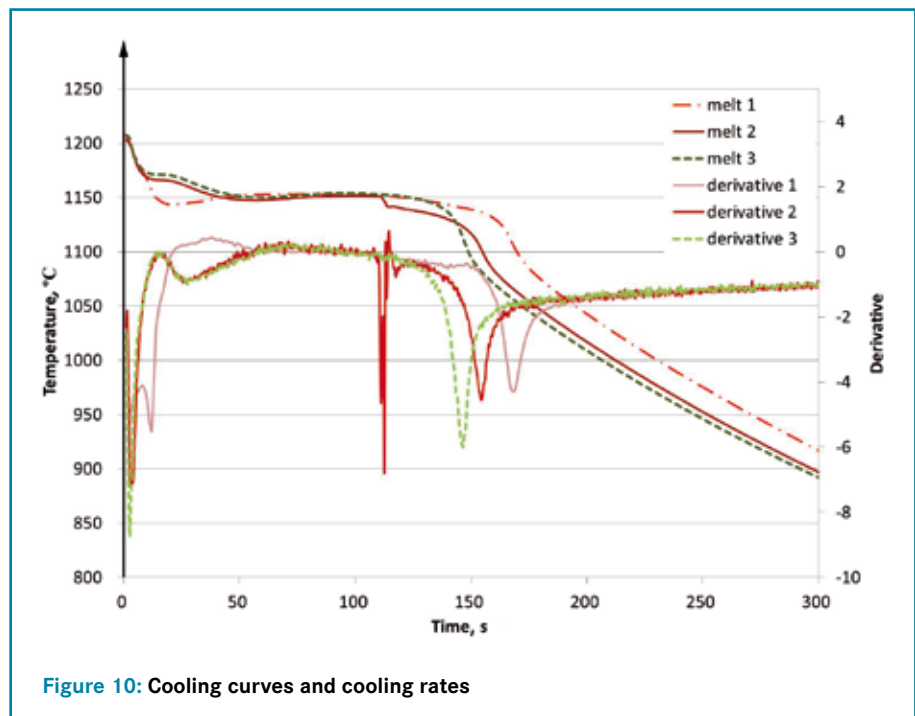


Figure 10: Cooling curves and cooling rates

- [10] Chisamera, M.; Riposan, I.; Stan, S.; Militaru, C.; Anton, I.; Barsto, M.: Inoculated slightly hypereutectic gray cast irons. ASM International 21 (2012), pp. 331-338.
- [11] Lekstrom, M.; McLachlan, M. A.; Husain, S.; McComb, D. W.; Shollock, B. A.: Using the in situ lift-out technique to prepare TEM specimens. IOP, 2008.
- [12] Langford, R.; Rogers, M.: In situ lift-out; steps to improve yield and a comparison. Micron 39 (2008) no. 8, pp. 1325-1330.
- [13] Langford, R.; Clinton, C.: In situ lift-out using a FIB-SEM system. Micron 35 (2004), pp. 607-611.

Keywords: Grey iron, titanium, SEM, TEM.

C paper-III

E. Moumeni, D.M. Stefanescu, N.S. Tiedje, P.Larrañaga, J.H. Hattel, “*Investigation on the Effect of Sulfur and Titanium on the Microstructure of Lamellar Graphite Iron*”, Accepted for the Metallurgical and Materials Transactions A (In press), 2012 Dec.

Investigation on the Effect of Sulfur and Titanium on the Microstructure of Lamellar Graphite Iron

Elham Moumeni (Technical University of Denmark), D.M. Stefanescu (The Ohio State University, USA), N.S. Tiedje (Technical University of Denmark), P. Larrañaga (Azterlan, Spain), J.H. Hattel (Technical University of Denmark)

ABSTRACT

The goal of this work was to identify the inclusions in lamellar graphite cast iron in an effort to explain the nucleation of the phases of interest. Four samples of approximately the same carbon equivalent but different levels of sulfur and titanium were studied. The Ti/S ratios were of 0.15 to 29.2, and the Mn/S ratios of 4.2 to 48.3. Light and electron microscopy were used to examine the unetched, color-etched and deep-etched samples.

It was confirmed that in irons with high sulfur content (0.12 wt%) nucleation of type-A and type-D graphite occurs on Mn sulfides that have a core of complex Al, Ca, Mg oxide. An increased titanium level of 0.35% produced superfine interdendritic graphite ($\sim 10\mu\text{m}$) at low (0.012 wt%) as well as at high S contents. Ti also caused increased segregation in the microstructure of the analyzed irons and larger eutectic grains (cells).

TiC did not appear to be a nucleation site for the primary austenite as it was found mostly at the periphery of the secondary arms of the austenite, in the last region to solidify. The effect of titanium in refining the graphite and increasing the austenite fraction can be explained through the widening of the liquidus-eutectic temperature interval (more time for austenite growth) and the decrease in the growth rate of the graphite because of Ti absorption on the graphite. The fact that Ti addition produced larger eutectic cells supports the theory that Ti is not producing finer graphite because of a change in the nucleation potential, but because of lower growth rate of the graphite in between the dendrite arms of a larger fraction of austenite.

In the presence of high Ti and S, (MnTi)S star-like and rib-like inclusions precipitate and act as nuclei for the austenite.

INTRODUCTION

The main solidification parameters affecting the mechanical properties of hypoeutectic gray (lamellar graphite) irons include the fraction of primary austenite and the shape, size and distribution of graphite. In foundry practice they are controlled through the chemical composition (carbon equivalent and alloying elements) and inoculation. Recently, using appropriate titanium additions in a low sulfur 4% carbon equivalent gray iron Larrañaga *et al.*¹ increased significantly the austenite fraction. This was accompanied by the solidification of, what they termed, superfine lamellar interdendritic graphite, which was associated with high tensile strength of 300-350 MPa, without a significant increase in hardness, which remained in the range of 185-200HB.² The superfine graphite is short (10-20 μm) and stubby. Thermal analysis on standard cooling curve cups and keel blocks indicated an increase of the liquidus temperature with titanium, suggesting an austenite nucleation effect. The eutectic temperature decreased. Overall the liquidus/eutectic temperature interval significantly increased. This was interpreted as increased time for austenite solidification, which explains the increase in the austenite fraction. While the various inclusions were not positively identified, it was stated that Ti compounds that were found mostly in the matrix did not appear to act as graphite nuclei. Manganese sulfides were found mostly in the proximity of the graphite, which qualifies them for possible graphite nuclei.

It is well known that a number of pure metals such as Li, Ca, Ba³, Sr, and Na⁴ can be effective in promoting graphite nucleation in cast iron. All these metals are strong oxide and sulfide formers. Their use as pure metals for inoculation purposes is impractical. Attempting to explain the efficiency of metals such as Ca, Ba, Sr, Na in the inoculation of lamellar graphite iron, Lux⁵ suggested that these, and all elements from groups I, II and III from the periodic table, when introduced in molten iron, form salt-like carbides that develop epitaxial planes with the graphite, and thus constitute nuclei for graphite.

Later, Weis⁶ assumed that nucleation of lamellar graphite occurs on SiO₂ oxides formed by heterogeneous catalysis of CaO, Al₂O₃, and oxides of other alkaline metals. At about the same time the role of MnS in graphite nucleation was implied through experiments based on thermal analysis of cast iron.⁷ A Mn/S ratio of 12.3 was found to produce the lowest eutectic undercooling. Note that this is way in excess of the stoichiometric ratio Mn/S = 1.7. Eventually, a consensus was reached that graphite flakes nucleate on MnS or complex (MnX)S compounds which have low crystallographic misfit with graphite.^{8,9,10} Typically, an optimized amount of sulfur in the presence of manganese and other elements such as Fe, Si, Al, Zr, Ti, Ca and Sr will promote the nucleation of graphite.^{11,12}

Sommerfeld and Ton¹³ found that the manganese sulfides contained additional elements such as Al, or Mg when small amounts of Mg were added to the melt. The Al compound was identified as Al₂O₃, while the Mg was thought to be part of the sulfide, (MnMg)S. The (MnMg)S particles had the same shape, color and distribution as the MnS particles. The most efficient type-A graphite nucleation was obtained at a Mn/S ratio of 6.7, but the authors mentioned that the most important factor is the Mn- and S- contents and not their ratio. Thermo-Calc simulations suggested that additions of Al to the melt causes the early (1580°C) formation of a SiO₂·Al₂O₃ phase, which can serve as nucleant for the MnS sulfides. For a hypoeutectic iron (3.4%C, 1.5%Si, 0.7%Mn, 0.05%S, 0.04%Ti) the Thermo-Calc calculation suggested the following sequence of phase formation: austenite at 1195°C, followed by Ti₄C₂S₂ at 1185°C, followed by graphite at 1148°C, followed by MnS at 1146°C. Note that this calculation is based on the assumption of thermodynamical equilibrium that ignores kinetic effects. In addition to the sulfides, square-shaped TiN were also observed.

Riposan *et al.*¹⁴ documented that the additional elements found in the MnS inclusions are usually combined in complex oxides that serve as nuclei for the MnS. The chemistry of the complex oxides and sulfides is based on a large number of factors including the chemistry of the inoculant, of the pre-conditioner, the iron charge and the alloying elements. They proposed that graphite nucleation starts with the precipitation of complex oxides of Al, Si, Zr, Mg, Ti, followed by growth of complex (Mn,X)S sulfides, which constitute the nuclei for flake graphite.

A similar theory of double-layered (cored) nucleation was proposed earlier for spheroidal graphite (SG). Using the results of SEM analysis, Jacobs *et al.*¹⁵ contended that SG nucleates on duplex sulfide-oxide inclusions (1 μm dia.); the core is made of Ca-Mg or Ca-Mg-Sr sulfides, while the outer shell is made of complex Mg-Al-Si-Ti oxides. This idea was further developed by Skaland and Grong¹⁰. They argued that SG nuclei are sulfides (MgS, CaS) covered by Mg silicates (e.g., MgO·SiO₂) or oxides that have low potency (large disregistry). After inoculation with FeSi that contains another metal (Me) such as Al, Ca, Sr or Ba, hexagonal silicates (MeO·SiO₂ or MeO·Al₂O₃·2SiO₂) form at the surface of the oxides, with coherent/semi-coherent low energy interfaces between substrate and graphite.

Titanium is well-known to be a deoxidizer and structure refiner in steel. For the case of cast iron, Basutkar *et al.*¹⁶ argued that titanium additions nucleate dendrites favoring the formation of small equiaxed dendrites. Wallace and co-workers^{17,18} found that titanium additions refined the secondary arm spacing in both gray and ductile iron. Ruff and Wallace¹⁹ concluded that the number of austenite dendrites can be increased by reducing the carbon equivalent, adding elements, such as Ti and B, which increase the undercooling by reducing the nucleation potential for graphite or restricting the growth of the eutectic grain, or by adding materials that serve as substrates for austenite nucleation (nitrides, carbonitrides and carbides of various elements such as Ti and V). Okada²⁰ suggested that Ti additions resulting in the formation of TiC, produce low carbon regions at the solid/liquid interface, favoring formation of type-D graphite. Using SEM/EDS analysis, Zeng *et al.*²¹ identified the presence of different Ti compounds in hypoeutectic gray irons

containing about 0.08%S and up to 0.02%Ti. The compounds included TiN (35at%N), (MnTi)S and TiC. Nakae and Fujimoto²² identified a graphite type A-to-D transition temperature, $T_{A/D}$, using thermal analysis. Titanium additions increase the $T_{A/D}$ temperature and thus favor type-D graphite formation at smaller undercooling. Yet, no explanation for this behavior was provided.

Wilford and Wilson²³ studied the influence of up to 0.4% Ti in gray iron. They stated that first, Ti will react with N producing TiN or Ti(CN) that affects the solidification of primary austenite. The excess Ti will then react with S. Formation of TiS decreases the available S for MnS formation and increases undercooling which is responsible for type-D graphite formation.

Lux⁵ argued that element of group IV of the periodic table, including Ti and V, form metallic carbides but do not have a nucleation effect, as they do not increase the number of eutectic cells. Sun and Loper²⁴ also reasoned that, while the atomic structure of TiC is such as to act as nucleus for graphite, the degree of mismatch between the lattices would minimize the nucleation effectiveness of Ti nitrides and carbonitrides. The effect of Ti on graphite shape may not be related to graphite nucleation, but to graphite growth. It is well known that sulfur and oxygen significantly affect graphite shape. According to Park and Verhoven,²⁵ Scanning Auger Microscopy of fractured graphite surfaces reveals monolayers of S segregated at the iron/graphite interface during solidification. Because of this, S is expected to increase the undercooling required at a given growth rate for both type-A and type-D graphite. Increasing the S level at low Mn contents will result in increased undercooling and finer graphite. It is possible that the effect of Ti is similar to that of S.

This work was undertaken in an attempt to clarify the role of titanium and sulfur in promoting increased fraction of austenite and superfine graphite. A detailed analysis of the graphite through light and electronic microscopy is provided, with particular attention given to the various inclusions that may serve as nuclei for the phases of interest.

EXPERIMENTAL PROCEDURE

Two gray iron melts, B401(high in sulfur) and B621 (low in sulfur), were produced in a medium frequency induction furnace. The complete melting procedure is described in ref. 2. After melt down and superheating at 1500°C, a 50kg ladle was used to pour iron into two EN-1563 Type II keel blocks (25mm). An amount of 0.2% of a commercial inoculant (chemical analysis: 68.1%Si, 0.89%Al, 1.65%Ca, 0.45%Bi, 0.38%Ba and 0.37% lanthanides.) was deposited on the bottom of each keel block mold before pouring. The remaining of the iron in the ladle was returned to the furnace. After adjustment of carbon, ferro-titanium (65%Ti) was added to the melt. The melt was superheated again and a second set of keel blocks was poured.

A detailed metallographic investigation was performed on samples obtained from the keel blocks through both light and electron microscopy. The images have been taken before and after etching. Some of the samples were color-etched using the etchant: %25 (80g) NaOH, 6% (20g) KOH, 6% (20g), picric acid, and (200mL) 63% water. A 2%Nital was used for deep etching for the SEM analysis.

The scanning electron microscopy investigation has been carried out using an XL-30 low-vacuum and environmental scanning microscopy (ESEM), equipped with Energy Dispersive X-ray Analyzer (EDAX). The unetched samples were studied to identify the chemistry of the inclusions and to try to establish a connection between the inclusions and graphite morphology.

RESULTS

The chemical composition of the test samples is given in Table 1. The following equation is used to calculate the weight percent of the carbon equivalent²⁶:

$$CE = \%C + 0.31 \cdot \%Si - 0.027 \cdot \%Mn$$

It can be seen that the compositions of the studied irons are slightly hypoeutectic. The only important difference between the compositions of these irons is the amount of S and Ti. Note that

the Ti/S ratio increases from 0.15 to 29.2, and the Mn/S ratio from 4.2 to 48.3. Two of the irons, 401.5 and 621.1 have similar Ti/S ratio, but iron 401.5 has six times more Ti and S than iron 621.1. Another set of two irons, 401.1 and 401.5, have similar Mn/S ratios, but iron 401.5 has 6 times more Ti than iron 401.1.

Table 1. Chemical composition (wt%) of the test samples

Sample no.	CE	C	Si	Mn	P	S	Ti	N	Ti/S	Mn/S
401.1	4.07	3.44	2.07	0.54	0.036	0.120	0.018	0.0037	0.15	4.5
401.5	4.03	3.42	2.02	0.50	0.037	0.120	0.360	0.0033	3	4.2
621.1	4.12	3.51	2.01	0.55	0.015	0.018	0.060	0.0071	3.33	30.6
621.5	4.06	3.45	2.03	0.58	0.015	0.012	0.350	0.0057	29.2	48.3

Light microscopy investigation

The effect of S and Ti on the morphology and size of the graphite is shown in Fig. 1. It is seen that the low-Ti irons exhibit in all cases mostly coarse type-A graphite (Fig. 1a, c). Increasing the Ti/S ratio produces finer graphite at the same S level (compare Fig. 1a and b, or Fig. 1c and d). However, a clear difference is seen between the samples having low- or high-S. At the same Ti/S ratio, the sample with high S and Ti (401.5) exhibits finer graphite. Indeed, some type-A graphite persist in the microstructure of sample 621.5.

A higher magnification of the high-S iron 401 reveals a large number of inclusions (Fig. 2). These inclusions will be identified later through SEM analysis. Titanium addition refines the graphite and also changes the morphology of the inclusions. Indeed, as seen in Fig. 2b, some very large star-like inclusions are noticed in the middle of the secondary arms of the austenite dendrites. These star-like inclusions are not present in the microstructure of the low-S high-Ti irons, as evident from Fig. 3. In the low-S high-Ti iron (Ti/S=29.2) the inclusions are mostly located at the borders of secondary dendrite arms.

The dramatic effect of high Ti/S ratio on the microstructure is clearly illustrated in Fig. 4 for the case of the high-S irons. Larger eutectic grains and less oriented dendrites are noticed.

The high magnification colored micrograph of low Ti/S ratio low S iron in Fig. 5 shows few inclusions, one TiC and one MnS. The Ti carbide is in the middle of the matrix, while the Mn sulfide is attached to a graphite flake.

Increasing the Ti/S ratio in the low S iron, raises manifold the number of inclusions. In Fig. 6 it is seen that the inclusions are pushed by the growing dendrites in the last regions to solidify. In an earlier report¹ it was shown that the fraction of primary austenite in the high-S iron 401.5 increased from 0.17 to 0.27 as the Ti/S ratio increased (Ti increased from 0.018 to 0.36%). However, titanium carbides do not seem to act as nuclei for the austenite since they are positioned in the interdendritic regions.

The picture on Fig. 6c presents a detail of the superfine graphite. It is short and stubby with a typical length of 10 to 20µm.

According to the ternary phase diagram of Fe-C-Ti presented in Fig. 7, for a 3.5%C iron, TiC can precipitate at temperatures considerably higher than the liquidus of cast iron. Thus, it is reasonable to assume that Ti carbides forms in the liquid, before the beginning of the austenite solidification, and are pushed in the last regions to solidify by the austenite dendrites.

Scanning electron microscopy (SEM) investigation

In the high-S low-Ti iron (B401.1), a large number of polygonal MnS inclusions were found (Fig. 8). More than 50% of these inclusions seem to be attached to the sides of the graphite flakes (Fig. 9a). Complex Al-Mg-Si-Ca oxide compounds were identified at the center of some of the MnS particles (Fig. 9b, c and d).

In the presence of both Ti and S (sample B401.5) a variety of inclusions with different morphologies was found. The smaller inclusions and their spectrum are shown in Fig. 10. The

majority of the inclusions in this sample are (MnTi)S, with a variety of morphologies (Fig. 11). As also shown in Fig. 2b, the (MnTi)S inclusions are mostly formed in the middle of the dendrites. It is reasonable to assume that they have acted as nuclei for the austenite dendrites. This would explain the significant increase in the fraction of austenite as the Ti/S ratio increased from 0.15 to 3. MnS inclusions were also found in this iron (Fig. 11d), and again, they seemed to act as nuclei for the graphite.

Deep etched microstructures of sample B401.5 (Ti/S=3) are shown in the Fig. 12. The presence of (MnTi)S inclusions in the austenite is confirmed (Fig. 12 a and b). It is the dominant inclusion. A few TiC inclusions were found in the austenite (Fig. 12 a, b), and many TiC inclusions were found in the proximity of the superfine graphite flakes (Fig. 12 c). Yet, as they do not show clear contact with graphite (they always seem to be on top and not on the side of the graphite), in our opinion, the appearance is not that of graphite nuclei.

The images of the deep-etched sample B621.1 (low-S low-Ti, medium Ti/S ratio) are presented in the Fig. 13. The microstructure exhibits coarse type-A graphite (length 100 to 200µm) and almost no inclusions (Fig. 13a). This sample exhibited very few inclusions. The spectrum of the cubic inclusions found indicates the composition of a titanium carbonitride Ti(CN). While the pick of Ti and N are at the same keV, this pick was very small in other TiC spectra.

A dramatic change in the microstructure occurs when the Ti/S ratio is raised to 29.2 for sample 621.5 with low-S high-Ti (0.012% S, 0.35%Ti). A large number of cubic TiC particles are observed (Fig. 14a). This is consistent with previous research¹ where it was found that the number of Ti compounds increases significantly as the Ti content in the iron increases. They are the dominant inclusions at this composition. As also documented earlier in this report, the TiC particles are pushed by the austenite dendrites to the last regions to solidify (Fig. 14a). There is no evidence to show that TiC could act as nuclei for the primary austenite. However, isolated instances where the TiC is in contact with the graphite have been found (Fig. 14c). We do not feel that this is enough proof to demonstrate a graphite nucleation effect by the TiC. A few MnS inclusions in contact with the graphite were also observed (Fig. 14b). The graphite flakes are thick and short (Fig. 14c, d).

A summary of the type and location of inclusions as a function of composition and the Ti/S ratio is given in Table 2. Note again that the amount of inclusions in the low-S low-Ti sample (621.1) was minimal.

Table 2. Summary of types and location of inclusions from SEM analysis

Sample	%S	%Ti	Ti/S	Mn/S	Graphite	Dominant inclusion	Inclusion location	Other inclusions
401.1	0.12	0.018	0.15	4.5	type-A	MnS	in contact with Gr	none
401.5	0.12	0.36	3	4.2	interdendritic/ superfine	(Mn,Ti)S	in austenite	MnS, TiC
621.1	0.018	0.06	3.33	30.6	type-A	TiC, Ti(CN)	in austenite	MnS
621.5	0.012	0.35	29.2	48.3	superfine + some type A	TiC	at austenite grain boundaries; in contact with graphite (?)	MnS

Some high magnification pictures of the superfine graphite are presented in Fig. 15. It is seen that the graphite flakes are very short, thick and that they bend and twist significantly. While most of the growth is along the A-direction, in some instances growth in the C-direction appears to occur (Fig. 15b). The graphite branch growing in the C-direction shows an exposed hexagonal plane and is very similar to the corral graphite. A more detailed analysis is required to support this statement.

DISCUSSION

There are two major effects of the Ti additions that need to be understood: the increased amount of austenite and the formation of the superfine interdendritic graphite. Arguments involving nucleation and growth kinetics of the phases must be considered.

As shown in Table 3, Ti addition to both low and high S irons results in an increase of the liquidus temperature, TL , and a decrease of the minimum eutectic temperature, TE_{min} . The classic explanation for the first effect is an increase in the nucleation potential. Indeed, the Ti addition to a melt with sufficient S (401.5 – 0.12%S), produces complex (MnTi)S that are nucleation sites for austenite but not for graphite. As formation of (MnTi)S depletes the melt from sulfur, less S is available for the precipitation of MnS inclusions that are the main nucleant for type-A graphite. This results in the depression of the eutectic temperature. Thus, for high S iron, Ti additions will increase the amount of austenite through enhanced austenite nucleation and increased liquidus-eutectic interval, which allows more time for austenite growth before the eutectic reaction. A higher amount of dendritic austenite will favor a type-A to type-D transition for graphite, as the graphite is constrained to grow between the dendrite arms. Titanium absorption on the graphite plates could also interfere with graphite growth, similar to the mechanism described by Park and Verhoven²⁵ for sulfur.

Table 3. Thermal analysis data and fraction of austenite

Sample no.	TL °C	TE_{min} °C	$TL - TE_{min}$ °C	Austenite fraction
401.1	1182	1147	35	0.17
401.5	1192	1145	47	0.27
621.1	1187	1148	39	0.27
621.5	1198	1144	54	0.38

For the low S irons, the situation is less clear. While the higher amount of austenite produced by Ti additions can still be attributed to the higher liquidus-eutectic interval (see Table 3), the reasons for the increase remain partially unexplained. The probable explanation for the higher liquidus is increased nucleation. Yet, we were not able to identify nucleation sites for the austenite in iron 621.5. The higher TE_{min} in the absence of Ti, and the highest TE_{min} for the highest purity iron from the series (621.5) can be understood through equilibrium thermodynamics. Indeed, low S and Ti content decrease the stable eutectic temperature by similar amounts (see Table 3 page 65 in ref.²⁶) and thus, purer irons should have higher eutectic equilibrium temperature. The kinetic effect of Ti absorption on the graphite will also act in the same direction and is probably responsible for the formation of the superfine graphite.

The fact that Ti addition produced larger eutectic cells supports the theory that Ti is not producing finer graphite because of a change in the nucleation potential, but because of lower growth rate of the graphite in between the dendrite arms of a larger fraction of austenite.

CONCLUSIONS

It was confirmed that when sufficient sulfur is present in the iron nucleation occurs on Mn sulfides that have a core of complex Al, Ca, Mg oxide. Both type-A and type-D graphite were observed to grow on the Mn sulfide. An increased titanium level of 0.35% produced superfine interdendritic graphite (~10µm) at low as well as at high S contents. The shape of the graphite was also dramatically altered. Ti also produced larger eutectic grains (cells).

While TiC additions increased the liquidus temperature, TiC did not appear to be a nucleation site for the primary austenite as it was found mostly at the periphery of the secondary arms of the austenite, in the last region to solidify. The effect of titanium in refining the graphite and increasing the austenite fraction can be explained through the widening of the liquidus-eutectic temperature interval (more time for austenite growth) and the decrease in the growth rate of the graphite.

In the presence of high Ti and S, (MnTi)S star-like and rib-like inclusions were found in the middle of the austenite dendrites. It is reasonable to assume that they are acting as nuclei for the austenite.

ACKNOWLEDGEMENTS

This work was made possible by a scholarship from the Technical University of Denmark to Elham Moumeni, for a short research appointment at Ohio State University. The samples were produced by Azterlan, Spain and analyzed at Ohio State University.

REFERENCES

1. P. Larrañaga, J. Sertucha, A. Loizaga, R. Suárez and D.M. Stefanescu, *Trans. AFS* **120** (2012) paper 12-034
2. P. Larrañaga, J. Sertucha, A. Loizaga, R. Suárez and D.M. Stefanescu, *Trans. AFS* **120** (2012) paper 12-035
3. B. Lux and H. Tannenberger, *Modern Casting* (March 1962) 57
4. D.M. Stefanescu, *Giesserei-Praxis* **24** (1972) 430
5. B. Lux, in *Recent Research on Cast Iron*, H. D. Merchant editor, Gordon and Breach (1968) 241
6. W. Weis, in *The Metallurgy of Cast Iron*, B. Lux, I. Minkoff and F. Mollard eds., Georgi Publishing Co., St Saphorin, Switzerland (1974) 69-79
7. J.F. Wallace, *Trans. AFS* **83** (1975) 373
8. L.R. De and Y.J. Xiang, *Trans. AFS* **99** (1991) 707-712
9. M. Chisamera, I. Riposan and M. Barstow, in *AFS International Inoculation Conference*, Rosemont, IL, USA (1998) paper 3
10. T. Skaland, F. Grong and T. Grong, *Metall. Trans.* **24A** (1993):2321 and 2347
11. K. Muzumdar and J. Wallace, *Trans. AFS* **81** (1973) 412-423
12. I. Riposan, M. Chisamera, S. Stan and T. Skaland, *Proceedings of the AFS Cast Iron Inoculation Conference* (2005) 31-41
13. A. Sommerfeld and B. Tonn, in *The Carl Loper Cast Iron Symposium*, Madison, WI USA (2009) 168-178
14. I. Riposan, M. Chisamera, S. Stan, C. Hartung and D. White, in *The Carl Loper Cast Iron Symposium*, Madison, WI USA (2009) 191-200
15. M.M. Jacobs, T.J. Law, D.A. Melford and M.J. Stowell, *Metals Technology*, **1**, Part II (Nov. 1974) 490
16. P. Basutkar, S Yew and C. Loper, *Trans. AFS* **77** (1969) 311-320
17. J.F. Wallace, *Trans. AFS* **83** (1975) 363-378
18. R. Naro and J.F. Wallace, *Trans. AFS* **77** (1969) 311-320
19. G. Ruff and J.F. Wallace, *Trans. AFS* **84** (1976) 705-728
20. A. Okada and H. Miyake, *KANSAI Univ. Press* (1996) 141
21. D. Zeng, Y. Zhang, J. Liu, H. He, and X. Hong, in *Science and Processing of Cast Iron VIII*, Y. Li et al. eds., Tsinghua Univ. Press (2006) 86-91
22. H. Nakae and K. Fujimoto, in *Key Engineering Materials*, Trans Tech Publ. Switzerland **457** (2011) 25-30
23. K.B. Wilford and F.G. Wilson, *British Foundryman* **78** (1985) 301 and 364
24. G.X. Sun and C.R. Loper, *Trans. AFS* **91** (1983) 639-646
25. J.S. Park and J.D. Verhoven, *Metallurgical and Materials Trans. A* **27A** (1996) 2740-2753
26. D.M. Stefanescu, in *Metals Handbook* vol. 15, 9th ed. (1988) 61-70
27. Ohtani H., Tanaka T., Hasebe M., Nishizawa; T. Calculation of the Fe-C-Ti Ternary Phase Diagram, *Calphad* **12** (1988) 225-246

LIST OF FIGURES

Fig. 1. Unetched microstructures: a) Sample 401.1 - 0.12%S, 0.018%Ti, Ti/S=0.15; b) Sample 401.5 - 0.12% S, 0.36% Ti, Ti/S=3; c) Sample 621.1 – 0.018%S, 0.06%Ti, Ti/S=3.33; d) Sample 621.5 – 0.012%S, 0.35%Ti, Ti/S=29.2

Fig. 2. Microstructure of high-S irons; unetched: a) 401.1, 0.12%S, 0.018%Ti; b) 401.5, 0.12%S, 0.36%Ti

Fig. 3. Microstructure of high Ti/S sample 621.5 – 0.012%S, 0.35%Ti; unetched.

Fig. 4. Color etched micrographs of the high-S irons at low magnification: a) Sample. 401.1 - 0.12%S, 0.018%Ti; b) Sample. 401.5 - 0.12%S, 0.36%Ti

Fig. 5. Color etched micrographs of the sample. 621.1 – 0.018% S, 0.06% Ti at high magnification

Fig. 6. Color etched micrographs of the sample. 621.5 – 0.012% S, 0.35% Ti at high magnification: a) inclusions in the interdendritic regions; b) inclusions in the interdendritic regions; c) detail of superfine graphite

Fig. 7. Section through the Fe-Ti-C ternary phase diagram²⁷

Fig. 8. Unetched sample 401.1- 0.12% S, 0.018% Ti; a) MnS in contact with graphite; b) MnS spectrum

Fig. 9. Sample 401.1 – Deep-etched with Nital 2%: a) MnS in contact with graphite; b) MnS with oxide nucleus; c) MnS with oxide nucleus (higher magnification); d) spectrum of the oxide nucleus

Fig. 10. Unetched sample. 401.5 - 0.120% S, 0.36% Ti

Fig. 11. Unetched SEM micrographs of sample 401.5 showing (Mn,Ti)S and MnS inclusions: a) (Mn,Ti)S rib-like inclusion; b) (Mn,Ti)S star-like inclusion; c) (Mn,Ti)S inclusion; d) MnS inclusions in contact with graphite

Fig. 12. Deep etched micrographs of sample 401.5 - 0.120%S, 0.36%Ti: a) (MnTi)S inclusions in the austenite dendrites; b) (MnTi)S inclusions in austenite (higher magnification); c) Superfine graphite and TiC

Fig. 13. Deep etched micrographs of sample 621.1 – 0.018%S, 0.06%Ti: a) coarse type-A graphite; b) Ti carbonitride; c) spectrum of the carbonitride

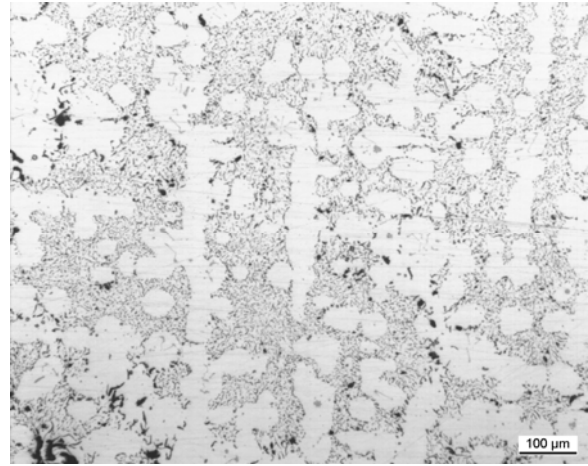
Fig. 14. Deep etched micrographs of sample 621.5 - 0.012%S, 0.35%Ti: a) TiC at austenite grain boundaries; b) TiC in austenite, MnS on superfine graphite; c) Cluster of small TiC and TiC in contact with superfine graphite; d) Superfine graphite and TiC

Fig. 15. SEM micrographs of superfine graphite from deep etched sample 621.5: a) superfine graphite; b) growth in A- and C-direction

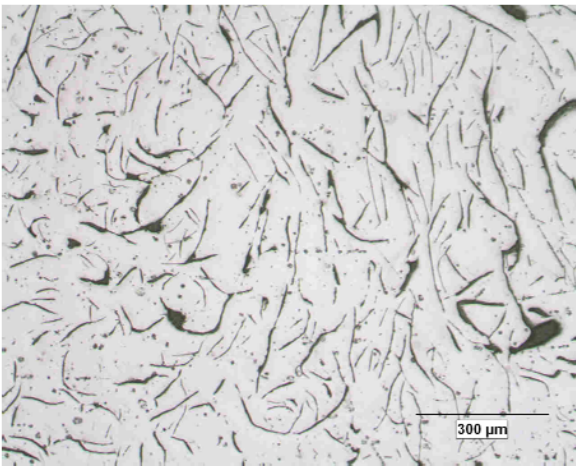
FIGURES



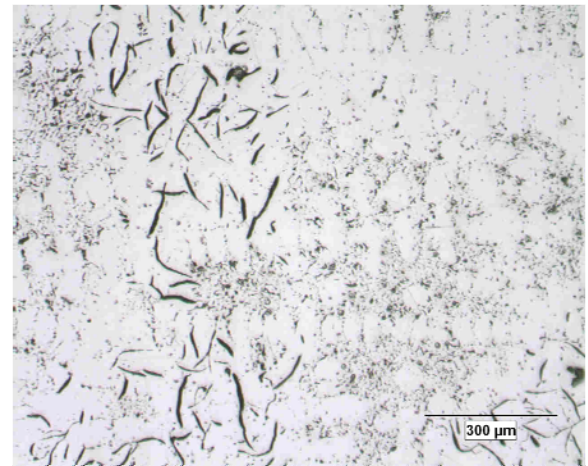
a) Sample 401.1 - 0.12%S, 0.018%Ti, Ti/S=0.15



b) Sample 401.5 - 0.12% S, 0.36% Ti, Ti/S=3



c) Sample 621.1 – 0.018%S, 0.06%Ti, Ti/S=3.33



d) Sample 621.5 – 0.012%S, 0.35%Ti, Ti/S=29.2

Fig. 1. Unetched microstructures

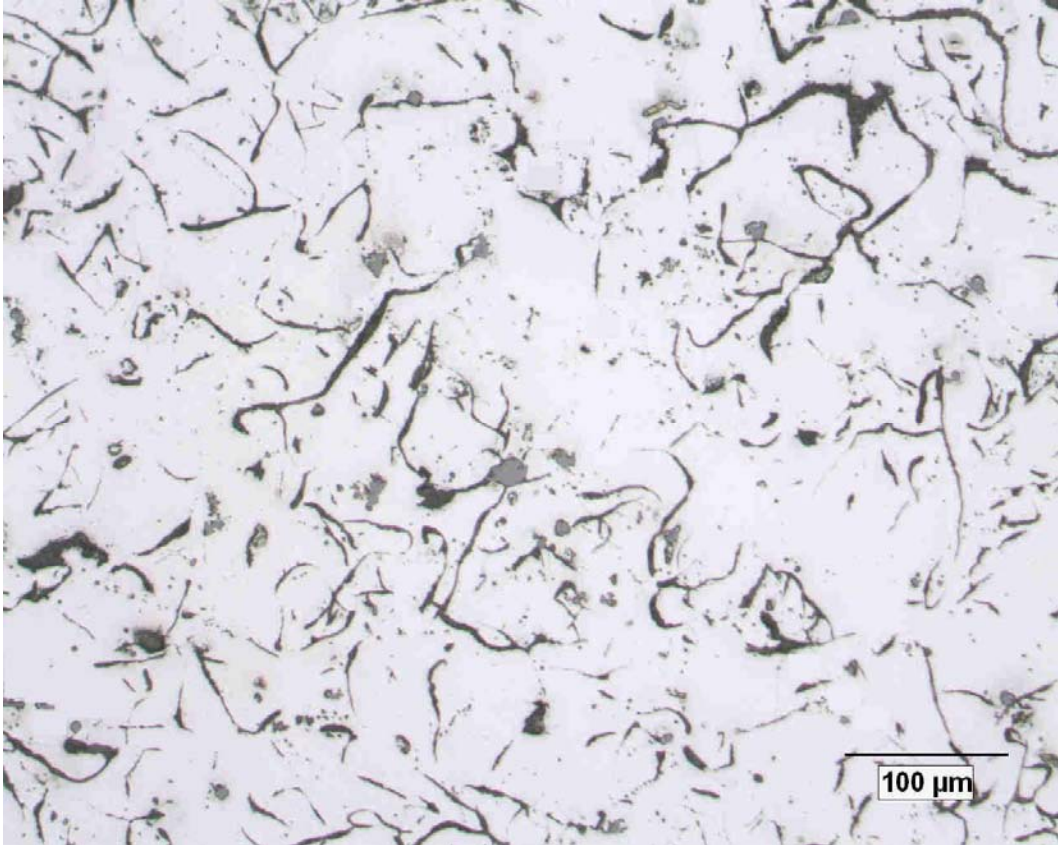


Fig. 2a 401.1, 0.12%S, 0.018%Ti;

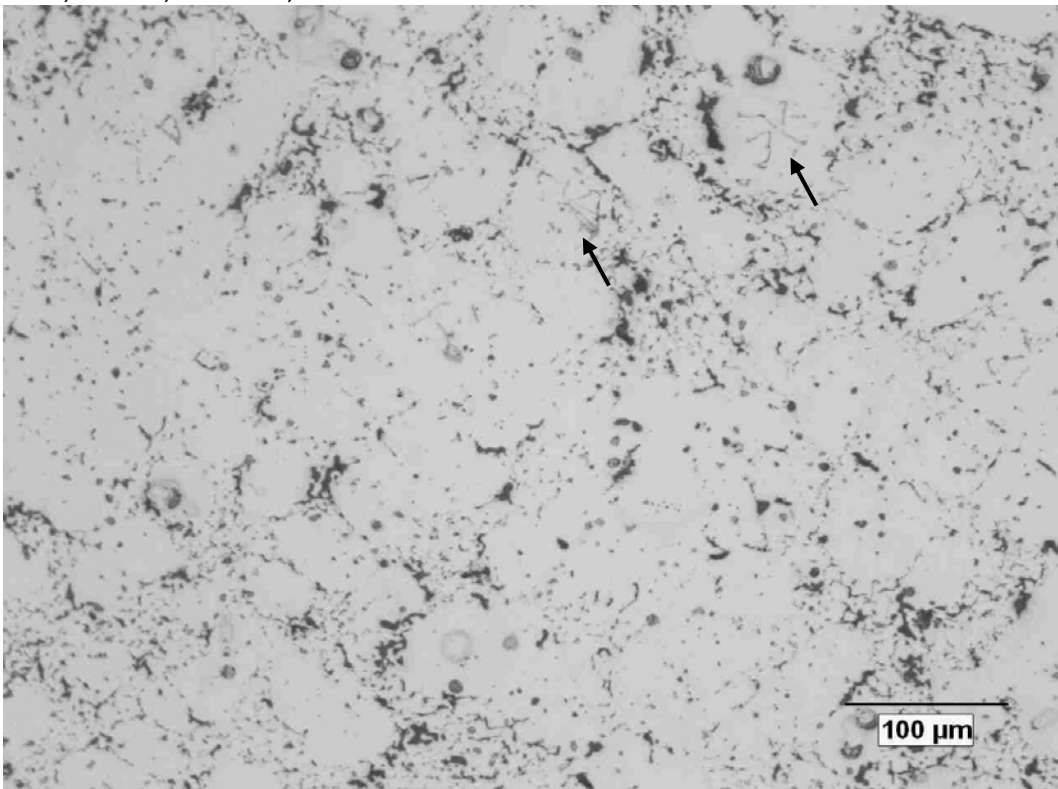


Fig. 2b 401.5, 0.12%S, 0.36%Ti

Fig. 2. Microstructure of high-S irons; unetched:

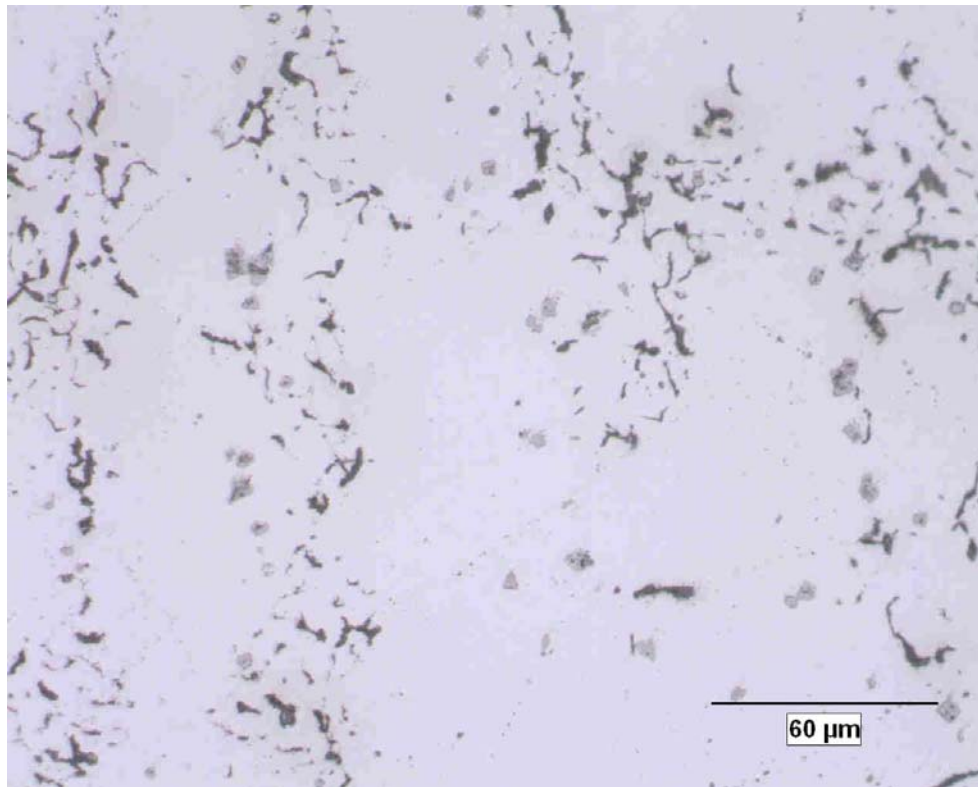
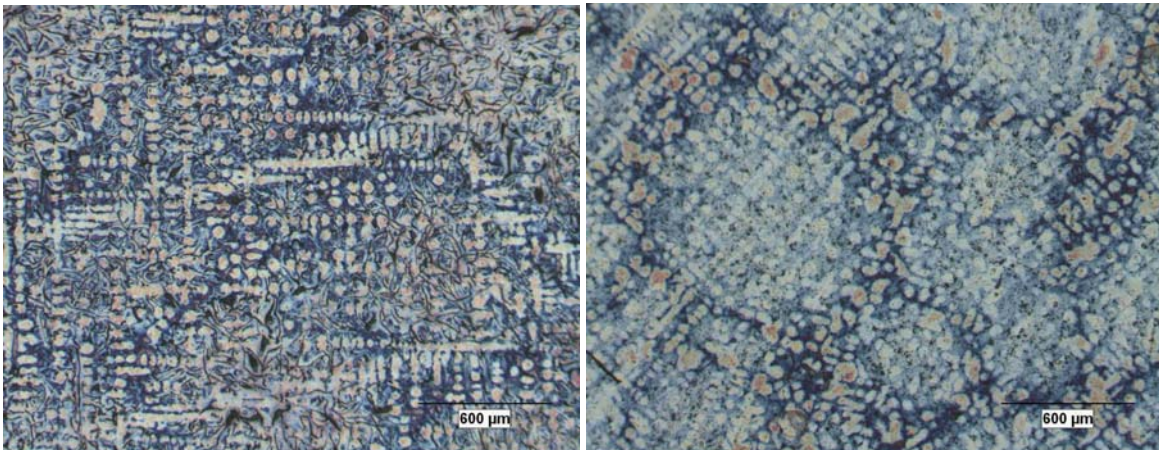


Fig. 3. Microstructure of high Ti/S sample 621.5 – 0.012%S, 0.35%Ti; unetched.



a) Sample. 401.1 - 0.12%S, 0.018%Ti

b) Sample. 401.5 - 0.12%S, 0.36%Ti

Fig. 4. Color etched micrographs of the high-S irons at low magnification

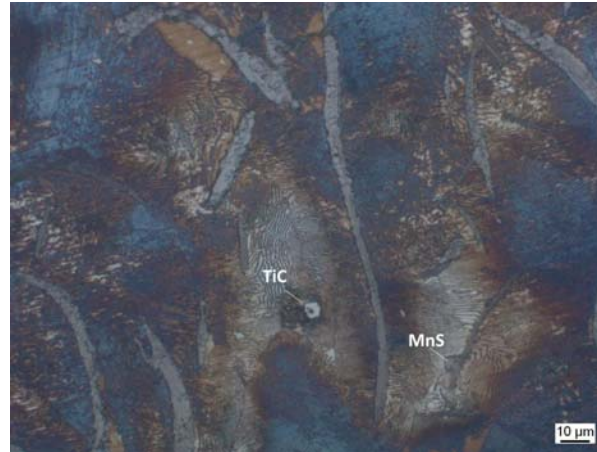
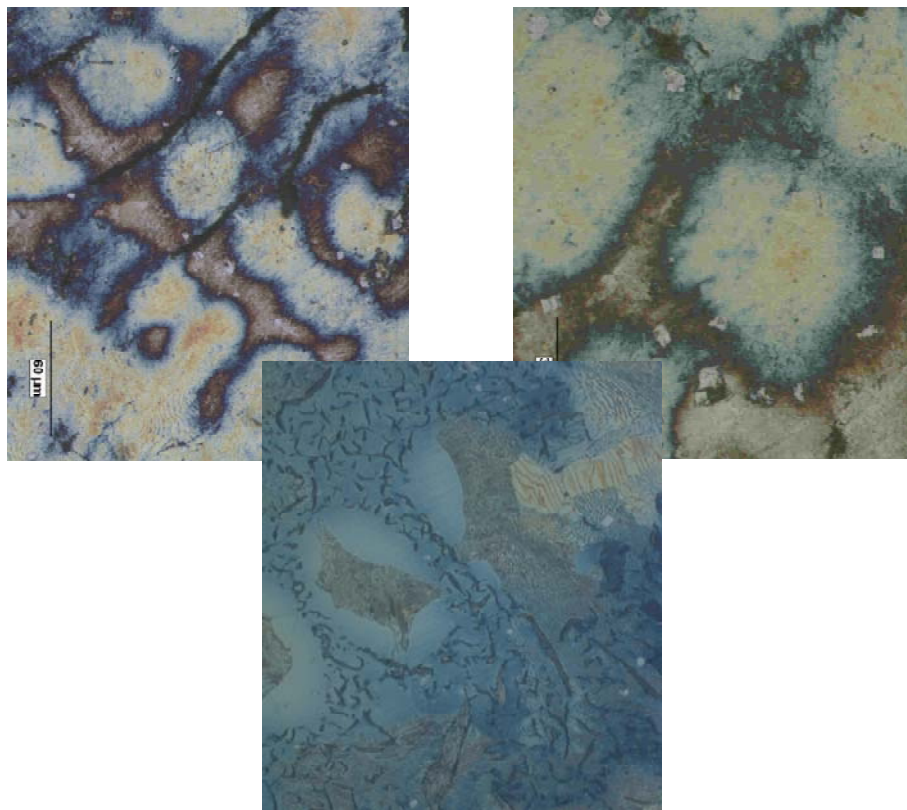


Fig. 5. Color etched micrographs of the sample. 621.1 – 0.018% S, 0.06% Ti at high magnification



a) inclusions in the interdendritic regions

b) inclusions in the interdendritic regions

c) detail of superfine graphite

Fig. 6. Color etched micrographs of the sample. 621.5 – 0.012% S, 0.35% Ti at high magnification

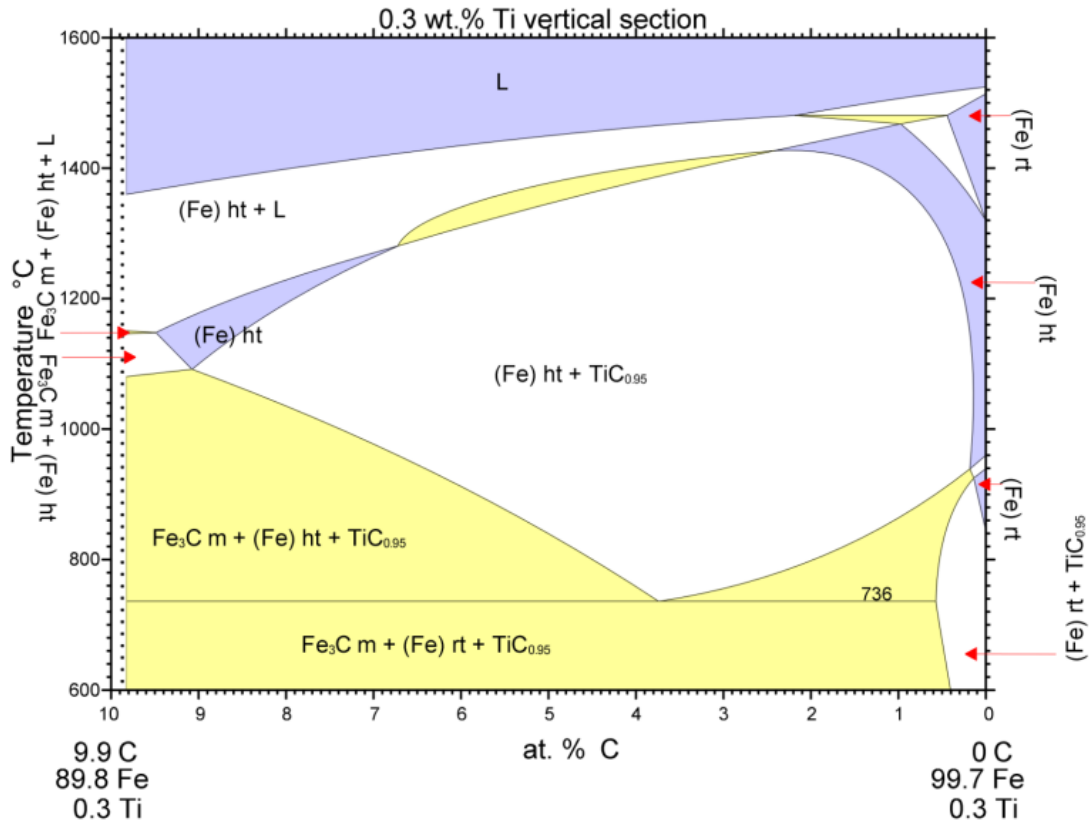


Fig. 7. Section through the Fe-Ti-C ternary phase diagram²⁷

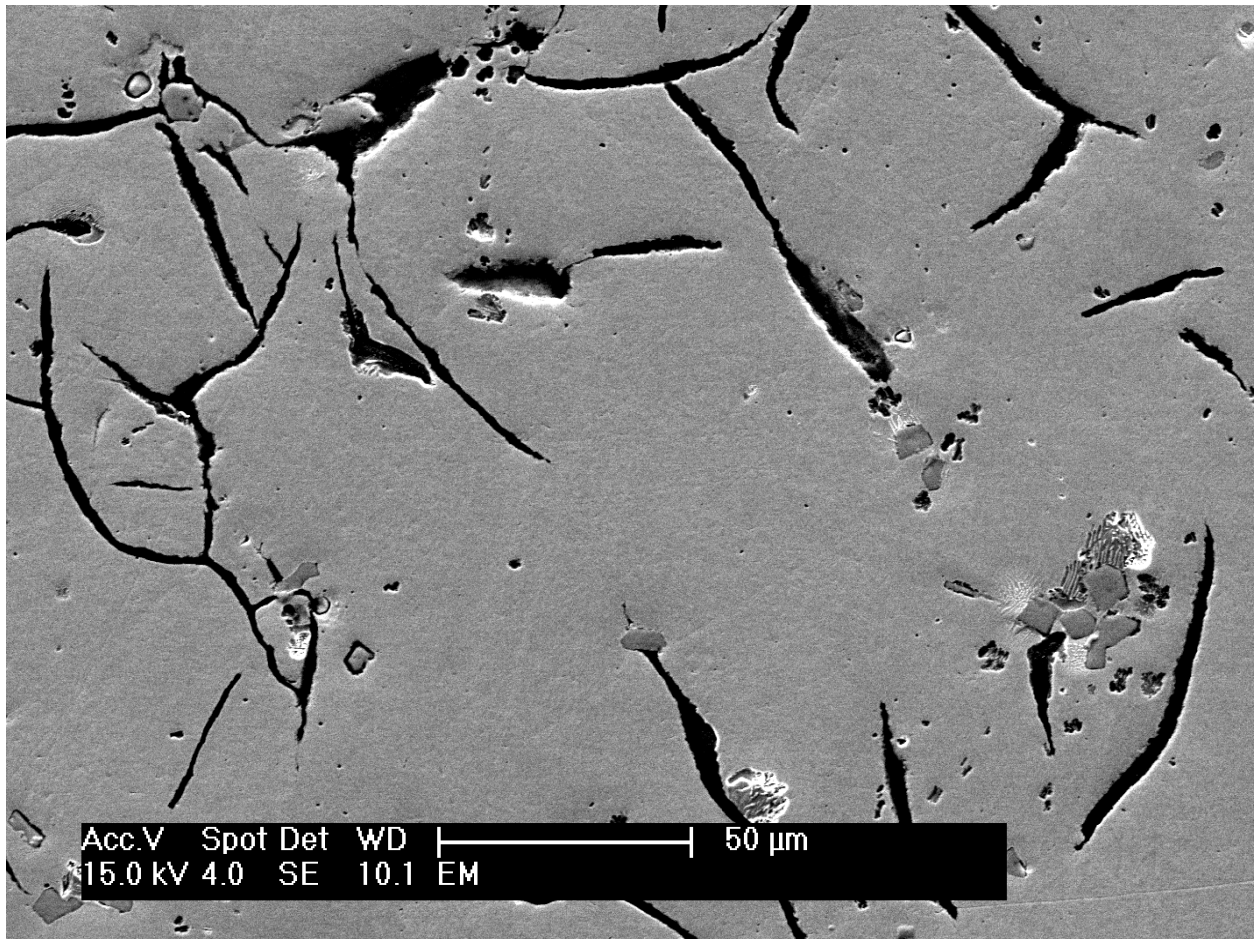


Fig. 8a MnS in contact with graphite

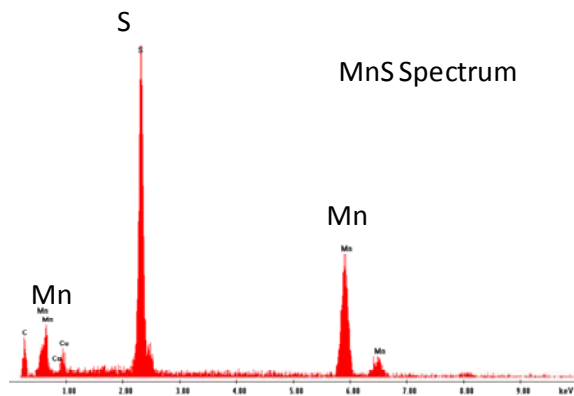
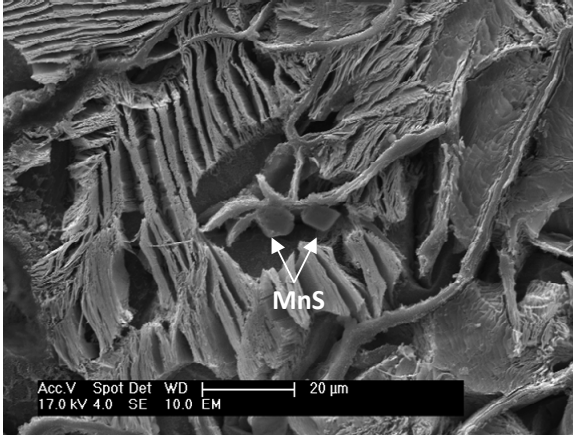


Fig. 8b MnS spectrum

Fig. 8. Unetched sample 401.1- 0.12% S, 0.018% Ti



a) MnS in contact with graphite



b) MnS with oxide nucleus

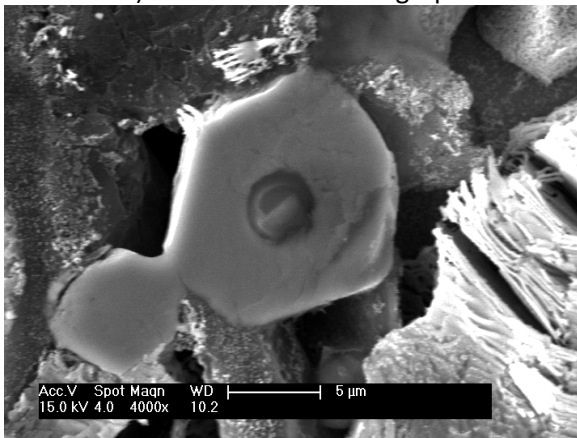


Fig. 9c MnS with oxide nucleus (higher magnification);

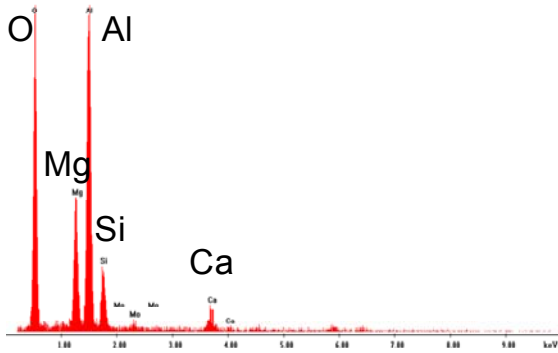


Fig. 9d spectrum of the oxide nucleus

Fig. 9. Sample 401.1 – Deep-etched with Nital 2%

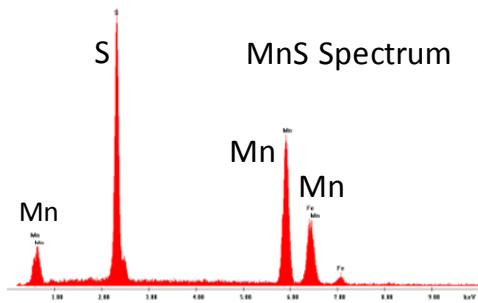
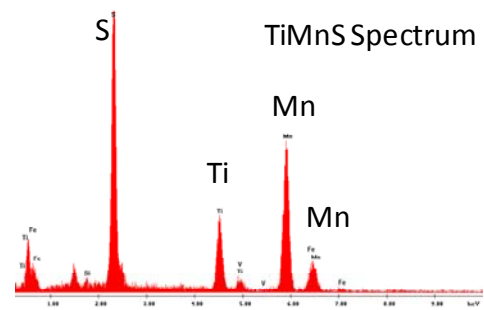
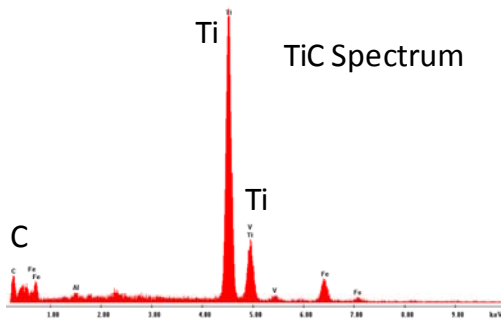
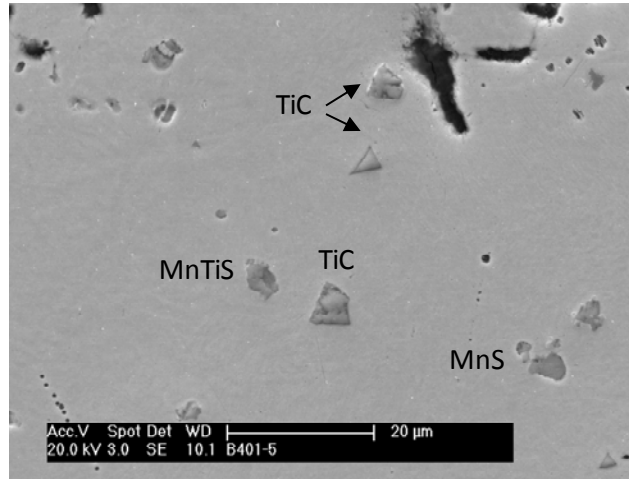
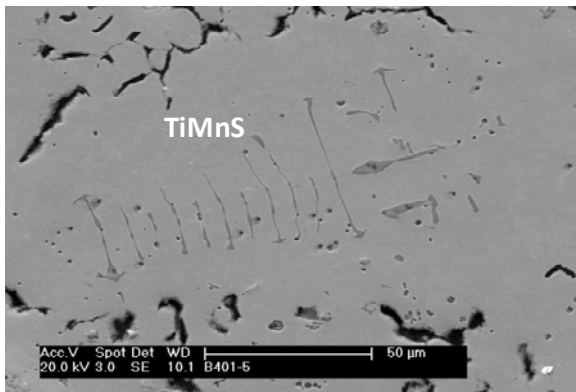
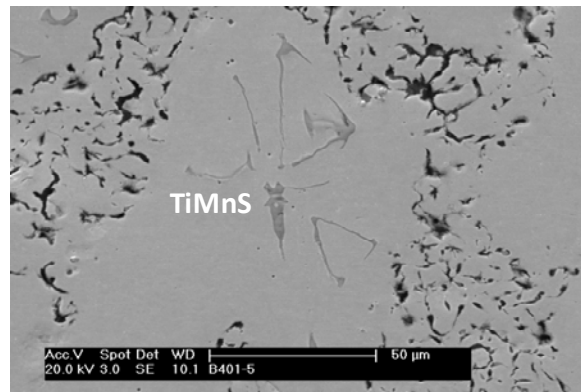


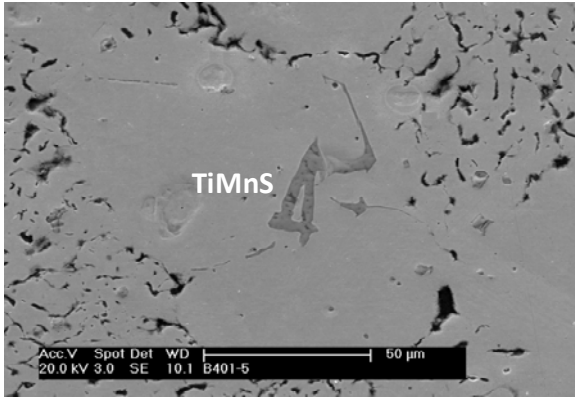
Fig. 10. Unetched sample. 401.5 - 0.120% S, 0.36% Ti



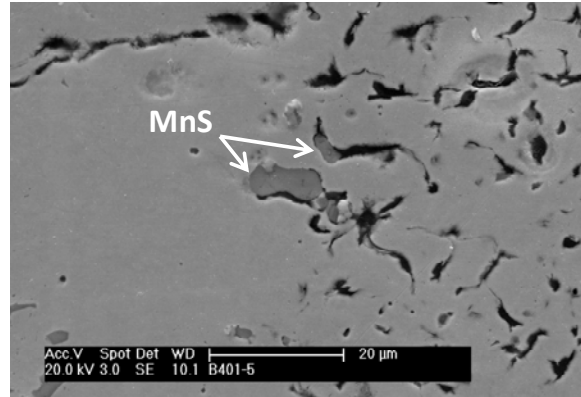
a) (Mn,Ti)S rib-like inclusion



b) (Mn,Ti)S star-like inclusion

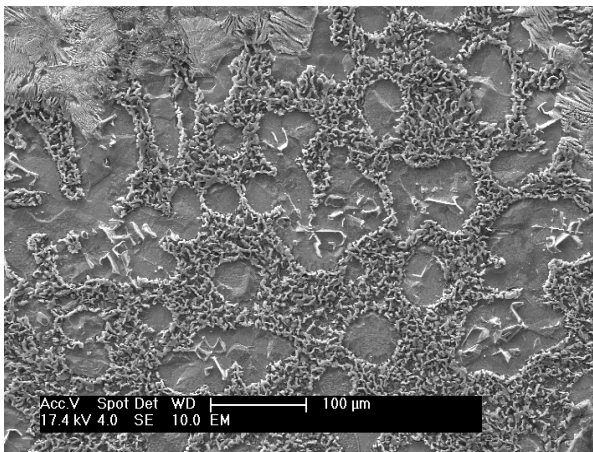


c) (Mn,Ti)S inclusion

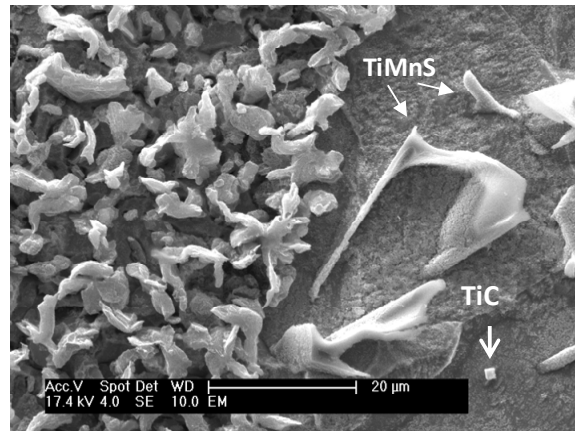


d) MnS inclusions in contact with graphite

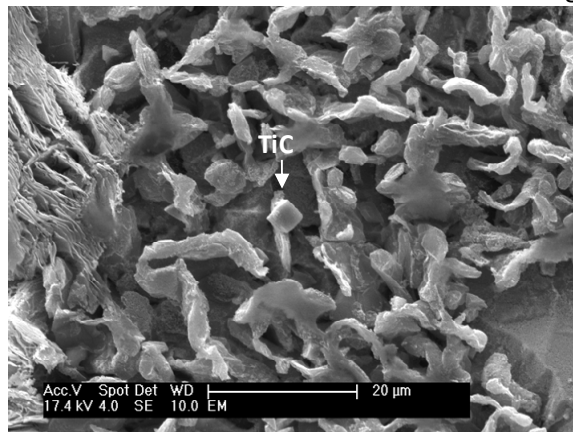
Fig. 11. Unetched SEM micrographs of sample 401.5 showing (Mn,Ti)S and MnS inclusions



a) (MnTi)S inclusions in the austenite dendrites

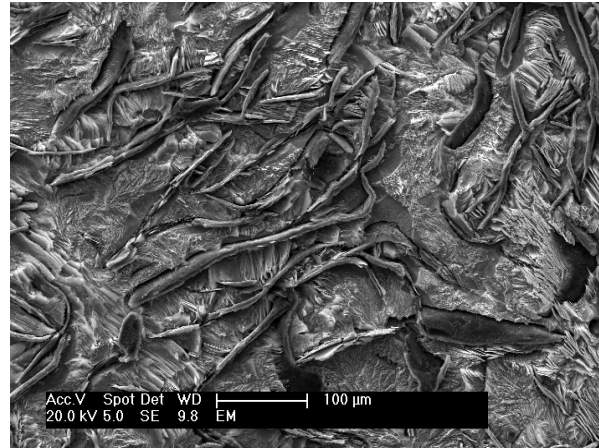


b) (MnTi)S inclusions in austenite (higher magnification)

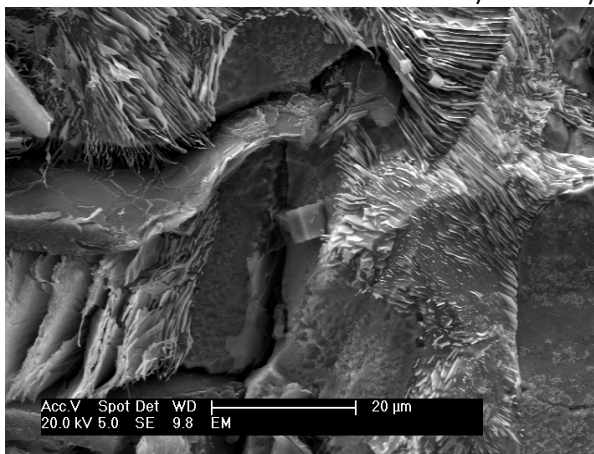


c) Superfine graphite and TiC

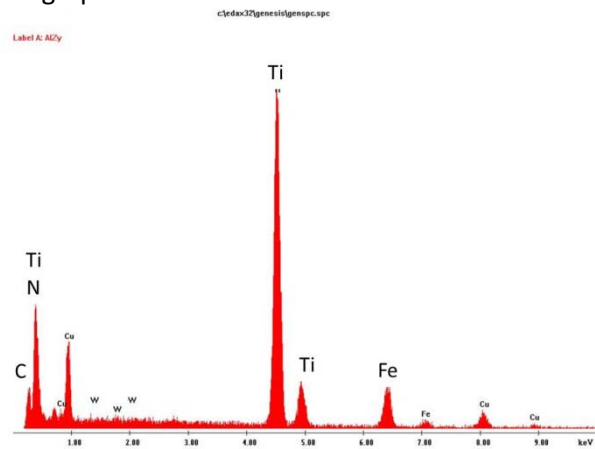
Fig. 12. Deep etched micrographs of sample 401.5 - 0.120%S, 0.36%Ti



a) coarse type-A graphite

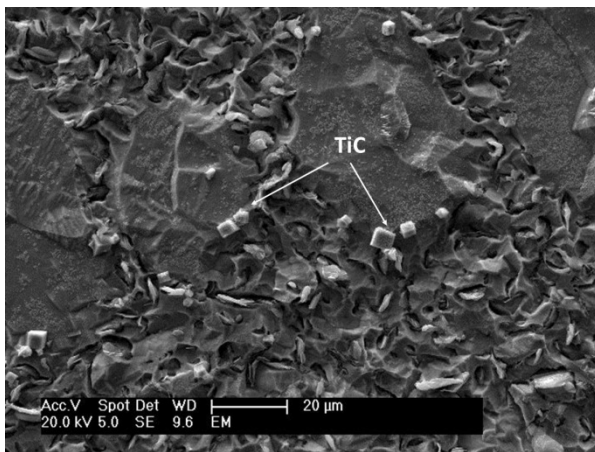


b) Ti carbonitride

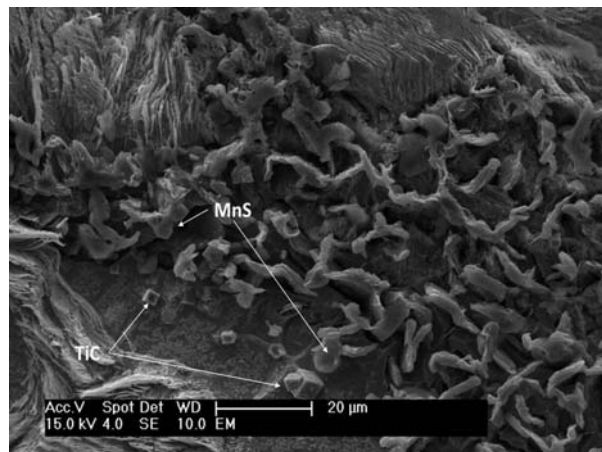


c) spectrum of the carbonitride

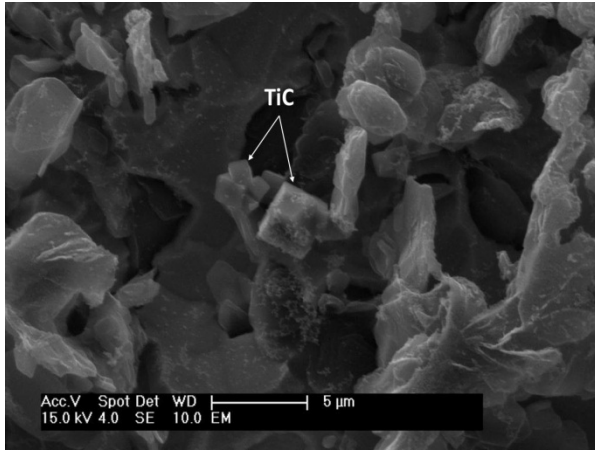
Fig. 13. Deep etched micrographs of sample 621.1 – 0.018%S, 0.06%Ti



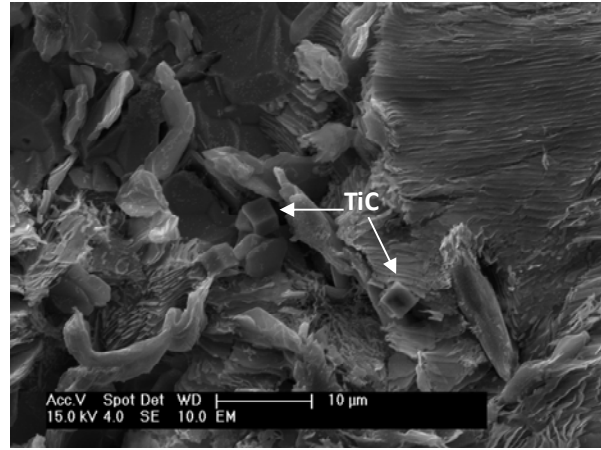
a) TiC at austenite grain boundaries



b) TiC in austenite, MnS on superfine graphite



c) Cluster of small TiC and TiC in contact with superfine graphite



d) Superfine graphite and TiC

Fig. 14. Deep etched micrographs of sample 621.5 - 0.012%S, 0.35%Ti

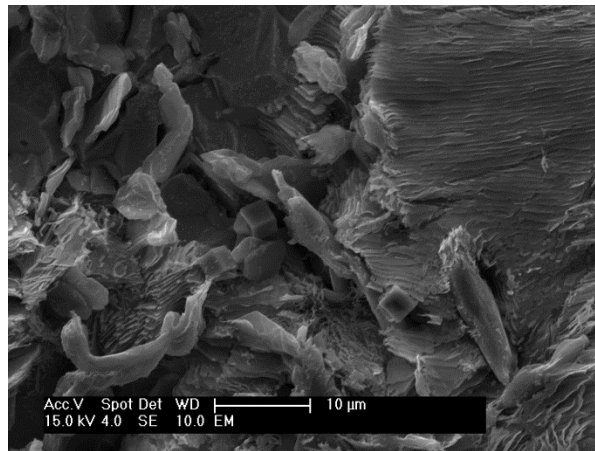


Fig. 15a superfine graphite

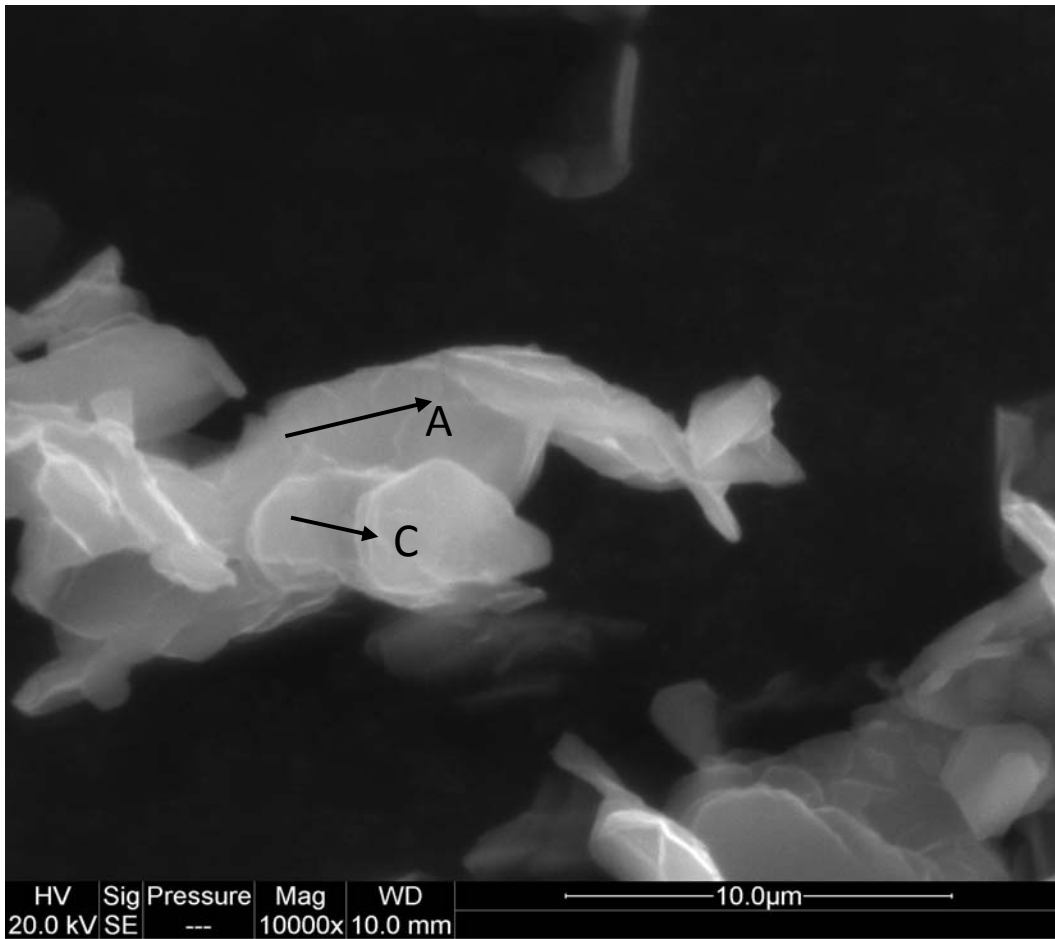


Fig. 15b growth in A- and C-direction

Fig. 15. SEM micrographs of superfine graphite from deep etched sample 621.5

D paper-IV

E. Moumeni, N.S. Tiedje, F.B. Grumsen, H.K. Danielsen, A. Horsewell, J.H. Hattel, “*A TEM Study on the Ti-alloyed grey iron*”, Submitted to the journal of Materials Science and Technology, April 2013

Materials Science and Technology

A TEM Study on Ti-alloyed grey iron

--Manuscript Draft--

Manuscript Number:	
Full Title:	A TEM Study on Ti-alloyed grey iron
Article Type:	Original Research Paper
Keywords:	cast iron, FIB, SEM, TEM, SAD, Dark field and bright field images, Diffraction pattern
Corresponding Author:	Elham Moumeni, PhD student Technical university of Denmark Lyngby, DENMARK
Corresponding Author Secondary Information:	
Corresponding Author's Institution:	Technical university of Denmark
Corresponding Author's Secondary Institution:	
First Author:	Elham Moumeni, PhD student
First Author Secondary Information:	
Order of Authors:	Elham Moumeni, PhD student
	Niels Skat Tiedje, Associate professor
	Flemming Bjerg Grumsen, Laboratory Engineer
	Hilmar Kjartansson Danielsen, PhD
	Andy Horsewell, Professor
	Jesper Henri Hattel, Professor
Order of Authors Secondary Information:	
Abstract:	<p>In this investigation the microstructure of the graphite flakes in titanium alloyed cast iron is studied using electron microscopy techniques. Dual beam SEM/FIB has been used for TEM sample preparation. TEM study has been carried out on graphite flakes in grey cast iron using selected area electron diffraction. Based on the selected area diffraction pattern analysis, crystallographic orientations are identified and compared. The orientation relationship between iron and graphite crystals at the interface is studied and discussed.</p> <p>It is observed that the graphite microstructure in the Ti-containing iron consists of both hexagonal and rhombohedral crystal structures, but there is expansion in the unit cell. The high-Ti and low-Ti specimens are compared and the differences are discussed.</p>
Suggested Reviewers:	Jacque Lacaze, Professor Jacques.Lacaze@ensiacet.fr

A TEM Study on Ti-alloyed grey iron

E. Moumeni, N.S. Tiedje, F.B. Grumsen, H.K. Danielsen, A. Horsewell, J.H. Hattel

Technical University of Denmark, DTU Mechanical Engineering, Kgs Lyngby, Denmark

Abstract

In this investigation the microstructure of the graphite flakes in titanium alloyed cast iron is studied using electron microscopy techniques. Dual beam SEM/FIB has been used for TEM sample preparation. TEM study has been carried out on graphite flakes in grey cast iron using selected area electron diffraction. Based on the selected area diffraction pattern analysis, crystallographic orientations are identified and compared. The orientation relationship between iron and graphite crystals at the interface is studied and discussed.

It is observed that the graphite microstructure in the Ti-containing iron consists of both hexagonal and rhombohedral crystal structures, but there is expansion in the unit cell. The high-Ti and low-Ti specimens are compared and the differences are discussed.

Keywords: cast iron, FIB, SEM, TEM, SAD, Dark field and bright field images, Diffraction pattern

1. Introduction

Alloying elements are responsible for the amount and shape of precipitated graphite in cast iron, as well as for the microstructure of iron matrix and formation of inclusions [1] [2]. Shape, size and distribution of graphite are some of the important parameters that determine the mechanical properties of cast iron [2] [3] [4] and they can be modified by addition of alloy elements. Considerable research has been done to describe the effect of alloy elements on graphitic cast iron. However, the relationship between alloy elements and properties of samples cannot be simplified due to interaction between individual parameters.

Titanium is one of the elements which can significantly affect the shape and size of graphite [5]. Addition of Ti considerably decreases graphite nucleation and growth [6]; it changes the shape and size of graphite to become superfine interdendritic and increases the undercooling [7] [8]. Ti in grey iron increases the tendency of branching in graphite precipitates [9]. It has also been reported that addition of Ti to some extent increases the fraction of primary austenite [8]. Titanium in cast iron melts reacts with sulphur, carbon and manganese. Therefore, it decreases the amount of sulphur available for forming graphite nuclei and for modifying the graphite shape. Sommerfield and Tonn [10] used thermodynamic simulation to show that before the onset of austenite formation, $Ti_4C_2S_2$ will form at 1185C. Nakae and Fujimoto [11] showed that the maximum undercooling (ΔT_{MAX}) and the critical temperature for the A-type to D-type graphite transition (TA/D) increase with the Ti addition. In this work Ti alloyed grey iron has been studied in order to learn the structure of graphite and the orientation relationship between iron and graphite. For this purpose, a comprehensive TEM study is carried out to understand the characteristics of this group of irons including interdendritic superfine graphite.

The crystallographic structure of graphite has been studied by many scientists [12] [13] [14] [15]. It has been suggested that the growth of graphite is mainly determined by the composition of the

1 liquid iron in which the graphite grows during solidification [16]. For the flaky graphite, the growth
2 direction of the graphite lattice is observed to be mainly perpendicular to the graphite–basal planes
3 [3]. In cast irons and natural graphite, crystallographic defects such as stacking faults, twins,
4 various tilt and rotation boundaries have been observed in the graphite structure [17] [18] [19].
5 These defects provide important information on the growth mechanism. It is therefore of great
6 interest to study graphite crystallography in detail to improve our understanding of the growth
7 mechanisms behind graphite growth.
8

9
10 The usual structure of graphite which is hexagonal was proposed by Hull [20] and confirmed by
11 Bernal [21] and Hassel and Mark [22]. It basically consists of basal layers of carbon atoms bonded
12 in a continuous hexagonal network. The layers are stacked ideally in an ABAB sequence but since
13 the layers are relatively widely spaced and bonds are weak they may easily slide or tilt relative to
14 one another. Double and Hellowell [17] suggested that growth mechanism of spheroidal graphite
15 was mainly based on a cone-helix model. They showed the filamentary segments of graphite by
16 optical microscopy. The same authors [12] have also shown that all forms of graphite, precipitating
17 from a metallic solution, must evolve from a basic hexagonal ring structure, and grow into an open
18 monolayer sheet. Subsequent growth of this precursor can lead to a multi-layer sheets-flake
19 graphite crystal, to rolled or wrapped concentric shells spheroidal graphite. They believe that
20 spheroidal graphite is the preferred morphology in a clean melt, while flake graphite is an impurity
21 modified form.
22

23
24
25 Later, lines were reported on X-ray photographs that did not correspond with the hexagonal
26 structure. However, it was possible to index them in terms of a rhombohedral cell using the same
27 continuous hexagonal network but with an ABCABC stacking sequence [23] [24]. A schematic
28 picture of these two models is shown in Fig. 1.
29

30 In the sixties, with improved microscopy techniques, dislocation structure and twins in graphite
31 were observed [23]. In a graphite crystal, with the layers of planes arranged in the hexagonal
32 stacking sequence, the associated stacking fault will create a region with a rhombohedral stacking
33 sequence.
34
35
36
37

38 a) Hexagonal

b) Rhombohedral

39 Fig. 1. Two models for graphite crystal structure (made by the software JEMS [26])
40

41 It is suggested [18] [24] [25] that twinning plays an important role in formation of spheroidal
42 graphite. It is argued that spiral growth along the axis of screw dislocations emerging from the
43 nucleus is responsible for formation of nodular graphite too [26]. Velichko [27] believed that in the
44 crystal of flaky graphite there is intermediate rotation around the c-axis. Amini and Abbaschian
45 [28] proposed a three-stage model for formation of the graphite spheres including: i) basal and
46 prismatic planes leading to isotropic growth, ii) circumferential growth of graphite tiles, and iii)
47 radial growth of pillars.
48

49
50 Several different reactions normally contribute to graphite formation in cast irons. The bulk of the
51 graphite formed by eutectic solidification forms the inner part of the larger particles, while
52 precipitation from austenite and the stable eutectoid reaction deposit the outer layers. Therefore, the
53 remaining iron/graphite interface forms in the solid state [29]. Thus, in order to understand the
54 evolution of the interface, all three phases must be considered.
55

56
57 Ferrite/graphite interfaces in commercial cast irons have been shown to prefer two particular
58 orientation relationships [29]. Both relationships are found in grey and ductile irons. Adsorption of
59
60
61
62

1 impurities at the graphite/liquid interface affects the formation of lamellar graphite. Sulphur and
2 oxygen are found by Scanning Auger Microscopy (SAM) to be adsorbed at the graphite/melt
3 interface during solidification of grey iron [30].The adsorbed elements influence the growth sites
4 on the basal planes and thereby stabilize the interface, resulting in the formation of flakes
5
6

7 **2. Experiments**

8
9 The bulk samples for these experiments are from the low and high-Ti content flaky graphite cast
10 iron. The samples were cast as tensile test specimens. The chemical composition of the samples is
11 presented in Table 1.
12

13 Table 1. Chemical compositions

14 Sample	C	Si	Mn	Ti
15 Low-Ti iron	3.44	2.07	0.54	0.02
16 High-Ti iron	3.45	2.03	0.58	0.35

17
18 In this work a dual beam microscope in which both electron beam and focused ion beam columns
19 are applied is used for TEM sample preparation. The TEM samples were studied using an FEI
20 Tecnai T20 G2 located at DTU-CEN and a JEOL JEM 3000F TEM (300 kV) located at DTU-Risø.
21 The sample preparation was carried out at DTU-CEN using an FEI Helios EBS3 dual beam
22 FIB/SEM microscope.
23
24
25
26

27 2.1. Sample preparation using dual beam (FIB-SEM) instrument

28
29 The dual beam microscope combines a focused ion beam (FIB) column and a scanning electron
30 microscope column in one unit [31]. This combined system enables us to carry out TEM sample
31 preparation, precision cross-sectioning and automated 3D process control. The Ga⁺ ion beam is
32 applied for material removal and imaging, while the electron beam in the SEM column is used for
33 imaging and spectroscopic analysis using generated x-rays detected in the energy dispersive x-ray
34 detector (EDX).
35
36

37 While preparing the TEM sample, it is important that the ion-beam does not pollute it with Ga ions,
38 which can be avoided by low voltage and current cleaning at the final stages of preparation.
39
40
41

42 2.1.1. In-situ ‘lift-out’:

43
44 One of the main advantages of the ‘lift-out’ technique over other sample preparation methods is
45 that most of the time the original bulk sample does not need to be initially prepared itself or only a
46 minor preparation is needed.
47

48 Before starting the sample preparation, one has to decide on the final dimensions of the sample.
49 The final dimensions of the FIB lift-out will depend on several parameters such as the dimensions
50 of the final sample; the analysing method that will be applied to study the lift-out specimen (the
51 TEM samples for this work were thinned down to about 80-130nm), the size of the features of
52 interest and the FIB milling time available.
53
54

55 Most FIB lift-outs begin with using the ion beam assisted chemical vapour deposition (CVD)
56 process to deposit a 0.5-2 μm thick platinum metal line onto the specimen surface (Fig. 2.a). The
57 platinum line may be used to mark the region of interest, and to protect the underlying region from
58 being sputtered away during subsequent milling steps. Next, high beam currents with
59
60
61

1 correspondingly large beam sizes are used to mill large amounts of material away from the front
2 and back portion of the region of interest (Fig. 2.b). The front and back trenches are usually
3 positioned about 0.5 μm from the Pt layer. Once the specimen reaches a thickness of about 1 μm
4 due to the FIB milling at the both sides, it is tilted 45° or more with respect to the ion beam. Then,
5 the remaining edges of the specimen are cut free. The Omniprobe manipulator, which is used to
6 handle the sample, is positioned to touch the FIB-milled sample foil. The FIB is then used to attach
7 the Omniprobe to the sample by deposition of Pt using the FIB's CVD and the sample will be lifted
8 out by manipulating the Omniprobe (Fig. 2.c). Then, the Omniprobe/sample assembly is positioned
9 onto a grid and the CVD operation is again used to attach the sample to the grid. The sample will
10 then be FIB milled to electron transparency using lower voltage and low beam density FIB milling
11 practices (Fig. 2.d).
12
13
14

- | | | |
|----|-----------------------------------------|-----------------------------------------|
| 15 | | |
| 16 | a) Pt deposition (First high-Ti sample) | b) Milling the material away from the |
| 17 | | front and back portion of the region of |
| 18 | | interest |
| 19 | | |
| 20 | | |
| 21 | c) Sample, attached to the Omniprobe, | d) TEM image of the sample prepared |
| 22 | lifted out of the bulk material | for TEM study at low magnification. |
| 23 | | |
| 24 | | |

25 Fig. 2. In-situ lift-out sequences
26
27
28
29

30 2.2. TEM investigation 31

32
33 Transmission electron microscopy (TEM) is one of the important techniques for studying
34 microstructure at the very small scales (down to nano-) in great detail. Using TEM, we look
35 through a piece of material with electron beams, usually at high magnification (in our experiments
36 up to 30000x). The techniques that we have applied in this work are bright field (BF) and dark field
37 (DF) imaging and selected area electron diffraction patterns (SAED).
38

39 In bright field imaging, electrons pass through the specimen and they can be scattered or absorbed
40 by the specimen and at suitable specimen orientations can undergo Bragg diffraction. An image
41 created by electrons from the direct beam is called a bright-field image. If a diffracted beam is used
42 it will create a dark-field image [32]. With dark field images, specific crystallographic planes that
43 are oriented such that they are diffracting, and can be viewed in order to see specific features such
44 as dislocations, regions of ordering or strain fields etc. Dark field images typically have
45 considerably higher contrast than bright field images although the overall intensity is greatly
46 reduced. The beam can be moved relative to the objective aperture so that either electrons that have
47 gone directly through the sample are viewed (BF) or so that electrons diffracted by specific
48 crystallographic planes go through it (DF).
49

50
51 Diffraction contrast arises because the intensity of the diffracted beams depends on the orientation
52 of the diffracting planes in different regions of the specimen. Also, local variations in orientation
53 around defects cause local changes in Bragg conditions, allowing us to identify types of defects
54 within crystals. From diffraction patterns we can 1) measure the spacing between crystal layers; 2)
55 determine the orientation of a single crystal or grain; 3) find the crystal structure of an unknown
56 material and 4) measure the size, shape and internal stress of small crystalline regions.
57
58
59
60
61
62
63
64
65

1 **3. Results and discussion**

2
3
4 3.1. TEM imaging

5
6 The TEM bright field imaging was carried out to get an overview of the graphite microstructure.
7 The low-Ti and high-Ti samples were investigated to find their overall differences and similarities.
8 The sampling areas of interest are depicted in Fig. 2a and Fig. 3. The low-Ti TEM sample is taken
9 from a relatively coarse flake longitudinally. Thus, it does not include any graphite/iron interface.
10 The high-Ti samples include the graphite/iron interface. This has enabled us to study the
11 orientation relationships between two phases.
12

13 In Fig. 4, Fig. 5 and Fig. 6 some of the bright field images of the above mentioned samples are
14 shown. In the Fig. 4a from the low-Ti sample, a long grain (more than 1 μm) of graphite can be
15 seen. The high-Ti samples have finer microstructure. The twin boundaries can be seen in the Fig.
16 4b and they outline the very fine grains indicating that twinning plays an important role in the
17 growth of the graphite lamellae.
18
19
20
21
22

23 a) Low-Ti sample b) Second high-Ti sample

24 Fig. 3. Sampling area of the TEM specimens.

25
26
27
28 a) Low-Ti sample, large graphite grains b) High-Ti sample, graphite/iron grains

29 Fig. 4. TEM bright field images

30
31 The lamella, part of which is shown in Fig. 5, includes a longitudinal cross section of graphite and
32 its interface with the iron matrix from both sides. The high disorder in the microstructure is seen in
33 this area. In the high-Ti samples, a larger number of voids and defects is found too. The platelets
34 of graphite are predicted to have weak and brittle attachment to each other. The cracks or voids
35 which are seen in Fig. 5 may occur during the growth of the graphite or during TEM sample
36 preparation. Considering the fact that graphite is a very brittle material, one could say that the
37 fractures or voids in the crystals would happen during solidification as stresses caused by cooling
38 and growth of the solid phase imposes stresses on the graphite which may deform and break.
39

40 Twinning seems to be one of the main mechanisms of the anisotropic growth of this type of
41 graphite which has happened at high undercooling (Fig. 6). These are seen as simple planar
42 interfaces, often with parallel twin boundaries. One possibility is that growth of the precipitated
43 graphite could also be determined or facilitated by some form of repeated crystal twinning.
44
45
46
47
48
49
50

51 a) High-Ti sample, voids and defects b) High-Ti sample, the marked area in fig 7a

52 Fig. 5. High-Ti sample, bright field imaging

53
54
55
56
57 Fig. 6. High-Ti samples, bright field image

1 A detailed crystallographic analysis was done on the samples. Diffraction patterns were taken in
2 several different areas to analyse grain boundaries and coherency between the two phases. The
3 Kikuchi lines in the iron structure close to the interface of iron/graphite were followed when tilting
4 the sample in order to find the major zone axes of iron. Kikuchi patterns in the graphite areas were
5 not clear enough for this method. SAED patterns were acquired in both iron and graphite at either
6 side of the interface at the iron zone axes. When doing SAED on the graphite, diffraction patterns
7 belonging to both the rhombohedral and hexagonal crystal structure of graphite were found. The
8 graphite structure was found to consist of several elongated grains which had similar but slightly
9 different orientation relationships. Some of the grains had a rhombohedral crystal structure and the
10 orientation of these grains was similar to the hexagonal grains, the (001) planes being almost
11 parallel. There was no specific orientation relationship between the iron and the investigated
12 graphite grains, but since the orientation relationship between the graphite grains themselves varied
13 slightly, perhaps some of them do correlate with the iron crystal structure.

14 In order to identify the grains belonging to hexagonal and rhombohedral crystal structures, dark
15 field imaging technique was applied. The graphite structure in the high-Ti samples was found to be
16 expanded considerably in the “c” direction, that is the (001) interplanar spacings were larger than
17 expected. The value of expansion varies in different areas; the expansion measured in the
18 diffraction pattern images was up to 8% in the “c” direction. The expansion in the “a” direction,
19 along (001) planes, was significantly lower at below 3%. The expansion was not found in the low-
20 Ti specimens. Interstitial Ti atoms in the graphite structure were thought to be a possible reason for
21 this expansion, but in fact no titanium was detected in the graphite areas by EDS. It can be
22 speculated that the many defects in the graphite crystal structure such as stacking faults might
23 cause the expansion in the high-Ti samples, too.

24 Fig. 7 shows an area with three different diffraction patterns. Pattern 1 belonging to the
25 rhombohedral unit cell while patterns 2 and 3 belong to the hexagonal unit cell. The dark field
26 images show that the rhombohedral grain is very elongated and has a very straight interface with
27 both hexagonal grains on either side of it.

28
29
30
31
32
33
34
35
36
37
38
39
40 a) b) c)
41
42 d) e) f)

43 Fig. 7. a) SAED pattern of the shown area in the bright field image (b) contains three different
44 diffraction patterns (indexed in image d). Dark field imaging was carried out on each of the
45 patterns (c, e & f).
46
47
48

49 Fig. 8 shows an area with many smaller grains where the diffraction pattern (not in zone axis)
50 shows a ring pattern with clear preferred orientations. This indicates that the graphite grains have
51 some preferred orientations to each other, but do not have completely the same orientation. Some
52 diffraction from iron is also visible in the pattern as single spots, not ring patterns.
53
54
55
56
57
58
59
60
61
62
63
64
65

1
2 a) b) c)
3
4 d) e) f)
5

6 Fig. 8. TEM images of ferrite/graphite interface: a) the bright field image (BF) shows the region that the
7 diffraction pattern (SAED) is taken from (b). Dark field imaging (DF1 - 4) ; c) area 1 originates from the iron
8 matrix while d, e, f) are from diffraction spots 2, 3 & 4 from the graphite.
9

10 11 12 13 **4. Conclusions**

14 The graphite particles in Ti-containing cast iron were investigated and found to consist of many
15 small grains which have slightly different orientation relationships. Most of these grains have a
16 hexagonal crystal structure, but a few of them have a rhombohedral crystal structure. There seems
17 to be a good correlation between the orientation of two crystal structures, the (001) planes being
18 almost parallel. There did not seem to be any specific orientation relationship between the
19 investigated graphite grains and the iron matrix.
20
21
22

23 **5. Acknowledgements**

24 The authors would like to thank the “Center for electron nanoscopy” at the Technical University of
25 Denmark for their technical and scientific support.
26
27
28
29
30

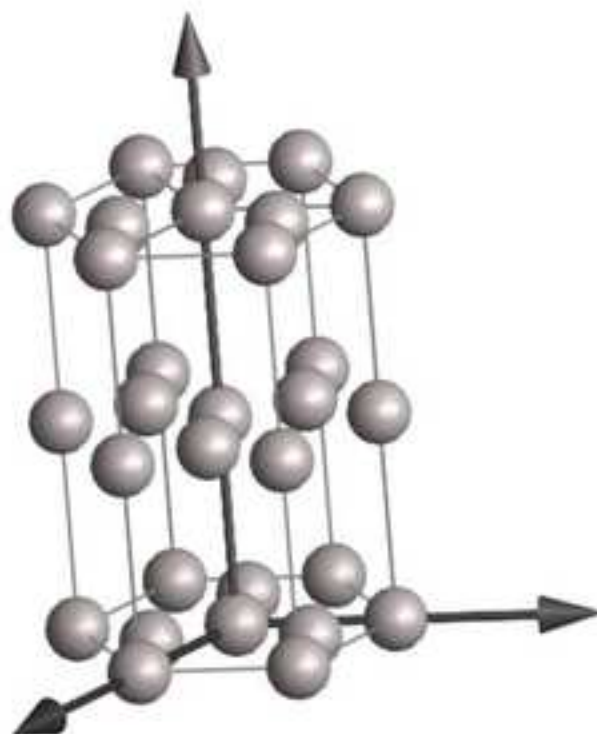
31 **6. References**

- 32
33
34
35
36
37
38 [1] ASM Handbook, Volume 1, Properties and Selection: Irons, Steels, and High-Performance
39 Alloys.
40 [2] N. Tiedje, "Solidification, processing and properties of ductile cast iron," *Materials Science*
41 *and Technology*, vol. 26, no. 10, pp. 505-514, 2010.
42 [3] A. Velichko, A. Wiegmann and F. Mücklich, "Estimation of the effective conductivities of
43 complex cast iron microstructures using FIB-tomographic analysis," *Acta Materialia*, vol. 57,
44 no. 5023–5035, 2009.
45 [4] A. Hatton, M. Engstler, P. Leibenguth and F. Mücklich, "Characterization of graphite crystal
46 structure and growth mechanisms using FIB and 3D image analysis," *Advanced Engineering*
47 *materials*, vol. 13, no. 3, pp. 136-144, 2011.
48 [5] Y. Lerner, "Titanium in the rapidly cooled hypereutectic gray iron," *Journal of materials*
49 *engineering and performance*, vol. 12, no. 2, p. 141, 2003.
50 [6] N. Valle, K. Theuwissen, J. Sertucha and J. Lacaze, "Effect of various dopant elements on
51 primary graphite growth," *Mater. Sci. Eng.*, vol. 27, 2011.
52 [7] P. Larrañaga, J. Sertucha, A. Loizaga, R. Suárez and D. Stefanescu, "Gray Cast Iron with High
53 Austenite-to-Eutectic Ratio Part II – Increasing the Austenite-to-Eutectic Ratio through
54 Inoculation," *Modern Casting*, no. March, 2012.
55 [8] P. Larrañaga, J. Sertucha, A. Loizaga, R. Suárez and D. Stefanescu, "Gray Cast Iron with High
56
57
58
59
60
61
62
63
64
65

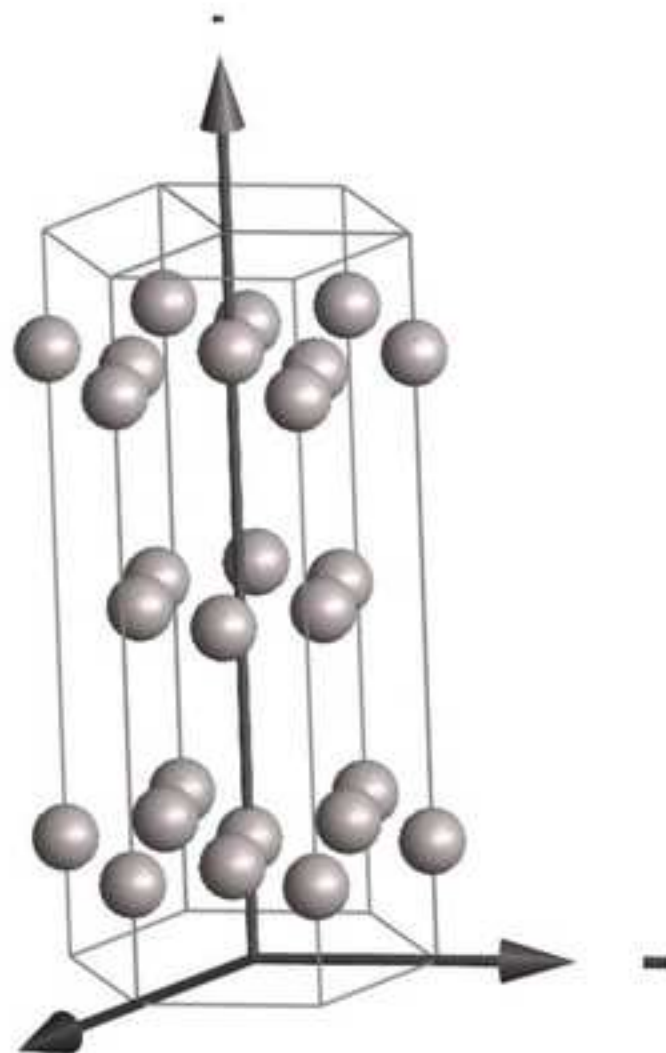
- 1 Austenite-to-Eutectic Ratio Part III - High Strength, Low Hardness, High Carbon Equivalent
2 Gray Iron with Superfine Graphite," *Modern Casting*, no. March, 2012.
- 3
4 [9] M. Chisamera, I. Ripoșan, S. Stan, G. Grasmò and D. Wilkinson, "Preconditioning of
5 electrically melted grey cast irons," *U.P.B. Sci. Bull., Series B*, vol. 71, no. 3, 2009.
- 6 [10] A. Sommerfeld and B. Tonn, "Theory of graphite nucleation in lamellar graphite cast iron," in
7 *The Carl Loper cast iron symposium*, Madison, WI USA, 2009.
- 8 [11] H. Nakae and K. Fujimoto, "Influence of Ti on Graphite Morphological Transition in Flake
9 Graphite Cast Iron," *Key Engineering Materials*, vol. 457, pp. 25-30, 2011.
- 10 [12] D. Double and A. Hellawell, "The nucleation and growth of graphite - The modification of
11 cast iron," *Acta metallurgica materialia*, vol. 43, no. 6, pp. 2435-2442, 1994.
- 12 [13] N. Llorca-Isern, J. Tartera, M. Espanol, M. Marsal, G. Bertran and S. Castel, "Internal features
13 of graphite in cast irons. Confocal microscopy: useful tool for graphite growth imaging,"
14 *Micron*, vol. 33, no. 4, pp. 357-64, 2002.
- 15 [14] A. Velichko, C. Holzapfel and F. Mücklich, "3D Characterization of Graphite Morphologies in
16 Cast Iron," *Advanced Engineering Materials*, vol. 9, no. 1-2, 2007.
- 17 [15] M. Baihe, F. Keming and B. Weimin, "On The Microstructure of Graphite Spherulites in Cast
18 Irons by TEM and HREM," *Acta metall. mater.*, vol. 38, p. 2167, 1990.
- 19 [16] J. Tartera, N. Llorca-Isern, M. Marsal and J. Rojas, "Similarities of nucleation and growth of
20 spheroidal and compacted graphite," *Int. Journal of Cast Metals Research*, vol. 16, p. 131,
21 2003.
- 22 [17] D. Double and A. Hellawell, "Cone-helix growth forms of graphite," *Acta Metallurgica*, vol.
23 22, pp. 481-466, 1974.
- 24 [18] J. Mounchoux, C. Verdu, G. Thollet, A. Reynaud and R. Fougères, "Morphological changes of
25 graphite spheroids during heat treatment of ductile cast irons," *Acta mater.*, vol. 49, p. 4355-
26 4362, 2001 .
- 27 [19] W. Bian, Keming Fang, M. H. Fan, B. Miao and D. North Wood, "Structure and growth of
28 platelets in graphite in graphite spherulites in cast iron," *Journal of Materials Science*, vol. 29,
29 pp. 255-261, 1994.
- 30 [20] A. W. Hull, "A New Method of X-Ray Crystal Analysis," *Phys. Rev.*, vol. 10, no. 2, p. 661-
31 696, 1917.
- 32 [21] J. D. Bernal, "The Structure of Graphite," *Proceedings of the Royal Society of London, Series*
33 *A*, vol. 106, pp. 749-773, 1924.
- 34 [22] O. Hassel and H. Mark, *Z. Phys.*, vol. 25, p. 317, 1924.
- 35 [23] I. Minkoff, *Physical Metallurgy of Cast Iron*, Wiley, Chichester, 1983.
- 36 [24] F. Laves and Y. Baskin, "On the Formation of the Rhombohedral Graphite Modification,"
37 *Zeitschrift für Kristallographie - Crystalline Materials*, vol. 107, no. 5-6, pp. 337-356, 1956.
- 38 [25] E. Freise and A. Kelly, "The deformation of graphite crystals and the production of the
39 rhombohedral form," *Philosophical Magazine*, vol. 8, no. 93, pp. 1519-1533, 1963.
- 40 [26] P. Stadelmann, "JEMS reference," CIME-EPFL, CH-1015 Lausanne, 2004. [Online].
41 Available: <http://cimewww.epfl.ch/people/stadelmann/jemsWebSite/jems.html>.
- 42 [27] B. Miao, K. Fang, W. Bian and G. Liu, "On the microstructure of graphite spherulites in cast
43 irons by TEM and HREM," *Acta metall mater.*, vol. 38, no. 11, pp. 2167-2174, 1990.
- 44 [28] K. Theuwissen, M. Lafont, L. Laffont, B. Viguièr and J. Lacaze, "Microstructural
45 Characterization of Graphite Spheroids," *Transactions Indian Institute of Metals*, vol. online,
46 2012.
- 47 [29] S. Zhang, "Mechanism of the forming of nodular graphite," *Mater. Sci. Technol.*, vol. 16, no.
48 6, p. 615, 2000.
- 49
50
51
52
53
54
55
56
57
58
59
60
61
62
63
64
65

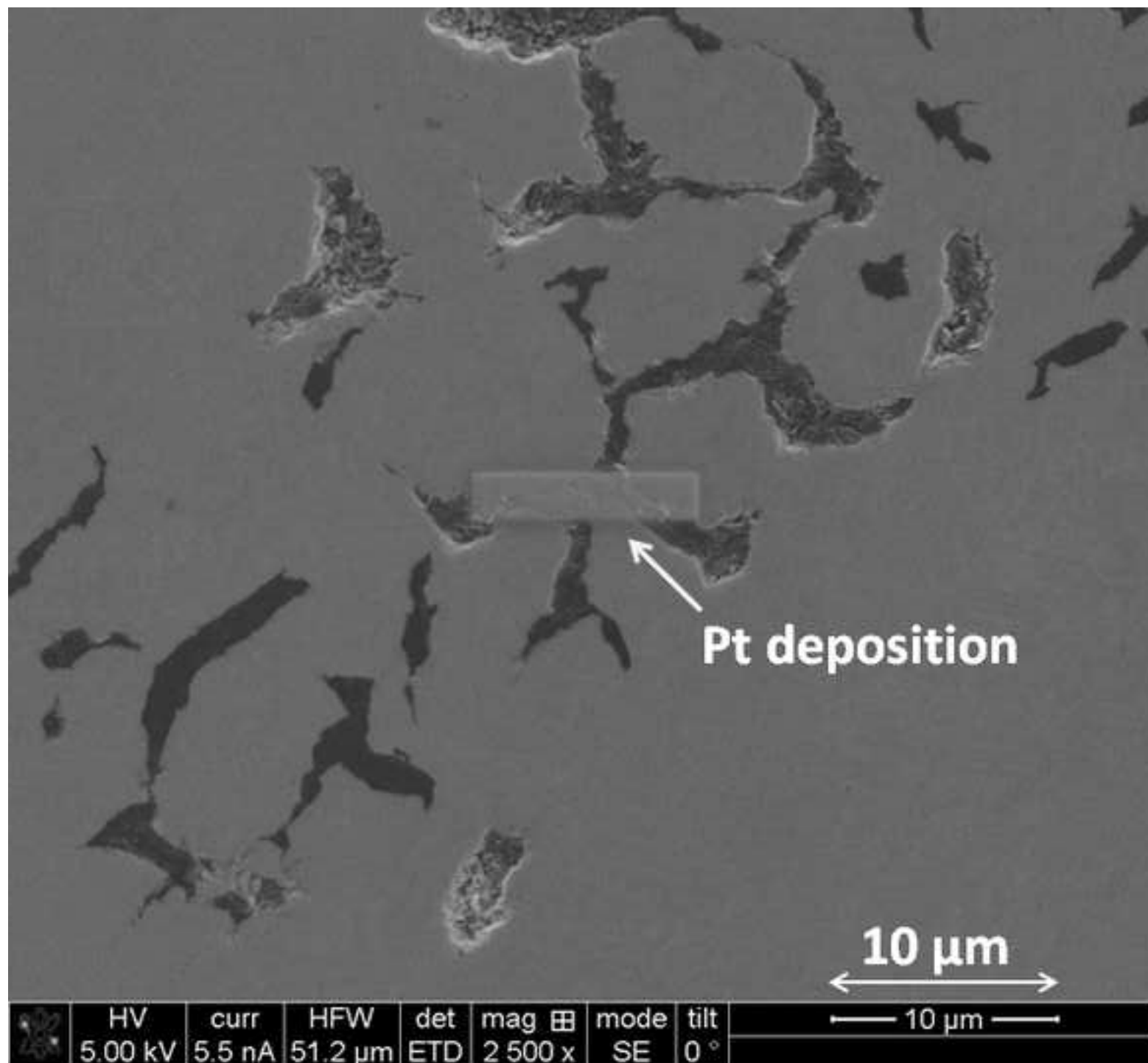
- 1 [30] A. Velichko, "Quantitative 3D Characterization of Graphite Morphologies in Cast Iron using
2 FIB Microstructure Tomography," in *PhD Thesis*, 2008.
- 3 [31] S. Amini and R. Abbaschian, "Nucleation and growth kinetics of graphene layers from a
4 molten phase," *Carbon*, vol. 51, no. January , p. 110–123, 2013.
- 5 [32] Sooho Kim and D. Phillips, "Orientation relationships in graphitic cast irons," *Metallurgical
6 Transactions A*, vol. 18A, pp. 1907-1913, 1987.
- 7 [33] W. Johnson and H. Smartt, "The Role of Interphase Boundary Adsorption in the Formation of
8 Spheroidal Graphite in Cast Iron," *Metallurgical Transactions A*, vol. 8A, pp. 553-565, 1977.
- 9 [34] A. Lucille and A. Giannuzzi, "Introduction to focused ion beam," North Carolina State
10 University, 2005, pp. 247-268.
- 11 [35] D. B. Williams and C. B. Carter, *Transmission electron microscopy*, Springer, 2009.
- 12
13
14
15
16
17
18
19
20
21
22
23
24
25
26
27
28
29
30
31
32
33
34
35
36
37
38
39
40
41
42
43
44
45
46
47
48
49
50
51
52
53
54
55
56
57
58
59
60
61
62
63
64
65

[Click here to download high resolution image](#)

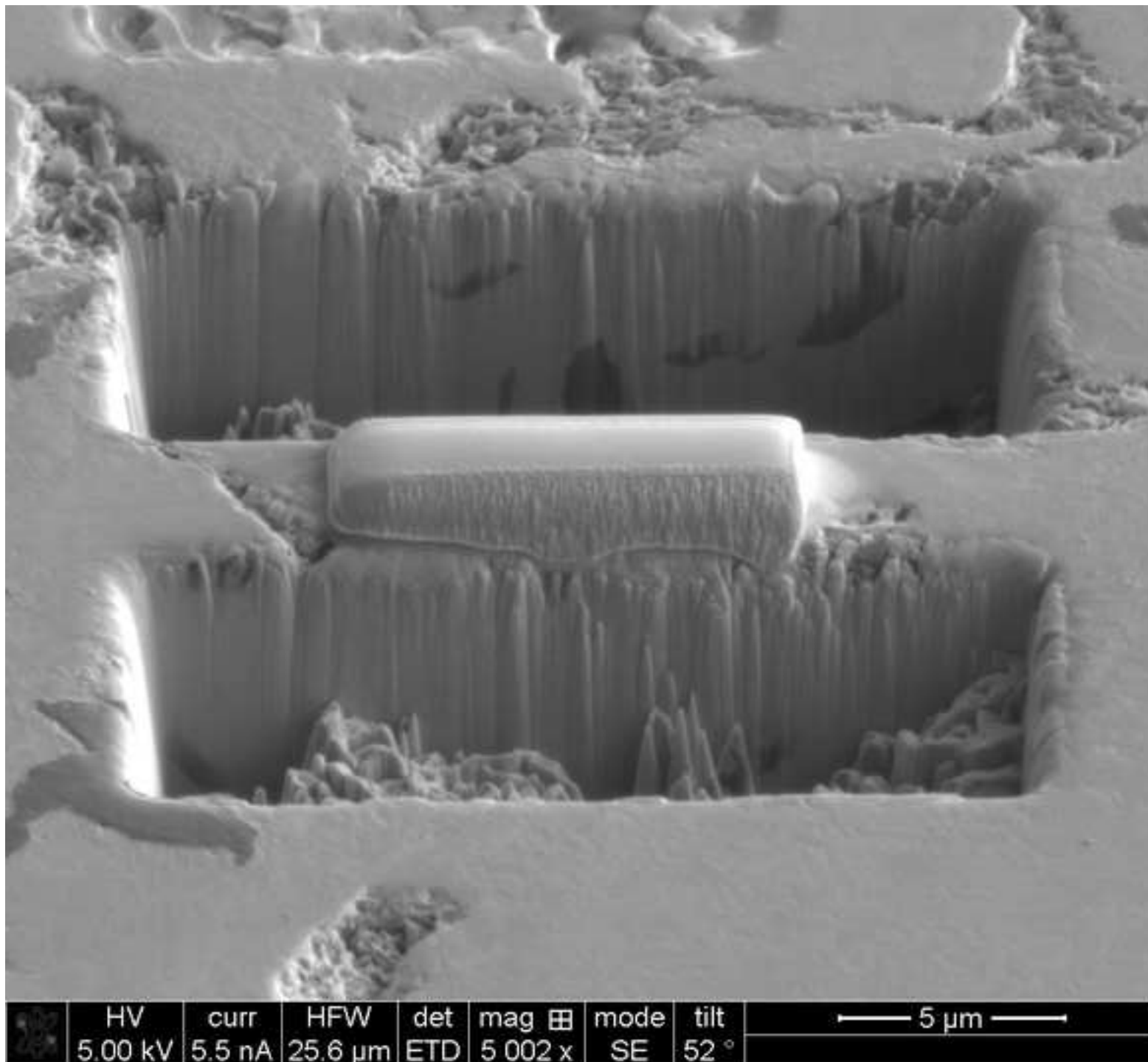


[Click here to download high resolution image](#)

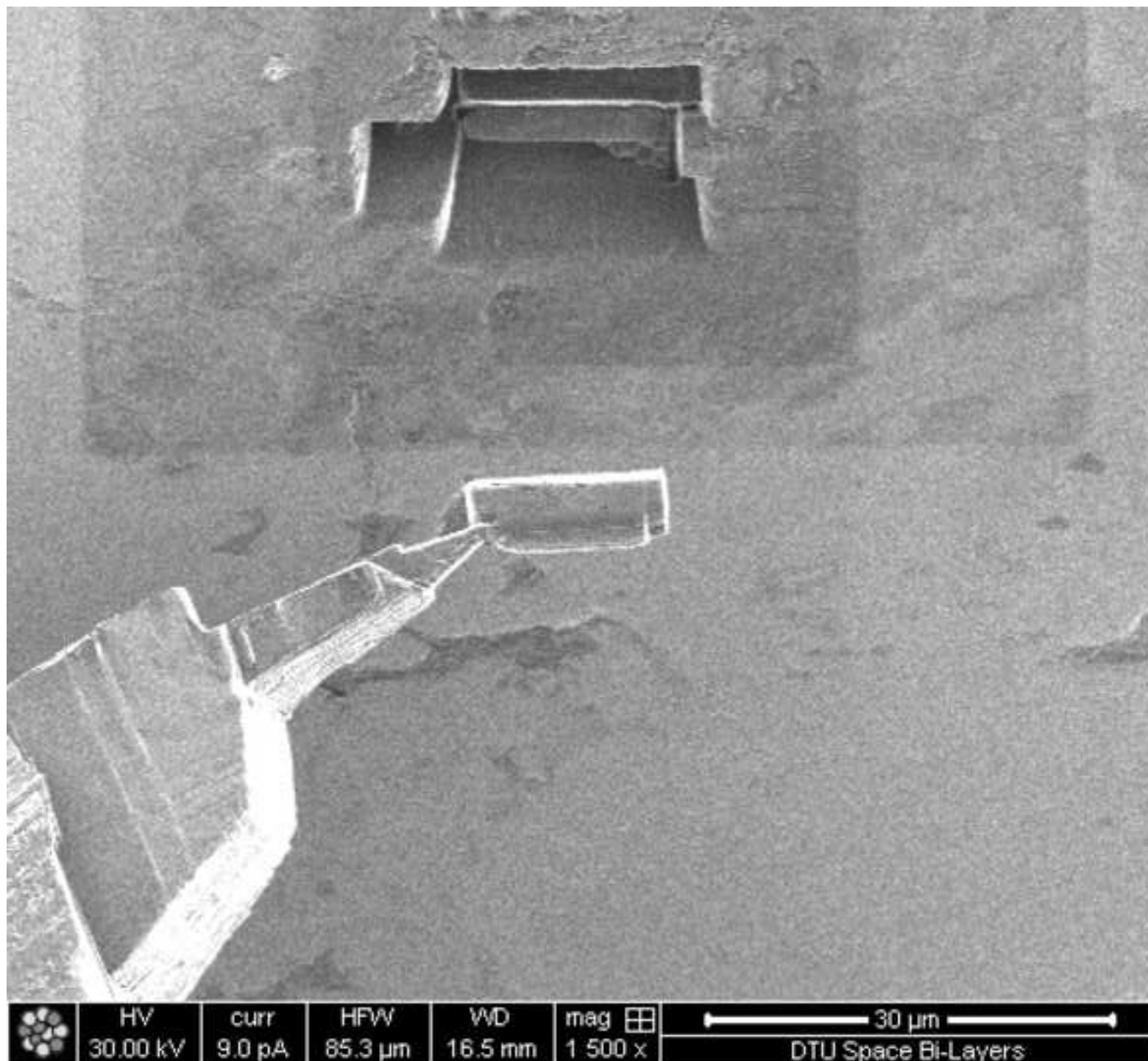


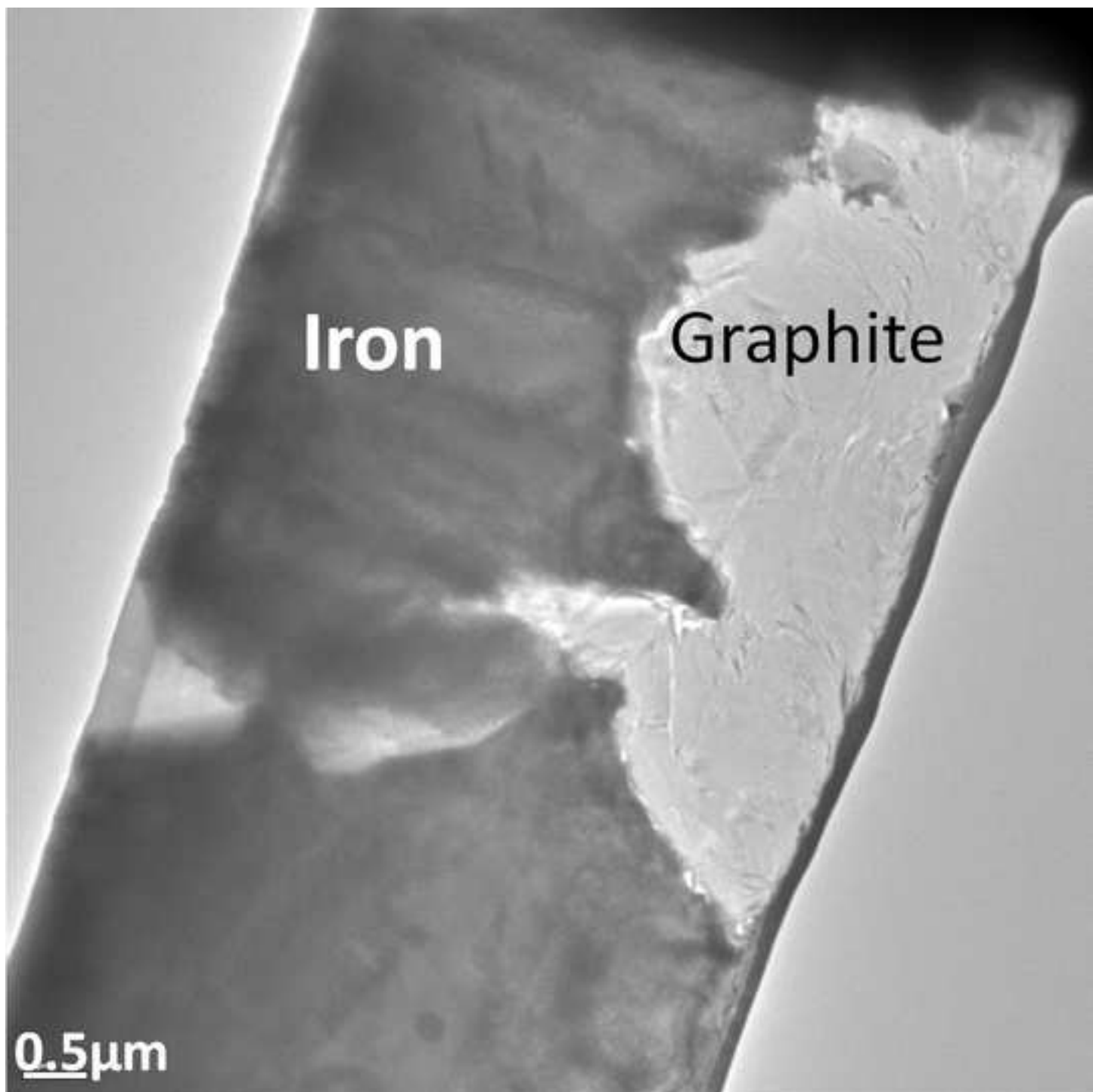


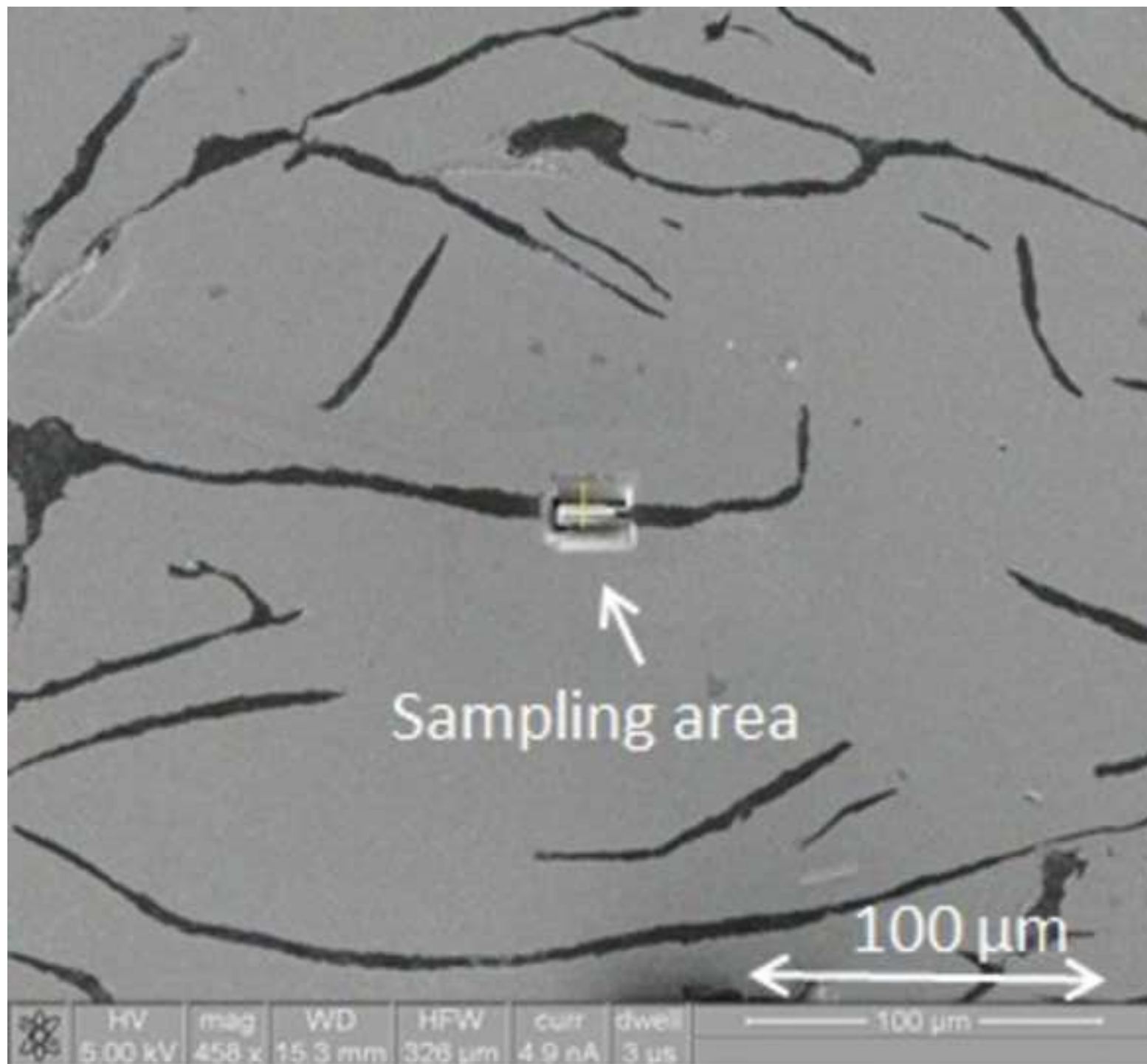
[Click here to download high resolution image](#)

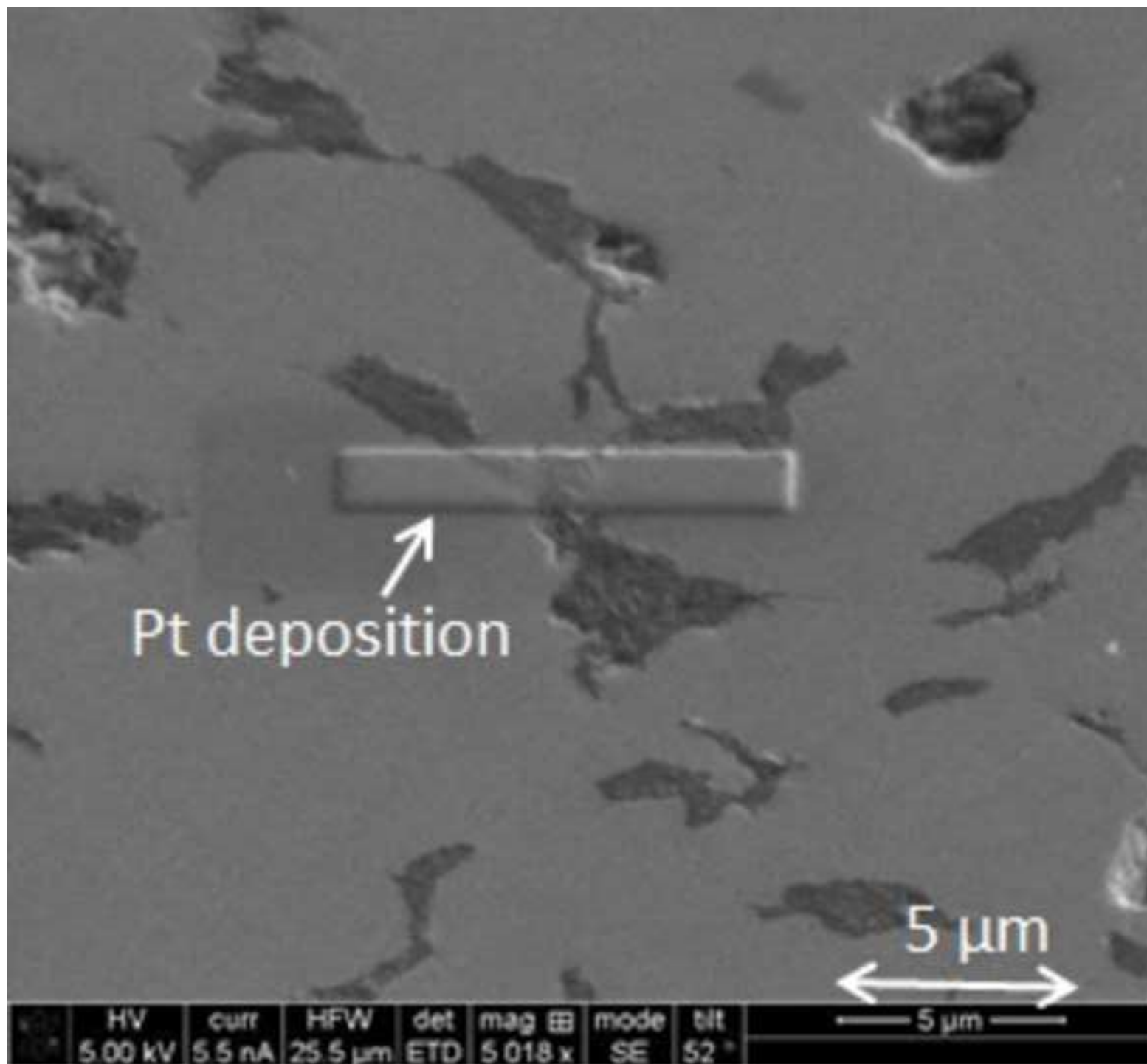


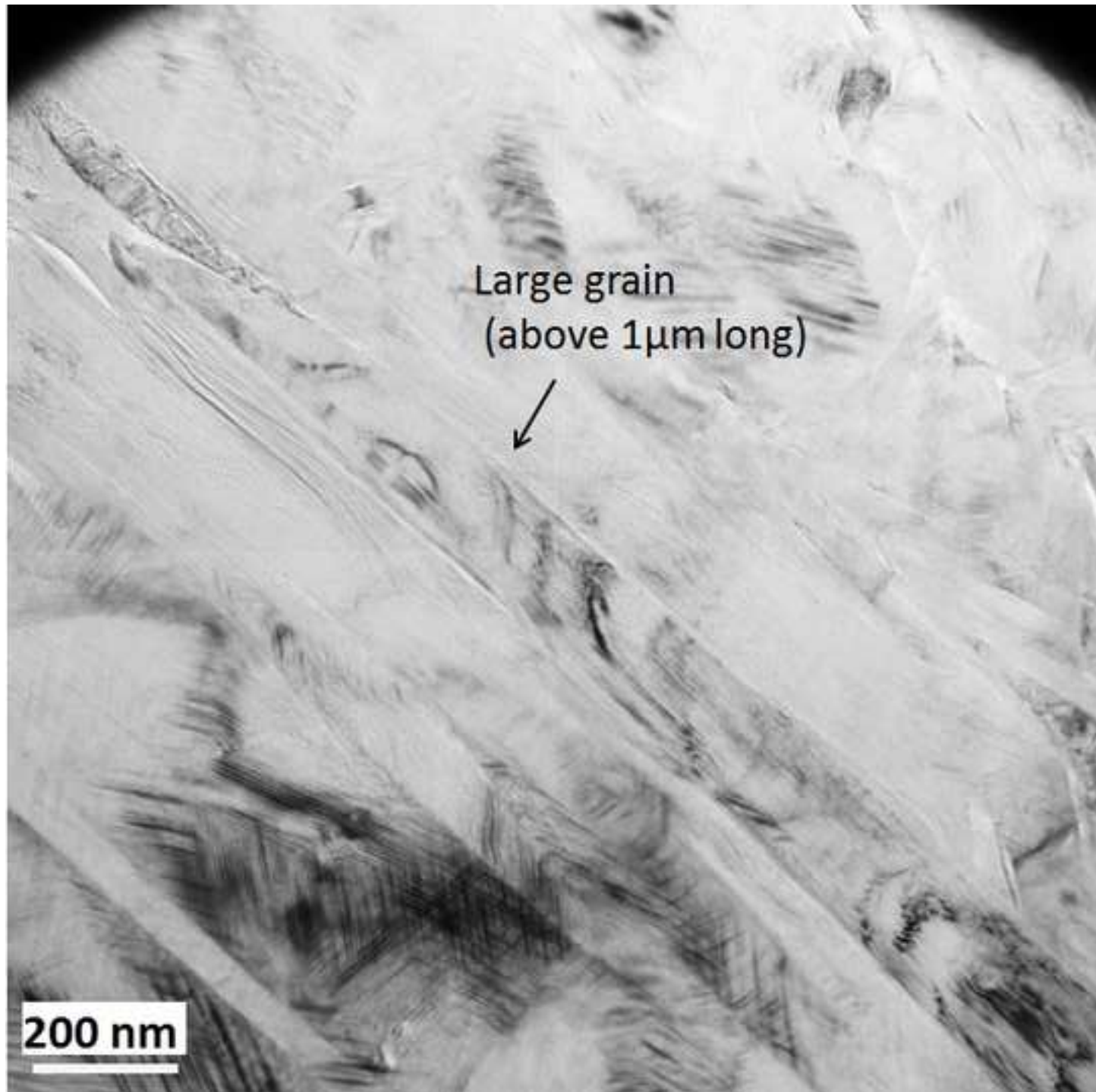
[Click here to download high resolution image](#)

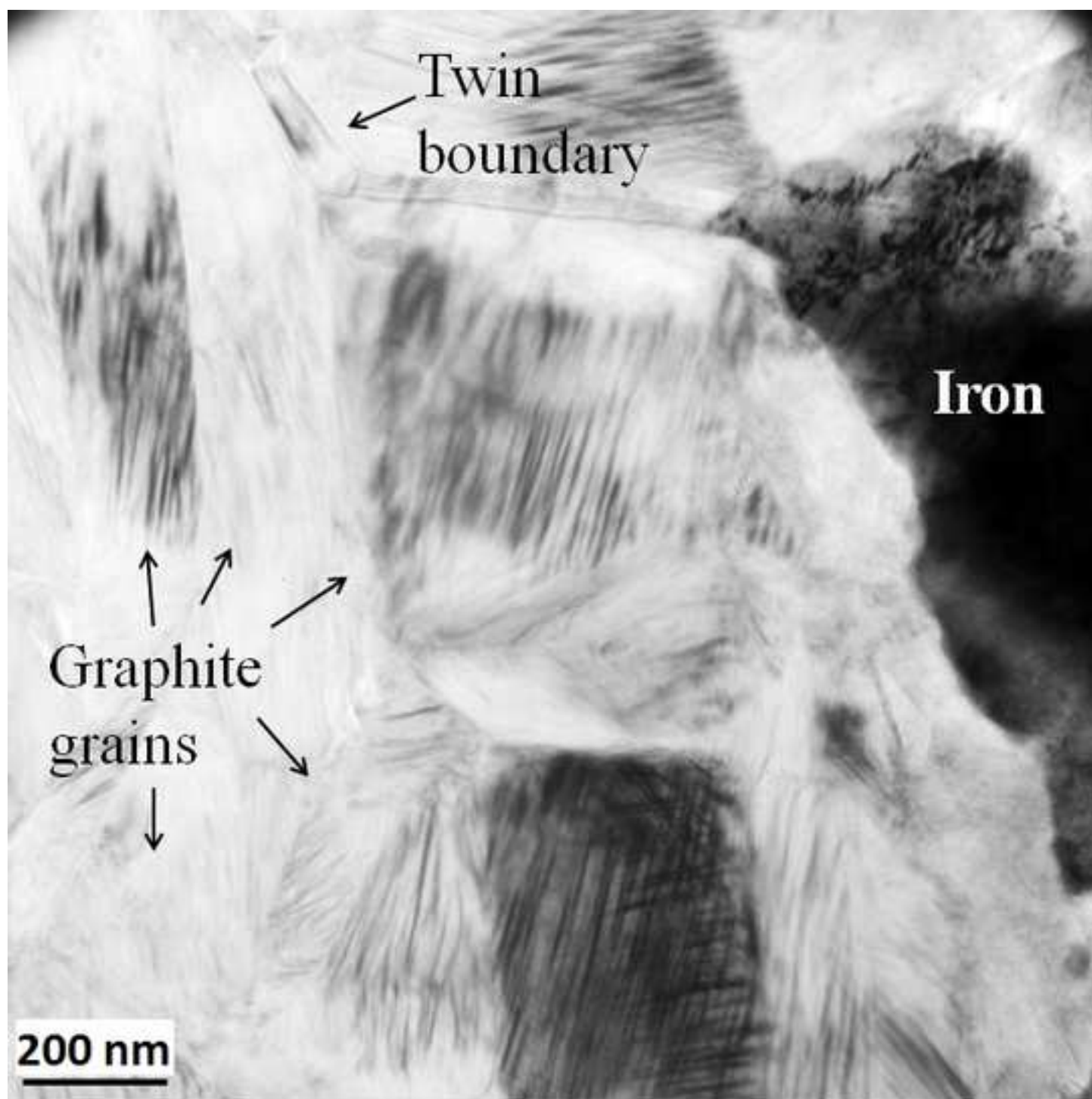


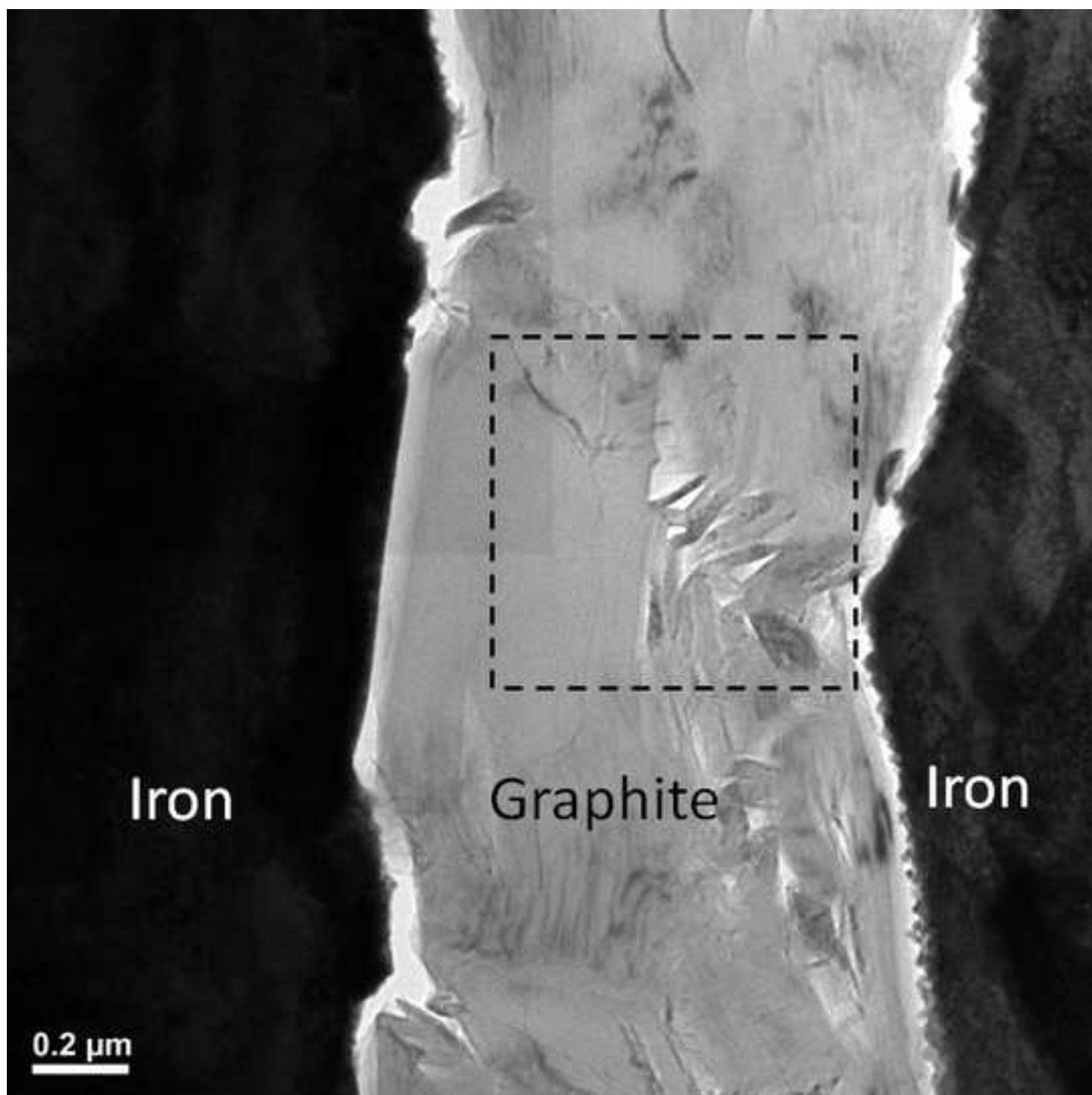




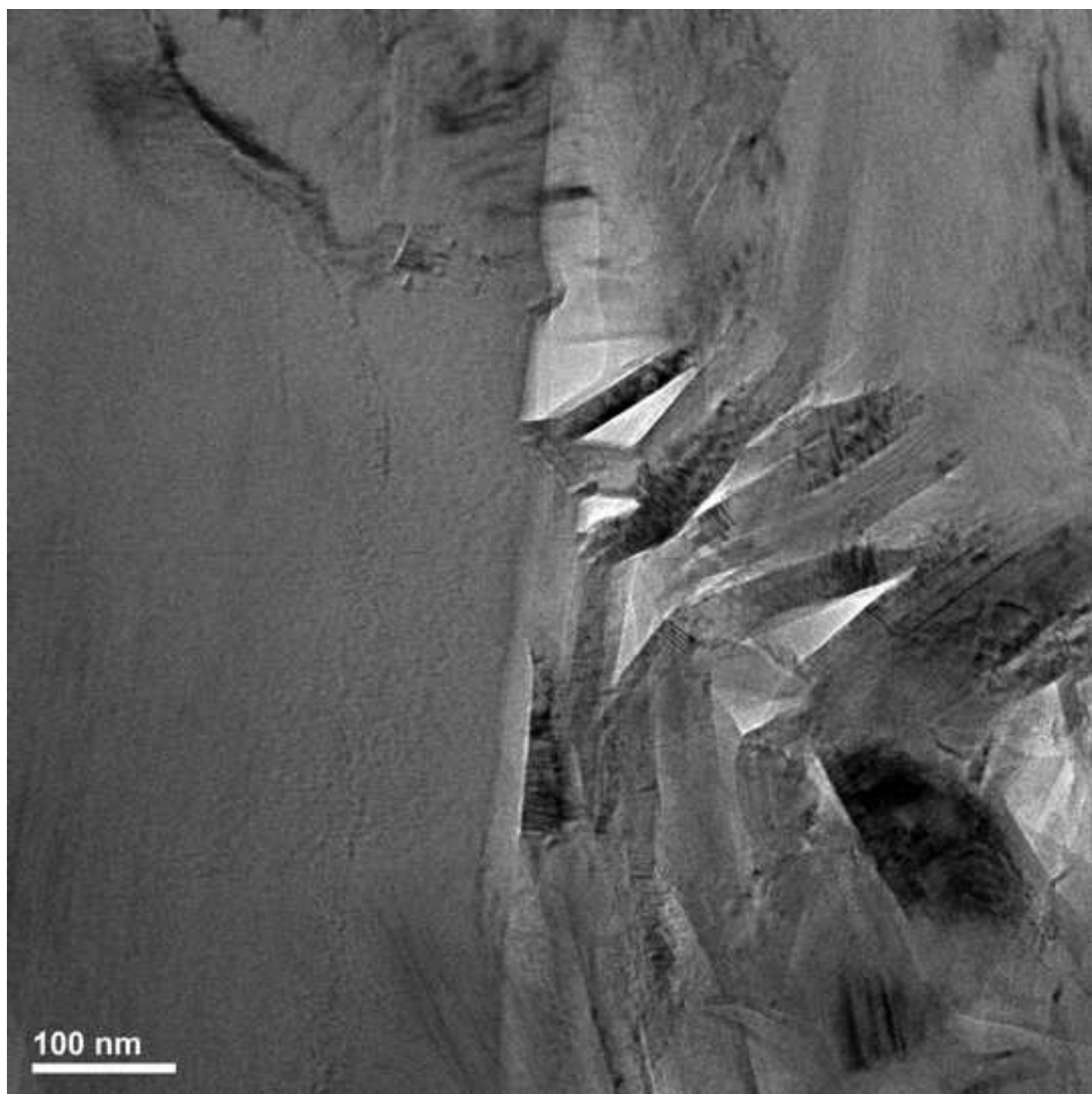




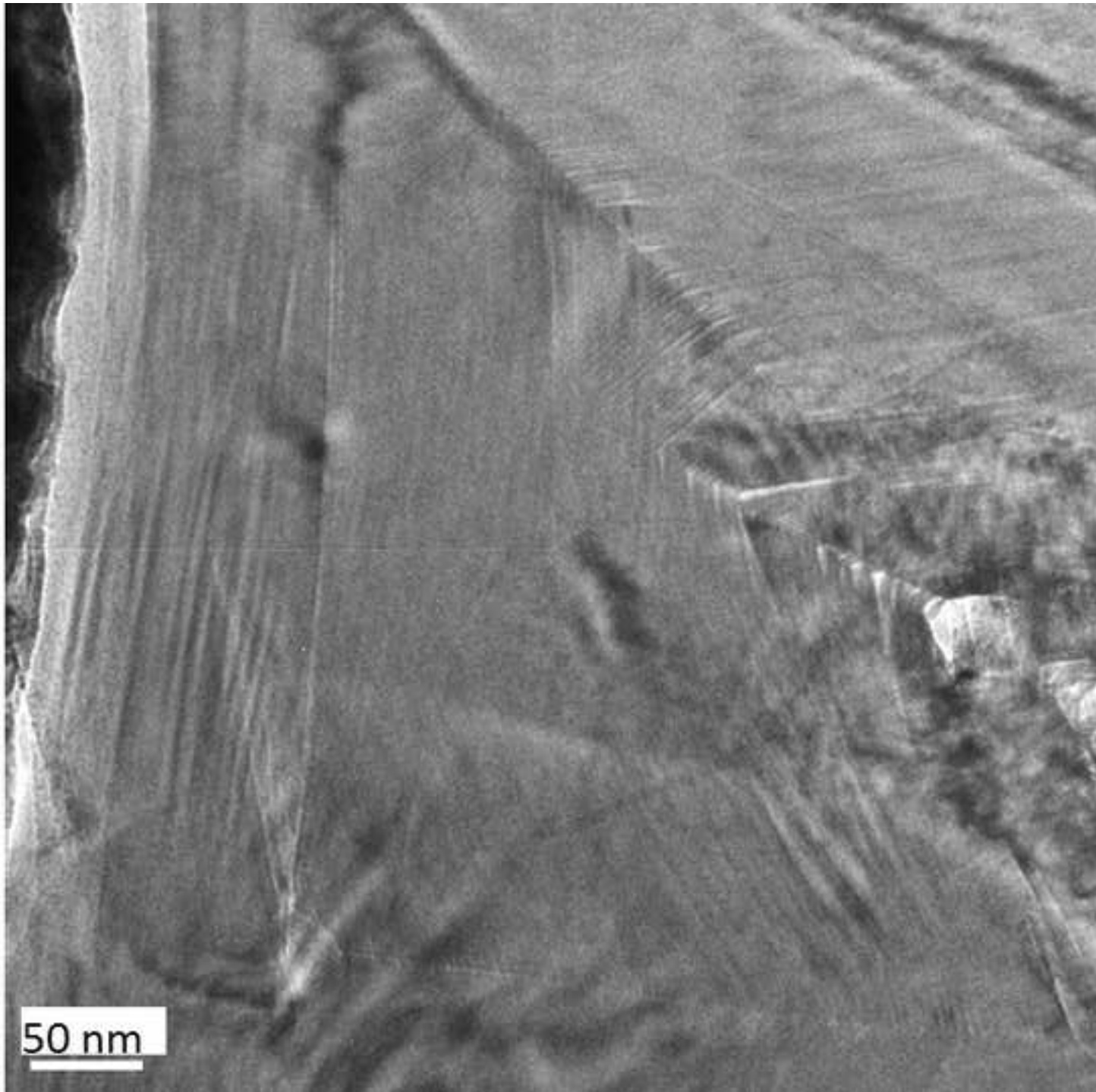




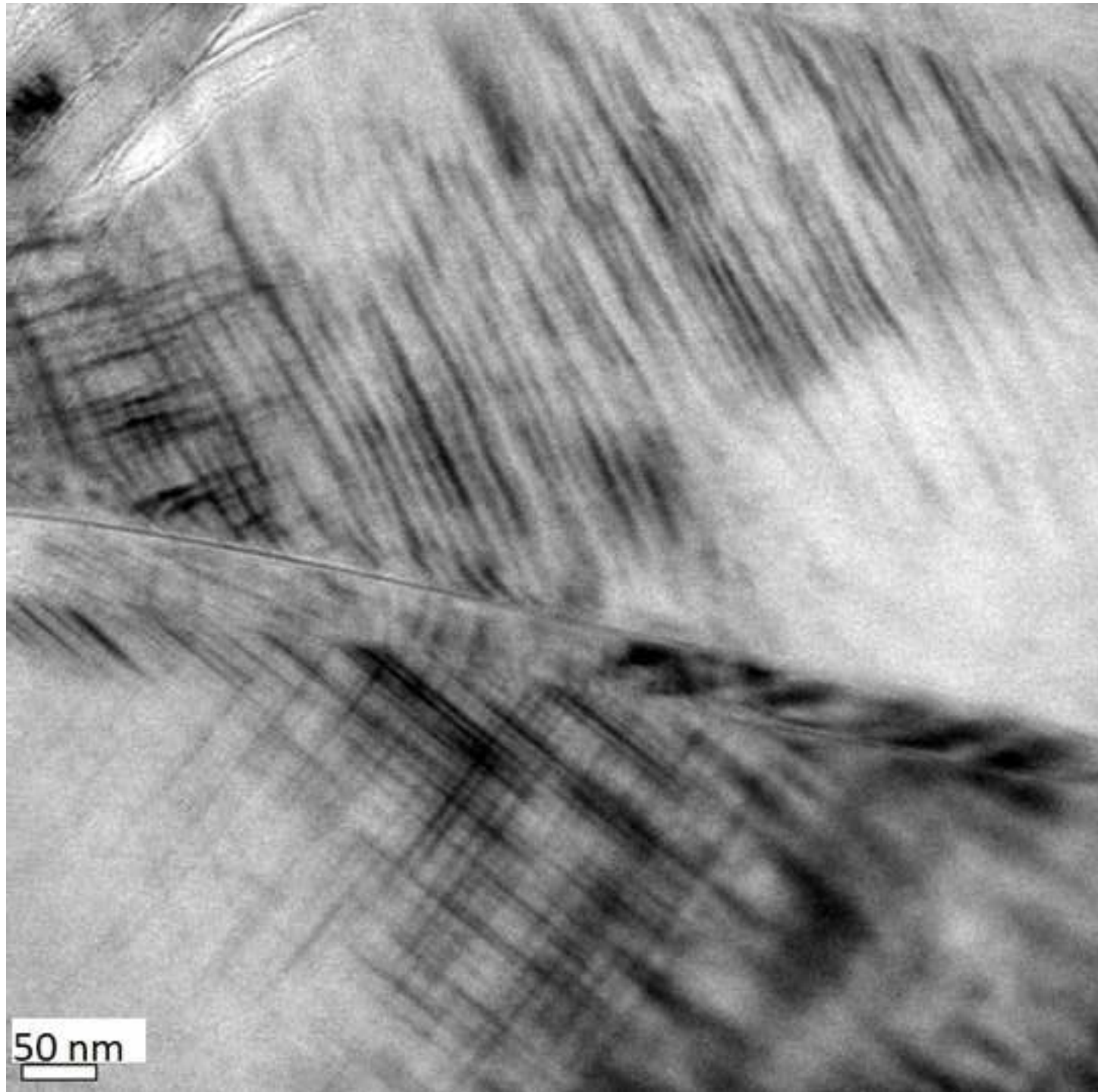
[Click here to download high resolution image](#)

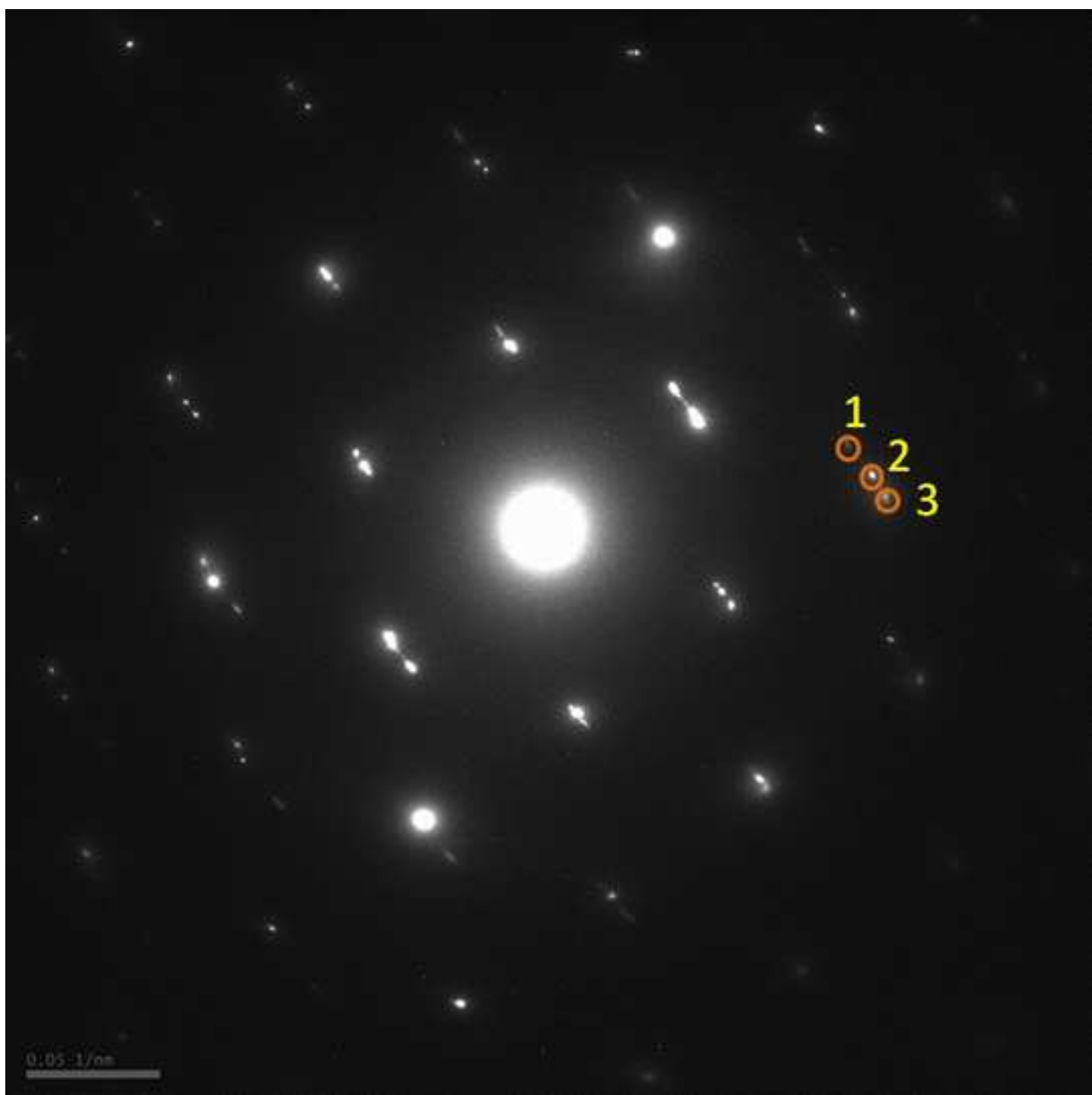


[Click here to download high resolution image](#)

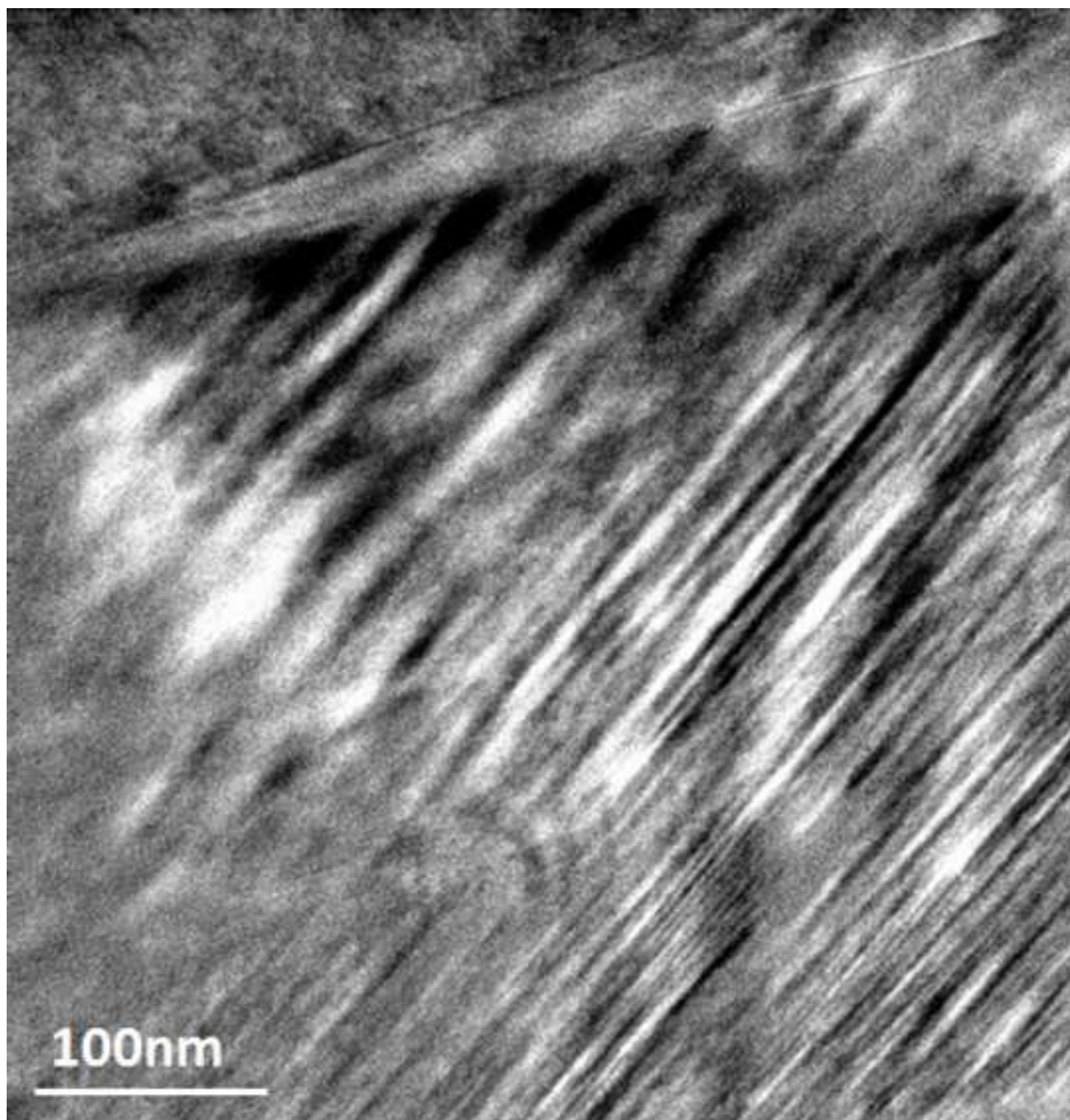


[Click here to download high resolution image](#)

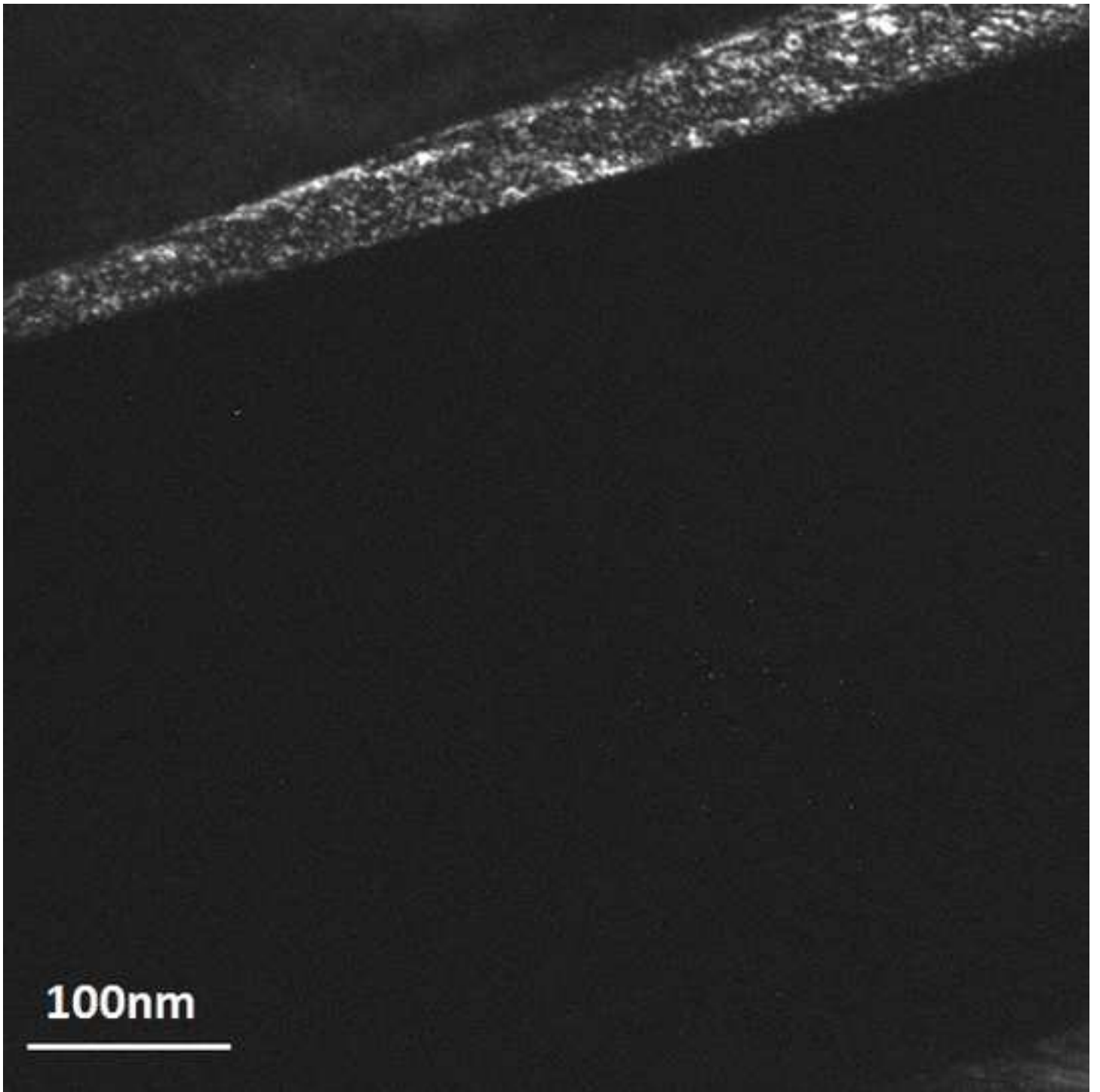




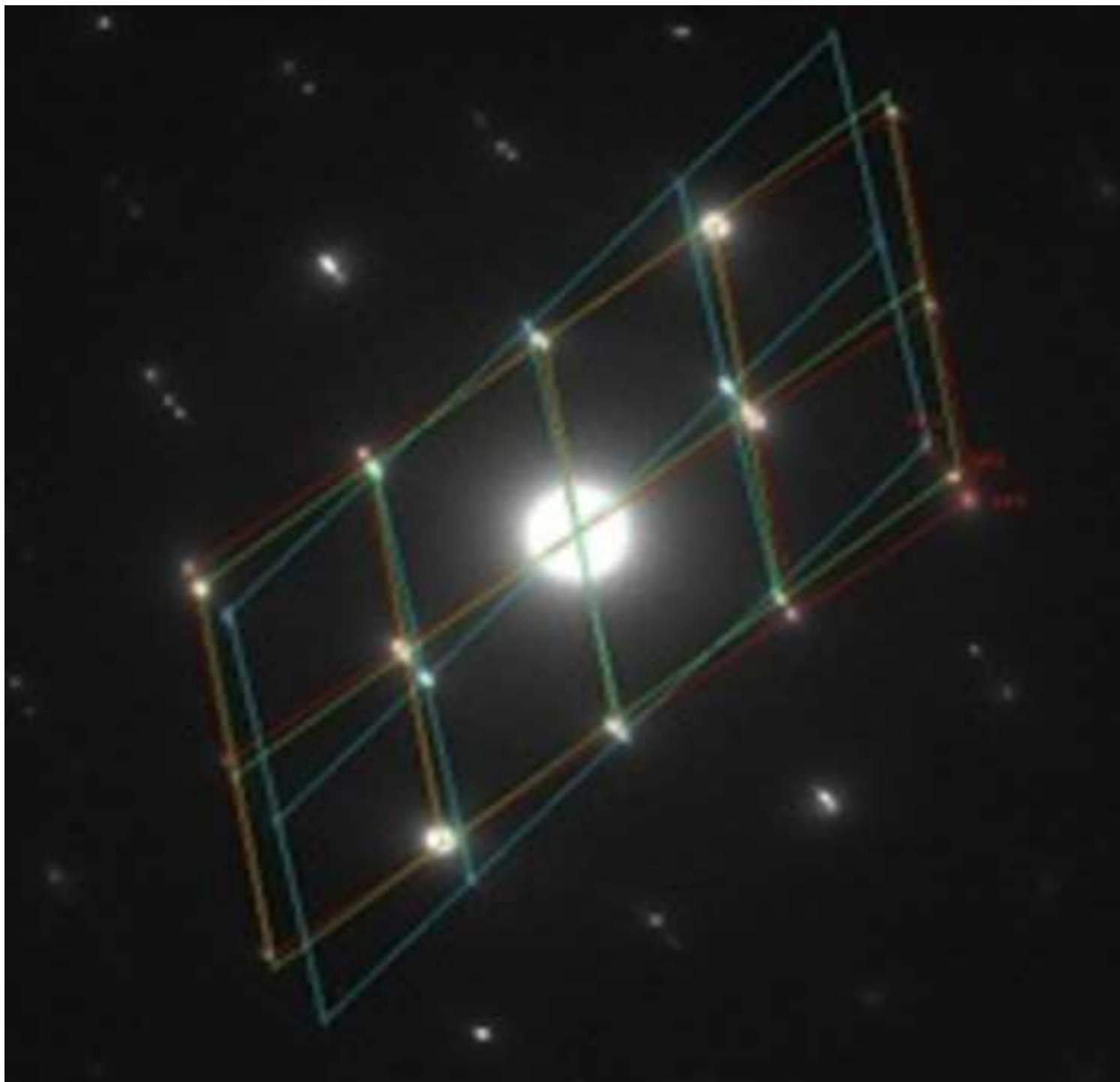
[Click here to download high resolution image](#)



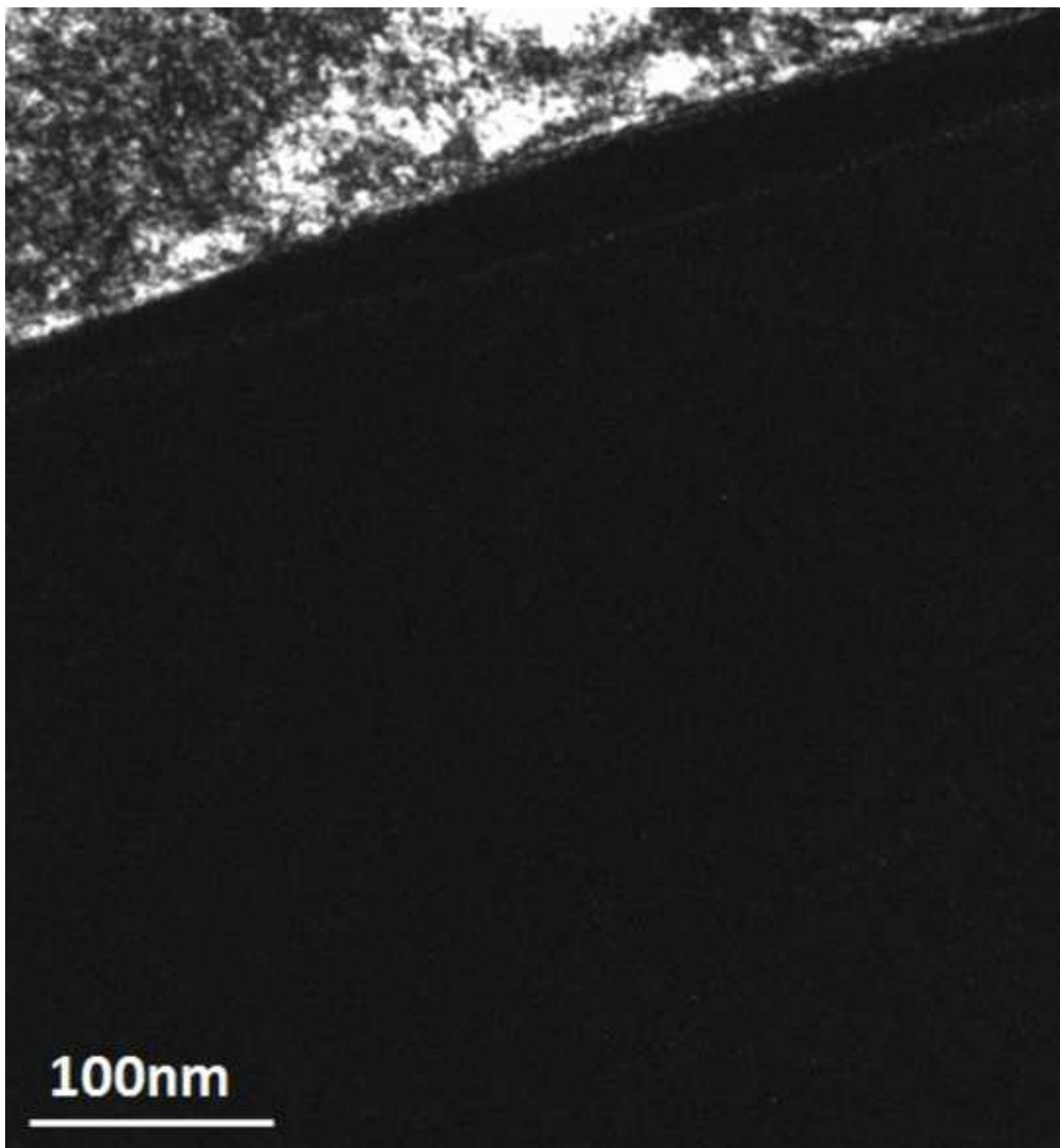
[Click here to download high resolution image](#)



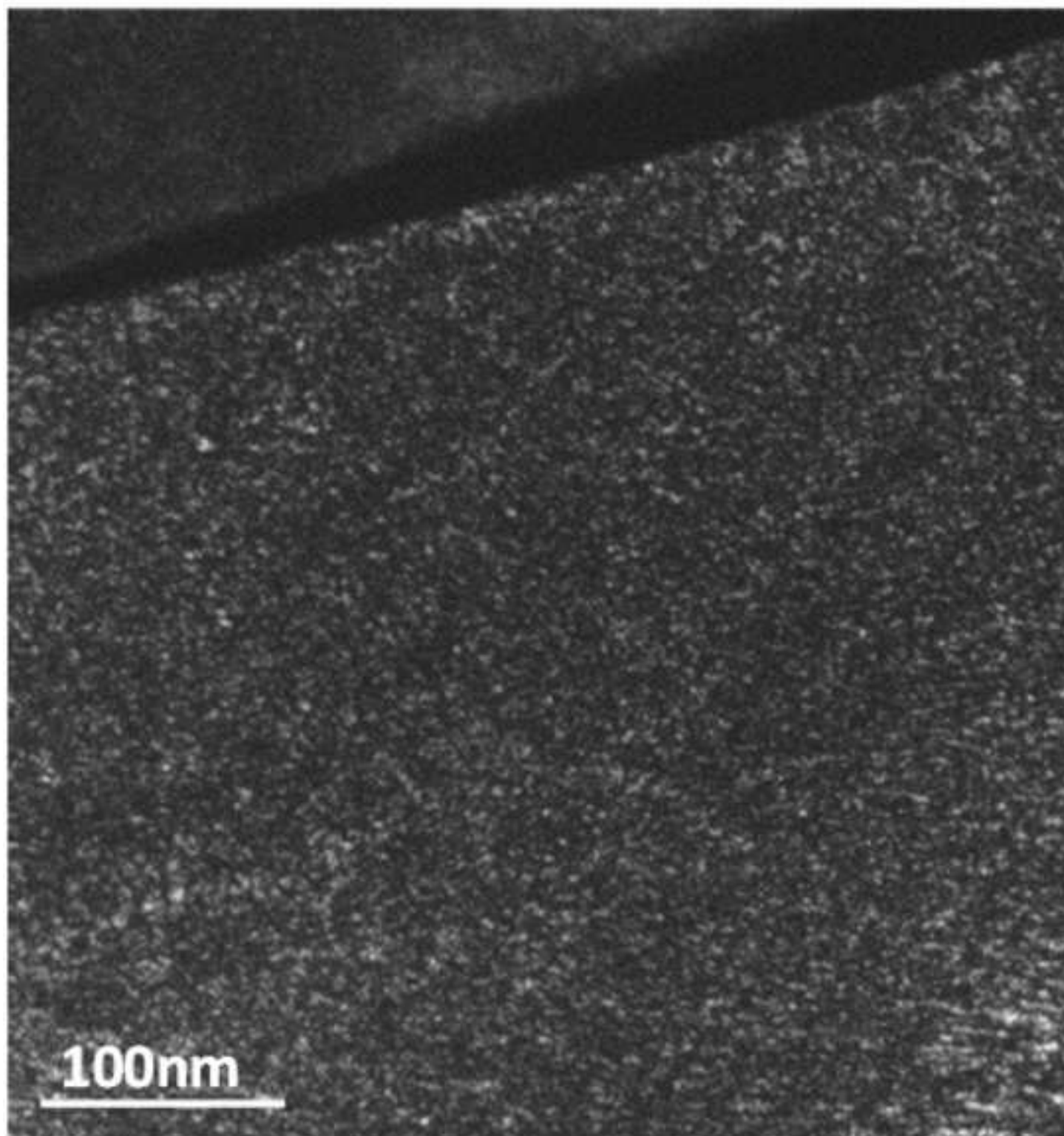
[Click here to download high resolution image](#)



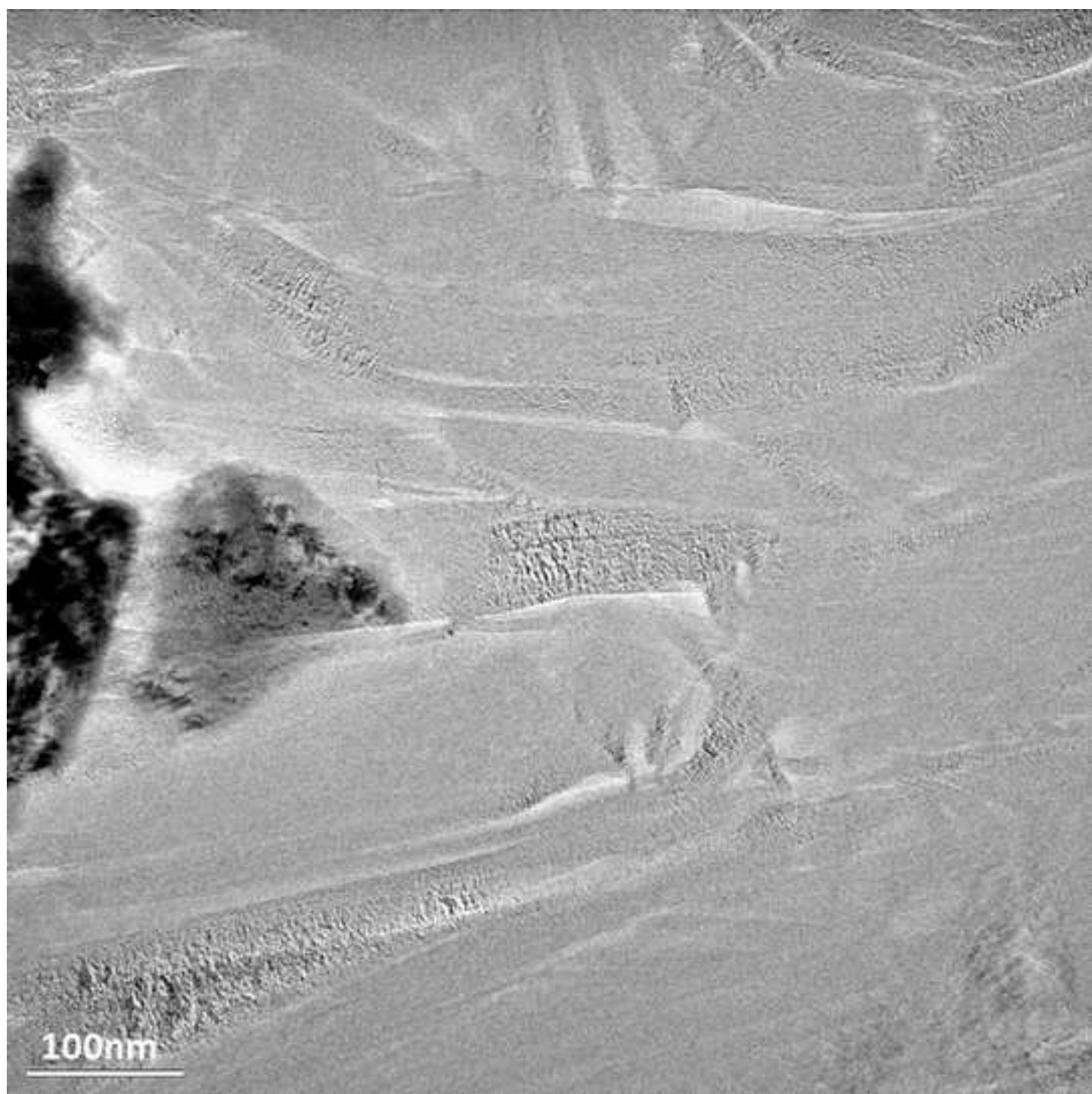
[Click here to download high resolution image](#)

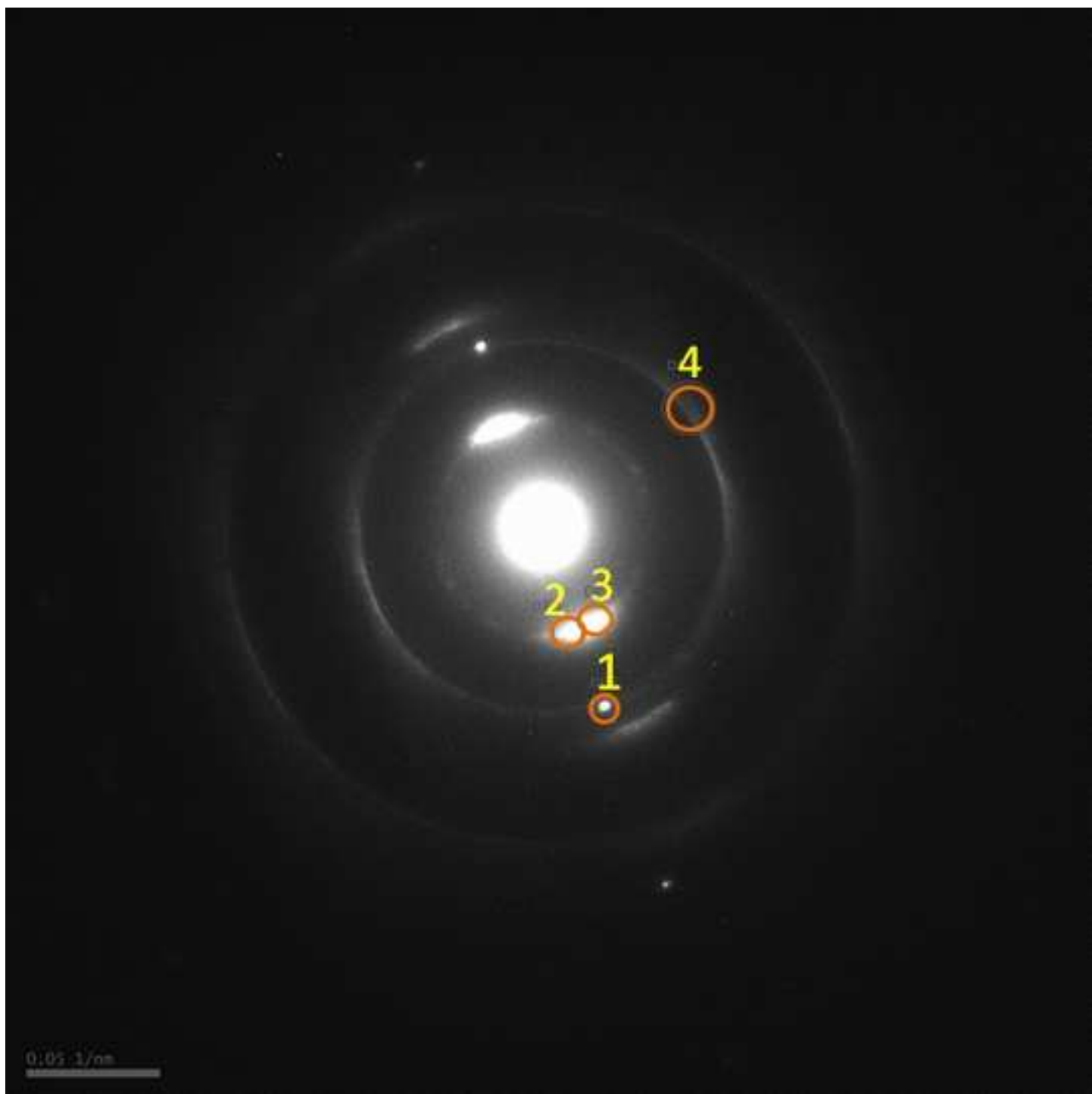


[Click here to download high resolution image](#)

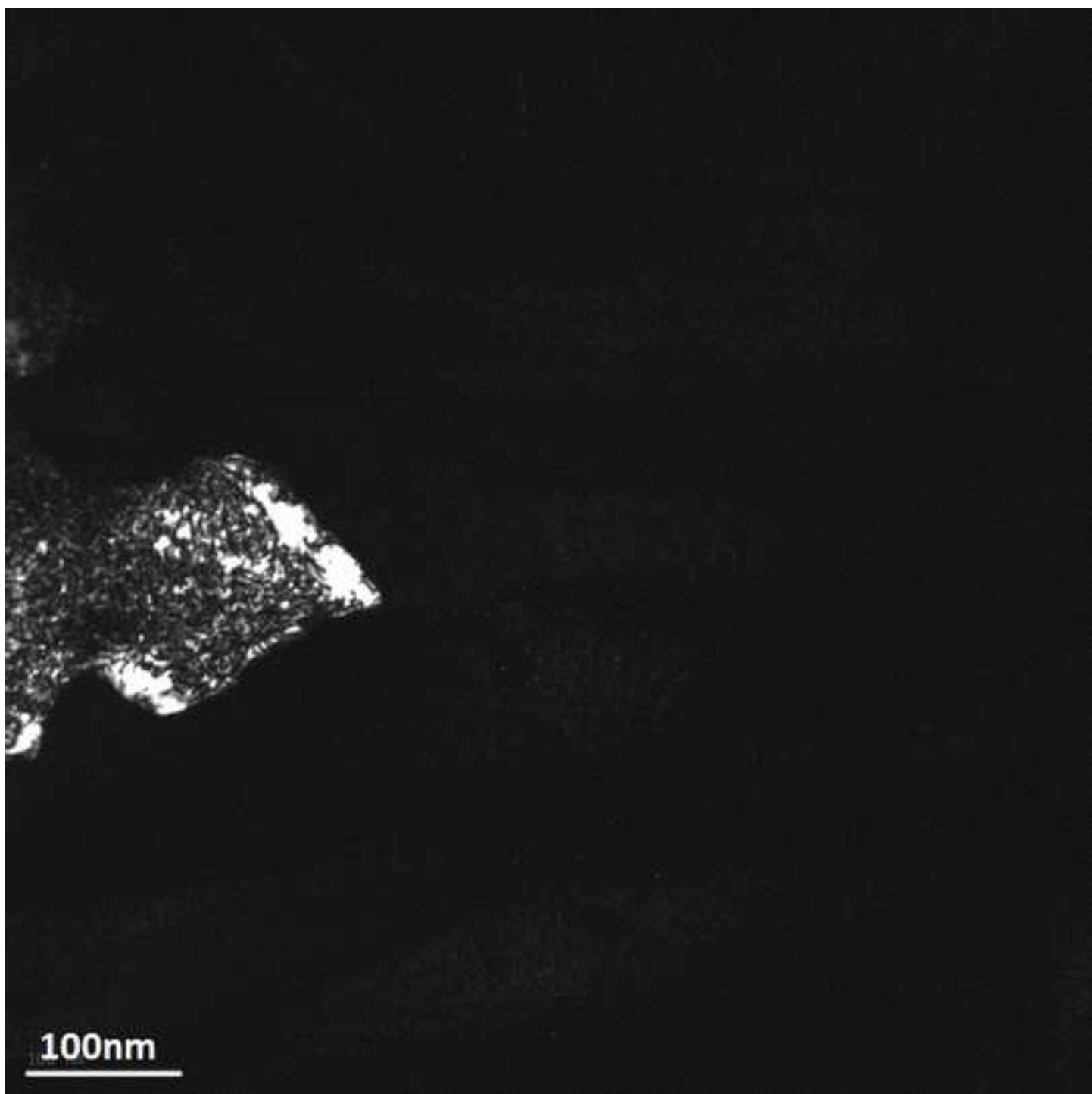


[Click here to download high resolution image](#)

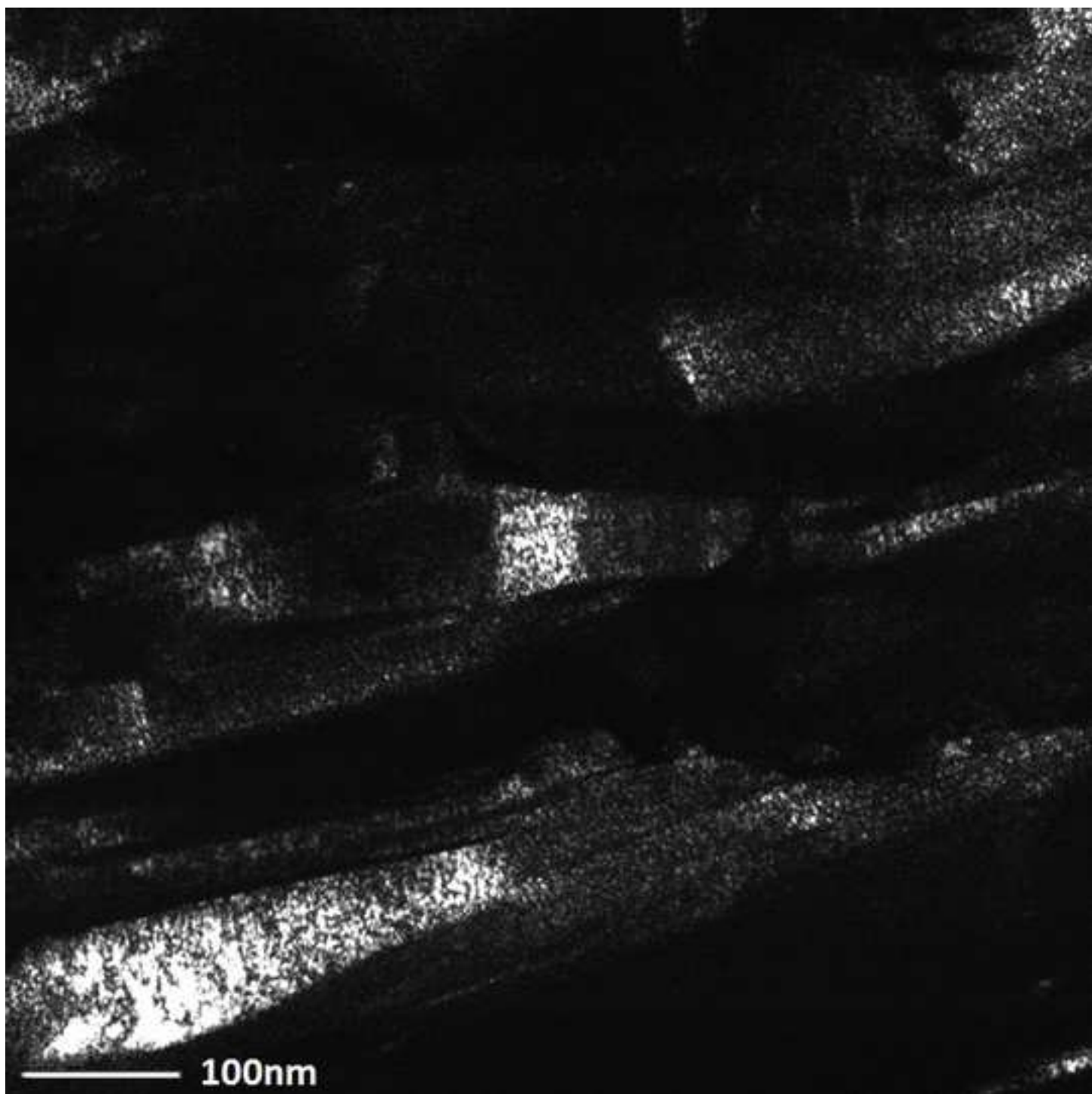




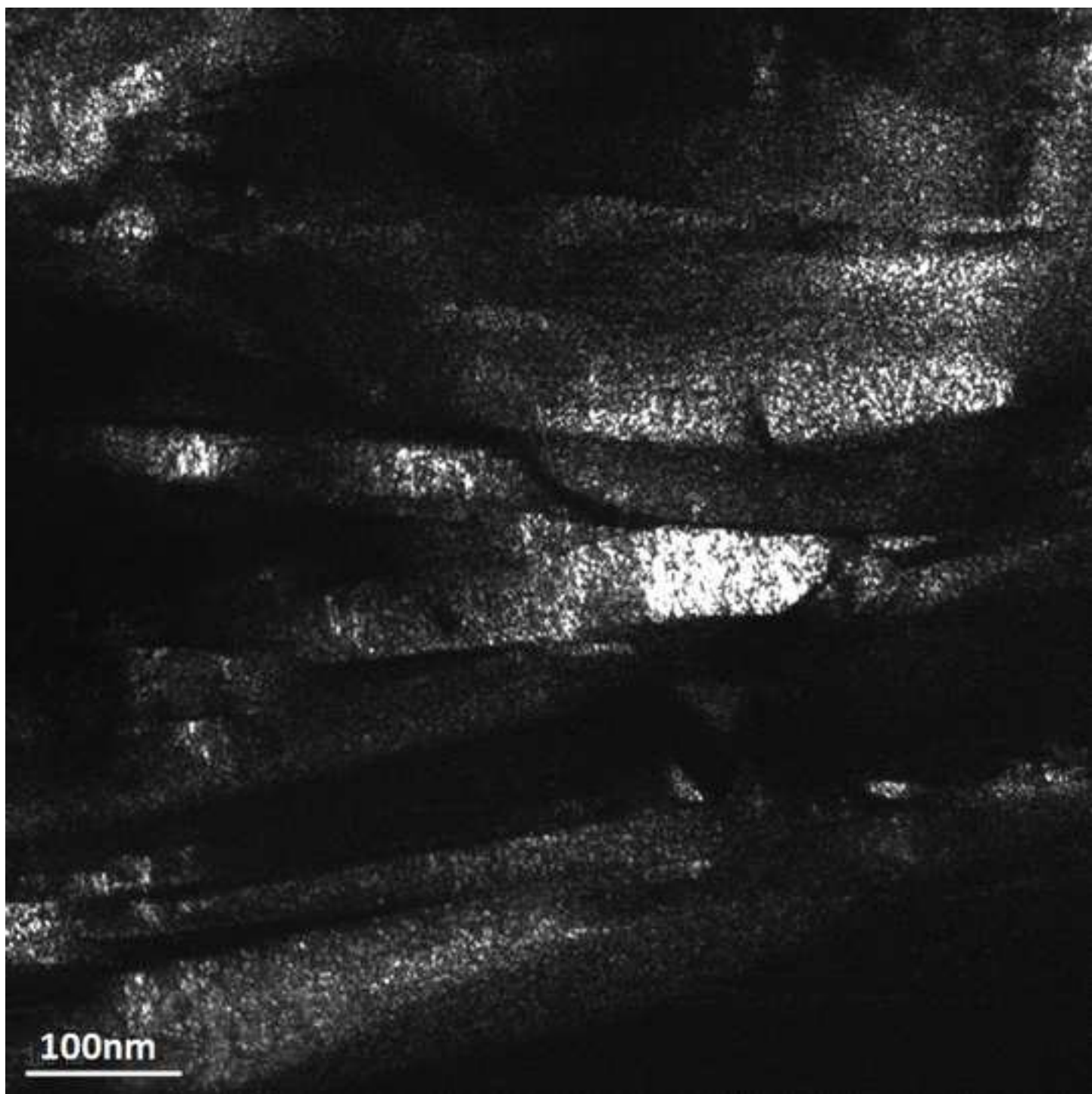
[Click here to download high resolution image](#)



[Click here to download high resolution image](#)



[Click here to download high resolution image](#)



[Click here to download high resolution image](#)

